Impacts of the Immune System on Small Molecule Pharmacokinetics

by

Andrew R. Willmer

A dissertation submitted in partial fulfillment
of the requirements for the degree of
Doctor of Philosophy
(Pharmaceutics)
in the University of Michigan
2023

Doctoral Committee:

Professor Kathleen A. Stringer, Co-Chair
Professor Gus R. Rosania, Co-Chair
Professor Edmund Capparelli, University of California San Diego
Professor Duxin Sun
Professor Haojie Zhu

Andrew R. Willmer

awillmer@umich.edu

ORCID iD: 0000-0002-5966-0068

To those who walk beside me,

one step before the next step

Acknowledgements

Throughout the completion of this work, I would like to acknowledge many people involved in both my research as well as my personal life. First and foremost, I want to thank my advisors Prof. Gus Rosania and Prof. Kathleen Stringer alongside the rest of my committee, Prof. Edmund Capparelli, Prof. Duxin Sun, and Prof. Haojie Zhu for their leadership and guidance throughout my graduate education.

I want to thank the many scientists I encountered along my journey, specifically Jen Diaz-Espinosa, and Mery Vet George De la Rosa for providing camaraderie and scientific support. Steve Dunne, Winnie Wen, Lucy Silmore, and Laura McLellan for helping to make this work possible. And Vernon LaLone alongside Mikhail Murashov for their mentorship early in my scientific career.

Additionally, I want to acknowledge all the people I have had the opportunity to collaborate with including the scientists from John's Hopkins; Dr. Nicole Ammermann, Dr. Rosemary Swansan, and Dr. Deepak Almeida for contributing sample data allowing for the computational analysis used in completion of this thesis. As well as Dr. Mina Nikanjam and again Prof. Edmund Capparelli for extending their tutelage of pharmacometrics analysis and inviting me to contribute to their University of California San Diego clinical pharmacology conference. And Prof. Amit Pai, Dr. Bo Wen, Dr. John Takyi-Williams, and Dr. Lu Wang from the University of Michigan Pharmacokinetics Core.

Finally, I want to acknowledge all my friends and family for their support both emotionally and tangibly throughout my academic journey.

Table of Contents

List of Tables

List of Figures

List of Equations

List of Appendices

Abstract

Many weakly basic drug molecules accumulate in the body after repeated dosing leading to adverse events or long-term morbidity. The macrophage is a lucrative cell of the immune system implicated in many instances of bioaccumulation. Due to the endophagocytic role it occupies in maintaining homeostasis and its disseminated nature in biological systems, macrophages create a perfect environment for the accumulation of drug molecules. As a result, macrophages can induce "context-dependent" pharmacokinetics, or deviations from standard, concentration-dependent pharmacokinetics. This phenomenon can cause time, load, or dose-dependent alterations in drug distribution profiles at therapeutic doses. By examining pharmacokinetic impacts of the macrophage and macrophage storage sites, such as the spleen, we can develop more robust and reliable predictive analyses.

The FDA approved drug clofazimine (CFZ), used in tuberculosis and leprosy, provides an exceptional experimental system to test the hypothesis of bioaccumulation as a mechanism underlying the context-dependent pharmacokinetics in weak bases. Under therapeutically relevant conditions, CFZ forms membrane-bound supramolecular crystal-like drug inclusions (CLDIs) within lysosomes of resident macrophages. Under daily dosing regimens, serum drug concentration remains constant while the organ-associated mass of drug continues to increase throughout the dosing duration. The pharmacokinetic analysis of CFZ within a single macrophage and macrophage containing organs can yield insights into the mechanistic underpinnings of cellular drug disposition, increasing half-life, and increasing organ associated

mass of the drug under constant administration. Integrating physiochemical knowledge of weakly basic molecules with whole body distribution patterns creates a framework for predicting context-dependent pharmacokinetic changes driven by the immune system. Utilizing this approach can directly point to optimal steady-state drug loading to reduce toxicity of exogenous drug molecules. Three global approaches, outlined in this document, were taken to address the impacts of the immune system on pharmacokinetics, (1) exploring the pharmacokinetic impact of a growing macrophage population in the spleen, (2) identifying accumulation patterns underlying drug transport within a single macrophage, and (3) evaluating the pharmacokinetic influence of removing the spleen, a drug-sequestering macrophage reservoir.

Through this research, CFZ concentration predictions in the spleen and serum were improved upon over static compartmental modeling approaches by increasing the half-life and expanding the volume of distribution over the course of dosing. By incorporating context-dependent adaptations seen in previous studies into CFZ pharmacokinetics models, more accurate, mechanistically driven computational predictions were observed. The mechanism behind this population driven change in pharmacokinetics was further shown to be driven by immunological factors and macrophage microenvironments. A single-cell computational macrophage model, constructed with physiologically relevant conditions, pointed to a thermodynamically favorable drug flux, leading to massive accumulation of drug into a single macrophage under therapeutic extracellular concentrations. This accumulation was shown to be disrupted in the presence of intracellular pathogens indicating infection as an important pharmacokinetic covariate in small molecule drugs which accumulate within the lysosome. And finally, by removing the spleen and thereby mechanically reducing the total volume of distribution, no tissue dependent differences in CFZ concentration or catabolism was observed.

However, the immune disruption caused by drug treatment after spleen removal points to an immune sensitivity that warrants consideration during prolonged drug treatment in asplenia.

Chapter 1 Introduction

With growing interest in biological therapeutic agents and complex formulations, the cost of medicine has continued to climb. The need for cost-effective innovative solutions is self-evident. Utilizing and understanding the unique pharmacokinetics of small molecule drugs under biological stresses to create self-assembling devices reduces the need for costly formulations and takes advantage of our existing biological machinery to reduce the financial burden on our society and improve medical care. This thesis addresses the need to re-evaluate the understanding of concentration dependent steady state in the context of xenobiotic therapeutics causing and undergoing phase transitions.

1.1 Background and Significance

1.1.1 Adverse Drug Reactions

Despite rapid medical advancements, adverse drug reactions remain a dominant cause of morbidity resulting in over 3.5 million visits to physicians and account for one-third of all adverse events in the hospital setting [1]. It is estimated that 3-7% of all hospitalizations are due to adverse drug events, with as high as 12% of total admissions in the elderly population [2, 3]. Despite the large impact from adverse drug reactions in our health systems, this is only a fraction of the population experiencing drug toxicity after considering the number of patients quietly enduring minor complications. Alongside improving hospital policies and clinical workflow,

building tools to enhance personalized dosing and precision medicine will vastly reduce drug related errors and adverse effects.

To reduce adverse effects and improve upon our collective understanding of drug dosing, pharmacokinetic frameworks and computational models have been at the forefront of dose selection in novel and existing drug products. Many commonly used medications, under therapeutic regimens, follow a predictable linear elimination pathway that is invariant with respect to dose. However, some medications exhibit “context-dependent” pharmacokinetics, which encompasses dose-, time-, and load-dependent variances in drug distribution over the course of dosing.

In addition, many weakly basic drug molecules tend to bioaccumulate after repeated dosing leading to adverse events or long-term morbidity. Drug accumulation can occur from a myriad of factors, all of which stem from ingesting a higher quantity of drug than is being eliminated. The circumstances which may cause accumulation can be due to patient factors, or physiochemical properties of drugs in biological systems. Amongst others, patient factors may include reduced renal clearance due to kidney failure or reduced metabolic clearance due to decompensated cirrhosis. From the physiochemical perspective, some drugs may exhibit high fat partitioning coefficients leading to large quantities of drug sequestered into fat tissue, other medications may complex with circulating blood proteins or cellular components leading to complexes too large to be cleared renally or metabolically [4]. Another form of bioaccumulation can occur due to xenobiotic moieties inducing phase-transitions. Such transitions can take many forms, including soluble-to-insoluble phase transitions where normally dissolved molecules begin to precipitate out of solution, and drug-lipid complexes that begin to accumulate in large physiologically relevant quantities, such as in phospholipidosis.

The macrophage is a lucrative cell implicated in many instances of bioaccumulation. Due to the endophagocytic role it occupies in maintaining homeostasis and its disseminated nature in biological systems, macrophages create a perfect environment for xenobiotic accumulation. The circumstances of accumulation are typically viewed in a negative light, but the fertile environment inside macrophages for accumulation may also provide opportunities to capitalize on unique formulations such as self-assembling drug eluting depots.

Rising medical costs over the last century have led to an ever-increasing state of financial and mental burden on patients. A reduction in adverse drug events will lead to fewer hospital and clinic visits alongside an improvement in patient quality of life. Innovative solutions are necessary to reduce the societal burden of medication side effects and adverse reactions. By developing a deterministic framework for identifying trends in bioaccumulation we can reduce risks of adverse events and improve viability of accumulating small molecule drugs in pharmaceutical development.

1.1.2 Context-Dependent Pharmacokinetics

Pharmacokinetic properties that change over the course of dosing can be considered context-dependent pharmacokinetics. Upon repeated dosing, the drug elimination, absorption, or distribution may be altered, resulting in changes to half-life, rate of absorption, bioavailability, or volume of distribution [5]. Most commonly, literature refers to this phenomenon as dose-dependent pharmacokinetics. Several mechanisms can be the cause of this adaptive pharmacokinetic profile, including drug saturation, variable absorption, metabolic inhibition, or even dose dependent molecular binding.

For instance, excessive loading of drug may saturate enzymes used to metabolically eliminate drug, and therefore change the system from linear pharmacokinetics to zero order pharmacokinetics. Ethanol is a classic example of a compound with dose-dependent pharmacokinetics, as oversaturation of metabolic enzymes leads to a change from first- to zero-order elimination kinetics at a relatively low dose [6]. The resulting rate of elimination shifts from concentration dependent clearance to a constant rate of clearance based on peak enzymatic activity. Prednisolone is another example of a compound with dose-dependent pharmacokinetics which binds to tissues at increased doses shifting the apparent volume of distribution at higher dosing intervals. Sulfasalazine, and anti-inflammatory medication, shows decreased absorption with higher doses, indicating different bioavailabilities and resulting pharmacokinetic profiles at different oral doses [7]. Clofazimine is a drug that also exhibits context-dependent pharmacokinetics. As the drug becomes sequestered in insoluble crystalline precipitates within macrophages, the volume of distribution increases and half-life increases accordingly [8, 9].

1.1.3 Macrophages and Their Role in Drug Distribution

The macrophage is a complex and unique cell with multifactorial utility within our bodies. Simultaneously carrying out essential immune function by ridding our body of infection and maintaining balance by eliminating unwanted molecules and precipitates. These cells occupy almost every tissue in our body including the lungs (alveolar macrophages), liver (Kupffer cells), bone (osteoclasts), and spleen. Depending on the occupied tissue, macrophages assist in the innate immune system, adaptive immune system, and play supportive roles in homeostasis and physiological functions.

Macrophages function as part of the innate immune system maintaining homeostasis by ingesting foreign materials, dead cells, and cellular debris [10]. Additionally, these cells can function as effectors for cell-mediated immunity by presenting antigens to T cells, thereby providing aid to the adaptive immune system in conjunction. From a physiological standpoint, alveolar macrophages are necessary for processing surfactants and aid in the isolation and sterilization of lung infections such as tuberculosis. Kupffer cells maintain functional iron metabolism, are essential in removing damaged erythrocytes, and aid in the clearance of gut derived pathogens. Additionally, Kupffer cells secrete anti-inflammatory cytokines and contribute to tissue repair [10]. The spleen, organized into red pulp and white pulp regions, contains many types of macrophages, mostly filtering blood and recycling aging red blood cells [11]. While differentiation and maturation of macrophages typically occurs in the bone marrow, splenic hematopoiesis has been reported in several animal models.

To maintain homeostatic balance within the body, the macrophages eliminate unwanted matter by phagocytosing and sequestering to the highly acidic lysosome. The lysosomal pH is primarily driven by many H+-ATPase transporters [12]. This property of macrophages allows for the destruction and breakdown of pathogens to ultimately utilize the products in other cellular processes. In the case of unwanted drug products, macrophages may accumulate small molecule drugs or drug precipitates in the bloodstream through phagocytosis. However, unlike other endogenous chemicals or biological remnants, macrophages may not have the biological machinery to digest all xenobiotic molecules in the same fashion.

1.1.4 Mycobacterial Infections, Treatment Challenges, and Epidemiology

Mycobacterial infections are a group of acid-fast pathogens unique amongst the litany of cellular infectious agents. While most bacterial agents are extracellular parasites, many mycobacterial infections reside and multiply within our cells [13]. This presents a distinct therapeutic challenge that creates significant morbidity and mortality globally.

Tuberculosis, caused by mycobacterium tuberculosis, was the deadliest infection worldwide in 2019 with 1.4 million deaths and a mortality rate of 12.3% [14]. Treatment success of drug sensitive tuberculosis is 80.1%, with lower success rates in patients co-infected with HIV or drug resistant strains [15]. With increasing numbers of multi-drug resistant and extensively drug resistant strains, large apparent need for innovation presents itself. While the title of deadliest infectious disease was overtaken by SARS-COV-2 in 2020, tuberculosis continues to be a significant epidemiological burden.

Less virulent non-tuberculosis mycobacterial infections such as M. avium and M. intracellulare are colonized in many bronchial and intestinal mucosal surfaces of healthy individuals. While not immediately pathogenic, these infections can become problematic for patients with immunodeficiency such as patients with AIDS or elderly patients with depleted T-cell-mediated defense. For these immunocompromised patients, up to 50% may develop mycobacterial infections at some point in their lifetime [13].

Tuberculosis is commonly isolated to the lungs with high likelihood of infection from aerosolized disease, making this pathogen highly contagious [16]. Tuberculosis continues to be a worldwide concern with increased incidence of multi-drug resistant, and extensively drug resistant strains. In 2019, tuberculosis was the largest cause of death by infectious disease and in the top 10 causes of death worldwide [17].

Tuberculosis is highly treatable with a common four to five drug combination therapy, with treatment duration typically spanning one to two years [18]. Despite the high treatability of the disease, burgeoning resistance to established therapies continues to limit treatment options. Tuberculosis can be classified as new onset, recurrent disease, latent, multi-drug resistant, or extensively-drug resistant tuberculosis. While drug sensitive tuberculosis was successfully treated in 80% of patients in 2019, multidrug resistant tuberculosis treatment is only successful in 58.7% of patients, and extensively drug-resistant tuberculosis was only successful in 27.1% of patients, establishing a need for improved therapeutic options [14].

1.1.5 Clofazimine as an Antimycobacterial Therapeutic and Bioaccumulating Agent

Clofazimine (CFZ) is a weakly basic small molecule drug that was approved by the FDA in 1986 for the treatment of lepromatous leprosy, a mycobacterial infection [19]. Leprosy was a significant health burden prior to 2012 but has since been mostly eradicated from most western societies [20]. The use of CFZ has significantly decreased since the near eradication of leprosy but has recently received increased clinical interest due to its efficacy in tuberculosis in both humans and pre-clinical animal studies [9]. The average daily dose of CFZ ranges from 100 to 200 mg per day, usually in combination with one or more additional antimycobacterial agents. However, the optimal dose of CFZ is largely unknown. With repeated administration in humans, the most commonly reported adverse events are skin and body fluid discoloration, alongside gastrointestinal discomfort and intolerance [19].

The exact mechanism of CFZ is not known but has been shown to have anti-mycobacterial activity *in vitro* and *in vivo* alongside anti-inflammatory properties [18, 21]. In recent years, CFZ has had increased interest in tuberculosis due to growing multi-drug resistant

strains and a WHO endorsed short course regimen utilizing CFZ. While CFZ has moderately desirable effects on mortality, treatment success, and culture conversions alongside low risk of adverse effects, an important patient satisfaction consideration of skin discoloration has led to reduced acceptability in a clinical context. As a result, fewer trials have been conducted prior to the development of multidrug and extensively drug resistant strains of tuberculosis. Where multi-drug resistant tuberculosis is concerned, CFZ is not used as widely as many other antimycobacterial agents such as bedaquiline and linezolid. To counteract increasing drug resistant strains, more therapies need to be identified and thoroughly understood to reduce the constant evolutionary pressure of this deadly disease. Currently the WHO recommends CFZ as a core second-line agent for drug-resistant tuberculosis [18].

In the United States, CFZ is available for use in tuberculosis under an investigative new drug protocol only. Little is known about the optimal dosing regimen, however, mice infected with tuberculosis exhibited a dose-independent response to CFZ monotherapy at a variety of dosing regimens [9]. The American Thoracic Society claims additional research is required regarding loading doses and optimal dosing of CFZ to increase its usage [18].

1.1.6 Intracellular Transport and Salt Formation Equilibrium

For mycobacterial infections, intracellular activity is desirable, and CFZ is a drug which preferentially accumulates intracellularly. Concentration dependent intracellular movement of drug particles always seeks equilibrium across membranes and throughout the system. CFZ has two sites of protonation with corresponding pKas of 2.31 and 9.29 indicating the predominant species of CFZ will be monoprotonated at lower physiological pH [22]. The pHmax, or pKa Gibbs, which is the maximum pH at which the solution is saturated with both the free base and

cationic species, of CFZ is 4.5. Figure 1.1 illustrates CFZs protonatable sites and solubility curve with increasing pH.

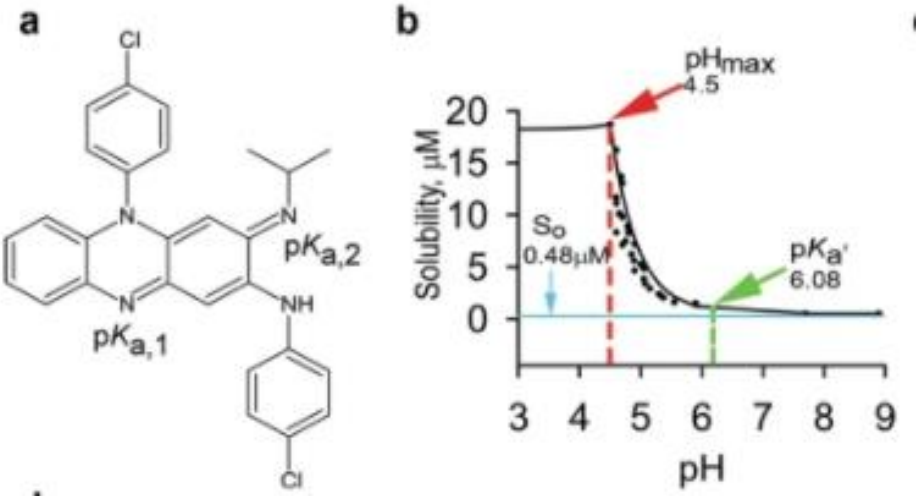

Figure 1.1: CFZ Structure and Solubility a) CFZ structure and protonatable sites, b) solubility curve with ascending pH [22]

Each organelle within the cell has a unique environment tailored to its function and a corresponding pH with optimal conditions to match the utility. The lysosomal environment has the lowest pH within the cell and therefore within this the predominant form of CFZ will be protonated. This is illustrated by the Henderson-Hasselbalch equation (Eq. 1.1) [23], which shows as the pH decreases, the ratio of basic species to acidic species must decrease as well, increasing the relative concentration protonated CFZ.

Equation 1.1: Henderson-Hasselbalch Equation

$$pH = pK_a + log\frac{[B]}{[BH^+]}$$

Equations 1.2 and 1.3 illustrate the reaction equilibrium of CFZ shown in Figure 1.2. Following Le Chatelier's principle acidic environments, like that of the lysosome, will alter the equilibrium between forms of CFZ and cause a right shift in equation 1.2. The buildup of protonated species will then cause a right shift in equation 1.3 resulting in increased CFZ hydrochloride salt formation.

Equation 1.2: Protonated CFZ Equilibrium

$$CFZ\ (aq) + H2O\ (l) \rightleftharpoons CFZH+\ (aq) + OH-\ (aq)$$

Equation 1.3: CFZ Hydrochloride Equilibrium

$$CFZH+\ (aq) + Cl-\ (aq) \rightleftharpoons CFZH+Cl-\ (aq)$$

Additionally, the weakly basic CFZ is affected by the ion trapping phenomenon during transmembrane diffusion. Due to the non-polarity of cellular membranes, charged or highly polar molecules have difficulty crossing the phospholipid bilayer membrane. This phenomenon comes into play when pH on either side of the membrane is not equivalent. At lower pH, the right shift in the reaction (Eq. 1.2) leads to increased formation of protonated species. As the protonated species increase in concentration, the reaction in 1.3 will proceed in the forward direction causing a reduction in unbound protonated CFZ. This will cause a further right shift in reaction 1.2 due to removal of products. With a large enough drug load, these phenomena in conjunction lead to supersaturation and eventually precipitation of drug product in acidic cellular organelles, such as the lysosome.

1.1.7 Solubility and Solubility Salt Product

The solubility of drugs in solution is the concentration at which aqueous drug becomes saturated and begins to precipitate out into the solid state. For a saturated solution of an ionic compound, the solubility product constant (Ksp) represents the solubility in an aqueous solution (Eq. 1.4).

Equation 1.4: Ksp

$$K_{sp} = [A^+]^a * [B^-]^b$$

For CFZ, the Ksp can be represented by the protonated form of CFZ and chloride ions in solution (Eq. 1.4) [22].

Equation 1.5: CFZ Ksp

$$K_{sp\_CFZ} = [CFZH^+] * [Cl^-]$$

With supersaturation of CFZ hydrochloride illustrated above, the salt product begins to precipitate out of solution. The CFZ hydrochloride salt then self-complexes to form a highly stable insoluble crystalline structure [8, 22, 24]. The insoluble crystal-like drug inclusion (CLDI) then becomes the thermodynamically favorable product, and results in the predominant species within the lysosome [8].

Mouse models of CFZ administration have shown broad accumulation in multiple organs including, but not limited to, the spleen, lung, liver, gastrointestinal tract, and fatty tissue. Within these tissues, insoluble hydrochloride CFZ salt products have been observed alongside the CFZ free base in varying ratios. So far, little is known about tissue dependent accumulation rates and relative organ partitioning in mice. However, the cell-specific targeting mechanism of CFZ to

xenobiotic sequestering macrophages has been shown to be extremely potent and selective [25, 26]. This behavior has led to large accumulation of CFZ in tissues rich with macrophages such as the lung, liver, and spleen. Since the thermodynamically favorable species and location of CFZ is the CLDIs in the lysosomal compartment of the macrophages, most of the drug is expected to be sequestered in the insoluble drug precipitates with continued drug loading.

Even less is known about the organ specific sequestration of CFZ in humans, however the commonly associated red skin discoloration and crystal-like drug inclusions in sputum samples (Figure 1.2) indicate a similar phenomenon is likely to occur [27, 28, 29].

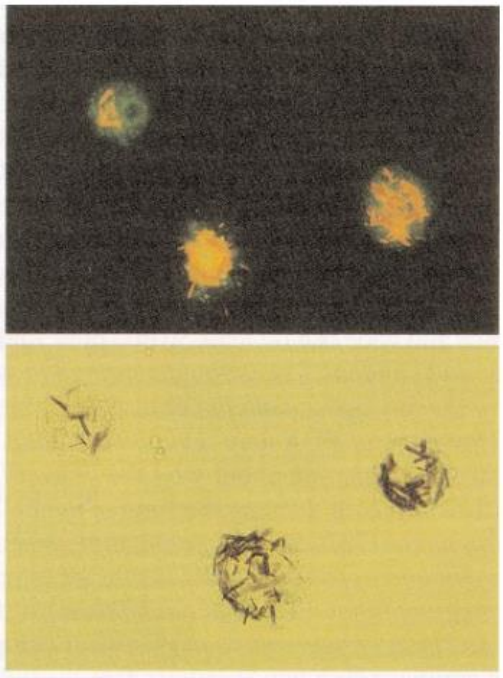

Figure 1.2: Human sputum sample identifying CFZ crystallization after 200 mg daily administration for 4 months [27].

1.1.8 Drug Accumulation, Phospholipidosis, and Lysosomal Targeting Agents

The combination of ion trapping and low Ksp of the CFZ hydrochloride salt creates an ideal environment for the lysosomotropic behavior of CFZ. However, in the search for identifying characteristics of a phase transition framework, global properties of lysosomotropic agents or phase transitioning agents should be well understood. Many lysosomotropic compounds are cationic amphiphilic drugs which enable accumulation in acidic cellular compartments [32]. Strong lysosomotropic character can be identified by physiochemical characteristics including basic ionization constant pKa > 7.5, tertiary nitrogen atoms, lipophilic (LogP between 2 to 6), high volume of distribution (Vd > 10 L/Kg), and large half-life (t½ > 10 hours). Additionally, clinically observed phenomenon such as, high calculated accumulation ratios or the induction of phospholipidosis are also factors increasing the likelihood of lysosomotropic drugs (Table 1.1) [32].

Table 1.1: Physiochemical properties of lysosomotropic medications [32]

Criteria for the selection of drugs with high likelihood of lysosomotropic effects.

Property	Parameter[a]	Desirable range	Indication
Induction of phospholipidosis	PLD induction (exp)	Positive	- Interaction with and accumulation in cell membranes – possible impact on membrane surface charge - Inhibition of lysosomal functions
Accumulation in cells	ACC class (calc)	2 – 5(3 – 5[b])	- Moderate to extremely high accumulation in endosomes/ lysosomes - Slow-down of endocytosis - Increasing endosomal/lysosomal pH
Protonizability	pKa (basic) (exp or calc)	≥ 7.5	- Acquiring positive charge in acidic environments (lysosomes and endosomes) - Increasing endosomal/lysosomal pH
	Physiological charge (calc)	≥ 1	- Positive charge at physiological pH
	Number of tertiary nitrogen atoms	≥ 1	- Presence of the most common protonizable center in molecular structure
Lipophilicity	logP (exp or calc)	2.0 – 6.0	- Ability of the neutral form to distribute into lipids, e.g. membrane - Ability to cross the membrane
Volume of distribution	V_d (exp)	≥ 10 L kg^{-1}	- Distribution and accumulation in tissues *in vivo*
Half-life in plasma/blood	$t_{1/2}$ (exp)	≥ 10 h	- Persistence in organism

Footnote: [a] exp – experimental parameter, calc – calculated parameter; [b] – for compounds out of domain of the model; PLD - phospholipidosis.

Phospholipidosis is the excessive intracellular accumulation of phospholipids, frequently caused by the complexation of cationic amphiphilic drug with cellular membranes or interference

with phospholipid synthesis and metabolism [33]. Phospholipidosis by cationic amphiphilic drug exposure can be observed in many tissues including liver, kidney, lung, brain, heart and even circulating lymphocytes, and preferentially localize in the lysosomes of affected cells. Over 50 known cationic amphiphilic drug (CAD) molecules are known to cause phospholipidosis either through lung uptake or extrapulmonary metabolism creating non-polar metabolites. CADs can induce phospholipidosis in three primary ways:

i. Directly binding with phospholipids
ii. Interfering with and limiting phospholipid metabolism
iii. Influencing the synthesis of phospholipids

The phase transition caused by phospholipid complexation can lead to drug accumulation and drug binding making clearance by normal metabolic or renal elimination difficult.
At high levels of lysosomal accumulation, antiviral activity has been noted [32]. This antiviral tendency has created a recent surge in research and development of clinical trials for accumulating molecules in the treatment of SARS-COV-2 in the wake of the COVID-19 pandemic, including CFZ [25, 34, 35]. The repurposing of these drugs for lysosomotropic or antiviral activity will require further investigation into optimal dosing regimens or a framework shift in targeting optimal accumulation to reduce side effects and toxicity.

1.1.9 Weakly Basic Phase Transitioning Xenobiotics

As CLDIs continue to form with repeated daily administration, increased sequestration changes the observed volume of distribution of CFZ. The number of macrophages as well as the size of sequestered crystals in an insoluble precipitate continues to increase. This leads to a

change in what would otherwise be considered a static parameter in the pharmacokinetic analysis of a heavily accumulating drug [8, 36]. This leads to the question: What is the underlying mechanism of this increase in volume of distribution, and how can this phenomenon be described? Aside from the volume of distribution, the half-life has also been shown to change over time [9]. This furthers our confidence that static pharmacokinetics cannot be applied in the case of CFZ. With heavy distribution to the spleen, it can be inferred that the large accumulation of macrophages in the organ is primarily responsible for the unusual distribution and elimination profile.

Many formulations are created to supersaturate or improve solubilities of xenobiotic therapeutic agents to create more cost-effective drug products. However, utilizing phase transitions to create more desirable pharmacokinetic profiles is a largely absent concept within our field. Through the pharmacokinetic analysis of some commonly used medications, a unifying framework could be established to describe pharmacokinetic changes in phase transitions. CFZ makes for an ideal xenobiotic drug utilized in describing soluble-to-insoluble phase transitioning pharmacokinetics, due to its extreme nature of precipitation [25, 26]. As previously discussed, CFZ undergoes a soluble to insoluble phase transition through the supersaturation of the protonated base, and subsequent complexation with chloride ions. The low Ksp then results in precipitation of the drug and formation of insoluble CFZ crystal.

Amiodarone is another medication that causes structural phase transitions in the form of phospholipidosis. Amiodarone is limited to a maximum total dose in patients due to cumulative side effects. As a result, lung toxicity is a limiting adverse reaction of the drug preventing continued use [37]. Bedaquiline is yet another heavily accumulating molecule that is also used for the treatment of multi-drug-resistant tuberculosis. The cationic amphiphilic nature of the drug

leads to intracellular binding of phospholipids. While reversable upon discontinuation of treatment, a prolonged half-life is exhibited due to the slow release from peripheral tissue [38]. The distribution and accumulation of cannabis is a less well understood due to legislative and regulatory roadblocks in academic research. However, it is speculated pharmacokinetic differences in chronic and occasional users could be present indicating the possibility for adaptive pharmacokinetics. Further investigation is needed to confirm or deny this possibility [39].

1.1.10 Small Molecule Drugs as a Mechanopharmaceutical Device

The center for drug evaluation and research at the FDA has approved on average 37 new therapeutic agents every year since 2008, with 53 drug approvals in 2020 [40]. The primary goal of these agents is to identify a new molecular target or reduce toxicity of existing molecules to gain a competitive market edge.

A mechanopharmaceutical device is a chemical moiety that is utilized for a purpose outside of the directed pharmacodynamic activity. CFZ is well suited for multiple mechanopharmaceutical applications due to the apparently unique properties of intracellular self-assembly. CFZ has been utilized as a mechanopharmaceutical device in the measurement of macrophage response to an increased endophagolysosomal cargo load [8]. The macrophage lysosomal targeting capabilities of CFZ make this drug an ideal tool to create a self-assembling drug eluting depot.

As new ideologies and pharmacokinetic opportunities present themselves, the theories developed under this framework may open the ability to develop therapeutic options that may have been previously flagged as dangerous or non-viable for clinical trials.

1.1.11 Nonlinear Pharmacokinetic Analysis of Chemical Moieties and Model Evaluation

Implementation of pharmacokinetic models using nonlinear mixed effects modeling have successfully been used to inform improved dosing regimens. GastroPLUS, NONMEM, SimCYP, and Winnonlin are some of the current hallmark software platforms that are used to understand drug distribution and interaction. These established platforms allow for complex data informed modeling of pharmacokinetic parameters to understand the varying properties of drug sequestration to better understand the time variant or dose variant properties of CFZ.

For simple one-compartment molecules, an algebraic solution is achievable to describe the pharmacokinetic behavior (Eq. 1.8). With only a single input and one compartment to evaluate over time, the differential equations used in defining drug kinetics have a definite solution. The solution in equation 1.8 utilizes the dose administered (Dose), Volume of distribution (Vd), clearance (CL), and time variant concentration (C(t)).

Equation 1.6: Single Compartment Concentration Over Time

$$C(t) = Dose/Vd * \exp(-CL/V*t)$$

Drugs with nonlinear properties are often difficult to predict algebraically as the rate of drug added or removed from a given organ or compartment may not be constant over time. As a result, differential equation solvers are needed to analytically approximate a solution. Since an algebraic solution is unattainable, incremental estimations can be made to approach a system of differential equations that best describe the system. The simplest approach to computationally solving a set of differential equations is using Euler's method of estimation (Eq. 1.9):

Equation 1.7: Euler Estimation of Multicompartmental Concentration over Time

$$C(t+dt) = C(t) + dC/dt * dt$$

Computationally, concentration values can be summed to estimate the change in the system. For Euler's method to remain accurate, the change in concentration and time must be sufficiently small, which can become computationally intensive. Within the field of pharmacometrics, more complex methods are used such as the Runge-Kutta method which allows for a tradeoff between accuracy and computational speed [41].

After generating a structural model that accurately defines the system, fleshing out error parameters becomes an important consideration in a modeling approach. Experimental errors and interindividual variability can both lead to dramatically different results than a simple model may account for and is often not easily distinguished. Interindividual variability introduces intrinsic differences in the population being studied. In pharmacometrics, the source of these variables can come from both intrinsic (age, sex, genetics, etc.) and extrinsic factors (BMI, physical activity, diet, etc.). These are not true errors, simply additional covariate factors that may sway the evaluation of the model. Evaluating and incorporating the most significant covariates will improve the overall accuracy of the predictions. Experimental errors on the other hand, can be classified into three main categories: execution, systematic, or random [42].

i. Execution errors are mistakes during the conduction of the protocol, including mislabeling samples, administering incorrect dose, improper storage, recording, etc.
ii. Systematic errors stem from the variance in tools and measurement techniques. This can span from different individuals taking measurements to the natural decalibration of instruments over time.

iii. Random errors are more esoteric in nature and not as easily defined. A random error can arise from biases in the ability to measure a dependent variable. This error can typically be reduced by increasing the number of measurements and sample size, as well as utilizing calibration curves.

The error in a system may be relative to the magnitude of difference (e.g., a 10% error in dose measurement), or absolute in nature (e.g., improperly calibrated scale). To account for the experimental errors, three main types of error models are used: additive, Poisson, and proportional error models (Table 1.2). Combination error models can also be incorporated that utilize both additive and proportional in some combined capacity.

Table 1.2: Error models and corresponding NONMEM implementation

Error Model	WLS	Extended Least Squares	NONMEM
Additive	W=1	Var = SD^2	Y = Y + EPS
Poisson	W=1/Y	Var = Y^2*SD^2	Y = Y + SQRT(Y)*EPS
Proportional	W=1/Y^2	Var = Y^2*SD^2	Y = Y + Y*EPS

In the pursuit of an objective approach to determine model superiority, objective function values must be used in combination with diagnostic plots to ensure external validity of predictions. Several types of objective function values have been utilized in pharmacokinetic modeling:

AIC – Akaike Information Criteria combines the number of estimated parameters (k) and maximum likelihood function (L) to identify the most likely global solution (Eq. 1.10):

Equation 1.8: Akaike Information Criteria

$$AIC = 2k - 2\ln(L)$$

BIC – Bayesian information criterion is similar to the AIC with two key differences. The estimated parameter value is multiplied by the natural log of the number of data points in the observed data. And the likelihood function incorporates a Bayesian estimation of change (Eq. 1.11 and 1.12):

Equation 1.9: Bayesian Information Criterion

$$BIC = k*\ln(n) - 2\ln(L)$$

Equation 1.10: Big L Estimation

$$L = \{p\ (x \mid \theta, M)\}$$

-2ln Likelihood – a two-part function that accounts for both the number of parameters and the absolute distance between predictions and observations (Figure 1.3). With more parameters the larger the objective function value, and therefore less extrapolatable results. With increased distance between the observed and predicted values the less likely the model is an accurate representation of the physiological system.

$$-2\log(L) = n\log(2\pi) + \sum_{i=1}^{n}\left(\log\left(\sigma_i^2\right) + \frac{\left(Y_i - \hat{Y}_i\right)^2}{\sigma_i^2}\right)$$

n = number of evaluated parameters

Y_i = measured observation

$\hat{Y}_i$ = prediction of observation

Figure 1.3: Breakdown of -2ln likelihood function

Objective function values are only useful when comparing models against one another with the same data set. To determine model superiority with statistical significance, reduction in objective function value follows the chi square chart. The difference in parameters corresponds to the degrees of freedom, and the p-value correlates to the desired significant difference in models. The resulting value is the minimum required reduction in objective function value to reject the null hypothesis (Figure 1.4a).

A

Full Model: $Cl = \theta_1 + \theta_2 * WT$

Reduced Model: $Cl = \theta_1$

Difference in # of Parameters	Δ-2LL	p-Value
1	>3.84	<0.05
1	>6.63	<0.01
1	>7.88	<0.005
1	>10.83	<0.001
2	>5.99	<0.05
2	>9.21	<0.01
2	>10.6	<0.005
2	>13.82	<0.001

B

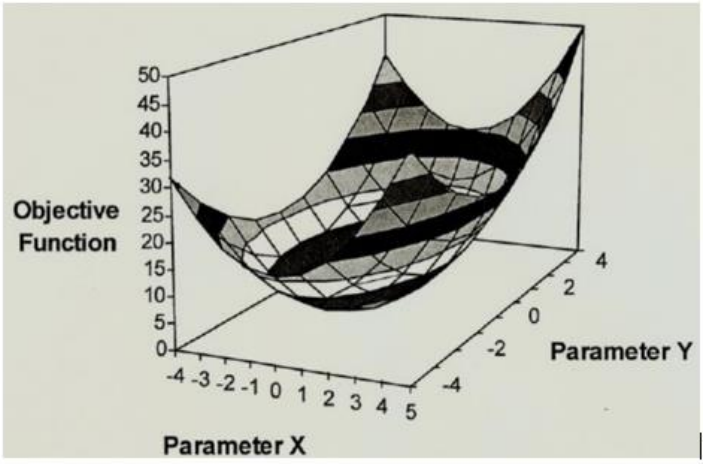

Figure 1.4: Optimization with Objective Functions. A) Reduction in -2ln likelihood required to meet significant p-value B) example parameter space for minimizing objective function value between parameters X and Y.

The larger the reduction in objective function value, the higher the likelihood the model used to describe the data is superior. Most models use a gradient style approach to minimize the objective function value over the available parameter range [43]. Parameter values are increased or decreased to detect a change in objective function value to identify the optimal global

minimum. The corresponding parameter estimates achieved at the global minima are then resulted as output (Figure 1.4b).

Determining model superiority can be somewhat complex and subject to qualitative interpretation. In addition to ensuring physiological relevance of pharmacokinetic parameters and minimizing objective function value, proper model fit must be also based upon visual predictive accuracy. A model with good external predictive capacity captures the entire dataset appropriately. If a model shows visual trends or time variant over/underestimations, this can indicate a suboptimal model that needs further improvement [44]. A handful of methods are used to identify the strength of the model outside of objective function value assessment.

i. Visualizing Accuracy of Predicted Values – residual plots and observations vs predictions are key in determining model accuracy. Residuals are the difference between predicted and observed values: Residual = (predicted) – (observed).

ii. Observations vs predictions – plotting the individual predictions against the observations will result in a 1:1 correlation along the x = y identity line in a perfect model. While this is far from probable, model generation strives to achieve this perfect correlation. In a realistic system, the data points will be scattered around the line of identity (x = y), with minimal trends. Either population or individual predictions can be plotted against the observations, however, individual predictions will show better correlation when interindividual variation is large.

iii. Weighted Residuals – similar to the observations vs. predictions, but only the calculated residuals are plotted over time. Again, any identified trends suggest a suboptimal structural model.

iv. Bootstrapping – bootstrapping is the statistical approach to resample a single dataset into many individual samples [45]. This approach is frequently used to approximate normally inestimable standard errors due to small sample size [46].

George Box, a famous statistician once said: “Since all models are wrong the scientist must be alert to what is importantly wrong.” [41]. What we can really take away from Box’s quotation is that no matter how advanced we create our models, we will still only be approximating the truth. This brings into perspective that the ultimate utility of a descriptive model is to focus our experimentation on the most cost and time efficient manner. A useful model is one that incrementally improves upon our current established understanding of a problem. Ultimately, pharmacokinetic models are best used as guidelines and to inform recommendations to clinical trials.

To remove as much uncertainty as possible, we want to include many known covariates to determine which model parameters are most likely to sway clinical response. By gathering clinical pharmacokinetic data with substantial demographic information, design of experiments and model comparison can aid in the identification of pharmacokinetic trends, active factors influencing distribution, and optimal pharmacodynamic responses [47]. Alternatively, a physiologically based predictive modeling approach can be used, where concentration data alongside known physiology and pharmacology can be combined into a holistic approach to model pharmacokinetic trends.

1.1.12 Mechanism Based Pharmacokinetic/Pharmacodynamic (PKPD) Modeling

Integrating pharmacokinetic, biochemical mechanisms, and disease state physiology can become a robust tool in the system level understanding of drug utility and dose optimization. The primary utility of PKPD modeling results in the connection of dose-concentration relationship to the concentration-response relationship to create a robust understanding of the dose-response relationship. The level of model complexity can fluctuate depending on the complexity of the system being described and the mechanistic level of detail incorporated into the model.

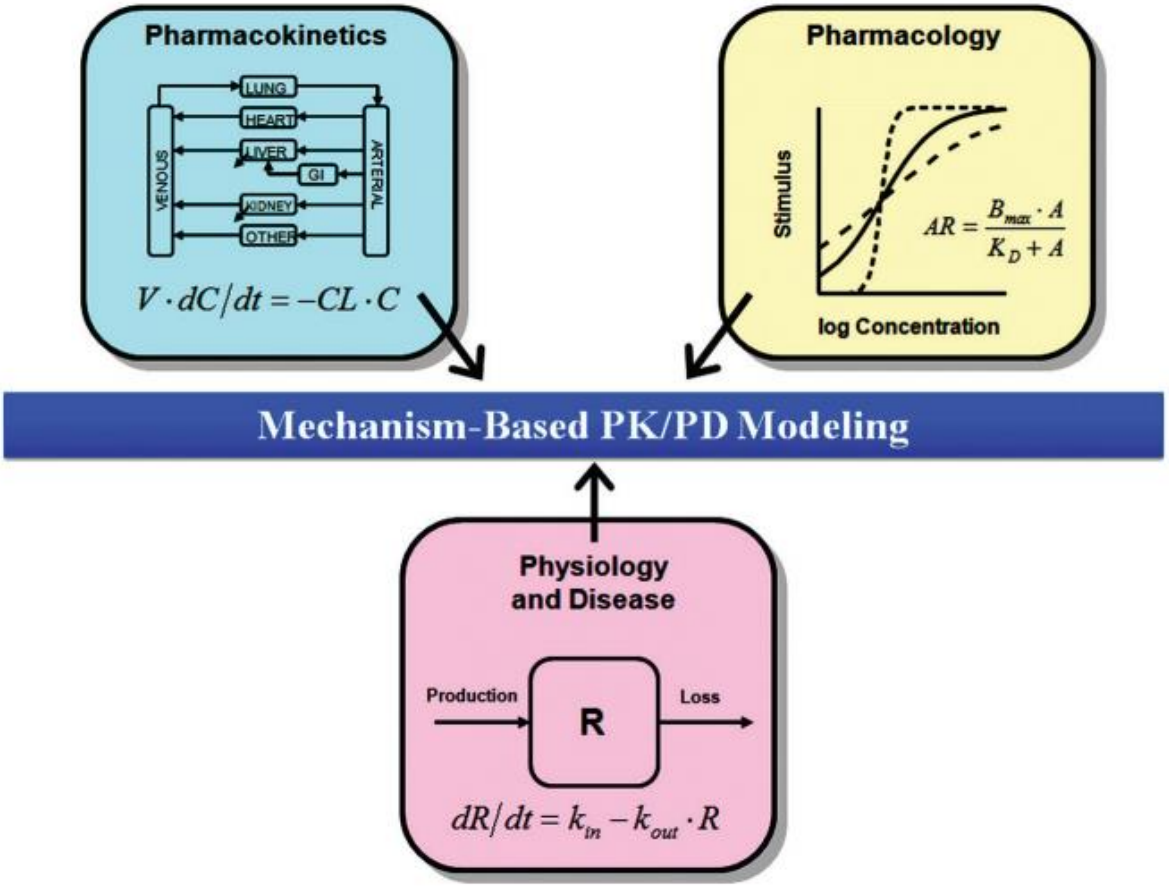

Figure 1.5: Multicomponent input into mechanistic pharmacokinetic (PK) pharmacodynamic (PD) modeling [48]

Typically, mechanism based PKPD modeling incorporates pharmacokinetic data from pharmacometrics simulations or known pharmacokinetic properties, pharmacology data in the

form of concentration-response information, and mechanistic insight through the form of physiologically informed activity or disease state adaptations (Figure 1.5) [48].

Understanding the basic attributes of the PKPD system being observed is crucial in the construction of an accurate model. A well understood system can be easily adapted and allometrically scaled assuming there are no interspecies mechanistic adaptations within the described system [48]. Allometric scaling between mice and humans is imprecise but can be extremely useful in narrowing our scope of human experimental design. Using a variety of established approaches of interspecies allometric scaling techniques, a more concise dosing scheme for phase transitioning xenobiotic molecules can be established. The general framework for interspecies allometric scaling starts with identifying the dose at which no observed adverse effect levels (NOAEL) can be detected. Using a human equivalent dose (HED) based on the relationship between the animal NOAEL and expected human relationship, a rough ballpark estimate can be achieved. From there, a human dose is selected based on the HED with an applied safety factor (Figure 1.6).

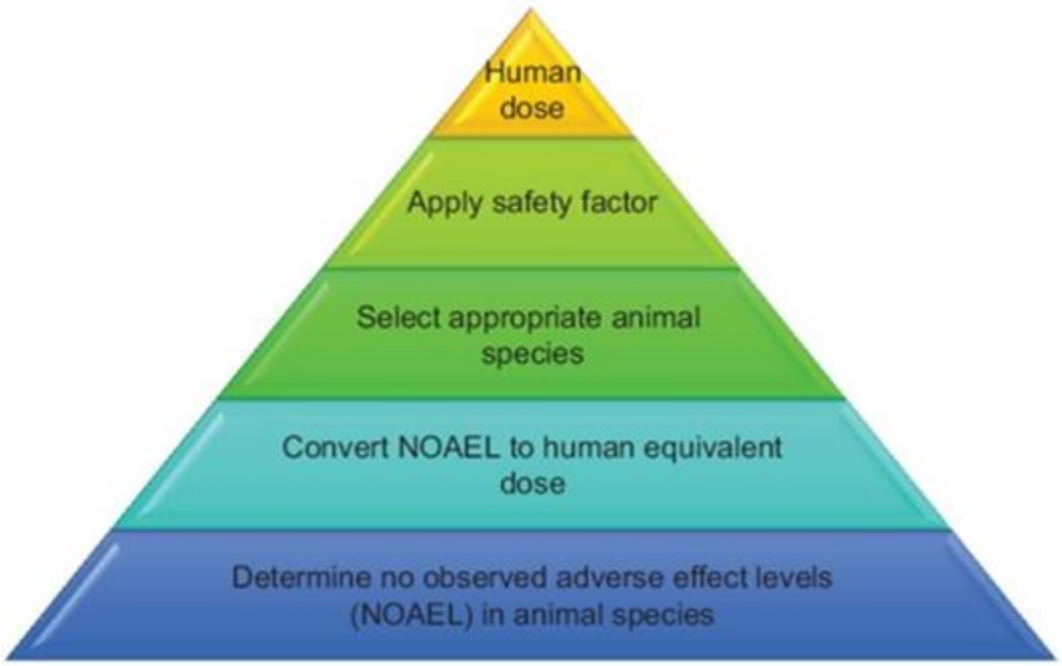

Figure 1.6: Steps to allometrically scaling animal dose to human equivalent dose in ascending order [49]

A variety of allometric scaling techniques exist including simple allometry or corrected allometry utilizing body weight, brain weight, and maximum lifespan potential [50]. Alternatively, body surface area or empirically derived dose concentration relationships can be utilized to generate human equivalent dose. These concentration dependent relationships build insight into the required dose expected to cause context-dependent pharmacokinetic phenomena in humans. By determining an interspecies allometric relationship, we can predict the in human dose at which pharmacokinetic properties begin to diverge. A mechanistically informed dose can then be proposed for use in human trials.

1.2 Innovation and Rationale

The intracellular transport of accumulating molecules is widely studied but is often overlooked in phase transitioning xenobiotics. Understanding thermodynamic equilibria and chemical kinetics of individual molecules can bridge insight into physiochemical properties and biological environments that drive accumulation.

Dosage selection for CFZ is a poorly understood process with a widespread need in the treatment of antimycobacterial infections. Consequently, a mechanistically informed model may enhance the likelihood of utilizing CFZ as a therapeutic option in the treatment of viral infections such as SARS-COV-2. Tuberculosis continues to be one of the top causes of death by infectious disease worldwide, and multidrug resistance is an ever-encroaching medical concern. Increasing the viability of CFZ as a therapeutic option will reduce worldwide medical disease burden, lower medical costs, and bolster our metaphorical toolbox of applicable drug therapies.

This thesis incorporates adaptive pharmacokinetic models encompassing soluble to insoluble phase transitions. Traditional pharmacokinetics approaches are limited in their ability to describe complex interactions with biological systems and new innovative approaches are necessary to capture the nonlinear growth of otherwise static pharmacokinetic properties of phase transitioning systems. Elucidating the complex interplay of pharmacokinetics and the immune system from an organ, cellular, and protein signaling perspective can lead to insights on mechanistic underpinnings of drug distribution and kinetics.

New paradigms of drug delivery are needed to increase the product viability of accumulating molecules and reduce patient morbidity. A mechanistically based modeling framework can create new avenues for existing therapies alongside novel therapeutic agents to tackle many infectious diseases as well as reduce the excessive burden of adverse drug reactions.

1.3 Central Hypothesis and Specific Aims

Central Hypothesis: Components of the immune system including organs, cells, and proteins impact pharmacokinetics of small molecule drugs. Integrating physiochemical knowledge of basic molecules with whole body distribution patterns creates a framework for predicting soluble-to-insoluble phase transitions and can directly point to optimal steady-state drug loading to reduce toxicity of xenobiotic molecules and discover strategies for self-assembling, drug eluting depots.

Specific Aim 1: Predict adaptive pharmacokinetics to identify unique depositions and distribution of drug that deviate from expected patterns of soluble molecules.

Specific Aim 2: Create a physiologically informed single cell model and computationally model drug transport during drug accumulation and elimination.

Specific Aim 3: Investigate the impact of immune system disturbance on context-dependent pharmacokinetics and the resulting influence on toxicity and sequestered drug load.

Chapters 2 through 6 further explore the experimental methods and results of my research pertaining to this central hypothesis and these specific aims. Chapters 2 and 3 explore the pharmacometrics approach outlined in Aim 1, Chapters 4 and 5 discuss the cellular mechanisms outlined in Aim 2, and Chapter 6 discusses the immune system disturbance outlined in Aim 3, collectively addressing the impacts of the immune system on pharmacokinetics.

1.4 References

1. Adverse Drug Events [Available from: https://health.gov/our-work/health-care-quality/adverse-drug-events.
2. Lundkvist J, Jonsson B. Pharmacoeconomics of adverse drug reactions. Fundam Clin Pharmacol. 2004;18(3):275-80.
3. Nair NP. Hospitalization in Older Patients Due to Adverse Drug Reactions – the Need for a Prediction Tool. Clinical Interventions in Aging. 2016:497.
4. Li L, Li X, Xu L, Sheng Y, Huang J, Zheng Q. Systematic evaluation of dose accumulation studies in clinical pharmacokinetics. Curr Drug Metab. 2013;14(5):605-15.
5. Lin JH. Dose-dependent pharmacokinetics: experimental observations and theoretical considerations. Biopharm Drug Dispos. 1994;15(1):1-31.
6. Rangno RE, Kreeft JH, Sitar DS. Ethanol 'dose-dependent' elimination: Michaelis-Menten v classical kinetic analysis. Br J Clin Pharmacol. 1981;12(5):667-73.
7. Powis G, Ames MM, Kovach JS. Dose-dependent pharmacokinetics and cancer chemotherapy. Cancer Chemother Pharmacol. 1981;6(1):1-9.
8. Rzeczycki P, Woldemichael T, Willmer A, Murashov MD, Baik J, Keswani R, et al. An Expandable Mechanopharmaceutical Device (1): Measuring the Cargo Capacity of Macrophages in a Living Organism. Pharm Res. 2018;36(1):12.
9. Swanson RV, Adamson J, Moodley C, Ngcobo B, Ammerman NC, Dorasamy A, et al. Pharmacokinetics and pharmacodynamics of clofazimine in a mouse model of tuberculosis. Antimicrob Agents Chemother. 2015;59(6):3042-51.
10. Hirayama D, Iida T, Nakase H. The Phagocytic Function of Macrophage-Enforcing Innate Immunity and Tissue Homeostasis. Int J Mol Sci. 2017;19(1).
11. Bronte V, Pittet MJ. The spleen in local and systemic regulation of immunity. Immunity. 2013;39(5):806-18.
12. Lukacs GL, Rotstein OD, Grinstein S. Phagosomal acidification is mediated by a vacuolar-type H(+)-ATPase in murine macrophages. J Biol Chem. 1990;265(34):21099-107.
13. Collins FM. Mycobacterial disease, immunosuppression, and acquired immunodeficiency syndrome. Clin Microbiol Rev. 1989;2(4):360-77.
14. Lin CH, Lin CJ, Kuo YW, Wang JY, Hsu CL, Chen JM, et al. Tuberculosis mortality: patient characteristics and causes. BMC Infect Dis. 2014;14:5.
15. Chaves Torres NM, Quijano Rodriguez JJ, Porras Andrade PS, Arriaga MB, Netto EM. Factors predictive of the success of tuberculosis treatment: A systematic review with meta-analysis. PLoS One. 2019;14(12):e0226507.
16. Nicas M, Nazaroff WW, Hubbard A. Toward understanding the risk of secondary airborne infection: emission of respirable pathogens. J Occup Environ Hyg. 2005;2(3):143-54.
17. Organization WH. Tuberculosis (TB). [Available from: www.who.int/news-room/fact-sheets/detail/tuberculosis.
18. Nahid P, Mase SR, Migliori GB, Sotgiu G, Bothamley GH, Brozek JL, et al. Treatment of Drug-Resistant Tuberculosis. An Official ATS/CDC/ERS/IDSA Clinical Practice Guideline. Am J Respir Crit Care Med. 2019;200(10):e93-e142.
19. Administration FaD. Lamprene Clofazimine FDA Label2003.

20. Global leprosy situation, 2012. Wkly Epidemiol Rec. 2012;87(34):317-28.
21. Yoon GS, Keswani RK, Sud S, Rzeczycki PM, Murashov MD, Koehn TA, et al. Clofazimine Biocrystal Accumulation in Macrophages Upregulates Interleukin 1 Receptor Antagonist Production To Induce a Systemic Anti-Inflammatory State. Antimicrob Agents Chemother. 2016;60(6):3470-9.
22. Woldemichael T, Keswani RK, Rzeczycki PM, Murashov MD, LaLone V, Gregorka B, et al. Reverse Engineering the Intracellular Self-Assembly of a Functional Mechanopharmaceutical Device. Sci Rep. 2018;8(1):2934.
23. Henderson LJ. Concerning the relationship between the strength of acids and their capacity to preserve neutrality. American Journal of Physiology. 1908;21(2):173-9.
24. Logan R, Kong AC, Axcell E, Krise JP. Amine-containing molecules and the induction of an expanded lysosomal volume phenotype: a structure-activity relationship study. J Pharm Sci. 2014;103(5):1572-80.
25. ClinicalTrials.gov. Dual Therapy With Interferon Beta-1b and Clofazimine for COVID-19 - Full Text View [Available from: clinicaltrials.gov/ct2/show/NCT04465695.
26. Rzeczycki P, Yoon GS, Keswani RK, Sud S, Stringer KA, Rosania GR. Detecting ordered small molecule drug aggregates in live macrophages: a multi-parameter microscope image data acquisition and analysis strategy. Biomed Opt Express. 2017;8(2):860-72.
27. Harbeck RJ, Worthen GS, Lebo TD, Peloquin CA. Clofazimine crystals in the cytoplasm of pulmonary macrophages. Ann Pharmacother. 1999;33(2):250.
28. Desikan KV, Ramanujam K, Ramu G, Balakrishnan S. Autopsy findings in a case of lepromatous leprosy treated with clofazimine. Lepr Rev. 1975;46(3):181-9.
29. Conalty ML. Rimino-phenazines and the reticulo-endothelial system. Ir J Med Sci. 1966;6(491):497-501.
30. Teuscher N. Accumulation: What It Means and How to Calculate It [Available from: www.certara.com/knowledge-base/accumulation-what-it-means-and-how-to-calculate-it/.
31. Meineke I, Gleiter CH. Assessment of drug accumulation in the evaluation of pharmacokinetic data. J Clin Pharmacol. 1998;38(8):680-4.
32. Norinder U, Tuck A, Norgren K, Munic Kos V. Existing highly accumulating lysosomotropic drugs with potential for repurposing to target COVID-19. Biomed Pharmacother. 2020;130:110582.
33. Halliwell WH. Cationic amphiphilic drug-induced phospholipidosis. Toxicol Pathol. 1997;25(1):53-60.
34. Yuan S, Yin X, Meng X, Chan JF, Ye ZW, Riva L, et al. Clofazimine broadly inhibits coronaviruses including SARS-CoV-2. Nature. 2021;593(7859):418-23.
35. Riva L, Yuan S, Yin X, Martin-Sancho L, Matsunaga N, Pache L, et al. Discovery of SARS-CoV-2 antiviral drugs through large-scale compound repurposing. Nature. 2020;586(7827):113-9.
36. Baik J, Stringer KA, Mane G, Rosania GR. Multiscale distribution and bioaccumulation analysis of clofazimine reveals a massive immune system-mediated xenobiotic sequestration response. Antimicrob Agents Chemother. 2013;57(3):1218-30.

37. Gleadhill IC, Wise RA, Schonfeld SA, Scott PP, Guarnieri T, Levine JH, et al. Serial lung function testing in patients treated with amiodarone: a prospective study. Am J Med. 1989;86(1):4-10.
38. McLeay SC, Vis P, van Heeswijk RP, Green B. Population pharmacokinetics of bedaquiline (TMC207), a novel antituberculosis drug. Antimicrob Agents Chemother. 2014;58(9):5315-24.
39. Huestis MA. Human cannabinoid pharmacokinetics. Chem Biodivers. 2007;4(8):1770-804.
40. Mikulic M. CDER Drug Approvals U.S. 2008-2020. Statista. 25 Jan. 2021.
41. Box GEP. Science and Statistics. Journal of the American Statistical Association. 1976;71(356):791-9.
42. Faculty of Medical and Health Sciences Department of Pharmacology & Clinical Pharmacology A. Error models and objective [Available from: functionshttp://holford.fmhs.auckland.ac.nz/teaching/medsci719/workshops/errormodels/.
43. Mould DR, Upton RN. Basic concepts in population modeling, simulation, and model-based drug development. CPT Pharmacometrics Syst Pharmacol. 2012;1(9):e6.
44. Nguyen TH, Mouksassi MS, Holford N, Al-Huniti N, Freedman I, Hooker AC, et al. Model Evaluation of Continuous Data Pharmacometric Models: Metrics and Graphics. CPT Pharmacometrics Syst Pharmacol. 2017;6(2):87-109.
45. Brownlee J. A Gentle Introduction to the Bootstrap Method Machine Learning Mastery. May 25th, 2018. .
46. Ette EI, Onyiah LC. Estimating inestimable standard errors in population pharmacokinetic studies: the bootstrap with Winsorization. Eur J Drug Metab Pharmacokinet. 2002;27(3):213-24.
47. JMP. Design of Experiments [Available from: www.jmp.com/en_us/applications/design-of-experiments.html.
48. Jusko WJ. Moving from basic toward systems pharmacodynamic models. J Pharm Sci. 2013;102(9):2930-40.
49. Meibohm B, Derendorf H. Basic concepts of pharmacokinetic/pharmacodynamic (PK/PD) modelling. Int J Clin Pharmacol Ther. 1997;35(10):401-13.
50. Amantana A, Chen Y, Tyavanagimatt SR, Jones KF, Jordan R, Chinsangaram J, et al. Pharmacokinetics and interspecies allometric scaling of ST-246, an oral antiviral therapeutic for treatment of orthopoxvirus infection. PLoS One. 2013;8(4):e61514.
51. Nair AB, Jacob S. A simple practice guide for dose conversion between animals and human. J Basic Clin Pharm. 2016;7(2):27-31.
52. Klemm AR, Pell KL, Anderson LM, Andrew CL, Lloyd JB. Lysosome membrane permeability to anions. Biochim Biophys Acta. 1998;1373(1):17-26.
53. Chakraborty K, Leung K, Krishnan Y. High lumenal chloride in the lysosome is critical for lysosome function. Elife. 2017;6.
54. Labs J. Overview 002771 - B6.129S2-Tlx1/J [Available from: www.jax.org/strain/002771.
55. Chao X, Wang S, Zhao K, Li Y, Williams JA, Li T, et al. Impaired TFEB-Mediated Lysosome Biogenesis and Autophagy Promote Chronic Ethanol-Induced Liver Injury and Steatosis in Mice. Gastroenterology. 2018;155(3):865-79 e12.

56. Sardiello M, Palmieri M, di Ronza A, Medina DL, Valenza M, Gennarino VA, et al. A gene network regulating lysosomal biogenesis and function. Science. 2009;325(5939):473-7.
57. James Sollome RCF. Systems Biology in Toxicology and Environmental Health2015.
58. Sangana R, Gu H, Chun DY, Einolf HJ. Evaluation of Clinical Drug Interaction Potential of Clofazimine Using Static and Dynamic Modeling Approaches. Drug Metab Dispos. 2018;46(1):26-32.

Chapter 2 An Adaptive Biosystems Engineering Approach towards Modeling the Soluble-to-Insoluble Phase Transition of Clofazimine

Aspects of this work have been published as an original research article in *Pharmaceutics 2022, 14(1), 17.*

2.1 Abstract

Clofazimine (CFZ) is a weakly basic small molecule antibiotic used for the treatment of mycobacterial infections including leprosy and multidrug-resistant tuberculosis. Upon prolonged oral administration, CFZ precipitates and accumulates within macrophages throughout the host. To model the pharmacokinetics of CFZ, the volume of distribution (Vd) was considered as a varying parameter that increases with continuous drug loading. Fitting the time-dependent change in drug mass and concentration data obtained from CFZ-treated mice, we performed a quantitative analysis of the systemic disposition of the drug over a 20-week treatment period. The pharmacokinetics data were fitted using various classical compartmental models sampling serum and spleen concentration data into separate matrices. The models were constructed in NONMEM together with linear and nonlinear sigmoidal expansion functions to the spleen compartment to capture the phase transition in Vd. The different modeling approaches were compared by Akaike information criteria, observed and predicted concentration correlations, and graphically. Using the composite analysis of the modeling predictions, adaptive fractional CFZ sequestration, Vd, and half-life were evaluated. When compared to standard compartmental

models, an adaptive Vd model yielded a more accurate data fit of the drug concentrations in both the serum and spleen. Including a nonlinear sigmoidal equation into compartmental models captures the phase transition of drugs like CFZ, greatly improving the prediction of population pharmacokinetics and yielding further insight into the mechanisms of drug disposition.

2.2 Introduction

Clofazimine (CFZ) is an anti-mycobacterial agent used to treat leprosy and multidrug resistant tuberculosis alongside some non-tuberculosis mycobacterial infections. Recently, CFZ has also been found to inhibit SARS-Cov-2 infection in vitro and in animal models [1,2], and its efficacy is currently being tested in a phase II clinical trial [3]. The precipitation and accumulation of this weakly basic drug in the lysosomes of macrophages is a phenomenon that has raised considerable interest in the drug targeting and delivery field, since it corresponds to the most potent, cell-specific drug targeting mechanism that has been discovered to date [4,5]. The accumulation of CFZ in macrophage lysosomes has been shown to occur by thermodynamically favorable conditions that lead to the precipitation of drug by pH-dependent ion trapping. The protonated species of the weak base in the lysosome of the macrophage, together with the formation of the very insoluble hydrochloride (CFZ-HCl) salt, form a highly stable crystal upon interaction of the protonated drug with chloride [6,7,8]. In macrophage lysosomes, the hydrochloride crystals are found within membrane-associated complexes referred to as crystal-like drug inclusions (CLDIs). This phenomenon has been observed throughout the body, but it occurs primarily in macrophages of the spleen, liver, gut, and lungs. The large amount of CFZ that accumulates in macrophages over time directly leads to a pronounced expansion of the volume of distribution (Vd) of the drug [9].

Although it has been used clinically use for many decades, [10,11] CFZ pharmacokinetics are characterized by an increasing, dose-dependent half-life and high inter-individual variability [12], which complicates pharmacokinetics analysis. In an experimental mouse model used to analyze the mechanisms underlying the complex pharmacokinetics of CFZ, the dynamic half-life of CFZ was associated with the formation and accumulation of the hydrochloride salt as CLDIs grew and expanded within macrophage lysosomes [13]. This increasing accumulation was accompanied by changes in the distribution of the drug within the organism, as well as the formation of local drug depots that remained long after treatment stopped [6]. While the soluble phase of CFZ is the pharmacologically active moiety that can freely exert anti-bacterial or anti-viral activity [1,2,10], the CLDI drug depot could be beneficial since it concentrates in macrophages, which are directly involved in combating infection. Crystal-like drug inclusions have also been shown to increase with repeated dosing in both mice and humans [6]. Due to the high concentration of macrophages in the spleen, this organ sequesters CFZ at 10 to 100 times the concentration of other tissues [6,14].

Recently, the pharmacokinetics of CFZ in tuberculosis patients was described as a 3-compartment model [12]. In order to improve upon the standard compartmental modeling approaches used to analyze the pharmacokinetics of CFZ, we sought to develop an adaptive pharmacokinetics modeling approach that would be better capture the soluble to insoluble phase transition and subsequent increasing Vd of the drug and to compare its predictive accuracy to a standard compartmental model. Using mice as a model organism, our analysis of CFZ pharmacokinetics during a 20-week treatment period demonstrates how such an adaptive pharmacokinetics modeling approach can provide insights into the changes in serum and spleen

concentrations measured during prolonged treatment increases our understanding of the pharmacokinetics parameters that explain the context-dependent accumulation of CFZ.

The results reported herein are the first time that volume of distribution changes resulting from soluble-to-insoluble phase transitions of drug molecules are directly modeled and analyzed, using a population pharmacokinetics modeling approach that should be applicable to the study of CFZ pharmacokinetics in the human population. The significance of this analysis is not only relevant to improving understanding of the mechanistic underpinning of CFZ pharmacokinetics, but it will help advance the development of macrophage-targeted drugs and the design of self-organizing drug depot systems.

2.3 Materials and Methods

2.3.1 Data Acquisition and Compartmental Pharmacokinetic Modeling

Individual mouse data were obtained from a previously published study in which CFZ concentrations were measured in the serum and spleen of healthy BALB/c mice given 25 mg/kg of CFZ by oral gavage once daily, Monday through Friday, over a 20-week period, together with measurements of the mass of the organ. Three mice were sacrificed then sampled at seven discrete intervals (7, 14, 28, 56, 84, 114, and 140 days) after starting therapy and prior to administering the daily dose. CFZ concentrations were measured by liquid chromatography/mass spectrometry (LC/MS) using a previously validated method [13]. Animal procedures were approved by the Animal Ethics Sub-Committee of the University of KwaZulu-Natal (reference numbers 068/13/Animal and 025/14/Animal) [13]. A population pharmacokinetic model was constructed to describe the expected pharmacokinetic changes during repeated dosing. The serum and spleen drug concentration data were used as input into NONMEM (v. 7.3.0) to

determine the best predictive modeling approach based on the goodness of fit. To better understand the pharmacokinetics of CFZ prior to the phase transition, we created a collection of different (one-, two- and three-compartment), standard pharmacokinetics models, assuming drug stays in solution without precipitating in host organs. With these models, the data were fit during the first 4 weeks of CFZ dosing (Table A.1) when minimal drug was expected to precipitate as CLDIs. The model with the highest predictive accuracy in the soluble phase was then used to compare the steady state predictions with the measured drug concentrations over the entire 20-week dosing interval.

2.3.2 Optimizing Compartmental Pharmacokinetics Modeling by Incorporating an Adaptive Vd Function

Four adaptive Vd models were used to capture different Vd expansion functions (linear, exponential Hill equation, logistic function, and rational square root sigmoid). The adequacy of each model was then tested and compared to the baseline, standard compartmental pharmacokinetics model with a constant Vd, to determine the best compartmental modeling approach and adaptive Vd function that fits the measured, temporal changes in the pharmacokinetics of CFZ over the 20-week treatment period. The baseline, standard compartmental model with a constant Vd is referred to as the “base model”. The predictive value of including a peripheral compartment to the base model was separately assessed to determine whether the phase transition can be captured by adding an additional compartment. Model superiority was determined by plotting the concentration predictions over time, comparing correlation of the residuals, coefficients of variation (CV%), and comparing Akaike information criterion (AIC) [15]. NONMEM models were constructed under the ADVAN9 subroutine using

first order conditional estimation with interactions (FOCEI), and a multiplicative error model was used across all evaluated models. Between subject variability (ETA) was added to the growth function parameters involved in rate of expansion and maximum total expansion of the spleen volume.

2.3.3 Model Validation

In pursuit of a robust estimation of the expansion of volume of distribution, a varying number of parameter estimates from the soluble phase model were used to fix the initial conditions of the full model with the expansion function. We will refer to the 'soluble model' or 'soluble phase model' as the two-compartment model without an expansion function, intended to capture the kinetics of CFZ molecules in solution, prior to the phase transition leading to the formation of CLDI precipitates that result in drug accumulation in the spleen. Bootstrapping was then conducted on a subset of the models using 1000 runs in Wings for NONMEM (WFN). Parameter estimates, confidence intervals, standard deviations, and coefficients of variation were evaluated alongside histogram plots to determine the optimal expansion model (Figure A.1). The chosen model with fixed V1 and K12 was then evaluated across each of the expansion functions in Figure 2.1 utilizing the entire 20-week dataset. Despite using the same structural compartmental model, the soluble phase model was evaluated alongside the base model. As the soluble model only extrapolates the concentration predictions from the first four weeks of data, the resulting predictions can be compared to the base model which evaluates CFZ pharmacokinetics over the course of the phase transition.

2.3.4 Variable CFZ Mass Sequestration

At any given timepoint, the cumulative dose fraction of CFZ sequestered in the spleen was estimated by multiplying the spleen weight by the predicted spleen concentrations of the composite sigmoidal models to give the resulting mass of CFZ sequestered. This mass was then divided by the total dose of CFZ administered up until that timepoint (Equation A.2). The individual dose fraction sequestered is estimated by multiplying the spleen weight by the predicted concentration at each individual timepoint and subtracting the cumulative mass up until the previous timepoint. The mass sequestered between timepoints is then divided by the mass of the dose administered between the corresponding timepoints to estimate the fraction of dose sequestered (Equation A.3). Mass balance was verified for each of the constructed models based on the predicted concentration values and measured organ weight.

2.3.5 Statistical Analysis of Experimental Data

The Akaike information criterion (AIC) reported in this chapter was calculated by multiplying the number of parameters by two and adding the reported objective function value (OFV) in NONMEM (Equation A.1) and was one criterion used to determine model superiority. Statistical improvement in AIC was based on direct comparison between models. The correlation coefficient of predicted and observed concentration values was evaluated for incremental improvement over the base model. Means and standard deviations were calculated between pharmacokinetic parameters of sigmoidal functions to arrive at a consensus value. Bootstrapping analysis was conducted in WFN with 1000 runs per model. Parameter estimates, AIC, and coefficients of variation were reported from the bootstrapping analysis. Statistics and regression completed outside of NONMEM were calculated in R Studio (Version 1.1.456).

2.4 Results

2.4.1 A Baseline, Compartmental Pharmacokinetics Model to Capture the Soluble-to-Insoluble Phase Transition of CFZ

From 11 different models, we selected the simplest compartmental model that best captured CFZ accumulation in the spleen: a bidirectional two-compartment model with elimination from the serum compartment. This model had the lowest objective function value and most physiological relevance of the 11 total compartmental models tested in the first four weeks of treatment (Table A.2). The concentration data from both the serum and spleen were sampled into separate compartments in the model. Serum concentration data was sampled into the compartment which received the drug upon administration, and spleen concentration data were sampled into a second, organ compartment that received drug from the blood. We only considered drug accumulation in the spleen, as most of the drug in organism was found to accumulate in said organ over the 20-week treatment period. This 2-compartment model was then modified to better capture the spleen and serum drug concentrations, over the full 20-week dosing period. To account for the non-linearity expected from CLDI formation, we added an adaptive function (V1) to the volume of the spleen compartment, the inter-compartmental rate constant from compartment two to compartment one (K21), and the elimination rate constant (K). The compartmental model and associated adaptive Vd equations are shown in Figure 2.1. The predictions for the 2-compartment model were directly compared to a 3-compartment model with a serum, spleen, and peripheral compartment (Figure A.2).

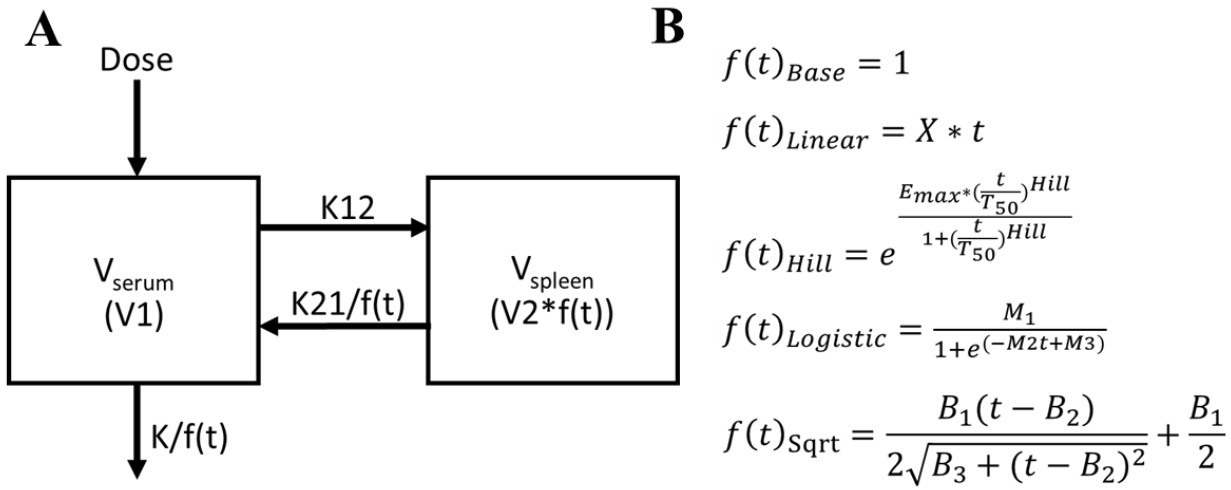

*Figure 2.1: Compartmental Model and Expansion Functions A) The 2-comparment model used in this study. Vserum = V1 which represents the volume in the serum compartment, and Vspleen = V2*f(t) which represents the volume in compartment 2 multiplied by the expansion function f(t), respectively; K12 and K21 represent the intercompartmental rate constants; K represents the elimination rate constant; and f(t) represents the adaptive volume of distribution with respect to continued dosing. The f(t) function was modified to illustrate the effect of differing sigmoidal equations on the goodness of fit of the experimental data. B) The five f(t) equations used to represent this compartmental model where X = rate of f(t) expansion, Emax = maximum allowable expansion by f(t), Hill = speed of expansion over time, T50 = time at which 50% of the maximum is reached, M1= maximum allowable expansion by f(t), M2 = steepness at inflection, M3 = lateral shift of the expansion curve, B1 = maximum allowable expansion by f(t), B2 = exact time of the inflection point, B3 = speed of expansion over time.*

2.4.2 Optimizing the Two-Compartment Model by including an Adaptive Vd Expansion Function

The pharmacokinetic parameters of the base model and each of the four adaptive Vd modeling approaches that were used to refine the two-compartment modeling fits are shown in Table 2.1, alongside the AIC and R2 values. The base model behaved as a standard 2-compartment model with a constant Vd. The linear model increased Vd linearly with respect to time, and the three sigmoidal models (Hill equation, logistic function, and rational square root sigmoid) all nonlinearly increased Vd with respect to time. The 3-compartment model is

identical to the base model with an additional peripheral compartment connected to the serum (Figure A.2).

Table 2.1. Pharmacokinetic parameter estimates for each of the five 2-compartment models are represented alongside the R2 and AIC values for each corresponding model. The values for V2, K12, and K21 listed here are the initial values prior to the changes made by the f(t) equation. Variable 1 represents the slope X for the linear function, Emax for the exponential Hill function, M1 for the logistic function, and B1 for the rational square root function. Variable 2 represents the T50 for the Hill function, M2 for the logistic function, and B2 for the rational square root sigmoid. Variable 3 represents the Hill coefficient for the Hill equation, M3 for the logistic function, and B3 for the rational square root sigmoid. CV% are reported beside the parameter estimates for each model.

Model	R^2	AIC	^V1 (L/Kg)	V2 (L/Kg)	K (day^{-1})	^K12 (day^{-1})	K21 (day^{-1})	Variable 1	Variable 2	Variable 3
Base Model	0.84	319.05	2.43	0.00516 (0%)	0.033 (0%)	0.183	0.00287 (33.8%)	---	---	---
Linear	0.95	255.8	2.43	0.0119 (32.8%)	0.275 (56.5%)	0.183	0.125 (49.1%)	*0.219 (66.7%)	---	---
Exponential Hill Equation	0.98	211.9	2.43	0.00708 (1.61%)	0.229 (12.6%)	0.183	3.36 (1.53%)	*6.99 (0%)	*49 (2.68%)	3.71 (2.59%)
Basic Logistic Function	0.97	238.9	2.43	0.00779 (4.73%)	0.00645 (111.3%)	0.183	0.0762 (96.2%)	*99.1 (56.2%)	*0.0701 (2.82%)	8.85 (3.60%)
Rational Square Root Sigmoid	0.99	200.8	2.43	0.00533 (2.00%)	0.107 (54.1%)	0.183	2.16 (53.4%)	*1150 (32.3%)	80.2 (3.20%)	*8.84 (36.5%)

^ *Fixed parameter estimates from soluble phase model.*

** Parameters with ETA values applied to the model.*

The base model had the fewest number of pharmacokinetic parameters and is therefore the simplest of the models tested in this study. The linear function had one additional parameter compared to the base model, and the three sigmoidal models, as well as the 3-compartment model, all had three additional parameters compared to the base model. Due to the difference in number of parameters, significance for comparing models was determined by comparing AIC values rather than OFV.

The base model showed the lowest correlation coefficient and highest AIC, meaning of the five models, this one is statistically the least likely to predict the observed data. The linear model showed incremental improvement over the base model with a statistically significant decrease in AIC and increase in R2 (0.95 compared to 0.84). Incorporation of a sigmoidal function to capture the change in Vd over the treatment period improved all three models over the linear model (logistic function to rational square root sigmoid respectively, Table 2.1). This finding indicates that any of the three sigmoidal equations could be used to better predict the soluble to insoluble phase transition, as compared to the base model or the linear model. The 3-compartment model, used to fit serum and spleen concentration data, yielded a resultant AIC of 300.8 and R2 of 0.92, showing superiority over the base 2-compartment model, but inferiority to all adaptive expansion models. The rational square root function showed the lowest AIC and had the highest R2 value of 0.99, reflecting the best fit to the data as observed by visual inspection (Figure 2.2). The Hill function almost fit the data as well as the rational square root function, with R2 of 0.98 and an AIC of 211.9. However, the CV% were smaller for each of the parameter estimates in the Hill function compared to the rational square root function. These two models were superior to all other models evaluated in this study. Most importantly, the pharmacokinetic parameter estimates converged to similar values when comparing the Hill and rational square root equation (Table 2.1), which were the two models that showed the best fit to the data.

Next, the accuracy of each of these four adaptive Vd models was evaluated by visual inspection of concentration versus time plots and direct comparison of the performance of the base 2-compartmental model and the 3-compartment model (Figure 2.2). During the 20-week time course of the experiment, CFZ concentration in the serum remained constant (~1 μg/mL)

over the 20-week dosing period, while the CFZ concentration in the spleen increases in a non-linear fashion over the duration of the experiment.

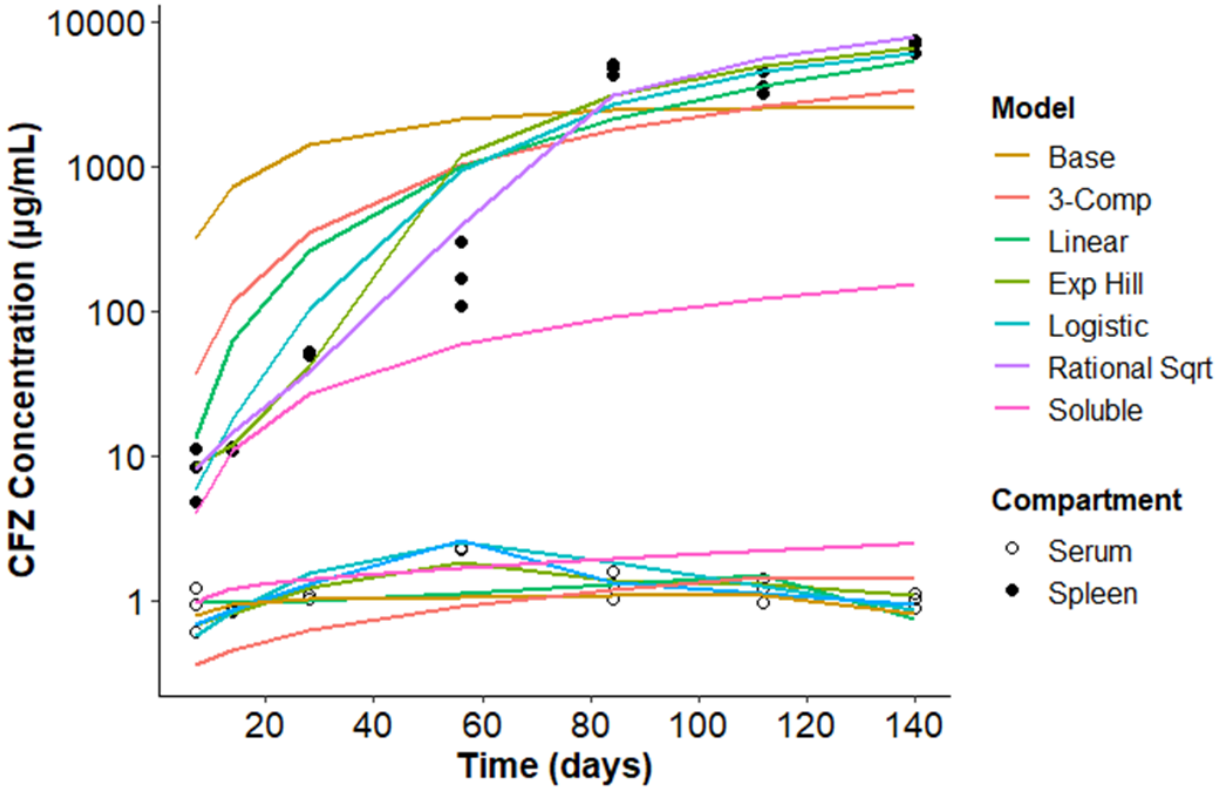

Figure 2.2. Visual predictive accuracy of CFZ concentration vs. time of four different expansion Vd models, the standard base 2-compartment model, the 3-compartment model, and the soluble phase model using the base model with data from the first 28 days of dosing with extrapolated predictions out to 140 days. The represented data were acquired from three mice for each serum and spleen timepoint except at 14 days where only two data points were available. The lines represent the corresponding concentration vs time predictions. Experimental data obtained from three mice at each time interval are displayed on the graph alongside the average model predictions for the population.

All six models utilizing the entire dataset accurately matched the observed serum concentrations. The base model overpredicted early and underpredicted late CFZ concentrations in the spleen. This trend indicates that the 2-compartment base model inadequately captures the accumulation of CFZ in the spleen over time. The linear expansion function, which allows the

Vd to expand linearly over time, yielded a more accurate fit than the base model (Figure 2.2). While still overpredicting the early time points and underpredicting the later timepoints, the linear Vd expansion equation improved upon the base model predictions, such that the simplest adaptive Vd function increased its predictive accuracy. At a higher level of complexity, using an exponential Hill equation, a logistic expansion function, or a rational square root equation as the adaptive Vd function, led to further improvement on the fits of the data. All three sigmoidal expansion functions more accurately captured the earlier and later timepoints than the linear or base models. Once again, the 3-compartment model showed superiority in visual predictive accuracy to the base model, and inferiority to the adaptive Vd models.

The visual comparison of the extrapolated predictions of the base model using the first 28 days (soluble model) and the base model with the full dataset further reveal the inability of the base model to fully capture the range of concentrations over the course of dosing. The soluble model accurately captures the early spleen concentration values, but when extrapolated to the full course of dosing, vastly underpredicts the later spleen concentration values. The base model with the full dataset more closely captures the higher spleen concentrations at the later timepoints but compensates by overpredicting the earlier spleen concentrations.

We further analyzed the improved fits obtained with the models by incorporating a sigmoidal equation to capture the Vd expansion function. Quantitatively, the AIC of the Hill equation showed a significant quantitative improvement over the base model (Table 2.1). The Hill equation improved the observations versus predictions in the expansion model (Figure 2.3A) compared to the base model (Figure 2.3B). The expansion model has an even distribution of residuals for both the serum and spleen concentrations without any clear trends. Whereas the base model shows underprediction of serum concentrations early in dosing, and an

overprediction of spleen concentrations in the early timepoints with underprediction in the later timepoints. This improvement was also apparent in the weighted residuals from the Hill equation expansion model (Figure 2.3C) and the base model (Figure 2.3D). The quantitative improvements for each of the other Vd expansion functions and 3-compartmental model are also reflected in the residual plots (Figure A.3).

Additionally, when comparing the fully optimized, unfixed models, the base model has a constant volume of distribution at 368.8 L/Kg and a terminal half-life of 21 days, which is vastly different than the predicted volume and terminal half-life of the base model in the soluble phase (43.45 L/Kg and 537.2 days respectively). The exponentiated Hill function bridges the base model and soluble model pharmacokinetic parameters by allowing the soluble and insoluble phases to be incorporated simultaneously. The Vd of the Hill function increases from 62.7 L/Kg to 147.9 L/Kg, and half-life increases from 1.26 days to 343.0 days. This implies that the base compartmental model is unable to capture the entire dataset and requires an element of nonlinearity to predict the distribution of CFZ more accurately.

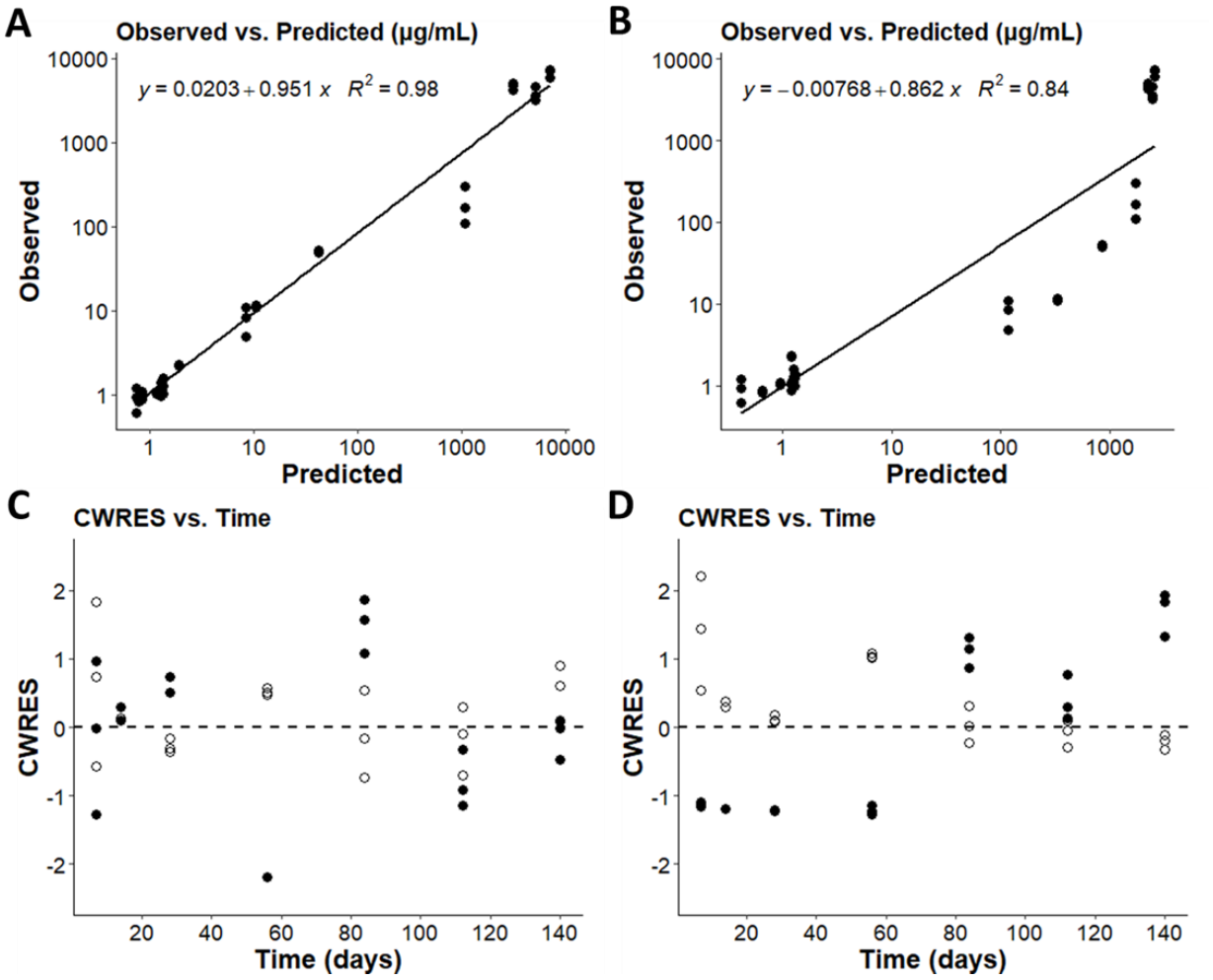

Figure 2.3: Observations vs predictions (A and B) and the conditional weighted residuals vs time (CWRES vs. Time; C and D) for the 2-compartment model with the exponential Hill expansion function and the base 2-compartment model. The weighted residuals for serum (open) and the weighted residuals for the spleen (closed) are plotted side by side. A and C are the diagnostic plots for the exponential Hill model. B and D are the diagnostic plots for the base 2-compartment model.

2.4.3 A Consensus Pharmacokinetics Model of the Expanding Vd of CFZ

Using all three sigmoidal equations to represent the adaptive pharmacokinetics of CFZ, two physiologically relevant pharmacokinetic parameters (Vd and half-life) were calculated to enable a consensus model that captures the drug concentrations and mass in the serum and spleen over the entire time course of the 20-week dosing regimen. For all models, the Vserum was kept

constant, and the increase in the volume of the spleen was captured by each of the three sigmoidal equations. The base pharmacokinetic parameters (K, K12, K21, V1, and V2) for each of the models were fixed to the estimates from the fully optimized, unfixed exponential Hill function, allowing the adaptive parameters from the expansion function to distinguish amongst the sigmoidal models.

The sum of the volume of the serum compartment and the spleen compartment was used to calculate a total Vd at each time point (Equation A.4). The total Vd obtained for each of the models, incorporating the different sigmoidal functions, was then plotted over time, allowing for the inspection of Vd expansion variability with each sigmoidal model (Figure 2.4A). Each individual sigmoidal function was then used to plot the half-life over time (Figure 2.4B).

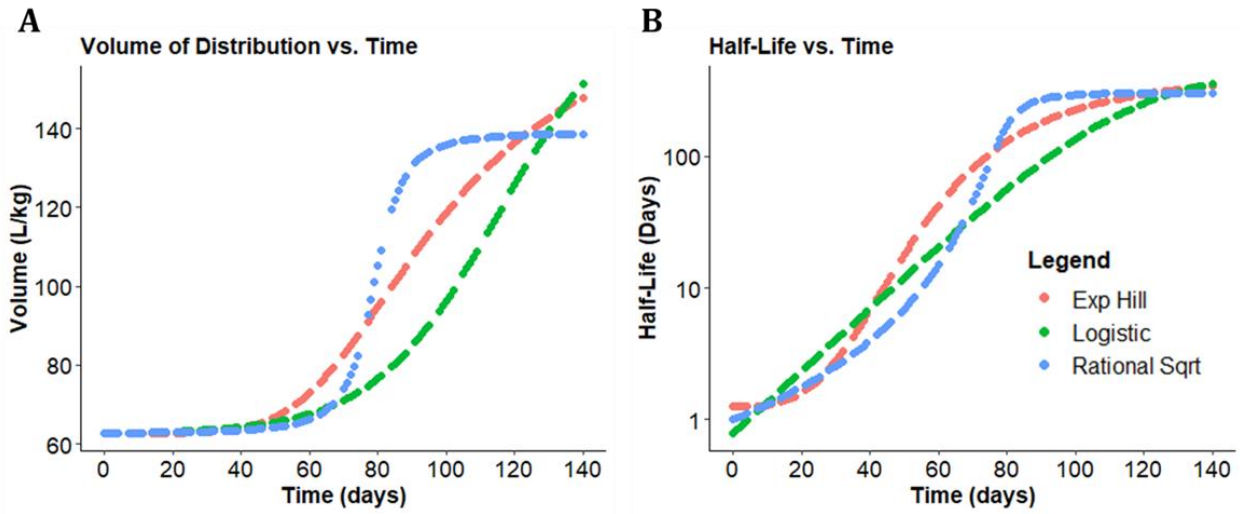

Figure 2.4: Changes in CFZ volume of distribution (Vd) and half-life over time. A) The total Vd increased non-linearly over the 20-week CFZ administration for each of the 3 sigmoidal functions. B) The half-life over time increased for each of the sigmoidal equations over the 20 weeks of CFZ dosing.

To integrate the different models, the mean and standard deviation values of the pharmacokinetic parameters from the three sigmoidal functions were used to calculate composite values for total Vd and half-life (Figure 2.5B, 2.5C). The total Vd functions were also plotted alongside the Vd of the serum and spleen compartments (Figure 2.5A). Based on this consensus view, the serum compartment had a mean Vd of 62.5 L/kg, while the Vd of the spleen compartment increased from 0.26 L/kg to 86.48 L/Kg. The resulting total Vd calculated by adding the serum and spleen compartment Vd increased 3-fold from 62.7 L/kg to 148.9 L/kg over the 20-week CFZ administration period. At each time point, the half-life was calculated based on first order elimination (Equation A.5). Accordingly, the mean consensus half-life increased from 1.05 days to 346.84 days.

These results indicate that there is an increasing amount of drug being sequestered over time with an associated non-linear increase in the Vd. The changes in half-life are modeled to be secondary to the changes in the Vd. The results shown here are driven by an adaptive volume in compartment two induced by a soluble to insoluble phase transition. Each sigmoidal expansion function predicts adaptive pharmacokinetic parameters as a surrogate for CLDI growth at varying rates and extents based on the supplied data set. The overall range of values for total Vd at week 1 extended from 62.7 L/kg to 62.8 L/kg (for the Hill function and rational square root function respectively), and a range for total Vd at week 20 from 143.9 L/kg to 155.1 L/kg (for the rational square root and logistic expansion function respectively). The overall discrepancy in total Vd between the sigmoidal functions over the course of dosing spanned a 0.16% difference at initiation to a 7.5% difference at the end of the dosing with the largest difference in functions (44.2%) apparent at 76 days. Similarly, the overall discrepancy in half-life between expansion

functions ranged from a 42% difference at week 1 to a 12% difference at week 20 with the largest difference in functions (100.6%) apparent at 76 days.

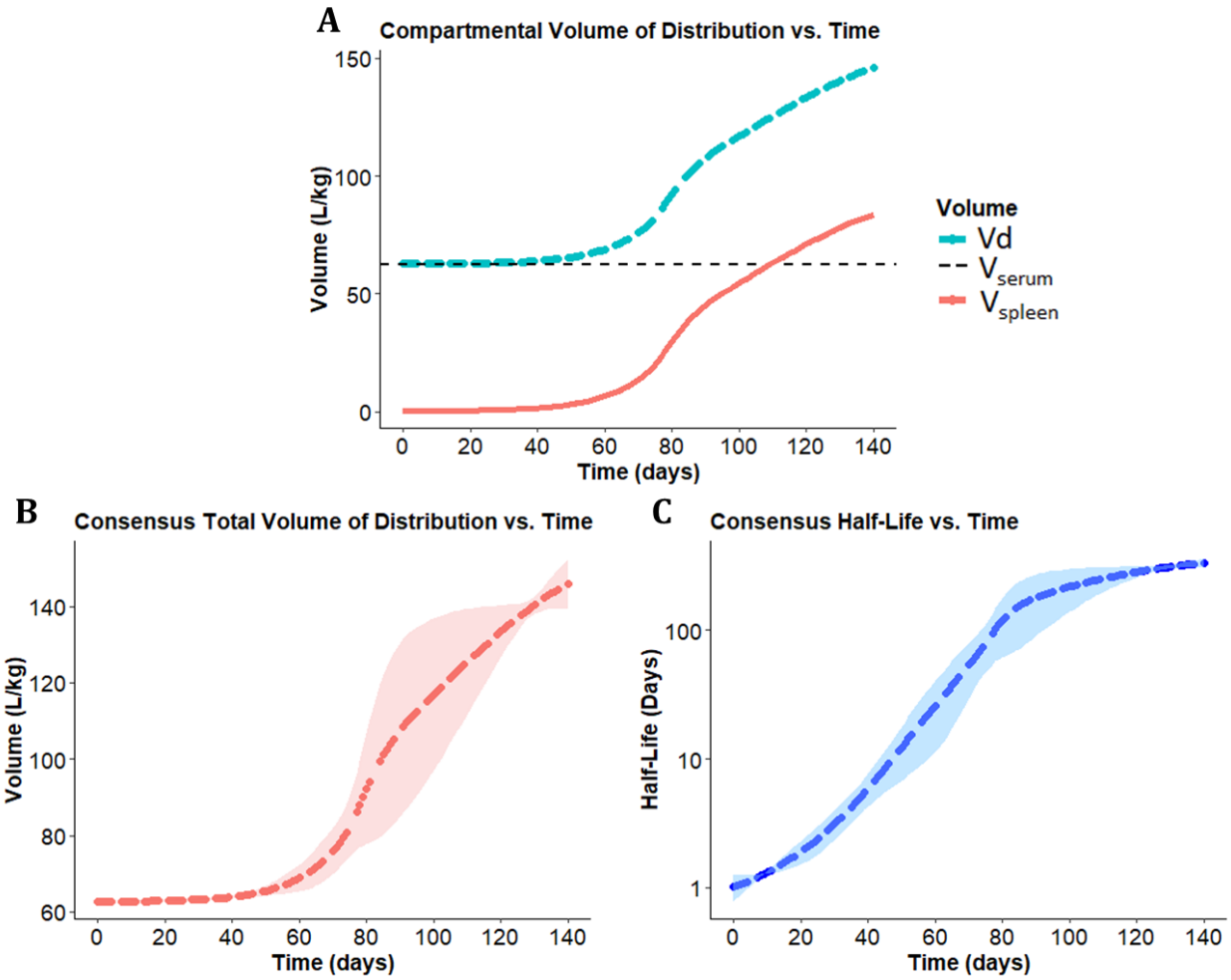

Figure 2.5: Changes in consensus values for CFZ total volume of distribution (Vd) and half-life over time. A) The mean Vd is shown for each compartment. The dashed black line indicates the Vd contributed by the serum compartment, the red line indicates the Vd contributed by the spleen compartment, and the blue line indicates the total Vd of the drug. B) Consensus total Vd over time with the shaded region indicating standard deviation. C) The consensus half-life over time shown alongside the standard deviation.

As shown in Figure 2.4A, each sigmoidal curve optimizes to a different curve shape. The difference of fit comes from several sources. First, while each expansion function is a sigmoidal curve, each function differs slightly due to variation in curvature. That is, there is no way to set

parameters of f(t)Hill¬ and f(t)Sqrt such that f(t)Hill = f(t)Sqrt for all timepoints t. Additionally, the rational square root and logistic growth curves are symmetric about their inflection point, while the exponential Hill curve is asymmetric in that its inflection point occurs before the function reaches half capacity.

The maximum estimated expansion of the spleen compartment is a 347-fold increase based on the Emax parameter of the exponentiated Hill function, and the maximum rate of volume expansion occurred at 81.8 days based on the inflection point of the expansion function. The time at 50% maximum volume expansion was calculated to be 98.1 days after initiating dosing based on the plotted exponential Hill equation. At a 25 mg/kg dosing regimen, this corresponds to a total load of 35.0 mg, or 1.75 g/kg of total CFZ load to reach 50% of maximum volume expansion. These predicted values alongside the estimated 273-fold increase in Vspleen at week 20 indicates that further increase in total volume is expected before reaching a loading capacity in the spleen. The resulting ETA values for the Hill coefficient and Emax parameters were very small (4.00*10-6 for both parameters) due to the homogenous mouse population and small sample size.

2.4.4 Analyzing CFZ Time-dependent Pharmacokinetics and Mass Accumulation in the Spleen

In addition to CFZ serum and spleen concentration predictions, we determined the fraction of the total dose of CFZ that bioaccumulates in the spleen over the 20-week treatment period. At each time point, the mass of CFZ calculated in the spleen by each of the sigmoidal expansion functions was divided by the cumulative dose of drug administered to mice up to that

time point (Figure 2.6A). The consensus mass of CFZ in the spleen was calculated by averaging the predicted CFZ mass from each of the sigmoidal expansion functions (Figure 2.6B).

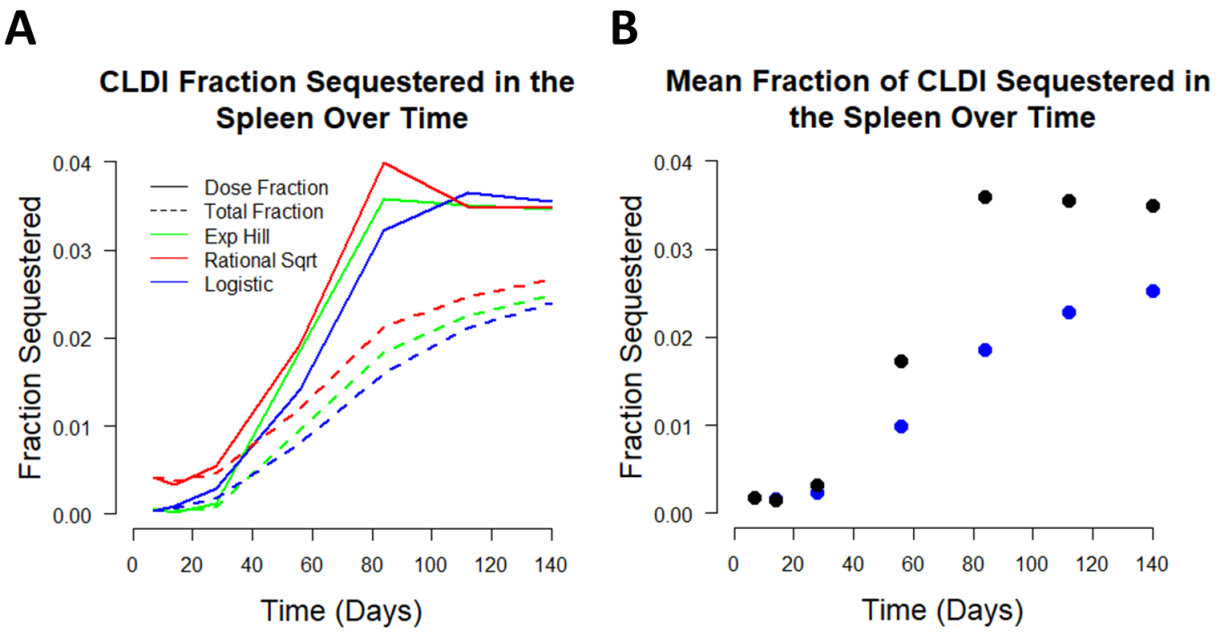

Figure 2.6: Sequestration of CFZ by the spleen. Dose fraction estimation was made by calculating the incremental CFZ mass increase with each dose compared to the predicted mass to determine the change in CLDI sequestration over time. Estimation of cumulative fraction sequestered was made by calculating the fraction of administered CFZ present in the spleen. A) Fraction of CLDI sequestered for both dose fraction and cumulative fraction for each of the 3 sigmoidal functions. B) Cumulative fraction of all CFZ sequestered over time (blue) and estimated sequestered fraction of each individual dose given (black).

When given a CFZ dose of 25 mg/kg per day, the mean cumulative fraction sequestered in the spleen among the consensus sigmoidal functions increased from 0.0017 on week one to 0.025 on week 20 equating to a 14.7-fold increase in drug sequestration over the 20-week period. The estimated fraction of CFZ sequestered per dose increased from 0.0017 on week one to 0.035 on week 20 with a peak of 0.036 on week 12. The cumulative dose fraction between sigmoidal models was consistent with a 165% difference at week 1 and a 10.5% difference at week 20. The

most pronounced change in the fraction of CFZ sequestered occurs between weeks four and eight, coinciding with the time during which CLDI formation becomes microscopically visible in mouse organs (at around 3 weeks treatment), after which the spleen dramatically increases in mass (between 4 and 8 weeks of treatment) [9]. This observation is consistent with the increase in drug accumulating intracellularly within macrophages of the spleen as the insoluble drug precipitates. The time course data shows an increasing fraction of administered drug is sequestered with each dose after 4 weeks of treatment. This is consistent with previous experimental observations indicating that CLDIs are visible in macrophages after 3 weeks of treatment, and then grow dramatically thereafter [9]. However, after 12 weeks of dosing, the estimated fraction of each dose that accumulates within the organism plateaus, suggesting that a maximum loading rate is reached at that time. This is consistent with the extent of CFZ accumulation within the host being determined by an active biological mechanism (e.g., the pH-dependent lysosomal acidification) that determines the upper limit of the rate at which the drug becomes sequestered within macrophage as the hydrochloride salt form.

2.5 Discussion

Our pharmacokinetic modeling of bioaccumulation shows the importance of considering phase transition kinetics in the evaluation of CFZ pharmacokinetic parameters. Of the 6 complete models evaluated in this study, the base 2-compartment model performed the worst due to the inability to capture the insoluble precipitated phase. The 3-compartment model improved upon predictions of the base 2-compartment model as it could capture the additional distribution due to the CLDI phase as a static environment but could not account for the variability of different amounts of precipitation at different total CFZ loads. The four expansion functions on the 2-

compartment model all outperformed the base 2-compartment and 3-compartment model since they were all able to adapt to the increasing sequestration of precipitated drug. The sigmoidal expansion functions performed comparably and superior to the linear growth model implicating a nonlinear expansion of CFZ Vd during the initial 20 weeks of dosing.

The limited sample size and long sampling interval introduces some inherent limitations to this study. While mice were administered drug orally, absorption was not considered in the model due to infrequent sampling early after dosing. The exponential Hill function and rational square root functions evaluated in this study yielded low AIC, excellent visual predictive accuracy, and physiologically relevant parameters consistent with the measured pharmacokinetics and the biological mechanisms of CFZ precipitation and bioaccumulation in mice. Despite the apparent improvements by the sigmoidal expansion functions, the ability to distinguish between minute differences in models was hindered by the size of the dataset, limiting the inspection of interindividual variability and complicating investigation of which sigmoidal function best models the behavior of CFZ. However, with more data, more detailed mechanistic models could be evaluated with other expansion functions. Additionally, only the pharmacokinetics of healthy mice we evaluated in this study. Further analysis is needed to explore the effects of infectious disease on the pharmacokinetics of CFZ. As macrophages are implicated in CFZ accumulation, an infectious agent may alter the context-dependent pharmacokinetics of the drug.

In mice, the accumulation and distribution of CFZ within the macrophages of different tissues is now a well characterized phenomenon. CFZ undergoes phase transitions in vivo that are paralleled by changes in the pharmacokinetic parameters that govern the half-life and Vd of the drug. With increasing CFZ load, the fraction of drug sequestered as CLDIs increases, with an

associated expansion in the Vd of the drug. This is a previously underappreciated phenomenon that demonstrates, with prolonged dosing, a range of CFZ accumulation patterns over time could lead to very different drug efficacy and toxicity profiles over the course of dosing [8]. Based on the observed increase in CFZ concentration in the spleen and other organs, CFZ does not reach steady state, even though serum concentrations are constant during the treatment regimen.

While this study presents an approach to model and analyze the drug load-dependent pharmacokinetics profile of CFZ in mice, the parameter values obtained from mice may not directly correlate with parameter values in humans. Nevertheless, the phenomenon analyzed in this study bears relevance to the human situation, since it is known that CFZ precipitates and accumulates in macrophages of patients treated with CFZ [14,16,17]. Despite differences in clearance and blood flow between humans and mice, this modeling framework establishes an adaptive compartmental approach which requires no external, theoretical compartments while also attempting to explain drug accumulation through the perspective of a context-dependent volume of distribution. From published articles showing CFZ crystals present in macrophages under a variety of total drug loads [18], we can safely assume that the principles of non-linear, adaptive Vd expansion demonstrated in this study will apply to CFZ dosing regimens with associated phase transitions. The increasing Vd, driven by CFZ precipitation and bioaccumulation indicates a need for re-evaluating methods by which steady state drug concentrations in serum are interpreted and their relevance to the local drug concentrations at the site of action.

In relation to the three-compartment approach for modeling CFZ pharmacokinetics in humans, our study suggests that adding more peripheral compartments may indeed improve predictive accuracy, but not beyond that of adaptive Vd models. This indicates that as CFZ

precipitates with continued dosing, dynamic modeling approaches more closely approximate CFZ pharmacokinetics, relative to fixed volume, multicompartment models. Although there is variability in the estimation of volume of distribution and half-life using the different sigmoidal equations, the different functions converge towards consensus parameter estimates that are all within 2-fold range of values. This indicates that the structure of the sigmoidal function is less important than the model flexibility in adapting to the expanding volume of distribution.

CFZ loading capacity has been previously studied under a different dosing regimen [6]. The total CFZ load reported in this analysis was equal in mass to the cited study but administered over a 2.5-fold longer period, potentially leading to significantly different patterns of drug sequestration and clearance. Due to the difference in fractional sequestration of CFZ at different total CFZ loads, we would expect the pharmacokinetics and drug accumulation to change in a dose-dependent fashion. By combining classical compartmental kinetics with the mechanistic implications of soluble-to-insoluble phase transitions, CFZ accumulation rate and capacity can be estimated in an organ-specific accumulation pattern.

From these data, it is not clear whether CLDIs contribute to the pharmacological activity of the drug, or whether they may lead to toxicity, which may include changes in the immune system or metabolic changes that accompany CFZ accumulation [3]. Clearly, the increase in CFZ mass with repeated dosing corresponds to a drug depot mechanism that is poised to influence how long the drug remains in the host after treatment in discontinued. When selecting a dose for treatment, both the potential for therapeutic benefit and adverse events needs to be considered for optimal use of the drug. In the case of a fastidious mycobacterial infection, long half-lives can be important in terms of preventing drug resistant microorganisms from taking a foothold, long after treatment is discontinued. Thus, this analysis serves to highlight many

research avenues that still remain to be explored in the context of the pharmacokinetics and pharmacodynamics of CFZ, even as this drug has been used across the world for the elimination of leprosy for half a century (and now for the treatment of multi-drug resistant tuberculosis and possibly for the treatment of viral infections).

This work may also constitute a wider modeling framework for bioaccumulating drugs or molecules with context-dependent pharmacokinetic properties. For example, azithromycin has been shown to accumulate intracellularly in human skin fibroblasts, implicating a cell dependent accumulation pathway [19]. Likewise, amiodarone accumulates in alveolar macrophages inducing phospholipidosis and potentially undergoing a context-dependent change in pharmacokinetics [20]. This unique approach to modeling allows further study of drugs in the development pipeline which have poorly understood pharmacokinetic attributes. The generalization of this model to new and existing pharmaceutical compounds may improve the efficacy to toxicity profile of dosing regimens.

2.6 Conclusions

Using mice as an experimental model and based on a dosing scheme of 25 mg/kg of CFZ daily, the changing pharmacokinetics of CFZ over a 20-week time course of treatment were modeled using an adaptive Vd function to capture the bioaccumulation of the drug in the organism. By incorporating nonlinearity into our pharmacokinetic models to capture soluble to insoluble phase transitions, it was possible to more accurately predict serum and tissue concentrations. It is likely that such adaptive pharmacokinetics modeling framework would also be applicable to the analysis of human clinical data, which could better inform our dosing strategies and understanding of CFZ efficacy and side effects. By analyzing the accumulation of

CFZ within macrophages that can be obtained in patient sputum samples, it is possible that human pharmacokinetics models of CFZ could be improved. While drug accumulation in mice tissues is analyzed after the animals are euthanized, one avenue to explore, analyze, and model the extent of CFZ accumulation in human PK datasets could involve noninvasive pharmacoimaging techniques, such as positron emission tomography (PET).

2.7 References

1. Yuan S, Yin X, Meng X, Chan JF, Ye ZW, Riva L, et al. Clofazimine broadly inhibits coronaviruses including SARS-CoV-2. Nature. 2021;593(7859):418-23.
2. Riva L, Yuan S, Yin X, Martin-Sancho L, Matsunaga N, Pache L, et al. Discovery of SARS-CoV-2 antiviral drugs through large-scale compound repurposing. Nature. 2020;586(7827):113-9.
3. ClinicalTrials.gov. Dual Therapy With Interferon Beta-1b and Clofazimine for COVID-19 - Full Text View [Available from: clinicaltrials.gov/ct2/show/NCT04465695.
4. Keswani RK, Yoon GS, Sud S, Stringer KA, Rosania GR. A far-red fluorescent probe for flow cytometry and image-based functional studies of xenobiotic sequestering macrophages. Cytometry A. 2015;87(9):855-67.
5. Rzeczycki P, Yoon GS, Keswani RK, Sud S, Stringer KA, Rosania GR. Detecting ordered small molecule drug aggregates in live macrophages: a multi-parameter microscope image data acquisition and analysis strategy. Biomed Opt Express. 2017;8(2):860-72.
6. Rzeczycki P, Woldemichael T, Willmer A, Murashov MD, Baik J, Keswani R, et al. An Expandable Mechanopharmaceutical Device (1): Measuring the Cargo Capacity of Macrophages in a Living Organism. Pharm Res. 2018;36(1):12.
7. Logan R, Kong AC, Axcell E, Krise JP. Amine-containing molecules and the induction of an expanded lysosomal volume phenotype: a structure-activity relationship study. J Pharm Sci. 2014;103(5):1572-80.
8. Woldemichael T, Keswani RK, Rzeczycki PM, Murashov MD, LaLone V, Gregorka B, et al. Reverse Engineering the Intracellular Self-Assembly of a Functional Mechanopharmaceutical Device. Sci Rep. 2018;8(1):2934.
9. Baik J, Stringer KA, Mane G, Rosania GR. Multiscale distribution and bioaccumulation analysis of clofazimine reveals a massive immune system-mediated xenobiotic sequestration response. Antimicrob Agents Chemother. 2013;57(3):1218-30.
10. Arbiser JL, Moschella SL. Clofazimine: a review of its medical uses and mechanisms of action. J Am Acad Dermatol. 1995;32(2 Pt 1):241-7.
11. Cholo MC, Steel HC, Fourie PB, Germishuizen WA, Anderson R. Clofazimine: current status and future prospects. J Antimicrob Chemother. 2012;67(2):290-8.

12. Abdelwahab MT, Wasserman S, Brust JCM, Gandhi NR, Meintjes G, Everitt D, et al. Clofazimine pharmacokinetics in patients with TB: dosing implications. J Antimicrob Chemother. 2020;75(11):3269-77.
13. Swanson RV, Adamson J, Moodley C, Ngcobo B, Ammerman NC, Dorasamy A, et al. Pharmacokinetics and pharmacodynamics of clofazimine in a mouse model of tuberculosis. Antimicrob Agents Chemother. 2015;59(6):3042-51.
14. Harbeck RJ, Worthen GS, Lebo TD, Peloquin CA. Clofazimine crystals in the cytoplasm of pulmonary macrophages. Ann Pharmacother. 1999;33(2):250.
15. Olofsen E, Dahan A. Using Akaike's information theoretic criterion in mixed-effects modeling of pharmacokinetic data: a simulation study. F1000Res. 2013;2:71.
16. Desikan KV, Ramanujam K, Ramu G, Balakrishnan S. Autopsy findings in a case of lepromatous leprosy treated with clofazimine. Lepr Rev. 1975;46(3):181-9.
17. Conalty ML, Barry VC, Jina A. The antileprosy agent B.663 (Clofazimine) and the reticuloendothelial system. Int J Lepr Other Mycobact Dis. 1971;39(2):479-92.
18. Yoon GS, Keswani RK, Sud S, Rzeczycki PM, Murashov MD, Koehn TA, et al. Clofazimine Biocrystal Accumulation in Macrophages Upregulates Interleukin 1 Receptor Antagonist Production To Induce a Systemic Anti-Inflammatory State. Antimicrob Agents Chemother. 2016;60(6):3470-9.
19. Gladue RP, Snider ME. Intracellular accumulation of azithromycin by cultured human fibroblasts. Antimicrob Agents Chemother. 1990;34(6):1056-60.
20. Honegger UE, Zuehlke RD, Scuntaro I, Schaefer MH, Toplak H, Wiesmann UN. Cellular accumulation of amiodarone and desethylamiodarone in cultured human cells. Consequences of drug accumulation on cellular lipid metabolism and plasma membrane properties of chronically exposed cells. Biochem Pharmacol. 1993;45(2):349-56.

Chapter 3 Quantitative Analysis of the Phase Transition Mechanism Underpinning the Systemic Pharmacokinetics Self-Assembly of Clofazimine

Aspects of this work have been published as an original research article in *Pharmaceutics 2022, 14(1), 15.*

3.1 Abstract

Clofazimine (CFZ) is a poorly soluble, weakly basic, small molecule antibiotic clinically used to treat leprosy and is now in clinical trials as a treatment for multidrug resistant tuberculosis and Covid-19. CFZ exhibits complex, context-dependent pharmacokinetics which are characterized by an increasing half-life in long term treatment regimens. The systemic pharmacokinetics of CFZ have been previously represented by a nonlinear, 2-compartment model incorporating an expanding volume of distribution. This expansion reflects the soluble-to-insoluble phase transition that the drug undergoes as it precipitates out and accumulates within macrophages disseminated throughout the organism. Using mice as a model organism, we studied the mechanistic underpinnings of this increasing half-life and how the systemic pharmacokinetics of CFZ are altered with continued dosing. To this end, M. tuberculosis infection status and multiple dosing schemes were studied alongside a parameter sensitivity analysis (PSA) to further understanding of systemic drug distribution. Parameter values governing the sigmoidal expansion function that captures the phase transition were methodically

varied, and in turn, the systemic concentrations of the drug were calculated and compared to the experimentally measured concentrations of drug in serum and spleen. The resulting amounts of drug sequestered were dependent on the total mass of CFZ administered and the duration of drug loading. This phenomenon can be captured by altering three different parameters of an expansion function corresponding to key biological determinants responsible for the precipitation and the accumulation of the insoluble drug mass in macrophages. Through this analysis of the context dependent pharmacokinetics of CFZ, a predictive framework for projecting the systemic distribution of this and other drugs exhibiting similarly complex pharmacokinetics can be constructed.

3.2 Introduction

In chapter 2, a nonlinear, two-compartment model [1] was elaborated to optimally capture the pharmacokinetics of clofazimine (CFZ), a lipophilic, weakly basic antibiotic indicated to treat mycobacterial infections [2,3,4]. Additionally, CFZ is a candidate for treating SARS-Cov-2 infection [5,6,7]. CFZ also acts as an immunomodulatory agent by inhibiting the function of various cellular proteins, including the sodium-potassium ATP-ase [8,9]. CFZ exhibits an increased volume of distribution with extended dosing, resulting in a prolonged half-life with respect to total drug administered [10]. Over a 20-week treatment period, experiments using mice as a model organism [11] revealed that drug accumulation was most prominent in the spleen, which harbors large numbers of xenobiotic sequestering macrophages. It can be inferred from previous studies that this increase in half-life corresponds to an increasing volume of distribution that resulted from drug precipitation and massive accumulation in macrophages [12].

To accommodate for the increased drug load, increased numbers of xenobiotic sequestering macrophages and splenomegaly have been observed [10,12,13].

Based on quantitative observations employing a combination of microanalytical techniques together with physicochemical characterization of drug precipitates, CFZ accumulation in the spleen occurs through the formation of intracellular Crystal-Like-Drug-Inclusions (CLDIs), which are stabilized within macrophage lysosomes upon long term oral administration [14]. The mechanism underlying CLDI formation involves the precipitation of drug as a crystalline hydrochloride salt form exhibiting varying amounts of molecular disorder [15] following ion-trapping of the protonated weak base within the acidic lysosomes of macrophages [16]. Microscopically, CLDIs begin to appear in mice after three weeks of continuous oral administration. Accordingly, the mechanism underlying CLDI formation and stabilization within macrophages is the most likely and directly measurable candidate mechanism explaining the abnormal pharmacokinetics of the drug, including its dose-dependent, increasing half-life and its varying volume of distribution [12].

3.3 Materials and Methods

3.3.1 Introduction of Nonlinearity into 2-Compartment PK Model

As reported in the chapter 2, in order to obtain additional insights into the biological mechanism driving CLDI formation and the corresponding changes in the volume of distribution with respect to time of administration, we assessed how the different parameters governing the soluble-to-insoluble phase transition of the drug impacted the accumulation of CFZ in the organism. Elaborating on these findings using a parameter sensitivity analysis, in this chapter we explored how the manner in which the drug is sequestered and retained within the macrophages

of the spleen would impact the concentrations of drug circulating in the blood. For this purpose, we focused on modeling the increase in the drug volume of distribution of the spleen with the three-parameter rational square root (RSR) function [1]:

Equation 3.1: RSR Function

$$f(t) = \frac{B_1(t - B_2)}{2\sqrt{B_3 + (t - B_2)^2}} + \frac{B_1}{2}$$

Equation 3.1 refers to the expansion function used to apply nonlinearity into the model in Figure 3.1, and it is also referenced as the 'RSR function', 'expansion function', or 'sigmoidal curve.' Incorporating this equation into a 2-compartment pharmacokinetic model (Figure 3.1), we predicted deviations from the expected results derived from modeling the pharmacokinetics of drug molecules in solution. The results obtained by incorporating this phase transition into the analysis closely paralleled the observed time course of drug accumulation in the serum and spleen. Most conveniently, the RSR function contains three parameters: the first of which captures the upper limit of the function (B1) when the spleen's volume of distribution reaches a maximum; the second which captures the time of inflection (B2) when the rate of CLDI growth changes from increasing to decreasing with respect to time; and a third parameter (B3) which affects the overall curvature of the function, reflecting the rate at which drug precipitates out of solution. By varying each parameter individually, the systemic pharmacokinetics of the drug were directly related to the experimentally measured, soluble-to-insoluble phase transition of CFZ in the spleen. Changing B1, B2, and B3 impacted the predicted concentration of CFZ in the serum and spleen, its half-life, and ultimately, the amount of drug that precipitated out and accumulated in the organism each day during the treatment period. By conducting this analysis

of CFZ pharmacokinetics under multiple dosing schemes and in both M. tuberculosis infected and uninfected mice, these results further our understanding of how the biological mechanisms of CLDI formation, underlying the soluble-to-insoluble phase transition of the drug, ultimately explain the context-dependent pharmacokinetics of the drug in relation to sequestered drug mass and rate of drug administration.

3.3.2 Data Acquisition and Compartmental Pharmacokinetics Modeling

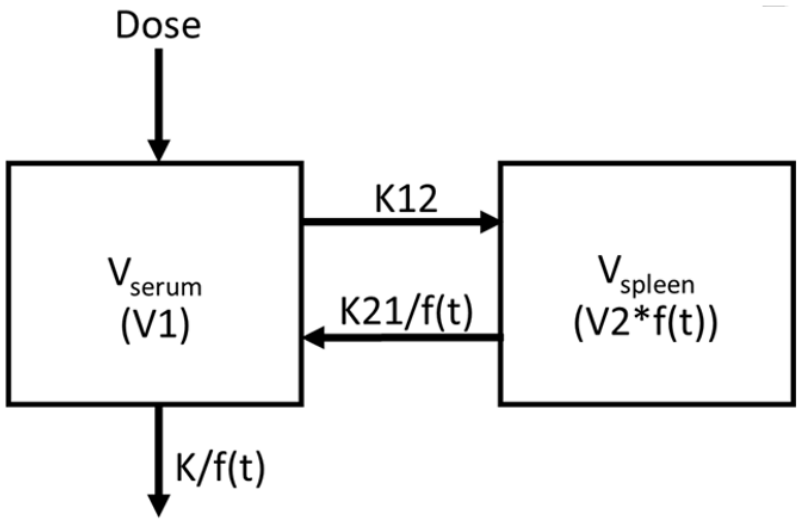

Figure 3.1:. The previously published 2-compartment, context-dependent pharmacokinetic model [1] using the RSR expansion function as f(t).

Pharmacokinetics data for the sensitivity analysis was obtained from a previously published 20-week trial with uninfected BALB/c mice which were orally administered 25 mg/kg of CFZ for 5 days each week [11]. Animal procedures were approved by the Animal Ethics Sub-Committee of the University of KwaZulu-Natal (reference numbers 068/13/Animal and 025/14/Animal) [11]. Concentrations of CFZ were measured in the serum and spleen of these

mice alongside the masses for each organ. To quantitatively analyze the changes in drug concentration in mice over time, a population pharmacokinetic model was constructed in NONMEM (ver. 7.3.0). Model validation was conducted using bootstrapping in Wings for NONMEM (WFN) to generate parameter estimates, objective function value (OFV), 95% confidence intervals, and coefficients of variation (CV%). After bootstrapping 1000 runs of the RSR function with fixed V1 and K12, parameter sensitivity was then evaluated. The dose of drug administered and the measured concentrations of drug in serum and spleen were used as input. To illustrate this modeling approach (Figure 3.1), analysis was focused on serum and spleen compartments. To capture the observed changes of drug mass in the spleen, a three-parameter sigmoidal function f(t) (Equation 3.1) was used to model the time-dependent volume of distribution in the spleen, reduced efflux of drug from spleen to serum compartment (K21), and reduced efflux from the system (Ke). Equation 3.1 was selected for further evaluation based on lowest Akaike information criteria (AIC) [1] and the direct relationship between the maximal volume of distribution, the inflection point, and the curvature to the corresponding parameters B1, B2, and B3.

3.3.3 Parameter Sensitivity Analysis (PSA)

To analyze how each parameter in the optimized RSR model contributed toward capturing the overall, systemic pharmacokinetics of the drug, parameters B1, B2, and B3, of Equation 3.1 were varied while holding all other parameters constant. To visualize how the variation in the parameter values affected the pharmacokinetics of the drug, 10-fold increases and 10-fold decreases in the parameters were used to perform simulations using NONMEM. By varying each parameter by an order of magnitude, we accounted for a large variation of possible

optimization values. These simulations involved calculating the predicted concentration of CFZ in each compartment over a 20-week time course using the range of different parameter values. In addition, other important measures such as the time-dependent pharmacokinetic variables and volume of distribution in the spleen (VSpleen) were recorded. OFV, a -2-log likelihood measure of error between observed and predicted CFZ concentration, was calculated from the simulations. By visual inspection, the results of changing the parameter values were assessed in relation to the curve with the best fit to the concentration vs. time data, which was calculated based on the optimized parameter values and using the same model as previously published [1]. Root mean squared logarithmic error (RMSLE) was used alongside the OFV to further evaluate goodness of fit (Equation B.1). Confidence intervals, coefficients of variation (CV%), and parameter estimates were generated by bootstrapping analysis.

3.3.4 Total Volume of Distribution and Half-Life Calculations

The total volume of distribution for the two-compartment model was defined as the volume of distribution in compartment 1 (Vserum) added to the volume of distribution in compartment 2 (Vspleen), resulting in the equation:

Equation 3.2: Total Volume of Distribution

$$\boldsymbol{V_{total} = V_{serum} + V_{spleen} = V_1 + V_2 * f(t)}$$

Half-life was calculated by two independent methods; (1) model predicted half-life, and (2) observed half-life. The model predicted half-life was calculated continuously by adapting the

model's output of elimination rate constant based on a single-compartment, first-order exponential decay model according to the following equation:

Equation 3.3: Half-Life Calculation

$$t_{½} = \frac{\ln(2)}{K_e(t)}$$

where Ke(t) ¬corresponds to the variable, time-dependent elimination rate constant calculated by the RSR nonlinear model. The observed half-life was calculated from the terminal rate constants of washout data obtained after loading mice with drug for varying treatment periods and then discontinuing treatment, as performed in the aforementioned study. Serum and spleen CFZ concentration data after the cessation of dosing was measured at 4, 8, 12, 16, and 20 weeks to generate a load-dependent relationship between half-life and duration of dosing. The terminal rate constant from single dose data was used alongside multi-dose data to provide an initial estimate of half-life. Log-linear regression from drug washout data was used to identify the terminal rate constant at the cessation of dosing, which was then converted into half-life. The half-lives with respect to total drug administered were compiled and compared to the predicted half-life using the phase-transition model incorporating the RSR function.

To calculate the total drug mass in the spleen, we used an approximate density of 1 mg/g in the spleen tissue [17] and a calculated average spleen mass of 176 mg from the harvested mice organs.

3.3.5 Dose Dependent Mass Sequestration Analysis:

To analyze the mechanistic underpinnings of the phase transition, we utilized additional CFZ pharmacokinetics data in mice under several different dosing regimens [11,12]. Eight different dosing schemes, including three regimens with CFZ loading doses (Table 3.2), were used to determine relationships between spleen mass, fractional drug sequestration, and total CFZ drug load. Additionally, M. tuberculosis infection status was analyzed as a covariate in the distribution of CFZ. Concentration data for mice infected with aerosolized M. tuberculosis H37Rv (ATCC 27294) were obtained from a previously published study [11]. The relationship between dosing regimens was subjected to pharmacometrics analysis utilizing the RSR function, , and both linear and log-transformed linear regression conducted in RStudio. Additionally, the cumulative fraction of drug sequestered was evaluated under multiple different dosing regimens. Cumulative fraction sequestered was calculated by dividing the measured mass of drug in the spleen by the total administered mass of drug since the start of dosing.

3.4 Results

3.4.1 Comparative Analysis of Sigmoidal Functions and Utility of the RSR Equation to Describe the Mechanistic Underpinnings of CFZ Pharmacokinetics

In chapter 2, three different sigmoidal expansion functions f(t) were used to capture the time-dependent change in the volume of distribution. Based on these three different functions, the volume of distribution of the spleen first grows rapidly, then hits an inflection point, and ultimately approaches an upper limit. Consistent with obvious differences in how the shape of the curve is governed by these equations and the corresponding parameters, the parameterization of each of these functions caused notable differences in model output. For the purpose of the mechanistically-relevant, parameter sensitivity analysis performed in this study, the RSR

equation (Equation 3.1) was used as an expansion function. The RSR equation is parameterized in such a way that the relationships between model parameters and the mechanisms of volume of distribution expansion (and the corresponding drug mass that accumulated in the spleen) was quite simple and direct. Thus, we decided to use the RSR function to obtain additional insights into the relationship between CFZ's soluble-to-insoluble phase transition and the resulting changes in the systemic concentration of the drug.

Unlike the Exponential Hill Equation and the Logistic Growth Equation, the maximum value achieved by the RSR function corresponds only to B1, such that the maximal volume of distribution is directly relatable to B1. Furthermore, the RSR equation reaches half its maximal value at time (t*), which corresponds to the time of inflection, where t* = B2. Finally, one can estimate the curvature using the maximum slope (f'max) where,

Equation 3.4: RSR Slope

$$f'_{max} = \frac{B_1}{2\sqrt{B_3}}$$

Accordingly, the curvature change is inversely proportionally to the square root of B3 and there exists a linear relationship between maximum slope and B1.

Notice that in the RSR model, the maximum achieved value and time to reach 50% capacity both correspond to a single parameter (B1 and B2, respectively). Further, B3¬ can be used to approximate the intensity of curvature for the sigmoid curve, with an increase in B3 flattening out the curve. In contrast to the RSR function, the maximum value of the exponential Hill equation is exponentially dependent on Emax, and t* is dependent on all three parameters. Thus, with the Hill equation, fitting both the derivative and its maximum value is complicated by their

mutual dependency on all three parameters, implying single parameter adjustments are not directly correlated to a single pharmacokinetic phenomenon. In the Logistic Growth equation, t* and the maximum slope are both dependent on two parameters. Thus, the Hill and logistic growth equations are more complicated due to the highly 'coupled' parameter values, which jointly altered the curvature of the expansion function. The logistic growth model is much less coupled than the Hill model, but it relies on two parameters to determine the time to reach the half capacity inflection point. Thus, as the most "uncoupled" modeling framework, the RSR function greatly facilitated mechanistic interpretation of the quantitative analysis.

3.4.2 Preliminary Analysis of Parameters on Growth Function f(t)

To begin addressing the extent to which different parameters of the RSR equation impacted the shape of the curve, the three parameter values B1, B2, and B3 were varied individually and their effect on the function's output was plotted and analyzed by visual inspection (Figure 3.2). Accordingly, B1 sets an upper limit for the curve, creating a horizontal asymptote which is approached with continued dosing. As such, B1 proportionally increases the magnitude of the RSR function (Figure 3.2A). In contrast, B2 creates a shift in the inflection point of the sigmoidal curve along the x-axis (Figure 3.2C). Particularly, it achieved this by shifting the time of inflection which corresponded to the time of half-maximal output value (t*), or where the second derivative f'(t) was equal to zero. B3 is also related to the expansion time by describing the rate at which the expansion function increases over time (Figure 3.2E). Nevertheless, large changes must be made to parameter B3 to influence the curvature of the function. A decrease in B3 corresponds to an increased slope or sharpened curvature while an increase in B3 accordingly diminishes slope and soften curvature. Accordingly, there are

differences in the sensitivity of the model for each of these parameters due to different scalar changes necessary to show significant difference in curve shape or function value.

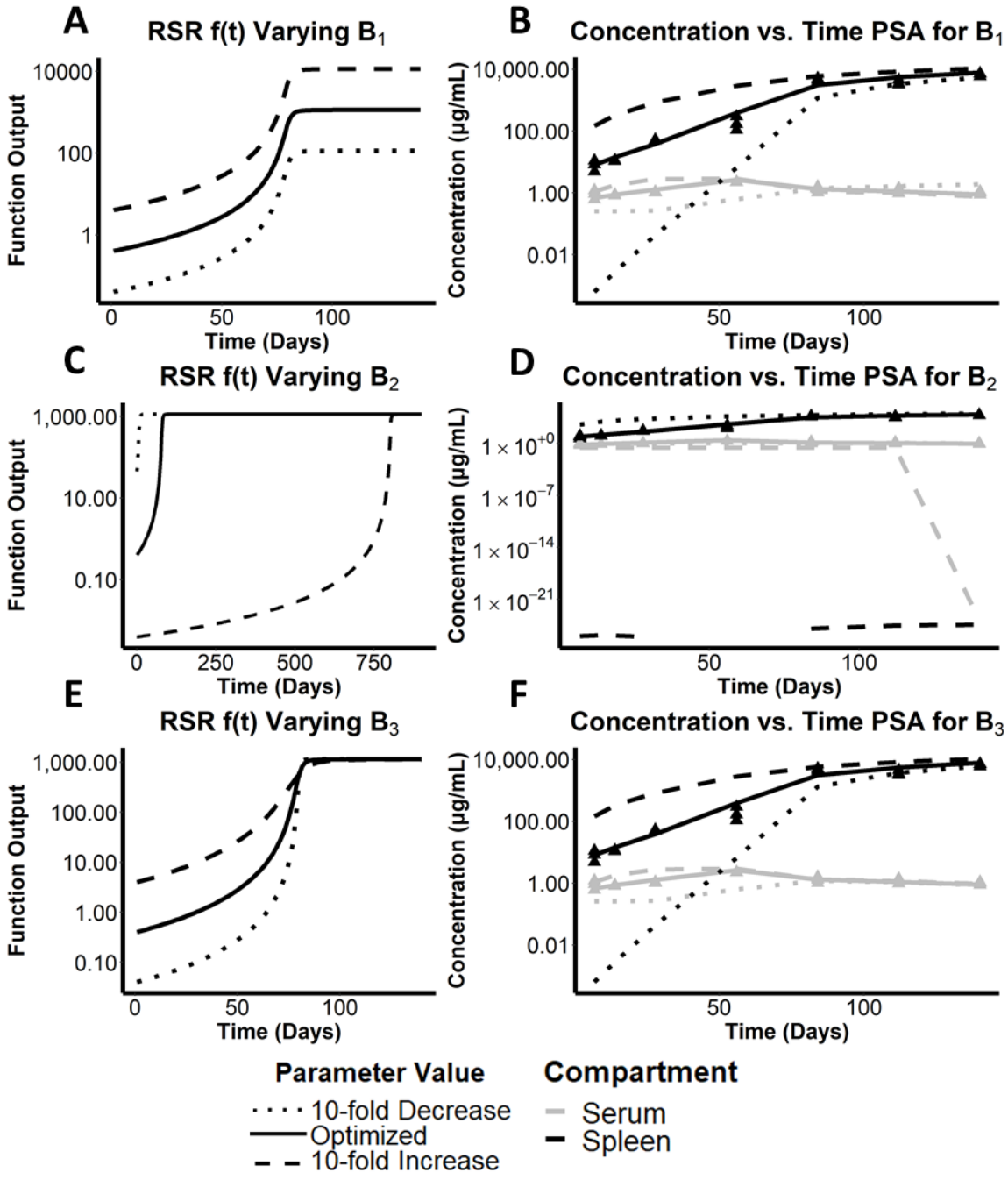

Figure 3.2:Mathematical analysis of parameters governing the phase transition. Plots A, C, and E demonstrate the parameterization of the RSR f(t) function by increasing/decreasing each parameter from the optimal values by an order of magnitude, where the solid line is the optimized value, the dotted line is a 10-fold decrease, and the dashed line is a 10-fold increase; A) B1 with a 10-fold increase and decrease, C) B2 with a 10-fold increase and decrease, and E) B3 with a 10-fold increase and decrease. Plots B, D, and F show the predicted concentration/time changes with respect to a 10-fold increase (dashed lines) and decrease (dotted lines) of parameter: B) B1, D) B2, and F) B3 compared to the predicted concentration over time for the optimized parameters. The triangle points represent the observed data points in both the serum (grey) and spleen (black).

.

3.4.3 Assessing the Effect of the Maximal Cargo Capacity of the Spleen on the Systemic Pharmacokinetics of CFZ

To capture the change in volume of distribution of the spleen compartment, we must look more closely at B1. B1 determines the upper limit of Vspleen, as f(t) approaches B1 during the 20-week treatment period. Mechanistically, B1 reflects a function of biological steady state at a given dose which incorporates spleen growth, increase in the number of xenobiotic sequestering macrophages, and the maximum cargo capacity of the cells that sequester the accumulated drug without leading to overt toxicity. Accordingly, a 10-fold increase in B1 would lead to a corresponding increase in the total drug cargo of macrophages in the spleen (Figure 3.2A, dashed line) relative to the baseline cargo (Figure 3.2A, solid line). Whereas a 10-fold decrease in B1 would lead to a corresponding decreased cargo load of macrophages in the spleen, implying an expected decrease in maximal drug concentration in the organ (Figure 3.2A, dotted line). Further, B1 directly scales f(t) which affects the flow rate from the spleen into the serum and elimination out of the serum, as shown in the model diagram in Figure 3.1.

Accordingly, by varying the optimized B1 parameter using the 2-compartment pharmacokinetic model incorporating the RSR equation, the results of the simulations indicated how a change in the total cargo capacity of macrophages in the spleen would influence the systemic pharmacokinetics of the drug. Interestingly, noting difference in magnitude using a logarithmic scale for concentration, the most significant impact of varying parameter B1 was observed in the spleen drug concentrations during the first 60 days of drug administration (Figure 3.2B, black lines). The upper (dashed line) and lower (dotted line) bounds of the spleen concentration deviated by an order of magnitude or more from the optimized B1 parameter value that yielded the best fit to the measured drug concentrations in spleen. In contrast, the effect of varying

parameter B1 on the drug concentrations in the serum was far less significant over the entire 20-week time course (Figure 3.2B, grey lines), indicating that the circulating concentrations of CFZ were largely independent of the maximal value of the RSR function. We infer that the total amount of precipitated drug and the expansion of the volume of distribution, as well as the maximal carrying capacity of the macrophages in the spleen, are largely independent of serum concentrations. As expected, changes in B1 were also reflected in the predicted mass of CLDIs in the spleen (Figure 3.2B). Accordingly, an increased cargo capacity would be associated with more precipitated CFZ in CLDIs, whereas a decreased cargo capacity would be associated with less precipitated CFZ in CLDIs.

3.4.4 Quantitative Analysis of the Relative Importance of Different Parameters to the Simulated Systemic Pharmacokinetics of CFZ

To establish the relative importance of parameters B1, B2 and B3 on the systemic pharmacokinetics of CFZ, we used RMSLE as a measure of error (Table 3.1). RMSLE accounts more accurately for changes in order of magnitude by using the difference in natural logarithms between the adjusted parameter model and the optimized model at each timepoint instead of the exact difference used in the more standard root mean squared error (RMSE) analysis. RMSLE was highest for an increased B2, and second highest from a decrease in B2. This indicates that the amount of time that CFZ needs to be dosed to reach the inflection point of the phase transition, and thus the amount of drug exposure that the organism needs to experience the maximal rate of CLDI accumulation, plays the most significant role in terms of its impact on the systemic pharmacokinetic of CFZ.

OFV was also calculated for each parameter sensitivity analysis performed in this study. The OFV is proportional to the sum of the difference of squares between observed concentration data and predicted concentrated data [6], so it functions similarly to standard RMSE which accounts for direct difference rather than logarithmic or proportional error. It follows that overestimates due to large changes in parameter values could be weighted as higher error than vast underestimates, both of which are expected by varying each parameter by an order of magnitude in the PSA. Accordingly, the highest OFV is observed for an increase in B1, and the second highest OFV comes from an increase in B2. Thus, changing the upper limit and the time of inflection both become important when accounting for direct differences between the model and observed data. Diagnostic plots and corresponding values for the PSA are shown in Figures B.1-B.4.

Scaling parameters by changing their order of magnitude through 10-fold increases and decreases suggest that shifts in B2 cause the most drastic changes in model output. Conceptually, this parameter controls the highly time-dependent nature of the acceleration of the phase transition event, so it is natural that such a parameter impacts the model so strongly. To further investigate the dependence of the model on B2, we generate 95% Confidence Intervals (CIs) for each parameter alongside the coefficients of variation (CV%). Table 3.1 shows that, when normalized, B2 has by far the tightest bound about which we can be 95% confident in the model's predictive capabilities. This agrees with the earlier hypothesis that the kinetics leading to time of drug precipitation impact the physiological outcomes, such as drug concentration, more than theoretical notions of maximum cargo capacity or rate of precipitate accumulation. This is shown by the much smaller CV% in B2 compared to B1 and B3. Additionally, this sensitivity

analysis provides insight into which parameters of expansion functions provide the most robust and replicable estimates.

Table 3.1: Quantitative measures of model sensitivity including RMSLE and OFV values for 10-fold changes are represented for each of the expansion function parameters. Optimized model-specific parameters (P), as well as their 95% confidence intervals (CI) are included for each RSR parameter. CV% was calculated by dividing standard deviation by the mean and multiplying by 100%.*

Parameter	RMSLE for 10-fold Increase	RMSLE for 10-fold Decrease	OFV for 10-fold Increase	OFV for 10-fold Decrease	P*	CI	CV%
B_1	0.239	0.321	316.419	209.998	1150	[449 , 1150]	32.3%
B_2	0.749	0.297	335.703	326.066	80.2	[76.7 , 82]	3.20%
B_3	0.237	0.314	317.759	211.809	8.84	[4.92 , 13.1]	36.5%

3.4.5 Estimation of Increasing Half-Life as a Function of Increasing Volume of Distribution

Using washout data from single dose administration and after 4, 12, 16, and 20 weeks of dosing at 25 mg/kg/day [11], log-linear regression was used to estimate the terminal rate constant of the serum and spleen concentrations over time. The half-life of each total CFZ load was thus evaluated and plotted against a linear regression to identify the trend in half-life with increasing drug load (Figure 3.3A). The half-life of CFZ in the serum increased from 2.9 days after a single dose to 50.6 days after 20 weeks of dosing, resulting in a 17.4-fold increase in half-life in the serum. In comparison, the half-life of CFZ in the spleen increased from 4.9 days after a single dose to 74.5 days after 20 weeks of dosing, resulting in a 15.2-fold increase in half-life in the spleen. While characterized by different rates and extents, the increase in half-life in both the serum and spleen are dependent on the total amount of CFZ administered. By estimating the half-life in both the serum and spleen as a function of total CFZ administered, we can restrict our

estimations of the expansion of the volume of distribution throughout the dosing period, to encompass physiological data more accurately. Utilizing the RSR function we optimized the pharmacometrics model with restricted ranges on both the elimination rate constant (Ke) and the B1 expansion variable to result in less than 2-fold difference from the observed half-life. The restricted RSR function was plotted alongside the calculated half-life values in the spleen and serum (Figure 3.3B). Under these conditions, the optimized fit of the RSR under-estimated the half-life in low-loading conditions and over-estimated the half-life under higher loading conditions. This indicated that, while the model could strongly predict drug concentration in both the serum and spleen, the overall prediction of half-life from these two compartments can be improved with additional experimental data and the development of a more refined model aimed at better capturing the elimination kinetics of the drug following discontinuation of treatment.

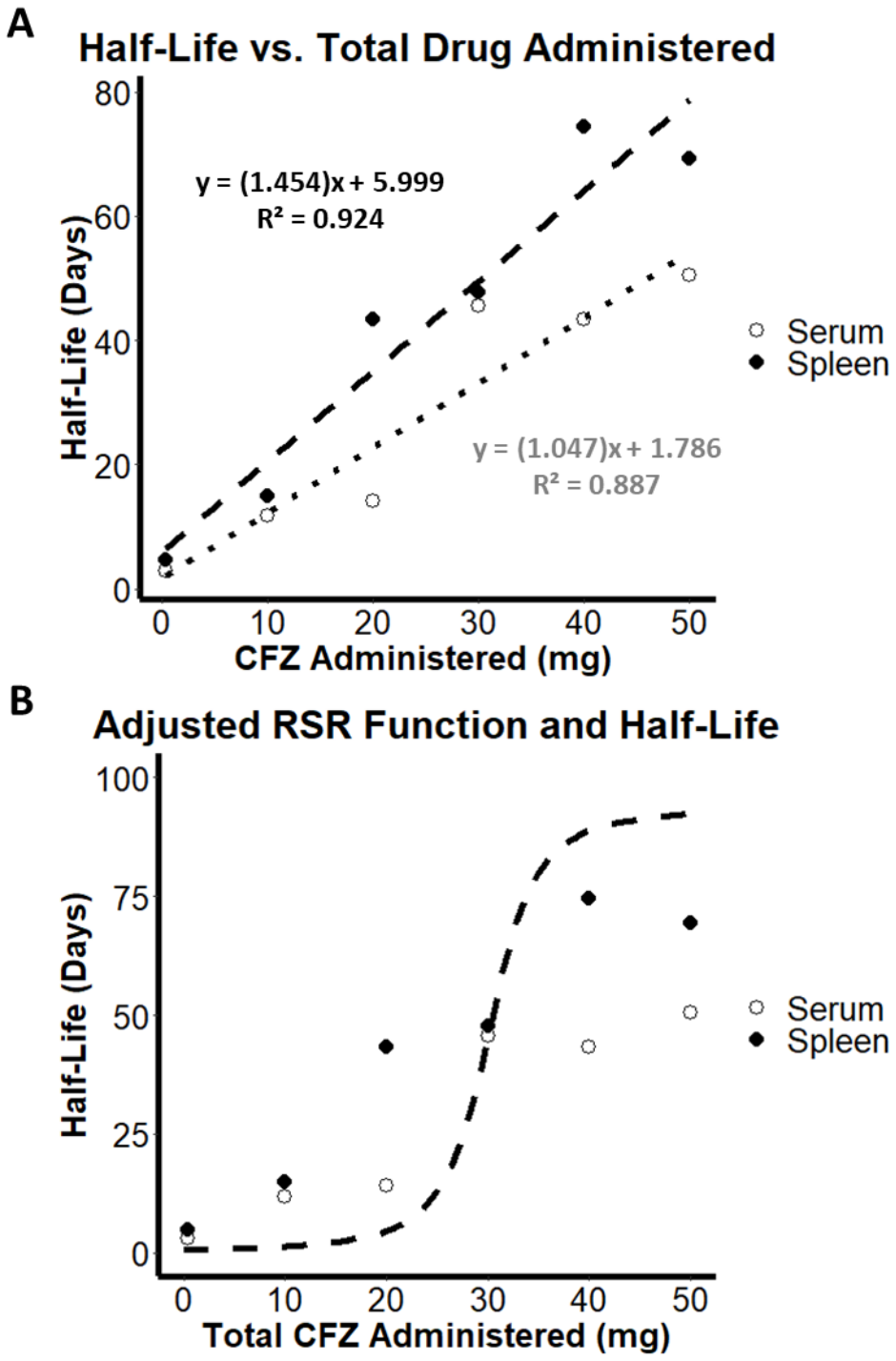

Figure 3.3:Drug half-life in the organism is related to the cumulative dose administered. A) Load dependent relationship between total CFZ administered and the resulting half-life follows a linear regression in the serum (dotted) and spleen (dashed). B) Calculated serum (open circle) and spleen (closed circle) half-lives plotted against the predicted half-life from the body with the RSR function optimized within 2-fold range of upper and lower observed half-life.

3.4.6 Patterns and Evidence of Load-Dependent Pharmacokinetics from Variable Dosing Data

Based on the insights obtained by focusing on the relationship between the phase transition of CFZ and the systemic pharmacokinetics of the drug, a natural follow up question was: to what extent are these parameters and equations impacted by variation in the dosing regimens? To address this question, eight published CFZ dosing regimens using a range of dosing schemes, including regimens with 2-week loading doses, were analyzed (Table 3.2) [11,12]. As a result, the total load of clofazimine administered up until each timepoint was evaluated as a covariate rather than the daily dose.

*Table 3.2: Eight dosing regimens were evaluated from literature. *Evaluated at 3 weeks instead of 2 weeks. † Infected with M. tuberculosis (studies 3-8). References: Studies 1, 3-8 [11], Study 2 [12]. BALB/c mice were used in each of the observed dosing regimens.*

#	Dosing Regimen	Total Duration	Route of Administration	CFZ Load at 2 Weeks (mg)	CFZ Load at 8 Weeks (mg)	Total Drug Load (mg)
1	25 mg/kg/d, 5 days per week	20 weeks	Oral Gavage	5	20	50
2	36 mg/kg/d, 7 days per week	8 weeks	Mixed in Feed	18.9*	50.4	50.4
3†	6.25 mg/kg/d, 5 days per week	12 weeks	Oral Gavage	1.25	5	7.5
4†	12.5 mg/kg/d, 5 days per week	12 weeks	Oral Gavage	2.5	10	15
5†	25 mg/kg/d, 5 days per week	12 weeks	Oral Gavage	5	20	30
6†	50 mg/kg for 1 day, 25 mg/kg for day 2 to week 2 (5 days per week), 25 mg/kg/d for weeks 2 through 12 (3 days per week)	12 weeks	Oral Gavage	5.5	14.5	20.5
7†	100 mg/kg for 1 day, 75 mg/kg for day 2, 50 mg/kg for day 3 to week 2 (5 days per week), 25 mg/kg/d for weeks 2 through 12 (3 days per week)	12 weeks	Oral Gavage	11.5	20.5	26.5
8†	200 mg/kg for 1 day, 100 mg/kg for day 2, 75 mg/kg for day 3 to week 2 (5 days per week), 50 mg/kg/d for weeks 2 through 12 (3 days per week)	12 weeks	Oral Gavage	18	27	33

When sequestered drug mass in the spleen was plotted on a logarithmic scale in relation to the total amount of drug administered (Figure 3.4A), pharmacokinetics of CFZ appeared different in M. tuberculosis infected vs uninfected mice. To better understand these differences in quantitative terms, we performed a nonlinear regression analysis on the plotted data. Accordingly, the uninfected mice showed a log-linear increase in total drug mass sequestered with increasing drug load (blue curve in Figure 3.4A). In contrast, the infected mice showed a linear increase in total sequestered drug mass with increasing drug load (red curve in Figure 3.4B). These results suggested that infected and uninfected BALB/c mice accumulated drug at different rates and extents within the observed dosing regimens.

Additionally, when evaluating the mass of drug sequestered in the spleen at 2 and 8 weeks of administration across each of the 8 datasets, visual inspection of the plots revealed obvious differences in the dynamics of drug accumulation (Figure 3.4B, C). Upon further analysis, a moderate linear correlation ($R2 = 0.89$) between CFZ mass accumulated in spleen and total drug administered occurred during the first two weeks of treatment, implying a direct correlation between increasing drug load, and increasing drug mass in the organism. However, when looking beyond 2 weeks of treatment, a strong log-linear relationship ($R2 = 0.92$) between drug mass sequestered and total CFZ administered was observed by the eighth week, implying an exponential increase in CFZ mass sequestered in the spleen with respect to amount of drug administered. The shift from linear to log-linear correlation that occurred as a function of the total amount of drug administered mirrored the results of pharmacokinetics simulations performed with the nonlinear two compartment model incorporating the RSR function, in which nonlinearity from f(t) is much more apt to describe the data obtained at later time points, at which more total drug load has been supplied. These results suggest that in BALB/c mice,

infection status, duration of dosing, and total mass administered all influence the fraction of drug sequestered in the spleen at any particular time-point during the dosing period.

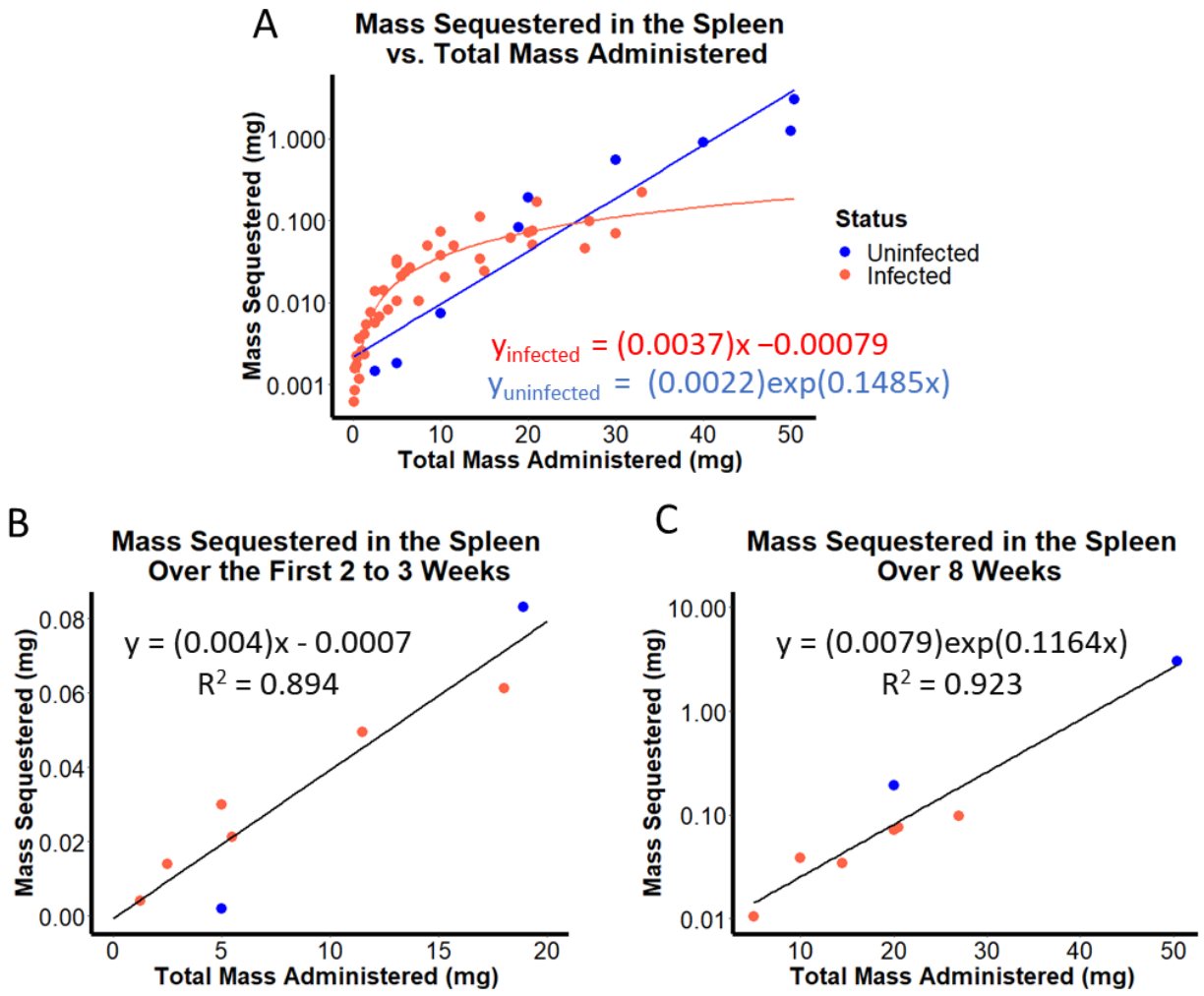

Figure 3.4: Healthy vs. Infected CFZ Mass Sequestered in the Spleen A) Mass sequestered in the spleen as a function of total CFZ administered across 8 dosing regimens with optimization run on the data from uninfected mice (blue) and M. tuberculosis-infected mice (red). B) Average mass sequestered after 2 or 3 weeks of drug loading at each of the 8 dosing regimens compared to the total drug administered. C) Average mass sequestered after 8 weeks of drug loading at each of the 8 dosing regimens compared to the total drug administered.

Proceeding to examine how the rate of drug sequestration under multiple dosing regimens varies in relation to drug exposure, the cumulative fraction of drug sequestered in the spleen was

plotted against the total CFZ load administered (Figure 3.5). For each of the eight observed dosing regimens, the cumulative fraction of CFZ sequestered in the spleen over the total CFZ administered was predictably different in infected compared to uninfected mice. This relationship was further analyzed by fitting the infected mice data with a linear regression line and uninfected mice data with exponential regression (Figure 3.5A). The relationship between total drug load and cumulative fraction sequestered after drug administration for 2 and 8 weeks (Figures 3.5B and 3.5C respectively) was then analyzed. After 2 weeks of dosing, there was no relationship between total amount of CFZ administered and the fraction of CFZ sequestered in the spleen over the 2-week dosing period ($R^2 = 0.0002$; Figure 3.5B). However, after 8 weeks of drug loading, there was a log-linear relationship between the total amount of CFZ administered and cumulative fraction sequestered over the 8-week dosing interval ($R^2 = 0.79$; Figure 3.5C). It can be inferred that this observed relationship between cumulative fraction of drug sequestered and total CFZ administered across many different dosing regimens is primarily being driven by CLDI formation.

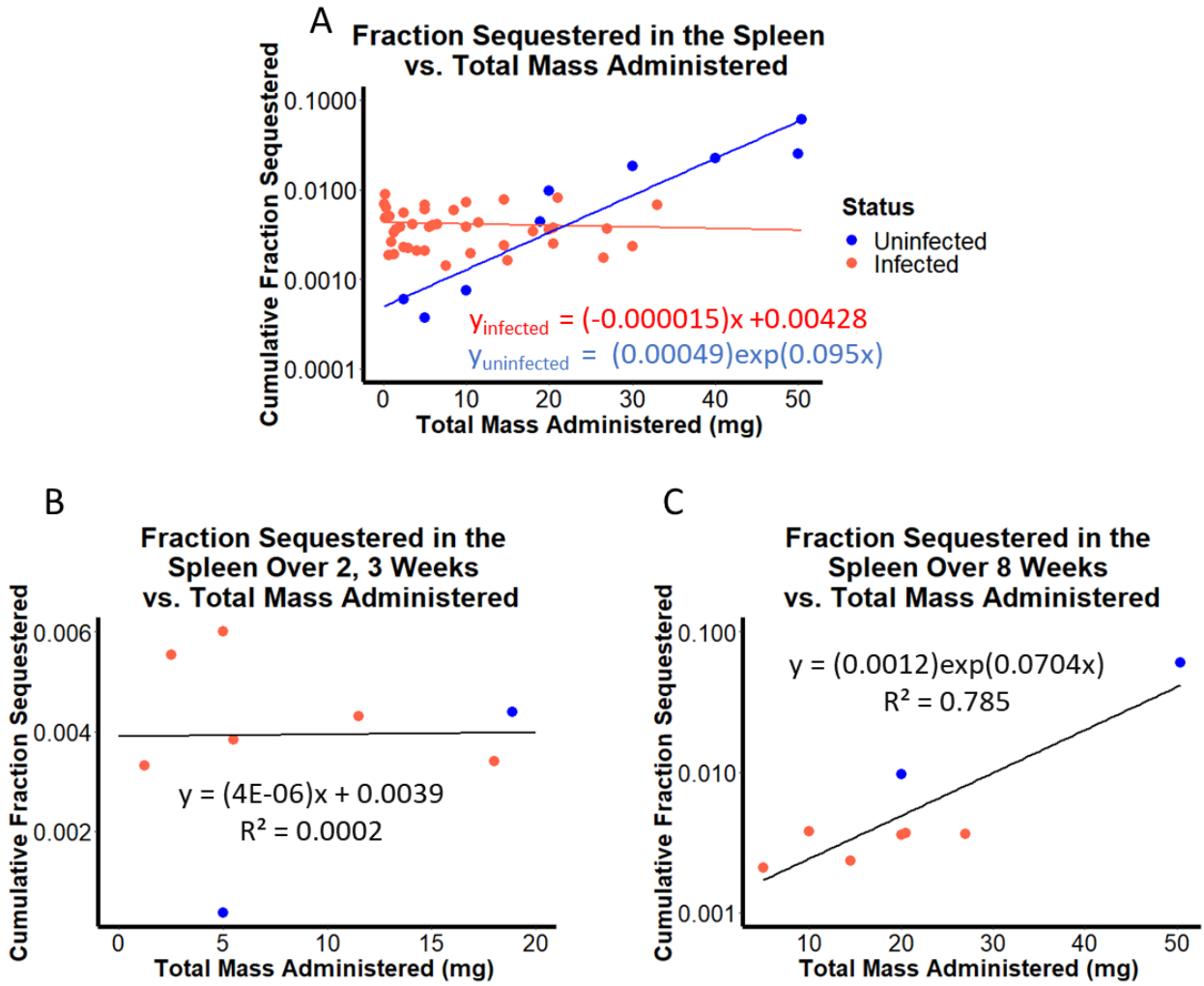

Figure 3.5:Healthy vs. Infected CFZ Fraction Sequestered in the Spleen A) Cumulative fraction sequestered in the spleen as a function of total CFZ administered across 8 dosing regimens in M. tuberculosis infected (red) and uninfected (blue) BALB/c mice. B) Cumulative fraction sequestered after 2 or 3 weeks of drug loading at each of the 8 dosing regimens compared to the total drug administered. C) Cumulative fraction sequestered after 8 weeks of drug loading at each of the 8 dosing regimens compared to the total drug administered.

3.4.7 Investigating the Effect of Infection Status on the Pharmacokinetics of CFZ.

After observing distinct relationships between the total quantity of drug sequestered in the spleen in uninfected and infected mice, additional studies revealed differences in the pharmacokinetics of CFZ in infected and uninfected BALB/c mice undergoing the same dosing regimen of 25 mg/kg/day, 5 days each week for 12 weeks. Comparing the concentration vs time

profiles in infected vs noninfected mice, the rates and extents of drug distribution were different (Figure 3.6). This implied that the presence of an M. tuberculosis infection changed the pharmacokinetics of CFZ. The reduction in CFZ sequestration that resulted from M. tuberculosis infection can be interpreted in terms of a delayed phase transition which does not expand the cargo capacity of the drug nearly as much as in the uninfected state, causing parameters B1 and B2 to decrease, and B3 to increase, consequently leading to f(t) becoming smaller and increasingly linear.

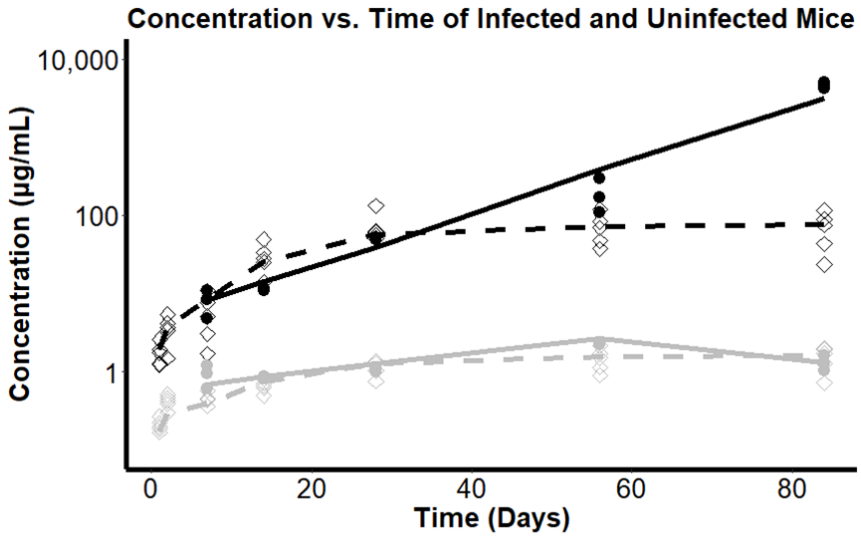

Infected Status	V_{spleen} at 12 Weeks (L)	Spleen Conc. at 12 Weeks (µg/g)	Sequestered Mass at 12 Weeks (µg)	B_1	B_2	B_3
Uninfected	5.48	4684	824	1150 (32.3%)	80.2 (3.20%)	8.84 (36.5%)
Infected	$2.62*10^{-4}$	69.6	12.3	3.53 (92.3%)	8.24 (7.93%)	138 (30.7%)

Figure 3.6:Concentration over time profile in the serum (grey) and spleen (black) over 12 weeks of dosing in mice administered 25 mg/kg/day . Concentration predictions in uninfected mice (solid lines) are shown alongside observed values (solid circles). Concentration predictions in M. tuberculosis infected mice (dashed lines) are shown alongside observed values (diamonds). The accompanying table compares the expansion function parameters alongside the relative volume of distribution, spleen concentration, and mass sequestered after 12 weeks of dosing. CV% are expressed in parentheses below the expansion function parameter estimates.

3.5 Discussion

To summarize, PSA was performed alongside dose dependent analysis of M. tuberculosis-infected and uninfected BALB/c mice to study how the context-dependent pharmacokinetics of CFZ vary over a long-term treatment period. By using the RSR equation to model an expanding volume of distribution in a two-compartment model, the pharmacokinetics parameters governing the soluble-to-insoluble phase transition of CFZ in mice spleen could be mechanistically associated with the dose- and time-dependent, systemic pharmacokinetics of this drug. For the most part, the serum concentrations of CFZ were largely determined independently from parameters governing the soluble-to-insoluble phase transition of CFZ and its accumulation as intracellular CLDI precipitates within macrophages. The increase in the half-life of CFZ was expectedly coupled to the expansion of the drug volume of distribution, which can be explained by the thermodynamic and cellular mechanisms responsible for the precipitation of the drug within macrophages [10,12,16]. The modeling approach presented here suggests that the actual concentrations of the drug in the blood are minimally affected by the mechanisms governing the phase transition of the drug throughout the dosing period. To the extent that drug precipitation within macrophages may account for the majority of CFZ accumulation in the organism, there is no reason to expect a steady state of insoluble CFZ is achievable unless the biological, maximal drug cargo capacity of all the macrophages in the organism is saturated. Nevertheless, once the drug precipitates out in the organism, the actual drug concentrations in blood remain nearly constant and insensitive to variations in the dosing regimens, as the circulating drug levels are determined by the thermodynamic equilibrium of drug present in solution with that present in the insoluble precipitates.

3.5.1 Exploring the RSR Function as a Tool to Describe Soluble-to-Insoluble Phase Transitions in a Population Pharmacokinetics Model

The analysis performed herein identified at least two main causes for the differences in the ability of different sigmoidal equations to fit CFZ's context-dependent pharmacokinetics data and then relate the parameter values to the observed soluble-to-insoluble phase transition phenomenon: the variation in curve shape and differences in the coupling of the parameters in relation to the most important features capturing the curvature of the function. In the case of variation in curve shape, the Hill equation had its maximum rate of change (inflection point) occurring at a time earlier than the time it takes to reach half its capacity, t*. This distinguished the Hill function from the Logistic Growth and RSR functions, in which inflection time and t* were equal. In terms of the coupling of parameters, modeling the pharmacokinetics of CFZ with the RSR equation facilitated a relationship between the spleen and serum concentrations of the drugs to the mechanistic underpinnings of the phase transition. This is due to the simple and direct correspondence between parameter values and the key features of the curve (the maximal value, the time at inflection point, and the slope at the inflection point). The individual parameters governing the shape of a sigmoidal curve may reflect the mechanistic complexities of a drug that undergoes a soluble-to-insoluble phase transition in the organism, and thus can facilitate the design and analysis of future experiments.

Knowing that parameter B2, which reflects the cumulative dose of drug that the organism is exposed to before the spleen exhibits its maximal rate of CLDI formation, can so drastically alter output, further studies of mouse models are warranted to analyze the most physiologically important factors that influence this parameter. In the clinical setting, interindividual variability

in B2 could lead to nonlinear, load-dependent differences in the number of doses needed for drug to precipitate out in the body. Additionally, changes in both B1 and B2 caused significant variability in predicted half-life and clearance. As such, estimating these parameters could be used to estimate how long CFZ can be expected to remain in the organism, which could be important for the drug's pharmacological activity, toxicological effects, as well as assessing the potential for drug-drug interactions.

3.5.2 Infection Status as Covariate in CFZ Accumulation

Many possibilities could account for the differences in drug accumulation and the associated volume of distribution of a drug in infected mice, as seen in this analysis. Potentially, infection status could affect the differentiation or function of xenobiotic-sequestering macrophages through differences in the immune signaling and response mechanisms arising from the infection. Localization of infection to the lungs may also influence the location and quantity of macrophages available to sequester drug. An alternate mechanism to be investigated is the effect of tuberculosis infection on the pH of macrophage lysosomes. Previous research demonstrates that CLDIs are destabilized as the pH is increased [17]. It is well-established in the literature that M. tuberculosis infection impairs macrophage function by inhibiting the acidification of the lysosome and phagosome, as well inhibiting the fusion of these compartments [18,19]. In turn, an infection could increase lysosomal pH in macrophages beyond levels found in the macrophages of healthy uninfected individuals.

More elaborate analysis of these pharmacokinetic differences between infected and uninfected mice is complicated for several reasons: one, there was sparse data obtained from infected mice that received dosing past 12 weeks or that were administered greater than 30 mg of

CFZ. Two, the number and proportions of macrophages may be different in the uninfected and infected mice. Three, there is not enough data to establish how the number and nature of macrophages in the different organs affects the accumulation of CFZ. It is entirely possible that after enough dosing, infected mice may also accumulate drug exponentially in the spleen, but there simply is not enough data available to analyze.

3.5.3 Load-Dependent Drug Sequestration

By analyzing data obtained from mice administered different dosing regimens under varying conditions, CFZ sequestration appeared both dependent on total CFZ load as well as duration of drug loading. A time-variant correlation between drug sequestration in the spleen and total cumulative drug load occurred during a prolonged course of treatment. In addition to the total drug mass that accumulated in the organism, the fraction of dose sequestered across dosing regimens was analyzed to establish a causal relationship behind the total amount of drug administered and disproportional differences in total drug mass sequestered. Under different dosing regimens, no correlation between drug load and fractional sequestration was observed during the first 2 weeks of treatment. Nevertheless, by 8 weeks of drug administration, a log-linear relationship was observed indicating a load dependent increase in fractional sequestration of CFZ in the spleen. The difference between the load-dependent correlations with increasing drug load is consistent with CLDI formation underlying the context-dependent pharmacokinetic profile of CFZ.

In terms of predicting the total amount of CFZ sequestered in the spleen, the results revealed that the rate of dosing and total drug load could play a pivotal role. The mass of CFZ accumulating in the organism as the insoluble phase will likely be dependent on dose and

frequency. Since at smaller doses a larger fraction of the drug exists in the soluble phase, metabolic elimination would exert a greater influence on the overall clearance of drug. While there is an apparent relationship between total drug load and the accumulated mass of CFZ in the spleen, this alone does not account for the full extent of CFZ mass present throughout the organism. The drug likely occupies different ratios in the soluble phase, and different clearance pathways depending on the extent of CLDI formation and distribution throughout the different organs of the body. Expectedly, the kinetics of drug precipitation in macrophages and CLDI formation would likely be influenced by both the rate and amount of dosing, together with the treatment period. This leads to interesting biological questions, which can be addressed in future experiments.

When evaluating half-life with the RSR function, the suboptimal fit is most likely due to the simple model used for estimating the elimination half-life. The elimination rate constant is assumed to decrease at the same rate the volume of distribution increases, whereas drug elimination in an organism may be much more complex. The decrease in half-life may not be directly proportional to increase in volume of distribution since multiple elimination pathways may exist in a dynamic physiological environment. Indeed, considering a single elimination pathway for analyzing elimination kinetics is useful but it is likely an oversimplification of the underlying pharmacokinetics of CFZ elimination, following discontinuation of treatment. More detailed analysis of drug elimination with increasing spleen mass and drug sequestration is another avenue worthy of additional, future research.

Despite the fact this study was conducted on mice, crystalline CFZ precipitation has been shown to occur in many organs of human patients after extended treatment [20, 21, 22, 23], including large splenic accumulation. While we may expect different rates of accumulation and

clearance in human patient, the phenomena observed throughout this study is expected to be applicable to humans as well. Considerations of the context-dependent, nonlinear pharmacokinetics of clofazimine described here are important for improved efficacy and reduced toxicity in human patients.

3.6 Conclusions

The results of this quantitative analysis imply that a time-varying volume of distribution expansion function f(t) can be useful for obtaining quantitative, mechanistic insights into context-dependent pharmacokinetics. CFZ exhibits both time- and load-dependent adaptations in drug sequestration alongside variable pharmacokinetics with infected status implicating both a biological and pharmacokinetic rationale for the adaptive pharmacokinetic profile. Based on modeling pharmacokinetics as a function of total cumulative dose of drug administered, incorporating a phase transition leads to a bifurcation in the relationship between drug accumulation and total amount of drug administered after a critical drug load is achieved. This is a distinctively nonlinear phenomenon that cannot be accounted for by the alternative, linear multicompartment models [24]. Arguably, while the existing data is insufficient to arrive at definitive conclusions, the observed trends indicate that modeling CFZ pharmacokinetics using a nonlinear two compartment model with an expanding volume of distribution is useful across many different dosing regimens. With additional experiments exploring the dose dependent soluble-to-insoluble phase transitions, a more accurate model could be constructed utilizing dose dependent covariates on the expansion function parameters, to improve upon our understanding of soluble CFZ clearance from insoluble CLDIs. It is important to note the results presented here were evaluated in mice, under CFZ monotherapy. Future research should aim to evaluate CFZ

phase transitions not only in mice, but also in both healthy and infected human subjects, under clinically relevant, multi-drug regimens.

3.7 References

1. Willmer AR, Dunne S, Swanson R, Almeida D, Ammerman NC, Stringer KA, et al. An Adaptive Biosystems Engineering Approach towards Modeling the Soluble-to-Insoluble Phase Transition of Clofazimine. Pharmaceutics. 2021;14(1).
2. Arbiser JL, Moschella SL. Clofazimine: a review of its medical uses and mechanisms of action. J Am Acad Dermatol. 1995;32(2 Pt 1):241-7.
3. Cholo MC, Steel HC, Fourie PB, Germishuizen WA, Anderson R. Clofazimine: current status and future prospects. J Antimicrob Chemother. 2012;67(2):290-8.
4. Ammerman NC, Swanson RV, Tapley A, Moodley C, Ngcobo B, Adamson J, et al. Clofazimine has delayed antimicrobial activity against Mycobacterium tuberculosis both in vitro and in vivo. J Antimicrob Chemother. 2017;72(2):455-61.
5. Yuan S, Yin X, Meng X, Chan JF, Ye ZW, Riva L, et al. Clofazimine broadly inhibits coronaviruses including SARS-CoV-2. Nature. 2021;593(7859):418-23.
6. Riva L, Yuan S, Yin X, Martin-Sancho L, Matsunaga N, Pache L, et al. Discovery of SARS-CoV-2 antiviral drugs through large-scale compound repurposing. Nature. 2020;586(7827):113-9.
7. ClinicalTrials.gov. Dual Therapy With Interferon Beta-1b and Clofazimine for COVID-19 - Full Text View [Available from: clinicaltrials.gov/ct2/show/NCT04465695.
8. Anderson R, Smit MJ. Clofazimine and B669 inhibit the proliferative responses and Na+, K(+)-adenosine triphosphatase activity of human lymphocytes by a lysophospholipid-dependent mechanism. Biochem Pharmacol. 1993;46(11):2029-38.
9. Wan W, Zhu S, Li S, Shang W, Zhang R, Li H, et al. High-Throughput Screening of an FDA-Approved Drug Library Identifies Inhibitors against Arenaviruses and SARS-CoV-2. ACS Infect Dis. 2021;7(6):1409-22.
10. Rzeczycki P, Woldemichael T, Willmer A, Murashov MD, Baik J, Keswani R, et al. An Expandable Mechanopharmaceutical Device (1): Measuring the Cargo Capacity of Macrophages in a Living Organism. Pharm Res. 2018;36(1):12.
11. Swanson RV, Adamson J, Moodley C, Ngcobo B, Ammerman NC, Dorasamy A, et al. Pharmacokinetics and pharmacodynamics of clofazimine in a mouse model of tuberculosis. Antimicrob Agents Chemother. 2015;59(6):3042-51.
12. Baik J, Stringer KA, Mane G, Rosania GR. Multiscale distribution and bioaccumulation analysis of clofazimine reveals a massive immune system-mediated xenobiotic sequestration response. Antimicrob Agents Chemother. 2013;57(3):1218-30.
13. Rzeczycki P, Yoon GS, Keswani RK, Sud S, Baik J, Murashov MD, et al. An Expandable Mechanopharmaceutical Device (2): Drug Induced Granulomas Maximize the Cargo Sequestering Capacity of Macrophages in the Liver. Pharm Res. 2018;36(1):3.
14. Baik J, Rosania GR. Macrophages sequester clofazimine in an intracellular liquid crystal-like supramolecular organization. PLoS One. 2012;7(10):e47494.

15. Keswani RK, Baik J, Yeomans L, Hitzman C, Johnson AM, Pawate AS, et al. Chemical Analysis of Drug Biocrystals: A Role for Counterion Transport Pathways in Intracellular Drug Disposition. Mol Pharm. 2015;12(7):2528-36.
16. Woldemichael T, Keswani RK, Rzeczycki PM, Murashov MD, LaLone V, Gregorka B, et al. Reverse Engineering the Intracellular Self-Assembly of a Functional Mechanopharmaceutical Device. Sci Rep. 2018;8(1):2934.
17. Miller WH, Hartmann-Siantar C, Fisher D, Descalle MA, Daly T, Lehmann J, et al. Evaluation of beta-absorbed fractions in a mouse model for 90Y, 188Re, 166Ho, 149Pm, 64Cu, and 177Lu radionuclides. Cancer Biother Radiopharm. 2005;20(4):436-49.
18. Chicurel M, Garcia E, Goodsaid F. Modulation of macrophage lysosomal pH by Mycobacterium tuberculosis-derived proteins. Infect Immun. 1988;56(2):479-83.
19. Queval CJ, Song OR, Carralot JP, Saliou JM, Bongiovanni A, Deloison G, et al. Mycobacterium tuberculosis Controls Phagosomal Acidification by Targeting CISH-Mediated Signaling. Cell Rep. 2017;20(13):3188-98.
20. McDougall AC, Horsfall WR, Hede JE, Chaplin AJ. Splenic infarction and tissue accumulation of crystals associated with the use of clofazimine (Lamprene; B663) in the treatment of pyoderma gangrenosum. Br J Dermatol. 1980;102(2):227-30.
21. Jopling WH. Complications of treatment with clofazimine (Lamprene: B663). Lepr Rev. 1976;47(1):1-3.
22. Sandler ED, Ng VL, Hadley WK. Clofazimine crystals in alveolar macrophages from a patient with the acquired immunodeficiency syndrome. Arch Pathol Lab Med. 1992;116(5):541-3.
23. Harbeck RJ, Worthen GS, Lebo TD, Peloquin CA. Clofazimine crystals in the cytoplasm of pulmonary macrophages. Ann Pharmacother. 1999;33(2):250.
24. Abdelwahab MT, Wasserman S, Brust JCM, Gandhi NR, Meintjes G, Everitt D, et al. Clofazimine pharmacokinetics in patients with TB: dosing implications. J Antimicrob Chemother. 2020;75(11):3269-77.

Chapter 4 An Expandable Mechanopharmaceutical Device for Measuring the Cargo Capacity of Macrophages in a Living Organism

Aspects of this work have been published as an original research article in *Pharmaceutical Research 2018 Nov 12;36(1):12.*

4.1 Abstract

Clofazimine (CFZ) is an FDA-approved, poorly soluble small molecule drug that precipitates as crystal-like drug inclusions (CLDIs) which accumulate in acidic cytoplasmic organelles of macrophages. In this study, we considered CLDIs as an expandable mechanopharmaceutical device, to study how macrophages respond to an increasingly massive load of endophagolysosomal cargo. First, we experimentally tested how the accumulation of CFZ in CLDIs impacted different immune cell subpopulations of different organs. Second, to further investigate the mechanism of CLDI formation, we asked whether specific accumulation of CFZ hydrochloride crystals in lysosomes could be explained as a passive, thermodynamic equilibrium phenomenon. A cellular pharmacokinetic model was constructed, simulating CFZ accumulation driven by pH-dependent ion trapping of the protonated drug in the acidic lysosomes, followed by the precipitation of CFZ hydrochloride salt via a common ion effect caused by high chloride concentrations. Interestingly, while lower loads of CFZ were mostly accommodated in lung macrophages, increased CFZ loading was accompanied by organ-specific

changes in macrophage numbers, size and intracellular membrane architecture, maximizing the cargo storage capabilities. With increasing loads, the total cargo mass and concentrations of CFZ in different organs diverged, while that of individual macrophages converged. The simulation results support the notion that the proton and chloride ion concentrations of macrophage lysosomes are sufficient to drive the massive, cell type-selective accumulation and growth of CFZ hydrochloride biocrystals. CLDIs effectively function as an expandable mechanopharmaceutical device, revealing the coordinated response of the macrophage population to an increasingly massive, whole-organism endophagolysosomal cargo load.

4.2 Introduction

In multicellular organisms, macrophages are well equipped to internalize extracellular solutes and particles through pinocytosis and phagocytosis, respectively. These processes allow them to execute a number of critical, immune surveillance functions, ranging from destruction of pathogens to removal and recycling of dead cells and aged tissue components [1-3]. In addition to being highly phagocytic, the endolysosomal system of the macrophage is especially adapted for accommodating and degrading foreign material due to higher expression levels of lysosomal acidification mechanisms [4], particularly the vacuolar-type proton ATP-ase (V-ATPase) [5]. However, there is no information about the extent of loading or the cargo storage capacity of macrophage populations *in vivo*, since the majority of measurements have been performed *in vitro* and in very short treatment periods by 'feeding' the cells with fluorescent tracer molecules [6] or inert beads of varying sizes [7,8] under artificial conditions.

Even though macrophages are found everywhere in the organism, their ability to influence the transport and disposition of small molecule drugs is mostly unknown. Due to their

ubiquitous presence and high rates of endocytosis, pinocytosis, and phagocytosis, they are recognized to play a major role in the clearance of drug nano- or microparticles from the circulation [9, 10]. Potentially, this action could be exploited for the delivery of small molecule drugs [11-14], particularly those that are poorly soluble because they are prone to form insoluble aggregates that may ultimately accumulate in macrophages [15, 16]. Furthermore, cationic, amphiphilic molecules, particularly weakly basic molecules, can become trapped within lysosomes following protonation in the acidic lysosomal microenvironment [17-19]. The sequestration of weakly basic, hydrophobic drug molecules within acidic subcellular (ion-trapping) compartments of macrophages is a well-documented phenomenon [17].

To study the *in vivo*, cargo storage capacity of macrophages in an intact, living organism, we have co-opted an FDA-approved and biocompatible antibiotic, clofazimine (CFZ), as a probe [15, 16]. CFZ is a weakly basic anti-mycobacterial agent that is clinically used to treat leprosy and multi-drug resistant tuberculosis [20-22]. It exhibits extensive bioaccumulation following oral administration, in both humans and animal models [23-25]. Because CFZ is both highly lipophilic (LogP=7.66) and contains an ionizable amine group (pKa=6.08), it is poised to accumulate in adipose tissue, intracellular membranes, and acidic organelles such as lysosomes. In both human and animal models it has been shown that, following prolonged oral dosing, CFZ forms insoluble Crystal-Like Drug Inclusions (CLDIs) within macrophage lysosomes [26].

Here, by exploiting CFZ's self-assembly into CLDIs, we decided to further probe the macrophage's response to an increasing load of drug cargo. Experimentally, CLDIs were microscopically monitored to determine the numbers of drug-sequestering macrophages in different organs. From these same organs, CLDIs were then biochemically isolated and the drug content chemically analyzed to determine the average amount of drug per CLDI-containing cell

[26, 27]. Additionally, we modeled the subcellular transport and precipitation properties of CFZ using a physiologically based pharmacokinetics approach to assess whether thermodynamics alone could explain the selective accumulation and stabilization of the drug in macrophage lysosomes. Based on the results, we propose that CLDIs function as an expandable mechanopharmaceutical device, which impacts the structural and functional properties of macrophages in different organs, and accounts for a drug loading-dependent increase in the volume of distribution (VD) of the drug.

4.3 Materials and Methods

4.3.1 Animal Studies and Treatment Protocols

Animal care was provided by the University of Michigan's Unit for Laboratory Animal Medicine (ULAM), and the experimental protocol was approved by the Committee on Use and Care of Animals (Protocol PRO00005542). Mice (4 weeks old, male C57Bl6) were purchased from the Jackson Laboratory (Bar Harbor, ME) and acclimatized for 1 week in a specific-pathogen-free animal facility. Clofazimine (CFZ) (C8895; Sigma, St. Louis, MO) was dissolved in sesame oil (Shirakiku, Japan) to achieve a concentration of 3 mg/ml, which was mixed with Powdered Lab Diet 5001 (PMI International, Inc., St. Louis, MO) to produce a 0.03% drug to powdered feed mix, and orally administered ad libitum. Mice were fed for 2, 3, 4, and 8 weeks, which yielded estimated whole body cargo loads of 3.5mg, 5.25mg, 7mg, and 14mg, respectively. A corresponding amount of sesame oil was mixed with chow for vehicle treatment (control). For washout experiments, mice were fed with drug free, vehicle-containing diet for eight weeks, after an eight week loading period with the CFZ-containing diet. At the end of

experimentation, mice were euthanized via carbon dioxide asphyxiation followed by exsanguination.

4.3.2 Macrophage Isolation

Following euthanasia, four different macrophage populations were isolated to study CFZ accumulation. Alveolar [27, 28] and peritoneal macrophages [26], and bone marrow monocytes [29] were all isolated using previously described techniques. To isolate Kupffer cells, the portal vein was injected with 10 mL of 1 mg/mL Collagenase D (Worthington Biochemical Corporation, Lakewood, NJ) in DMEM-low glucose (Life Technologies) with 15 mM HEPES (Life Technologies). The tissue was then removed, placed in a sterile petri dish, and minced into small (2-4 mm) pieces using a sterile scalpel blade. Collagenase solution (15 mL) was added, and the tissue was incubated (40 min, 37°C), with occasional pipetting to dissociate tissue. The suspension was then filtered through a 100 µm cell strainer (Fisher Scientific, Waltham, MA) and centrifuged (200 x g, 5 min). The supernatant was discarded, and the cells were resuspended in 15 mL DMEM-low glucose with 15 mM HEPES, and centrifuged (200 x g, 5 min). This was repeated for two additional washes. After the final wash, the cells were suspended in DMEM:F/12 (1:1) (Life Technologies) with 10% FBS and penicillin/streptomycin and macrophages were counted. For all cell groups, an aliquot was plated onto 4 or 8 chamber coverglass (#1.5, Lab-Tek II, Nunc, Rochester, NY), and for Kupffer cells, the plates were coated with Collagen 1 (Corning, Corning, New York) for imaging. The cells were allowed to attach overnight, washed with media, and imaged using a multi-parameter microscope imaging system (vide infra).

4.3.3 Multi-parameter Microscope Imaging and Analysis of Macrophage Sub-Populations

Multi-parameter polarization, brightfield, and fluorescence imaging and analyses of different macrophage subpopulations were performed using a custom-built imaging system, as previously described [27]. Brightfield, fluorescence, and polarization images were acquired on adherent cells. Images were analyzed using ImageJ software [30, 31]. Values for dichroism and optical density are reported as an average signal per cell, from 0-1. At least 150 cells of each type were analyzed at each time point. Following loading with 7 and 14 mg of cargo, macrophages were classified as xenobiotic sequestering based on whether or not they contained a detectable Cy5 signal from CFZ-HCl [26] using a K-means clustering analysis, with the clusters set to 2 based on of the Log10(Intracellular Cy5 fluorescence).

4.3.4 Biochemical Analysis of Cellular Drug Cargo

The drug concentration in cells was calculated after measuring drug content in isolated macrophage populations and organ homogenates using established methods [24, 26, 32, 33]. For isolated macrophage populations, cells were counted within each cell sample using a hemocytometer to determine the total recovered macrophage population. The cells were then centrifuged, and the media was removed. The cell pellet was suspended in 1 mL of DI water, and the drug was extracted and measured using a previously described spectrophotometric method [33-35]. Drug accumulation is reported as fmol CFZ/xenobiotic sequestering cell.

4.3.5 Sample Preparation for Microscopy

In preparation for microscopy, portions of the organ were removed, immediately submerged in OCT (Tissue-Tek catalog no. 4583; Sakura), and frozen (-80°C). For transmission electron microscopy, organs were prepared using previously described methods [23]. Immunohistochemistry of F4/80 (Abcam, 1:500 dilution) stained sections (5μm) was performed using Alexa-Fluor 488 (Abcam, 1:500 dilution).

4.3.6 Determination of Cargo Volume Occupancy

The volume occupied by biocrystalline drug molecules within a macrophage was estimated by using the reported crystal-packing density of 1.36 g/mL [33] for CFZ-HCl, which was then converted to a molar volume of 0.377 μm^3/ fmol. Cellular volume occupancy was then estimated using the measured drug content per cell and the calculated molar volume.

4.3.7 Determination of Vesicle Size and Shape

The size and shape of cargo loaded vesicles was microscopically measured within loaded macrophages obtained from CFZ-treated animals, using the Cy5 fluorescence channel to specifically monitor the vesicles containing CFZ-HCl. Using ImageJ [30, 31], the radius of each vesicle was determined. Vesicles which showed Cy5 fluorescence were counted as CFZ sequestering. The vesicle volume was estimated assuming spherical shape, while CLDI volume was estimated assuming a cylindrical shape.

4.3.8 Analysis of Organ Macrophage Counts

To determine the macrophage population numbers in lung, liver, and spleen from animals treated with CFZ, cryosections were obtained (5μm). The change in the number of macrophages in a volume of tissue was determined by dividing the total F4/80 signal staining intensity between an 8 week CFZ-treated sample by the total F4/80 signal staining intensity of a vehicle-treated sample (the area and thickness of the sections analyzed were kept the same). The total macrophage population was then determined by multiplying literature reported (baseline) macrophage population values for each organ [36] by the relative expansion factor determined via increased intensity of the macrophage marker's fluorescence signal, via immunofluorescence. To determine the fraction of macrophages that contained CLDIs, the fraction of cells which were positive for Cy5 fluorescence and F4/80 staining were determined by visual inspection, using a mask of the F4/80 staining. Five images per organ per animal were analyzed for each measurement.

4.3.9 Measurement of Drug Accumulation based on Whole Organ Homogenates

For chemical analysis protocol development, organs were obtained from euthanized, untreated mice. Samples from the different organs (20-30 mg) were homogenized in radioimmunoprecipitation assay buffer (500 μL; Sigma) with added protease inhibitors (Halt protease and phosphatase inhibitor cocktail and 0.5 M EDTA; Thermo Pierce, Rockford, IL). In order to determine the recovery yield, the organ homogenates were spiked with a known amount of drug. For analysis, homogenate (350 μL) was removed, and drug was extracted as described under "Biochemical Analysis of Cellular Drug Concentrations."

4.3.10 Determining the Fraction of Drug Sequestered by Macrophages of Different Organs

The total drug content of lung, liver, and spleen tissues at eight weeks of treatment was determined as described above, using established protocols [32]. Because CLDIs form and become stabilized exclusively within macrophages [23, 33, 37], we sought to determine the fraction of drug sequestered within macrophages of each organ. To accomplish this, tissues (n=3) were removed, weighed, and placed in a sterile petri dish, where they were manually minced and homogenized using a scalpel and syringe plunger. The resulting homogenate was filtered through a cell strainer (40 μm) to remove larger cellular clusters and debris. The filtrate was then centrifuged (300 x g, 10 min) to pellet the CLDIs. The supernatant was removed, and the CLDI pellet was resuspended in 10% sucrose in DPBS (Life Technologies, Carlsbad, CA) without calcium chloride or magnesium chloride, pH=7.4. CLDIs were further purified using a 3-layer sucrose gradient (50%, 30%, and 10% sucrose in DPBS) centrifugation method (3200 x g, 60 min). The pelleted CLDIs were then dissolved in 9 M H2SO4, and the mass of drug was determined using a plate reader (Biotek Synergy 2, Winooksi, VT) at wavelength 450 nm, and background corrected at wavelength 750 nm, which was determined using a standard curve with solutions of known concentration.

4.3.11 Determination of the Cargo Volume Occupied per Macrophage

Using the total recovered mass of drug associated with CLDIs isolated from the liver, lung, and spleen, the volume occupied by drug within individual xenobiotic-sequestering macrophages was estimated based on the number of CLDI containing cells, using the total expanded macrophage population present in the measured tissue sample, multiplied by the fraction of cells which contained a CLDI (determined microscopically). Using literature reported values for cellular volume of the macrophage [38], the percentage of cellular volume occupied

by drug was estimated by dividing the total recovered mass of drug associated within the isolated CLDIs, by the total (calculated) number of CLDI containing cells in the sample of tissue from which the CLDIs were isolated. The fraction of the phagocytic capacity occupied by cargo was calculated by dividing the measured cargo volume by the maximum phagocytic capacity of macrophages [8].

4.3.12 Biochemical Analysis of Drug Concentrations

The concentration of CFZ in plasma or organ homogenates was determined using a previously described method [24]. In brief, blood was collected in microtainer serum separator tubes (catalog no. 3659656; Becton Dickinson, Franklin lakes, NJ) and allowed to clot at room temperature and centrifuged (5,000 x g, 5 min). Samples (20 µl) were extracted with acetonitrile (60 µl, 90% extraction efficiency) for 10 min at 4°C with vortexing. After centrifugation (5,000 x g, 4°C), the supernatant was injected into Agilent 1200 RRLC coupled to 6410 Triple Quad LC-MS equipped with a Waters Xbridge C18 column (2.5 µm x, 2.1 mm x 100 mm). A standard curve was generated by extracting spiked drug samples using serum (or the organ homogenates) from a vehicle-only treated mouse mixed with CFZ stock solution from dimethyl sulfoxide, resulting in 10 different CFZ concentrations between 0 and 30 µM. The peak area was quantified using MassHunter Quantitative Analysis software, vB.04.00. This standard curve was then used to establish the concentration of drugs in experimental samples from blood of drug-treated mice (or from organ homogenates of these mice).

4.3.13 Determination of the Volume of Distribution of the Drug in Different Organs (VOD)

Following treatment with 5.25 or 14 mg of CFZ, mice (n=3 per time point) were euthanized and the liver, spleen, small intestine, fat, kidney, and lung were removed, weighed, and the mass of CFZ within each tissue and the concentration within plasma were determined as previously described [24]. The VOD of the drug within macrophages, tissue, and the whole body at the different loading amounts was determined using the ratio between the total drug within tissues or individual cells and the measured plasma concentration.

4.3.14 Solubility Measurements for CFZ and CFZ-HCl in Octanol

In order to determine the solubility values for CFZ and CFZ-HCl in 1-octanol (293245; Sigma-Aldrich), both forms of the drug were introduced in great excess to 1-octanol in glass scintillation vials. A small magnetic stir bar was added to each sample, and the samples were placed on the magnetic stirrer inside the incubator (37°C). After a 24-hour equilibration period, samples were removed from the incubator and immediately filtered using Spin-X centrifuge tube filters (0.45 μm cellulose acetate, 2 mL polypropylene tubes, Costar®) for 4 min at 5,000 x g. The concentration of the soluble drug in 1-octanol was spectrophotometrically determined (285 nm, 37°C; Synergy-2 plate reader; Biotek Instruments, Winooski, VT). For each sample, solubility measurement was performed in triplicate, and the average was reported. The standard curve was generated using CFZ crystals that were dissolved in 1-octanol at known concentrations (1-200 μM). Pure 1-octanol was used as a baseline absorbance.

4.3.15 Statistical Analysis of Experimental Data

All data are expressed as mean ± standard deviation (SD). For multiple comparisons, statistical analysis was performed with one-way analysis of variance (ANOVA) and Tukey's post hoc comparisons. All statistical analyses were performed using IBM SPSS Statistics version 24.0 (IBM Software, Armonk, New York). p values less than or equal to 0.05 were considered statistically significant.

4.3.16 Physiologically-based Drug Transport Modeling and Simulation of Intracellular Drug Supersaturation

We used an established, physiologically-based cellular pharmacokinetic modeling framework [39-41] to calculate the time-dependent changes in the concentration of a monovalent weakly basic small molecule drug inside each compartment within a cell following exposure of the cell to a constant extracellular drug concentration. For the present study, we used the open-source modeling software Virtual Cell®. All of the following models can be freely accessed at http://vcell.org. The model used here (awillmer: Macrophage Cargo Capacity) was built from the established Virtual Cell model: jsbaik: 1-Cell PK acid/base/neut total. For boundary conditions, we used the previously published, standard eukaryotic cell parameter values as input (Table B.1).

4.3.17 Modeling the Passive Transport Properties of a Weakly Basic Drug that Stably Accumulates and Self-Assembles in Macrophage Lysosomes

We used CFZ as a weakly basic model drug to predict its subcellular phase-transition dependent accumulation. Even though it has two ionizable groups, it can be modeled as a

monobasic compound because at physiological pH, the ionization of the amine with the lower pKa of ~2 will not influence the transmembrane fluxes to any significant extent. In lysosomes, CFZ accumulates as CLDIs, which mostly contain hydrochloride salts of the weak base (CFZ-HCl). Thus, using predetermined physicochemical properties of the free base as well as the salt form of the drug (apparent pKa = 6.08, and octanol/water partition coefficient logP (logKow = 7.66)) as input in the Virtual Cell model, we calculated the time-dependent subcellular distribution of both neutral and ionized molecular species as a function of an extracellular total drug concentration of 10 μM (concentrations in all subcellular compartments are linearly related to the extracellular concentration). We set the extracellular volume to a high value (Table B.1), so that the extracellular drug concentrations would remain nearly constant, without being affected by cellular drug uptake. In turn, the degree of supersaturation of the drug molecules in the different cellular compartments was calculated by dividing the concentrations of the protonated and unprotonated species of the drug in those compartments by the calculated solubility of the corresponding charged or neutral species in said compartments. Detailed theoretical calculations and equations used to determine the concentration of the ionized and unionized form of the weakly basic drug within subcellular compartments, and degree of supersaturation of the drug within various subcellular compartments can be found in the Supporting Information.

4.4 Results

4.4.1 Testing the in vivo adaptive response of different macrophage populations to a massive, whole organism cargo load

To determine how CFZ bioaccumulation as an expandable mechanopharmaceutical device affects macrophage function, we measured the response of different macrophage subpopulations to an increasingly massive CFZ load. Experimentally, at the smallest whole body cargo load measured (3.5 mg), the drug was mostly present in alveolar macrophages (Figure 4.1a). This cargo was associated with red, optically dense, cytoplasmic vesicles which exhibited little dichroism signal, corresponding to a disordered, amorphous, supramolecular organization [42, 43] (Figure 4.1b). A 7 mg whole body cargo load resulted in a modest increase in accumulation in the alveolar macrophages (Figure 4.1c), and a small percentage of the drug was apparent in the peritoneal and liver macrophages (Figure 4.1a). However, the structure of the intracellular cargo became more organized with increasing amounts of drug as reflected in the elevated optical density (Figure 4.1c) and dichroism (Figure 4.1d) of alveolar, peritoneal, and liver macrophages. At 14 mg, cargo loads redistributed into large, highly ordered CLDIs exhibiting strong dichroism signals in all macrophages (Figure 4.1b). Under all loading conditions, the less mature bone marrow monocytes were free of cargo. At a population level, these trends were confirmed by multi-parameter image-based cytometric analyses [16] (Figure 4.1c, d).

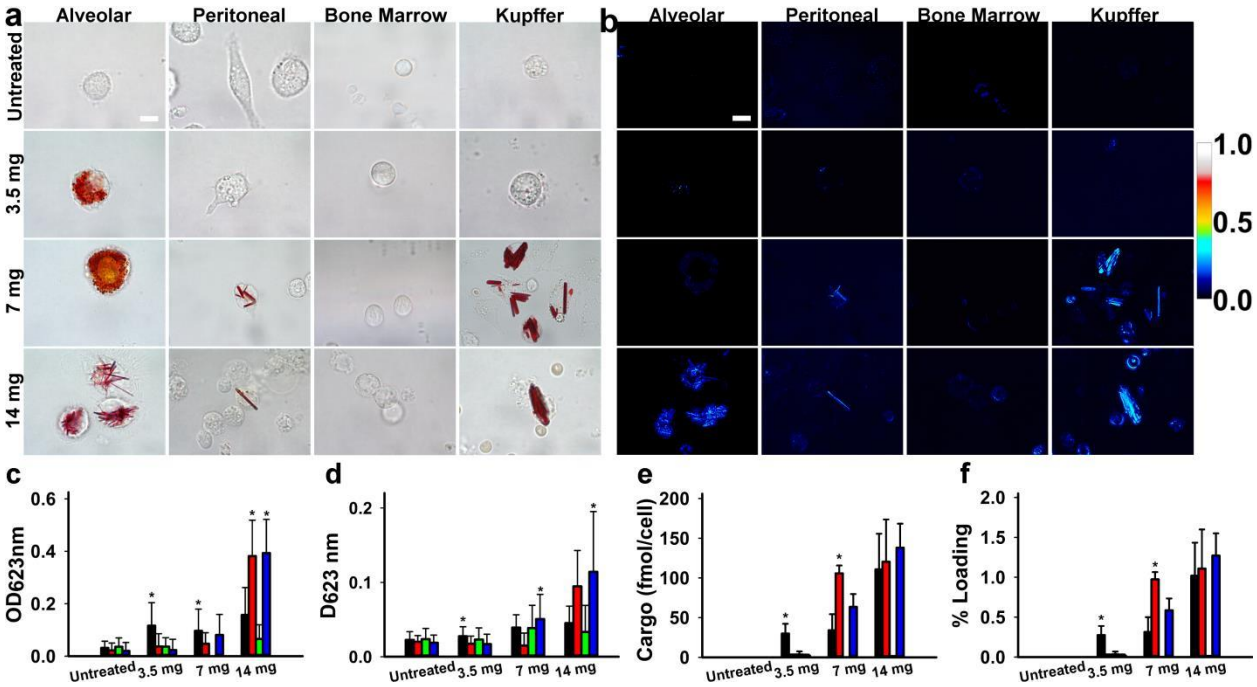

Figure 4.1: Microscopic imaging cytometry and quantitative chemical analysis indicate variations in cargo loading dynamics of different macrophage sub-populations. (a) Brightfield images of isolated macrophage and monocytes with increasing whole-body cargo loading. (b) Linear diattenuation images of isolated macrophage and monocytes with increasing whole-body cargo loading. Optical density (c), linear diattenuation (d), cargo loading per xenobiotic-sequestering cell (e), and percent of maximal cargo loading (f) of alveolar macrophages (black), peritoneal macrophages (red), bone marrow monocytes (green), and Kupffer cells (blue) with increasing cargo loading. Data are the mean (SD) of 150 cells per cell type and condition, for imaging studies, n=3 mice per cargo treatment for drug accumulation, (=p<0.05, ANOVA, Tukey's HSD) (Scale bar = 10 μm).*

The results of chemical analyses paralleled the observed changes in loading dynamics and the redistribution of cargo among the different macrophage populations. At low (3.5 mg) cargo loading, alveolar macrophages sequestered 29.9 ± 12.4 fmol of CFZ/cell, while the other populations showed minimal loading (Figure 4.1e). After a whole body load of 3.5 mg, less than 0.3% of the maximal phagocytic capacity of the alveolar macrophages was reached (Figure 4.1f). At a larger (7 mgs) whole body cargo load, alveolar macrophages accumulated 34.0 ± 20.3 fmol CFZ/cell, which primarily remained in a disordered form as reflected in the low dichroism signal (Figure 4.1b, d). Peritoneal and liver macrophage populations, due to their differential accumulation pattern (Figure 4.1b), increased their cargo loading per cell to 105.7 ± 10.0 and

63.5 ± 16.2 fmol/cell, respectively. It is noteworthy that at the highest loads of cargo (14 mg), all tissue macrophage subpopulations exhibited similar levels of cargo loading (Figure 4.1e), except for monocytes. Thus, the formation of CLDIs facilitated intracellular cargo loading coincided with a systemic redistribution of cargo among all macrophage sub-populations, such that the load became more evenly distributed in the cell. In these isolated macrophages, the highest cargo volume corresponded to ~1% of the maximal phagocytic capacity of cell (Figure 4.1f) [8]. As such, only a small fraction of the potential intracellular cargo space was occupied even at the highest whole body loads that were measured in vivo.

To achieve an even distribution of cargo (which was observed in the most massively loaded condition), macrophages visibly adjusted their intracellular, cytoplasmic membrane organization. For example, with a relatively low amount of loading (3.5 mg), the alveolar macrophage population accumulated an average of 21.6 ± 5.0 vesicles per cell, with each vesicle occupying a mean volume of 0.43 ± 0.29 μm3 (Table 4.1). Transmission electron micrographs of alveolar macrophages revealed numerous dark, lipid bound inclusions within the cytoplasm (Figure 4.2a).

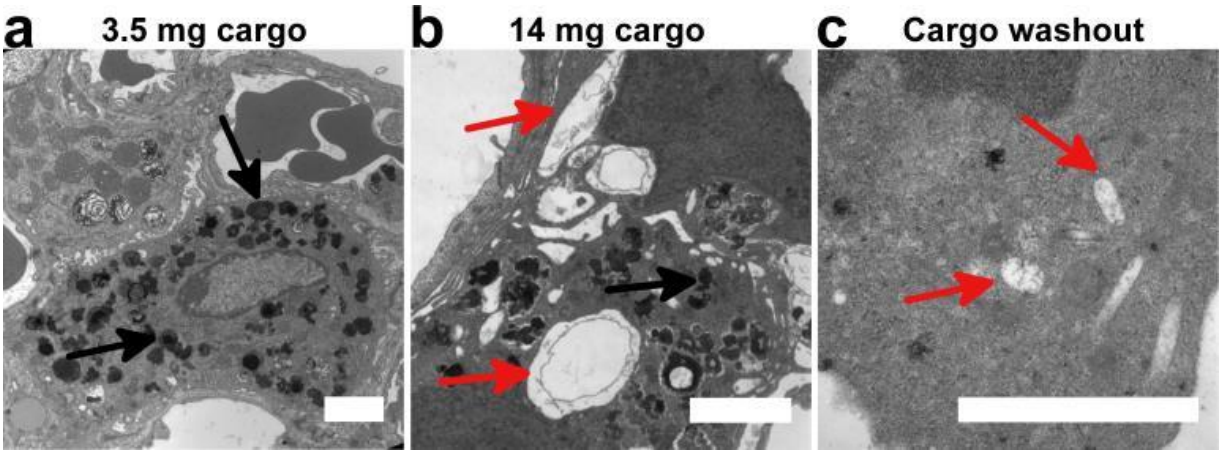

Figure 4.2:Macrophage cargo accumulation induces reorganization of internal membrane architecture. (a) Following whole-body cargo loading of 3.5 mg, small vesicles that fill the cytoplasm are apparent in alveolar

macrophages. (b) A higher cargo load (14mg) results in accumulation of crystal-like drug inclusions (CLDIs) throughout the cytoplasm. (c) CLDIs remain stable even following an eight-week washout period. Black arrows denote cargo-laden vesicles and red arrows denote cavities left from CLDIs removed during sample preparation. The scale bar is 2000 nm.

A larger (7 mg) whole body cargo load increased the number of cytoplasmic vesicles by >50% per cell (n=30 cells, $p<0.05$, ANOVA, Tukey's HSD), with the mean vesicular volume increasing by ~125% (Table 4.1). At the largest whole body cargo load tested (14 mg), an expansion of membrane-bound cytoplasmic vesicles was clearly visible (Figure 4.2b). At this point, the number of loaded vesicles per cell decreased by >40%. The expanded, membrane bound vesicles remained stable within the macrophages as long as eight-weeks following the discontinuation of drug administration (Figure 4.2c).

Table 4.1:Vesicle number, size, and volume occupancy in alveolar macrophages following cargo loading. (=p<0.05, ANOVA, Tukey's HSD).*

Cargo Loading	**Mean number of vesicles per cell ±SD (n=30 cells)**	**Mean vesicle volume ±SD (n=50 vesicles)**	**Mean total volume occupied by vesicles ±SD (n=50 vesicles)**
3.5 mg	21.6 ± 5.0	0.43 ± 0.29 μm^3	9.2 ± 6.7 μm^3
7.0 mg	32.6 ± 6.8*	0.97 ± 0.96 μm^3	31.7 ± 32.1 μm^3
14.0 mg	18.4 ± 11.1	13.8 ± 10.4 μm^3*	253.8 ± 244.5 μm^3

Of noteworthy significance, the amount of cargo in the isolated macrophage populations effectively accounted for most of the total cargo load measured in whole organ homogenates (Table 4.2). Based on the amount of cargo within each organ, the volume of blood that was cleared by the macrophages in the different organs was estimated (the organ-specific Volume of Distribution, VOD; Table 4.3). In pharmacokinetic terms, the whole body VD of a molecule is the ratio between the amount of drug in the organism and the plasma concentration of the drug [44]. VD represents the extent of tissue distribution [45] as reflected in the theoretical volume

required to contain an administered amount of drug at the same concentration found in plasma. With an increasing cargo load, each macrophage population significantly contributed to VOD and consequently, to VD (Table 4.3). Given that the volume of a single macrophage is ~1 pL, they contribute to VD via the solute-to-solid phase transition that accompanies CLDI formation. At the whole organ level, there was a nearly ~100-fold increase in the VOD within the liver and small intestine, a ~60-fold increase within the spleen and ~10-fold increase within the lung, paralleling an increasing whole body cargo loading from 5.25 to 14 mg (Table 4.4). Adipose tissue and kidneys, neither of which contain large populations of tissue macrophages compared to other organs, had modest increases in the VOD that were much lower than those observed in liver, spleen, lung, and intestine (Table 4.4).

Table 4.2:Estimated cargo loads of liver, spleen, and lung macrophages, at a 14 mg whole body load. Data represent the mean ± S.D., n=3 mice.

Macrophage Population	**Cargo mass (mg)**	**Percent Xenobiotic Sequestering**	**Total Xenobiotic Sequestering Cells (x 10^6)**	**Fmol Cargo/Xenobiotic Sequestering Cell**	**% Cell Volume Occupied by Cargo**
Liver	4.57 ± 0.78	88.5 ± 3.3%	80 ± 19	120.9 ± 35.3	2.11 ± 0.62%
Spleen	3.23 ± 0.27	83.9 ± 12.5%	22 ± 5.9	310.5 ± 86.9	5.42 ± 1.52%
Lung	0.32 ± 0.06	81.1 ± 3.2%	3.7 ± 1.7	183.2 ± 91.5	3.20 ± 1.60%

Table 4.3: Volume of distribution in liver, lung, and spleen macrophage, at a 5.25 and 14 mg whole-body loads (=p<0.05, Two-tailed Student's t-test). Data represent the mean ± S.D.*

Macrophage Population	**5.25 mg cargo V_{OD} (nL/macrophage)**	**14 mg cargo V_{OD} (nL/macrophage)**
Liver	$0.66 \pm 9.8 \times 10^{-5}$	33.51 ± 0.01*

Spleen	$0.49 \pm 2.5x10^{-4}$	64.25 ± 0.01*
Lung	$5.51 \pm 9.5x10^{-5}$	42.73 ± 0.01*

Table 4.4:Volume of distribution within specific organs, at a 5.25 and 14 mg whole-body load (=p<0.05, Two-tailed Student's t-test). Data represent the mean ± S.D.*

Tissue (n=3 per treatment)	**5.25 mg cargo V_{OD} (L/kg tissue)**	**14 mg cargo V_{OD} (L/kg tissue)**
Liver	33.9 ± 13.1	2232.5 ± 958.2*
Spleen	118.8 ± 85.4	6139.3 ± 2637.0*
Lung	91.2 ± 12.0	902.3 ± 524.1
Fat	91.8 ± 15.2	129.1 ± 61.1
Jejunum and Ileum	11.1 ± 6.3	1085.2 ± 606.2*
Kidney	31.1 ± 7.3	125.6 ± 55.5

The most important finding in the VOD analysis pertains to the role of organ-specific macrophage subpopulations in the redistribution of cargo loads and its ultimate impact on the measured differences in the VOD of the different organs. The difference in organ-specific VOD (Table 4.4) between animals exposed to a moderate (5.25 mg) or a large (14 mg) cargo load, seemed to result in an increasingly divergent loading pattern. With a 14 mg load, for example, the spleen VOD was >50 times greater than that of the kidney, while at a 5.25 mg load, the spleen VOD was only ~3 times greater than kidney. However, when looking at the specific accumulation of drug in macrophages (Table 4.2 and 4.3; and Figure 4.1e, f), it was apparent that the divergence in the whole organ distribution was due to differences in the number of macrophages per organ mass, since the cargo became more evenly distributed among the resident macrophages of the respective organs.

4.4.2 Passive transport acting in concert with a pH and chloride-dependent phase transition is sufficient to explain the function of CFZ as an expandable mechanopharmaceutical device

In order to determine whether passive transport can explain the selective precipitation and growth of CFZ hydrochloride crystals in lysosomes, we proceeded to dissect the subcellular transport and self-assembly properties of CFZ using a physiologically based, cellular pharmacokinetics modeling and simulation approach (Figure 4.3).

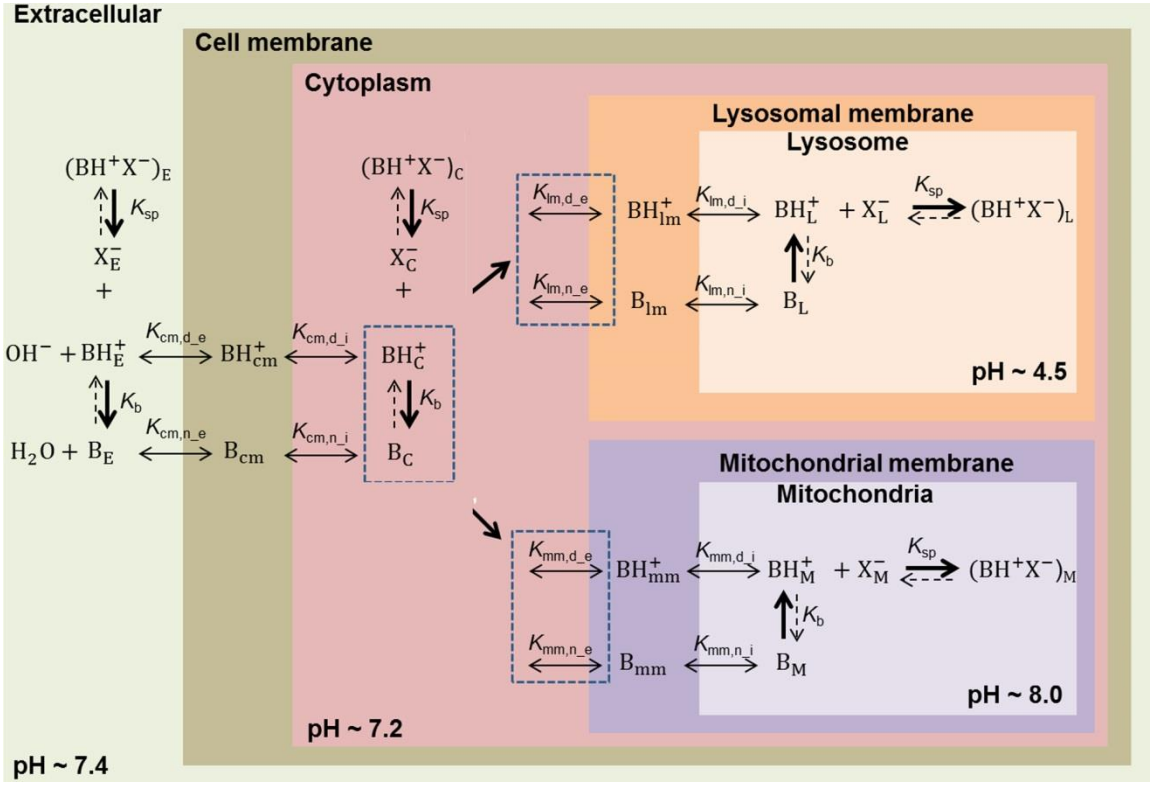

Figure 4.3:Diagrammatic representation of the integrated, transport and precipitation modeling approach used to determine the most likely cite of intracellular CFZ precipitation. The definition of each parameter value is given in Table C.1 in the Supporting Information

Previous analyses have identified the hydrochloride salt form of CFZ as the major fraction of the bioaccumulated drug [33, 37]. This hydrochloride salt form was specifically present in CLDIs, which are stabilized within acidic intracellular vesicles (as revealed by inhibiting the proton-pumping, V-ATPase which decreases CLDI formation and CFZ

accumulation) [37]. Without macrophages, CLDIs also failed to form and CFZ accumulated in tissues to a much lesser extent [37].

Consistent with these previous experimental observations [33, 37], our simulation results revealed how the unprotonated, neutral molecular species of CFZ accumulated intracellularly in the presence of a constant extracellular drug concentration (Figure 4.4a).As expected, because of the higher pH (relative to the drug's pKa) of the cytoplasm and mitochondria, the unprotonated free base concentration was highest in the cytoplasm (Figure 4.4b) and mitochondria (Figure 4.4c), relative to lysosomes (Figure 4.4d). Simulating the distribution of the ionized (protonated) molecular species of the drug over time, we observed that the protonated form remained nearly constant in the extracellular medium (Figure 4.4e). The concentration of protonated drug was lowest in cytoplasm (Figure 4.4f) and mitochondria (Figure 4.4g), but increased dramatically in the lysosomes (Figure 4.4h) due to ion trapping [46]. In fact, lysosomes possessed the highest drug concentration of all cellular compartments (Figure 4.4h). Because of the linearity of the model, the neutral and protonated, charged molecular species in all of the compartments proportionally decreased when the total initial extracellular CFZ concentration was reduced (for example, changing the units of micromolar to nanomolar).

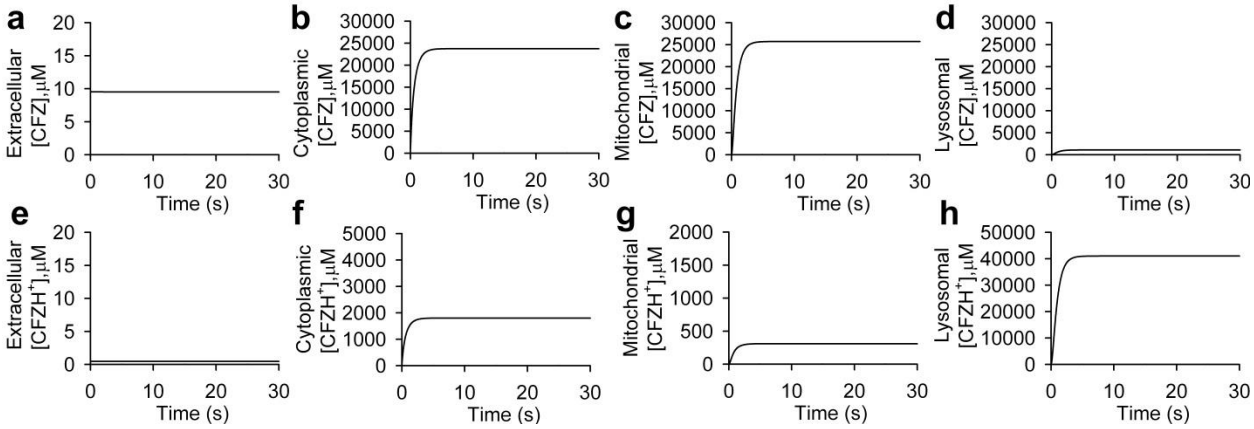

Figure 4.4: Time-plot simulations of intracellular concentrations of neutral and protonated species of clofazimine (CFZ) in different subcellular compartments. (a) Extracellular drug accumulation of neutral CFZ remains constant during the time course of the simulation; (b) neutral drug molecules enter and reach steady state in cytoplasm; (c) the mitochondrial compartment has the highest free base drug concentration due to a pH higher than the cytosol and significant lipid content; (d) lysosomes have low concentrations of the neutral species due to their low pH; (e) extracellular concentrations of ionized CFZ (CFZH+) are much lower than neutral CFZ species, and remains constant; (f) due to the physiological pH of the cytoplasmic compartment, there is very little protonated drug, as well; (g) the high pH of the mitochondria leads to a low concentration of protonated free base, although the concentration is higher than in the extracellular medium due to the mitochondrial membrane potential-dependent uptake; (h) the lysosomal compartment has the highest ionized drug concentration due to ion trapping.

In order to determine the propensity of the free base and ionized forms of the drug to precipitate in the different cellular compartments, we calculated the degree of supersaturation of both forms of the drug using their solubility properties obtained from experimental measurements (Table 4.5). Degrees of supersaturation were calculated by determining the ratio of simulated steady state CFZ concentration to CFZ solubility (Equations C.3 and C.4 in Appendix C). The greatest degree of supersaturation for the ionized form of the drug was observed in the lysosomal compartment (Table 4.5). Within the lysosomal lumen, the supersaturation of CFZ-HCl exceeded all other compartments by more than two orders of magnitude (Table 4.5). The primary reasons for the high supersaturation in the lysosomal lumen were the high chloride concentrations and a lysosomal pH lower than the pHmax of CFZ-HCl. Moreover, the degree of supersaturation of CFZ-HCl in the lysosome was exceeded by 3 to 6 orders of magnitude over that of CFZ free base (Table 4.5). This indicates that the conditions for

salt precipitation would be most favorable in the lysosomal lumen, and as a result, would be the first location within the cell that precipitation would be expected to occur, as concentrations in all compartments increase following drug administration. Note that the intracellular concentrations predicted by the transport model were linearly dependent on the starting drug concentrations in the extracellular medium, so the model effectively predicted the most likely site of intracellular drug precipitation based on the lowest extracellular concentration necessary to achieve supersaturation in any intracellular compartment.

Table 4.5:Steady-state degree of supersaturation of free base CFZ and CFZ-HCl based on a simulated, initial extracellular concentration of 10 µM (a)Because the local pH is higher than the pHmax, only the free base form is predicted to accumulate as the most stable precipitate. (b)The simulated, steady state concentration of CFZ free base in the given aqueous compartment was divided by the experimentally measured, intrinsic aqueous solubility of CFZ. (c)Based on this degree of supersaturation calculated with Equation C.4 in Appendix C, the solubility of CFZ-HCl in lysosomes, in the presence of 110 mM chloride at pH= 4.5, was 3 nM. Estimated degrees of supersaturation are represented as ratios.

Compartments	**Estimated degree of supersaturation of free base CFZ at steady state**	**Estimated degree of supersaturation of CFZ-HCl at steady state**
Extracellular	$^{(b)}1.98x10^{1}$	$0^{(a)}$
Cytosol	$^{(b)}4.95x10^{4}$	$0^{(a)}$
Mitochondrial lumen	$^{(b)}5.36x10^{4}$	$0^{(a)}$
Lysosomal lumen	$^{(b)}2.25x10^{3}$	$^{(c)}1.36x10^{7}$

4.5 Discussion

In this study, we propose that CFZ accumulation in macrophages leads to physical alterations in cell structure and function that result from CFZ's self-assembly into an expandable mechanopharmaceutical device. This expandable mechanopharmaceutical device specifically accumulates in macrophage lysosomes following prolonged oral drug administration, and its

effects are posited to result from a physical space occupied by the drug, independent of the drug's pharmacological activity. As an expandable mechanopharmaceutical device, we considered CLDIs as a physical probe that can be used to measure the cargo loading capacity of different macrophage subpopulations *in vivo*, and used it to directly determine the VD of the drug in different organs. While prior studies have determined that CLDI formation is compatible with the maintenance of normal ion homeostasis in lysosomes of macrophages [37], this is the first study to show that the mass and volume occupied by drug is specifically accumulating in lysosomes within these cells, while assessing its impact on the drug's volume of distribution (VD) [27, 33]. While it is often assumed that the VD of a therapeutic agent is a constant, our measurements indicate that this is not necessarily the case. Furthermore, based on our mathematical modeling and simulation analysis, lysosomal pH and chloride content were found to be sufficient to account for the selective accumulation of CFZ in macrophage lysosomes accounting for the cell type selectivity of this phenomenon.

When studying the impact of macrophages on transport phenomena, fluid tracers or nanoparticles that are readily ingested by macrophages have been previously used as functional markers of macrophage-mediated clearance. To assess whole organism cargo capacity of macrophages in vivo, our results show how an expandable mechanopharmaceutical device that self-assembles from a small molecule building block could potentially be used to stretch the cell's cargo carrying capacity with the largest possible cargo load that can be accommodated by a living organism. This led us to consider the following question: how exactly does the organism respond to the massive build-up of a whole-body macrophage cargo load? In the experiments reported herein, the null hypothesis was that all macrophages would accumulate the drug to the same extent in all organs, and that at some point a toxicological effect may become manifested.

However, our experimental results led us to reject this, in favor of an alternative hypothesis: different macrophage subpopulations initially vary in their ability to bioaccumulate drug, but gradually respond to an increasingly massive amount of cargo so that the load does not exceed the cargo capacity of the individual cells and becomes more evenly distributed across all of the macrophage populations throughout the different organs of the body. Based on theoretical considerations, a physiologically-based cellular pharmacokinetic model indicated that this phenomenon may be entirely determined by an energetically-favorable, thermodynamically-driven loading state that decreases the total free energy of the drug while maximizing the volume-to-surface area ratio of intracellular drug inclusions. The significantly different rates at which this occurs in macrophage subpopulations do not simply reflect the extent of perfusion of the different organs, nor do they reflect the partitioning of soluble drug or trapping of circulating drug particles in these organs since it varied as the whole organism drug load increased. Since undifferentiated, bone marrow monocytes did not accumulate drug to any significant extent, we infer that differences in drug accumulation kinetics reflect organ-specific variations in the differentiation of macrophages into specialized, xenobiotic sequestering cells.

In terms of how these findings impact pharmacokinetics, CFZ induced changes in VD which counters the underlying assumptions about the mechanistic underpinning of this pharmacokinetic parameter. VD is usually considered the apparent volume that a systemically administered drug distributes in to reach a measureable concentration in the blood. For many poorly soluble, weakly basic drugs, the VD can be in the order of thousands of liters, which greatly exceeds the volume of body water (60-100 liters). Large VD is generally thought to be due to the preferential partitioning of hydrophobic drug molecules into adipose tissue or cellular membranes and lipids. For poorly soluble drugs that are administered at high doses for prolonged

periods of time, if the drug molecules are metabolically stable and eliminated very slowly, bioaccumulation could eventually lead to a phase transition, with insoluble aggregates forming throughout the organism, expanding the VD. Accordingly, the experimental and theoretical analysis presented in this study suggests that the simple, thermodynamic partitioning mechanisms underlying the general concept of VD may need to be revisited, especially for poorly soluble weakly basic drugs like CFZ which massively bioaccumulate in the organism.

Indeed, the experimental results presented in this study add support to the role of macrophage lysosomal pH and chloride ion regulation in contributing to, and accounting for, most of the accumulation and distribution of CFZ *in vivo* [37, 47]. The results of our physiologically based model was consistent with CFZ precipitation occurring selectively in macrophage lysosomes, because the stability of CFZ hydrochloride precipitates in this organelle surpassed that of all other sites in the cell, as well as in the extracellular environment, by more than three orders of magnitude. Macrophages possess highly acidic lysosomes which can expand to accommodate large cargo loads, and the macrophage population itself is able to undergo changes in structure and function to adapt to the cargo. In the future, the mathematical model could be used to predict the intracellular concentration and precipitation of ionized vs. neutral molecular species of other weakly basic small molecule drugs and to identify other small molecule chemical agents that have similar subcellular disposition characteristics as CFZ.

4.6 Conclusion

To conclude, the results presented herein suggest a physical stimulus-dependent, macrophage-mediated biological response mechanism that is activated by the function of CFZ as a building block of an expandable mechanopharmaceutical device that accumulates within these

cells. Macrophages actively stabilize intracellular CFZ as insoluble complexes that are trapped within their endophagolysosomal compartment. To accommodate increasingly massive loads of cargo, macrophages increased in numbers and adapted their intracellular membrane organization to expand the intracellular cargo space; this resulted in a gradual but dramatic increase in VD. While resident macrophages of different organs demonstrate significant variations in their response to increasing loads of cargo, all differentiated macrophage populations were capable of sequestering very large loads. Of noteworthy significance, to our knowledge this is the first time that changes in the VD of a small molecule drug has been directly linked to an adaptive, immune system-mediated, xenobiotic sequestration response.

4.7 References

1. Epelman S, Lavine KJ, Randolph GJ. Origin and Functions of Tissue Macrophages. Immunity. 2014;41(1):21-33.
2. Murray PJ, Wynn TA. Protective and pathogenic functions of macrophage subsets. Nature Reviews Immunology. 2011;11(11):723-737.
3. Davies LC, Jenkins SJ, Allen JE, Taylor PR. Tissue-resident macrophages. Nat Immunol. 2013;14(10):986-995.
4. Mindell JA. Lysosomal Acidification Mechanisms. Annual Review of Physiology. 2012;74(1):69-86.
5. Wang S-P, Krits I, Bai S, Lee BS. Regulation of Enhanced Vacuolar H+-ATPase Expression in Macrophages. Journal of Biological Chemistry. 2002;277(11):8827-8834.
6. Hamczyk MR, Villa-Bellosta R, Andrés V. In Vitro Macrophage Phagocytosis Assay. In: Andrés V, Dorado B, editors. Methods in Mouse Atherosclerosis. New York, NY: Springer New York; 2015. p. 235-246.
7. Steinberg BE, Grinstein S. Analysis of macrophage phagocytosis: quantitative assays of phagosome formation and maturation using high-throughput fluorescence microscopy. Methods in molecular biology (Clifton, NJ). 2009;531:45-56.
8. Cannon GJ, Swanson JA. The macrophage capacity for phagocytosis. Journal of Cell Science. 1992;101(4):907-913.
9. Broz P, Ben-Haim N, Grzelakowski M, Marsch S, Meier W, Hunziker P. Inhibition of macrophage phagocytotic activity by a receptor-targeted polymer vesicle-based drug

delivery formulation of pravastatin. Journal of cardiovascular pharmacology. 2008;51(3):246-252.
10. Hirota K, Terada H. Endocytosis of Particle Formulations by Macrophages and Its Application to Clinical Treatment. In: Ceresa B, editor. Molecular Regulation of Endocytosis. Rijeka: InTech; 2012. p. Ch. 16.
11. Lemaire S, Tulkens PM, Van Bambeke F. Cellular Pharmacokinetics of the Novel Biaryloxazolidinone Radezolid in Phagocytic Cells: Studies with Macrophages and Polymorphonuclear Neutrophils. Antimicrobial Agents and Chemotherapy. 2010;54(6):2540-2548.
12. Carryn S, Chanteux H, Seral C, Mingeot-Leclercq MP, Van Bambeke F, Tulkens PM. Intracellular pharmacodynamics of antibiotics. Infectious disease clinics of North America. 2003;17(3):615-634.
13. Stamler DA, Edelstein MA, Edelstein PH. Azithromycin pharmacokinetics and intracellular concentrations in Legionella pneumophila-infected and uninfected guinea pigs and their alveolar macrophages. Antimicrob Agents Chemother. 1994;38(2):217-222.
14. Foulds G, Shepard RM, Johnson RB. The pharmacokinetics of azithromycin in human serum and tissues. Journal of Antimicrobial Chemotherapy. 1990;25(suppl_A):73-82.
15. Keswani RK, Yoon GS, Sud S, Stringer KA, Rosania GR. A far-red fluorescent probe for flow cytometry and image-based functional studies of xenobiotic sequestering macrophages. Cytometry Part A : the journal of the International Society for Analytical Cytology. 2015;87(9):855-867.
16. Rzeczycki P, Yoon GS, Keswani RK, Sud S, Stringer KA, Rosania GR. Detecting ordered small molecule drug aggregates in live macrophages: a multi-parameter microscope image data acquisition and analysis strategy. Biomedical optics express. 2017;8(2):860-872.
17. Logan R, Kong AC, Axcell E, Krise JP. Amine-Containing Molecules and the Induction of an Expanded Lysosomal Volume Phenotype: A Structure–Activity Relationship Study. Journal of Pharmaceutical Sciences. 2014;103(5):1572-1580.
18. Funk R, Krise J. Cationic amphiphillic drugs cause a marked expansion of apparent lysosomal volume: implications for an intracellular distribution-based drug interaction. Mol Pharmaceutics. 2012;9(5):1384-1395.
19. Kaufmann A, Krise J. Lysosomal Sequestration of Amine-Containing Drugs: Analysis and Therapeutic Implications. Journal of Pharmaceutical Sciences. 2006;96(4):729-746.
20. Arbiser J, Moschella S. Clofazimine: A review of its medical uses and mechanisms of action. Journal of the American Academy of Dermatology. 1995;32(2):241-247.
21. Cholo M, Steel H, Fourie P, Germishuizen W, Anderson R. Clofazimine: current status and future prospects. Journal of Antimicrobial Chemotherapy. 2011.
22. DrugBank. Clofazimine. In. drugbank.ca; 2013.
23. Baik J, Rosania GR. Macrophages Sequester Clofazimine in an Intracellular Liquid Crystal-Like Supramolecular Organization. PLoS ONE. 2012;7(10):e47494.
24. Baik J, Stringer KA, Mane G, Rosania GR. Multiscale Distribution and Bioaccumulation Analysis of Clofazimine Reveals a Massive Immune System-Mediated Xenobiotic Sequestration Response. Antimicrob Agents Chemother. 2013;57(3):1218-1230.

25. Sukpanichnant S, Hargrove NS, Kachintorn U, Manatsathit S, Chanchairujira T, Siritanaratkul N, Akaraviputh T, Thakerngpol K. Clofazimine-induced crystal-storing histiocytosis producing chronic abdominal pain in a leprosy patient. The American journal of surgical pathology. 2000;24(1):129-135.
26. Keswani R, Yoon G, Sud S, Stringer K, Rosania G. A Far-Red Fluorescent Probe For Flow Cytometric Xenobiotic-Sequestering Cell Functional Studies. Cytometry Part A. 2015(Accepted Manuscript).
27. Rzeczycki P, Yoon GS, Keswani RK, Sud S, Stringer KA, Rosania GR. Detecting ordered small molecule drug aggregates in live macrophages: a multi-parameter microscope image data acquisition and analysis strategy. Biomed Opt Express. 2017;8(2):860-872.
28. Yoon GS, Keswani RK, Sud S, Rzeczycki PM, Murashov MD, Koehn TA, Standiford TJ, Stringer KA, Rosania GR. Clofazimine Biocrystal Accumulation in Macrophages Upregulates Interleukin 1 Receptor Antagonist Production To Induce a Systemic Anti-Inflammatory State. Antimicrobial agents and chemotherapy. 2016;60(6):3470-3479.
29. Zhang X, Goncalves R, Mosser DM. The Isolation and Characterization of Murine Macrophages. In. Current Protocols in Immunology: John Wiley & Sons, Inc.; 2001.
30. Schneider CA, Rasband WS, Eliceiri KW. NIH Image to ImageJ: 25 years of image analysis. Nat Meth. 2012;9(7):671-675.
31. Abramoff MD, Magalhaes PJ, Ram SJ. Image Processing With ImageJ. Biophotonics International. 2004;11(7):36-42.
32. Yoon G, Sud S, Keswani R, Baik J, Standiford T, Stringer K, Rosania G. Phagocytosed Clofazimine Biocrystals can Modulate Innate Immune Signaling by Inhibiting TNF Alpha and Boosting IL-1RA Secretion. Mol Pharmaceutics. 2015.
33. Keswani R, Baik J, Yeomans L, Hitzman C, Johnson A, Pawate A, Kenis P, Rodriguez-Hornedo N, Stringer K, Rosania G. Chemical Analysis of Drug Biocrystals: A Role for Counterion Transport Pathways in Intracellular Drug Disposition. Molecular Pharmaceutics. 2015.
34. Trexel J, Yoon GS, Keswani RK, McHugh C, Yeomans L, Vitvitsky V, Banerjee R, Sud S, Sun Y, Rosania GR, Stringer KA. Macrophage-Mediated Clofazimine Sequestration Is Accompanied by a Shift in Host Energy Metabolism. J Pharm Sci. 2017;106(4):1162-1174.
35. Murashov MD, LaLone V, Rzeczycki PM, Keswani RK, Yoon GS, Sud S, Rajeswaran W, Larsen S, Stringer KA, Rosania GR. The Physicochemical Basis of Clofazimine-Induced Skin Pigmentation. Journal of Investigative Dermatology. 2017.
36. Lee S, Starkey P, Gordon S. Quantitative analysis of total macrophage content in adult mouse tissues. Immunochemical studies with monoclonal antibody F4/80. J Exp Med. 1985;161(3):475-489.
37. Woldemichael T, Keswani RK, Rzeczycki PM, Murashov MD, LaLone V, Gregorka B, Swanson JA, Stringer KA, Rosania GR. Reverse Engineering the Intracellular Self-Assembly of a Functional Mechanopharmaceutical Device. Scientific reports. 2018;8(1):2934.
38. Champion JA, Mitragotri S. Role of target geometry in phagocytosis. Proceedings of the National Academy of Sciences of the United States of America. 2006;103(13):4930-4934.

39. Trapp S, Rosania GR, Horobin RW, Kornhuber J. Quantitative modeling of selective lysosomal targeting for drug design. European biophysics journal : EBJ. 2008;37(8):1317-1328.
40. Min KA, Zhang X, Yu JY, Rosania GR. Computational approaches to analyse and predict small molecule transport and distribution at cellular and subcellular levels. Biopharmaceutics & drug disposition. 2014;35(1):15-32.
41. Rodgers T, Rowland M. Physiologically based pharmacokinetic modelling 2: Predicting the tissue distribution of acids, very weak bases, neutrals and zwitterions. Journal of Pharmaceutical Sciences. 2006;95(6):1238-1257.
42. Mehta SB, Shribak M, Oldenbourg R. Polarized light imaging of birefringence and diattenuation at high resolution and high sensitivity. Journal of Optics. 2013;15(9):094007.
43. Oldenbourg R. Polarized Light Microscopy: Principles and Practice. Cold Spring Harbor Protocols. 2013;2013(11):pdb.top078600.
44. Toutain PL, Bousquet-MÉLou A. Volumes of distribution. Journal of Veterinary Pharmacology and Therapeutics. 2004;27(6):441-453.
45. Smith DA, Beaumont K, Maurer TS, Di L. Volume of Distribution in Drug Design. Journal of Medicinal Chemistry. 2015;58(15):5691-5698.
46. de Duve C, de Barsy T, Poole B, Trouet A, Tulkens P, Van Hoof F. Commentary. Lysosomotropic agents. Biochem Pharmacol. 1974;23(18):2495-2531.
47. Keswani RK, Baik J, Yeomans L, Hitzman C, Johnson AM, Pawate AS, Kenis PJ, Rodriguez-Hornedo N, Stringer KA, Rosania GR. Chemical Analysis of Drug Biocrystals: A Role for Counterion Transport Pathways in Intracellular Drug Disposition. Molecular pharmaceutics. 2015;12(7):2528-2536.

Chapter 5 Molecular Design of a Pathogen Activated, Self-Assembling Mechanopharmaceutical Device

Aspects of this work have been published as an original review article in *Journal of Controlled Release* 2022 Jul;347:620-631.

5.1 Abstract

Weakly basic small molecule drugs like clofazimine can be used as building blocks for endowing cells with unnatural structural and functional elements. Here, we describe how clofazimine represents a first-in-class mechanopharmaceutical device, serving to construct inert, inactive and stimulus responsive drug depots within the endophagolysosomal compartment of cells of living organisms. Upon oral administration, clofazimine molecules self-assemble into stable, membrane-bound, crystal-like drug inclusions (CLDI) that accumulate within macrophages to form a "smart" biocompatible, pathogen activatable mechanopharmaceutical device. Upon perturbation of the mechanism maintaining pH and ion homeostasis of these CLDIs, the inert encapsulated drug precipitates are destabilized, releasing bioactive drug molecules into the cell and its surrounding. The resulting increase in clofazimine solubility activates this broad-spectrum antimicrobial, antiparasitic, antiviral or cytotoxic agent within the infected macrophage. We present a general, molecular design strategy for using clofazimine and other small molecule building blocks for the cytoplasmic construction of

mechanopharmaceutical devices, aimed at rapid deployment during infectious disease outbreaks, for the purpose of pandemic prevention.

5.2 Introduction

To facilitate cytoplasmic construction, many small molecule chemical agents are known to preferentially bioaccumulate within target organelles or specific cells, such as macrophages [1, 2]. If concentrated inside organelles at high concentrations, these poorly soluble organic molecules will exceed their solubility in the local microenvironments, forming insoluble precipitates [3-6]. As this soluble-to-insoluble phase transition occurs, precipitated molecules may adopt a disordered liquid or aggregated state, or they can self-assemble into ordered supramolecular structures such as liquid crystals or solid-state, three-dimensional crystals [7].

Taking advantage of this natural targeting phenomenon, organic small molecules could be designed and screened for their ability to create self-assembling, mechanopharmaceutical devices possessing unique physical, chemical, and biological features [8-12]. Due to the distinct properties of ordered molecular structures, self-assembled mechanopharmaceutical devices can be readily retrieved, isolated, or monitored in living organisms [13]. The cytoplasmic construction of mechanopharmaceutical devices has already been demonstrated as a strategy to endow cells of living organisms with functional supramolecular structures possessing unique fluorescence and photoacoustic signals, as well as a means to massively load cells for drug targeting and delivery purposes, and for measuring the phenotypic properties of the targeted cells [14].

However, perhaps the most clinically relevant application of a self-assembling mechanopharmaceutical device is the possibility of creating a self-assembling, pathogen activatable drug depot. Following oral drug administration, the absorbed drug molecules circulate in the blood and partition within macrophages, where they self-organize into supramolecular structures that function as biocompatible, intracellular reservoirs of precipitated

drug [15]. Following drug loading during a prolonged oral dosing period, sustained pharmacodynamic activity can be maintained through drug elution from the self-assembled drug reservoir, which is reflected in an increasing systemic half-life of the drug when administered in long-term treatment regimens [16].

5.3 Clofazimine as a Self-Assembling Biomolecule

5.3.1 Solubility and Lysosomal Targeting

One of the most studied pharmaceuticals to undergo a soluble-to-insoluble phase transition inside the organism following oral administration in therapeutically relevant conditions is the FDA approved drug clofazimine (CFZ). CFZ has cured over 14 million leprosy patients and is currently recommended by the WHO as part of the standard treatment of leprosy and MDR-TB [17].

Due to limited aqueous solubility (<0.01mg/L) [17] and high lipophilicity (logP=7.66), CFZ accumulates in fatty tissue during a short-term treatment regimen [18]. Concomitantly, the ionizable amine group (apparent pKa = 6.08) also leads to drug accumulation in acidic organelles such as the lysosome (pH 4.5-5.0). In both human and animal models, it has been shown that CFZ forms insoluble Crystal-Like Drug Inclusions (CLDIs) through ion-trapping and supramolecular complexation of the protonated monocationic form of the weakly basic drug, within the macrophage lysosome [19]. As a result of this soluble-to-insoluble phase transition, CFZ exhibits an increasing volume of distribution following a prolonged oral dosing period, which leads to the accumulation of drug in organs of the reticuloendothelial system to much greater extent than would be predicted by a simple partitioning into body fat. Thus, the continuously increasing volume of distribution, as a function of intracellular drug crystal

deposition, complicates traditional compartmental analysis of CFZ that stipulate a constant volume of distribution for pharmacokinetic parameter estimates [20, 21].

Due to the pKa of the amine functional group of CFZ, acting together with the acidic, lumenal pH of the lysosomes, CFZ becomes trapped inside lysosomes as the conjugate acid CFZH+. The concentration of chloride ions within the lysosomal compartment is higher than that of other anions, such that CFZ is primarily present as a hydrochloride salt ($CFZH^+Cl^-$). Being the most concentrated anion in the body, chloride is typically present at 10-to-100-fold greater concentration than any other anion (Figure 5.1A) [22, 23]. Due to the common ion effect arising from the high chloride concentration in lysosomes, the hydrochloride salt is markedly less soluble than the free base within the lysosome ($CFZH^+Cl^-$ lysosomal solubility = 3 nM vs CFZ solubility = 480 nM), lending itself to rapid precipitation with continued drug loading. Combined with significant protein binding, the vastly lower solubility of the lysosomal salt form of the drug becomes the primary determinant of the freely soluble CFZ concentrations that circulate in the blood and partition in the cells throughout the organism, allowing the drug to remain well below its active concentration. Thus, CFZ is well-tolerated despite its promiscuity.

The naturally acidic lysosome of macrophages contrasts with the slightly basic internal environment of the cytosol (pH 7.0-7.4) due to a high density of vacuolar-type H+-ATPase (V-ATPase) pumps on its membranes, which use the free energy of ATP hydrolysis to pump protons into the lumen of the lysosome [24-26]. The acidic environment of the lysosome plays an important role in the decomposition of nutrients and pathogenic organisms following phagocytosis. Although lysosomes exhibit specialized secretory functions in some cell types [27], the expression level of V-ATPase is relatively universal. Because the V-ATPase activity separates electric charge and generates a transmembrane voltage, another ion must move to

dissipate this voltage for net pumping to occur. This counterion may be either a cation (moving out of the lysosome) or an anion (moving into the lysosome) [26]. Evidence points to chloride as this counterion using a lysosomal chloride channel (ClC-3). As such, the inhibition of V-ATPase would lead to significant change in pH and chloride ion concentration [28]. Thus, as the main counterion in the lysosome, chloride ion concentrations are relatively high, around 110mM [22], which also serves to drive the precipitation of $CFZH^{+}Cl^{-}$.

The master regulator of lysosomal biogenesis, Transcription Factor EB (TFEB), is actively expressed in macrophages and its overexpression is an important determinant of macrophage's phagolysosomal function [29-31]. The expanded phagolysosomal compartment of macrophages is ideally suited to maintain low CFZ solubility, through the overexpression of V-ATPase and ClC-3, maintaining high proton and chloride concentrations upon $CFZH^{+}Cl^{-}$ precipitation (Figure 5.1B). Macrophages are thus equipped with the ability to maintain the acidic environment in the lysosomes concomitantly with the degradation of large amounts of proteins as may be present in phagocytosed bacteria [32]. Lysosomes are known to contain more than 60 different hydrolytic enzymes which require a low pH to conduct optimal catalytic activity. The macrophages therefore are especially equipped to maintain a pH gradient to compartmentalize these degradative enzymes within the phagolysosomal compartment while protecting the cytosol and the rest of the cell from their catalytic activity.

Lysosomal biogenesis, driven by TFEB, is upregulated upon CFZ administration, increasing the expression of resident lysosomal proteins in the cell [33, 34]. Upon phagocytosis of CLDIs, Akt phosphorylation is induced, likely contributing to TFEB activation and resistance to apoptosis [15]. It is possible that cytoplasmic construction in macrophage lysosomes benefits from specific transcriptional responses to drug accumulation through the activation of TFEB.

The respective increase in lysosomal biogenesis can control the expansion of the lysosomal compartment and allows for accommodation of incremental increase in drug loads. TFEB activation expectedly leads to increased expression of the V-ATPase, which reduces lysosomal stress, maintaining the low pH, and actively allowing for increased intracellular drug sequestration.

A

	Extracellular	Intracellular	
	Plasma & interstitial fluid	Cytoplasm	lysosome
pH	7.0-7.4	7.0-7.4-	4.5-5
Chloride	100mM	4mM	110mM
Iodide	50 - 300 nM	1 - 15 uM*	20 - 50 mM*
Bicarbonate	27mM	10mM	N/A
Sulfate	<1mM	5mM	N/A
Phosphate	<1mM	10mM	N/A

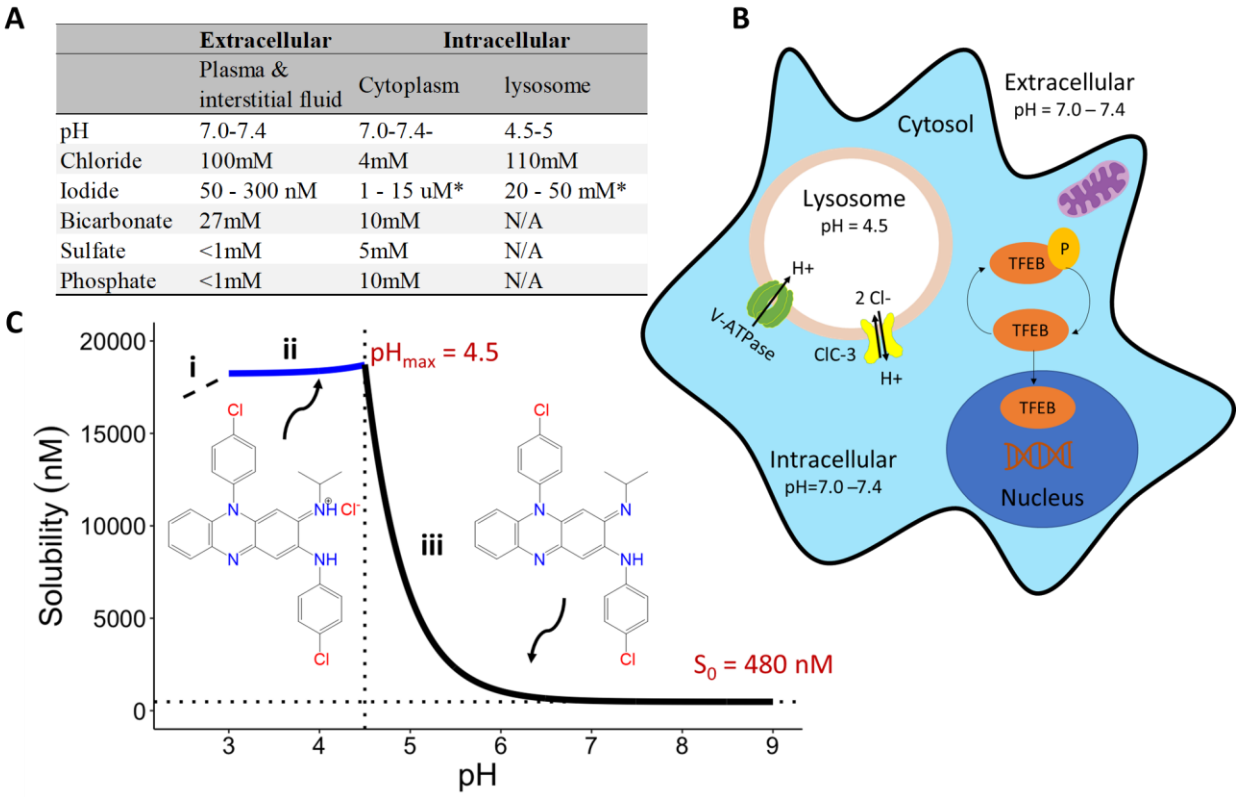

*Figure 5.1: Lysosomal acidification machinery determines CFZ solubility. A) Physiologically relevant anion concentrations in the interstitial fluid, cytosol, and lysosome. B) Cell model with relevant compartmental pH and molecular structures. C) pH-Dependent solubility curve, i) common-ion effect. ii) pH<pHmax, iii) pH>pHmax. Solubility of CFZH+Cl- salt form and CFZ free base with respect to pH change generated using literature reported solubility parameters (S0=480 nM, pHmax=4.5, and Ksp=332.3 μM2). The dashed line, solid blue line, and solid black line segments represent the solubility of the salt form with or without the common ion effects, and the solubility of the freebase respectively. Using established equations, total drug solubility with respect to pH change was created in RStudio Version 1.2.1335. The data points were calculated based on equations listed above for corresponding pH ranges. The embedded packages dplyr, coin, and ggplot2 were used to clean the calculated data and make the plot. * Thyroid tissue only*

Based on the Law of Mass Action, the high lysosomal chloride concentration determines the low solubility of the protonated form of CFZ according to the salt solubility product (K_{sp}) of $CFZH^+Cl^-$ (Eq. 5.1) [14, 35].

Equation 5.1: Ksp of CFZ

$$K_{sp} = [CFZH^+]_S \times [Cl^-]$$

As such, although the solubility of the protonated CFZ in pure water is much greater than the solubility of the unprotonated, conjugate base (Figure 5.1C), the high proton and chloride ion concentrations within the lysosome ensure that the solubility of the insoluble salt complex is lower than the intrinsic free base solubility. In the lysosomes, the lumenal microenvironment contains chloride ions at a high concentration, well above the 18 μM concentration of chloride ions that is present when the crystalline, hydrochloride salt form of the drug is dissolved in water at or below the pHmax, given the 1:1 stoichiometric relationship of $CFZH^+$ and Cl^- in $CFZH^+Cl^-$. In the lysosomes, the solubility of $CFZH^+$ at or below the pHmax is expectedly governed by the chloride concentration, decreasing the total solubility according to the common ion effect (Eq. 5.2; Figure 5.1C; region i).

Equation 5.2: Total Solubility below pH max

$$S_T = \frac{Ksp}{Cl^-} \times (1+10^{pH-pKa})$$

In pure water, when the pH is at the pH_{max}, the soluble $CFZH^+$ exists in equilibrium with the thermodynamically more stable solid form of the hydrochloride salt (Figure 5.1C; region ii), its concentration is determined according to the following equation:

Equation 5.3: Total Solubility at pHmax

$$S_T = \sqrt{Ksp} \times (1+10^{pH-pKa})$$

Lastly, when pH> pH_{max}, the total drug solubility in water is driven by the intrinsic solubility of the free base (Eq. 5.4).

Equation 5.4 Total Solubility above pHmax

$$S_T = S_0 \times (1+10^{pKa-pH})$$

As the pH is increased above the pHmax by adding base (e.g., NaOH) to a pure aqueous solution of $CFZH^+Cl^-$, the ratio of unionized to ionized species in solution will increase due to Henderson-Hasselbalch equilibrium. As the pH becomes increasingly alkaline, the total solubility of CFZ molecules will gradually decrease, approaching the intrinsic aqueous solubility of the free base, 480 nM (Figure 5.1C; region iii). Nevertheless, in a lysosome containing CLDIs, a rise in pH above the pHmax decreases the ratio of protonated to unprotonated CFZ, increasing the total solubility of the drug accompanying the release of precipitated drug sequestered as insoluble $CFZH^+Cl^-$ in the CLDI in a manner that is also dependent on the membrane permeability properties of the solubilized drug molecules.

5.3.2 Supramolecular Assembly of a Mechanopharmaceutical Device

With sustained extracellular concentrations of CFZ, ion-trapping and thermodynamic stability of the hydrochloride salt leads to supersaturation and precipitation within the lysosome.

The supersaturation of $CFZH^{+}Cl^{-}$ initiates the formation of disordered supramolecular drug complexes that eventually become organized as a three dimensional crystalline solid. CFZ is highly lipid soluble, allowing it to partition within and across the cellular membranes, achieving its pH-dependent equilibrium between the unprotonated and protonated base in the aqueous lumen of the various subcellular compartments. Nevertheless, the primary determinant of intracellular drug mass disposition is the low hydrochloride salt solubility of 3 nM in the lysosomes, which drives drug precipitation within the lysosome (Eq. 5.1). Data from transmission electron microscopy, deep etch freeze fracture electron microscopy, powder X-ray diffraction and Raman spectroscopy all point to the drug molecules present in CLDIs as a thermodynamically stable, solid 3D structure (Figure 5.2A-C). Based on *in vitro* experiments, the crystalline stability is due to the precise structure of the crystalline drug salt, and not simply due to the high logP [14, 35]. As the drug precipitates, grows and becomes organized within the macrophage lysosome, membranous lipid molecules associated with the surface of crystalline drug complexes to form the supramolecular, membrane bound CLDI complex (Figure 5.2D, E). Multiple intracellular deposits of CLDI structures can develop, leading to a prominent repository of self-assembled CLDIs within the cytoplasm (Figure 5.2F).

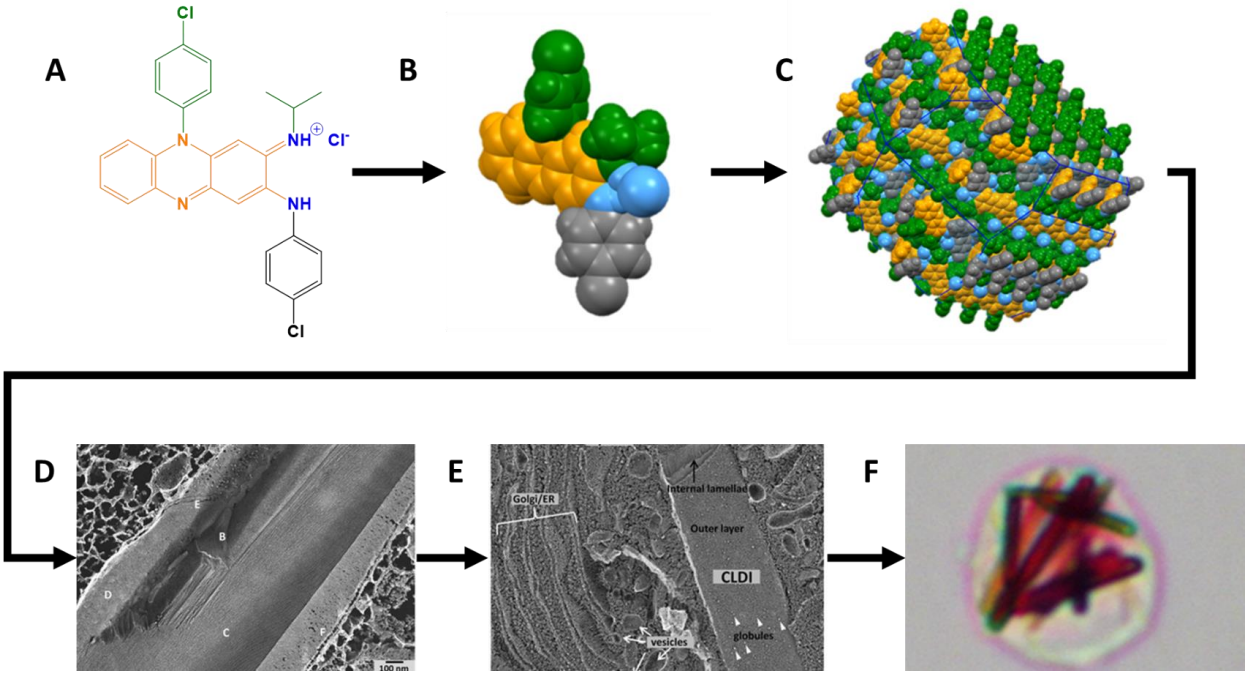

Figure 5.2: Image sequence for supramolecular CLDI organization A) CFZH+Cl- structure in ChemDraw B) CFZH+Cl-, 3D-molecular orientation in Mercury CCDC with colors corresponding to the colored functional groups in part A. C) Supramolecular crystalline organization in Mercury CCDC. D) Freeze fracture image of a macrophage sequestered intracellular drug inclusion [19]. E) Freeze fracture image of a membrane bound crystal formation [19]. F) Multiple CLDIs forming inside a macrophage [19]..

Despite the proportionally large volume taken up by intracellular CLDIs, macrophages loaded with CFZ remain alive and functional. While CFZ is expectedly bioactive at the concentration of the intrinsic free base solubility limit, the crystallized form of $CFZH^{+}Cl^{-}$ within CLDIs is biologically inactive against most of its known molecular targets, as its solubility is (at least) two order of magnitudes lower than the concentrations required for activity [15]. The difference in reactivity between the CLDI form of the drug and the freely soluble neutral form is an essential quality of this mechanopharmaceutical device granting CLDIs the ability to lie dormant within the cell until activated by an external stimulus.

5.3.3 Macrophages as Endogenous Tools of Self-Assembly

In addition to the essential role played by lysosomal proton pumps and chloride transporters present on the surface of the bounding membrane of macrophage lysosomes, macrophages can alter their internal membrane architecture to maximize the volume of substances sequestered within the lysosome, referred to as a “phagolysosomal cargo”. Continued accumulation of cargo has been associated with increased formation of larger volume vesicles and to the disappearance of smaller vesicles. It can be inferred that by expanding the volume of intracellular vesicles, macrophages maximize the available cargo capacity while minimizing the overall membrane surface area delimiting the cargo compartments [36, 37]. This allows for increased cargo accumulation within the cell, and consequently, an increase in volume of distribution of a bioaccumulating, precipitating drug.

In terms of the pharmacokinetics properties that allows for macrophage dependent self-assembly, CFZ is the only known drug that has been extensively studied in this regard. Measurements of the entire cell population of liver, lung, and spleen indicate an active macrophage response to the increasing drug cargo load. This biological response includes an increase in the number of macrophages occurring in parallel to changes in intracellular membrane organization that accumulates the self-assembled mechanopharmaceutical CLDI devices. In pathological states an expansion in the macrophage population is typically associated with a pro-inflammatory response [38, 39]. However, the accumulation of CFZ and its self-assembly in macrophages was accompanied by the activation of anti-inflammatory signaling pathways and was not associated with obvious toxicological manifestations [40, 41]. In addition, cargo loading of macrophages induced increases in the number of cells and accompanying increases in organ mass, resulting in splenomegaly following extensive drug loading [34]. Additionally, changes in histological organization have been observed, such as large clusters of

macrophages called granulomas [34, 42, 43]. These changes enable a spatially localized, collective intracellular cargo load associated with the self-assembly of this functional, mechanopharmaceutical device.

5.3.4 Pharmacokinetics of Clofazimine

The macrophage targeted accumulation of CLDIs expectedly alters the whole-body pharmacokinetics in a context-dependent manner. As drug sequesters within lysosomal compartments of macrophage cells, the volume of distribution continues to expand nonlinearly. Due to the dissemination of macrophages throughout the tissues of the body, widespread accumulation of CFZ in both free base and CLDI form have been observed in murine and human tissues (Table 5.1).

Table 5.1: CFZ serum and tissue concentration data under variable infections and dosing regimens. [16, 34, 44-48]

CFZ Dose	Dosing Duration	Infection Status	Number of Subjects	Peak Serum Concentration (μM)	Spleen Concentration (μM)	Lung Concentration (μM)	Liver Concentration (μM)	Ref
Human Serum and Tissue Concentrations								
200 mg SD	Single Dose	Healthy	8	0.861 +/- 0.289	N/A	N/A	N/A	1
300 mg daily for 1-2 weeks, 200 mg for 2-8 weeks	2 Months	Drug Resistant TB (PROBeX)	79	0.766 (0.340-1.452)	N/A	N/A	N/A	2
200 mg	14 Days	Drug Sensitive Tuberculosis	60	0.460 (0.145-0.871)	N/A	N/A	N/A	2
100 mg Three times per week	N/A	Leprosy	N/A	1.06	N/A	N/A	N/A	3
100 mg daily	N/A	Leprosy	N/A	1.48	N/A	N/A	N/A	3
300 mg daily	N/A	Leprosy	N/A	2.11	N/A	N/A	N/A	3
400 mg daily	N/A	Leprosy	N/A	2.95	N/A	N/A	N/A	3
High-Dose daily	Long-term	Leprosy	1	N/A	2532	N/A	443	4
100 - 300 mg daily	35 days to 243 days	Leprosy	3	N/A	2638 (1266 - 4009)	2251 (1266 - 2954)	3517 (1899 - 6752)	5
Mice Serum and Tissue Concentrations								
25 mg/kg	Single Dose	Healthy	5	0.91	3.65	1.6	5.87	6
25 mg/kg	1 week	Healthy	3	1.94 +/- 0.63	17.11 +/- 6.58	11.04 +/- 5.42	14.88 +/- 3.90	6
25 mg/kg	2 weeks	Healthy	3	1.79 +/- 0.063	23.59 +/- 1.10	23.78 +/- 5.84	23.74 +/- 0.61	6
25 mg/kg	4 weeks	Healthy	3	2.22 +/- 0.084	106.41 +/- 4.05	63.26 +/- 10.55	70.16 +/- 13.06	6
25 mg/kg	8 weeks	Healthy	3	4.75 +/- 0.063	402.46 +/- 203.40	110.96 +/- 14.22	126.54 +/- 56.02	6
25 mg/kg	12 weeks	Healthy	3	2.74 +/- 0.61	9884.67 +/- 864.49	86.15 +/- 17.22	173.80 +/- 17.75	6
25 mg/kg	16 weeks	Healthy	3	2.55 +/- 0.44	7945.84 +/- 1502.87	62.79 +/- 27.58	234.82 +/- 163.10	6
25 mg/kg	20 weeks	Healthy	3	2.11 +/- 0.25	14292.4 +/- 1483.6	78.89 +/- 11.50	226.21 +/- 26.69	6
36 mg/kg	3 weeks	Healthy	6	16.96 +/- 0.422*	2012.94 +/- 1446.43	N/A	675.2 +/- 222.31	7
36 mg/kg	8 weeks	Healthy	6	4.54 +/- 1.88*	27900 +/- 3129.64	N/A	10128 +/- 1126.42	7

**Plasma concentrations*

As can be noted in both species, the concentration of CFZ in tissue is greater than the concentration of CFZ in serum. In fact, while the tissue concentration increases with continual drug load, the serum concentration remains static in the low micromolar range. This discrepancy between drug in soluble aqueous environment and solid tissue is explained by the presence of insoluble drug precipitates within tissue-resident macrophages. This is further supported by microscopic evaluation of tissue samples in both humans and mice. Autopsy and sputum data has revealed CLDIs dispersed throughout multiple tissues in humans after prolonged treatment at a therapeutic dose, indicating that the observed phenomenon is relevant to the human condition, in an FDA-approved, clinical dosing regimen [49-52].

The deviation of the measured CFZ drug concentrations from the expected concentrations predicted by mathematical models used in standard pharmacokinetic analysis has made it difficult to determine standardized therapeutic regimens of CFZ for established indications. CFZ's pharmacokinetics are further complicated by the difficulty conducting therapeutic drug monitoring due to the discrepancy between blood concentrations and the respective tissue concentrations of interest, such as attempting to monitor lung concentrations in tuberculosis using serum concentrations as a surrogate marker. Nevertheless, the drug is extensively used throughout the world as a treatment for leprosy, multidrug resistant tuberculosis, and nontuberculous mycobacterial infections.

5.4 Chemical Kinetics of an Intracellular Pathogen Activatable Drug Depot

Upon prolonged oral administration, intracellular CLDIs self-organize into inert drug depots disseminated throughout the macrophage population of the host organism. After macrophages have been systemically loaded, crystallized CFZ remains compartmentalized within intracellular CLDIs, awaiting activation and solubilization. Interference with lysosomal acidification mechanisms, macrophage death, or lysosomal membrane permeabilization are all potential mechanisms by which the thermodynamically stable CLDIs can destabilize and begin to elute soluble drug into the cytoplasm and the surrounding extracellular space. This destabilization of the CLDI initiates a conversion between inactive $CFZH^{+}Cl^{-}$ molecules present in CLDIs to bioactive CFZ free base. CLDIs thus represent an unnatural, stimulus responsive drug depot system that is integrated into our body's natural defense system to combat an emergent infection.

5.4.1 Mechanisms of CLDI Destabilization

Established studies have shown evidence of lysosomal pH destabilization induced by a variety of infectious pathogenic organisms (Table 5.2). The same lysosomal destabilization mechanism that leads to the intracellular survival of pathogens can serve as the mechanism that triggers CLDI activation. It has been argued that the effect of a pathogenic organism on the ability of lysosomes to maintain acidic pH plays a role in the stark difference in the ability of mice to form CLDIs depending on their *M. tuberculosis* infection state [21]. As *M. tuberculosis* has been shown to arrest the acidification mechanism of lysosomes, the presence of infection may also prevent CLDI formation. When given to healthy patients, administered CFZ would be most prone to accumulate in CLDI form, warranting its consideration as a prophylactic treatment [53]. Because many other pathogens have been shown to destabilize the lysosome (Table 5.2), this phenomenon is more broadly applicable than to mycobacteria alone. For example, *Listeria monocytogenes* has been shown to prevent fusion with the lysosome through perforation of the phagosomal membrane using Listeria Lysin O. These perforations allow both pathogen escape and prevent the acidification of the compartment, which is necessary for lysosomal membrane fusion [54]. Similarly, *Toxoplasma gondii* block phagosome acidification, also preventing membrane fusion. Drug molecules that accumulate in endocytosed vesicles could also provide a parallel lysosomal accumulation pathway [55].

In a broader sense, the lysosome as a target for drug accumulation and release could be expanded not only to pathogens which directly deacidify the compartment, but also to those that disrupt the ability of macrophages to maintain ion homeostasis of cytoplasmic organelles. Several pathogens adopt lysosomal membrane permeabilization as a strategy for escape, such as *Listeria monocytogenes*, *Escherichia coli*, and human immunodeficiency virus (HIV) [56-58].

Although the universe of pathogens that interfere with lysosomal acidification, and could thus activate CLDIs, is diverse, large, and not fully known, we can illustrate the potential breadth of this approach with a handful of pathogens and mechanisms implicated in lysosomal deacidification (Table 5.2). The increase in lysosomal pH or otherwise inhibiting lysosomal function is a general, pathogen survival strategy. As macrophage lysosomes are key for our innate immune system to break down invading bacteria and viruses, it comes as no surprise that these invaders have evolved methods of lysosomal deacidification as a common pathway to weaken our defenses.

Table 5.2: Pathogen Activated Lysosomal Acidification. [53, 56-58, 59-63]

Pathogen	Mean Initial pH	Mean Final pH	ΔpH	Hypothesized Mode of Deacidification	Reference
Interference with Lysosomal Acidification Machinery					
Mycobacterium Tuberculosis	4.8	>5.8	>1	Interference with V-ATPase	[53]
β-Coronavirus	4.7	5.7	1	Indirect or direct perturbations in proton pump	[59]
Vibrio parahaemolyticus	*Unquantified Increase			VopQ interference with acidification	[60]
Streptococcus Oralis	*Unquantified Increase			H_2O_2 production	[61]
Legionella pneumophilia	^Unquantified Increase			V-ATPase inhibition with SidK	[62]
Candida albicans	4.5	7.3	2.8	Phagolysosome alkalinization through NH_3 production	[63]
Pathogen Induced Lysosomal Permeabilization					
Listeria Myocytogenes	Unquantified Increase			Host cell lysosome permeabilization with Lysteria Lysin O	[56]
Escherichia Coli	Unquantified Increase			Lysosomal permeabilization in type 1-fimbriated E. *coli*	[57]
HIV	Unquantified Increase			lysosomal permeabilization and cathepsin release	[58]

*LysoTracker, acidotropic fluorescent probe showed increase in pH
^SidK/V-ATPase biochemical study

While it has been shown that prolonged dosing of CFZ results in accumulation and nonlinear pharmacokinetics [20, 21], the same mechanism could be exploited as an avenue for developing prophylaxis against many kinds of pathogens, especially when used in combination with other antimicrobial or antiviral drugs. The pathogen-activated mechanism for drug release from the lysosome is a promising lead into the development and use of other small molecule weakly basic drugs which accumulate in the lysosome as additional components of a pathogen-activatable mechanopharmaceutical device. Upon infection by *M. Tuberculosis*, which has

already shown susceptibility to CFZ, the lysosomal microenvironment becomes perturbed, reducing the quantity of CFZ sequestered into the lysosomal compartment. By the same mechanism, pre-loading cells with CLDIs would also be protective against infection, and other drugs could be administered if any symptoms develop.

5.4.2 Computational Model of Mechanopharmaceutical Device Activation

To illustrate the kinetics of CFZ solubilization after drug sequestration, a single cell chemical kinetic model was developed in VCell (*awillmer: Drug Eluting Device*). Utilizing the measured solubility of CFZ free base (480 nM) and the calculated Ksp of the hydrochloride salt (3 nM), time dependent flux of drug leaving the lysosome was predicted under various fixed extracellular and lysosomal concentrations. Three unique lysosomal pHs were chosen to emulate destabilization conditions experienced by exogenous pathogens. At lysosomal pH of 4.5, normal physiological conditions are experienced, leading to $CFZH^{+}Cl^{-}$ as the predominate form. As a result, solubility of CFZ in the lysosome will be governed by the Ksp of $CFZH^{+}Cl^{-}$ (3nM) in the presence of high lysosomal chloride concentration. Following lysosomal destabilization through a transmembrane proton leak or V-ATPase inhibition, lysosomal pH was increased to 5.5, similar to the pH increase noted in experimental studies (Table 5.2). Based on the Henderson-Hasselbalch equation, with a 1 unit increase in lysosomal pH, the ratio of unionized to ionized CFZ would increase 10-fold (from 3 nM to 30 nM). And finally, a broken-down lysosomal membrane or lysed macrophage will lead to an equilibrium with the surrounding cytoplasm or extracellular matrix respectively. The pH in the presence of complete lysosomal destabilization was set to 7.4, leading to lysosomal free base CFZ concentrations approaching its solubility (480 nM).

Extracellular concentrations were varied in the cellular model to estimate a variety of physiologically relevant systemic concentrations. CFZ is both lipophilic and heavily protein bound, leading to a high volume of distribution and a low ratio of free unbound drug. As a result, the extracellular free, unbound drug concentration was varied from 0.01 nM to 10 nM, indicating an expected range of soluble CFZ concentrations in the free base form after termination of drug loading.

The single cell model was developed with four compartments: the lysosome, mitochondria, cytosol, and extracellular matrix (Figure 5.3A). The corresponding concentrations over time were predicted in each of these four compartments under fixed lysosomal and extracellular concentrations (Figure 5.3B). The duration of drug activation was estimated based on the predicted flux from the lysosomal compartment, and the previously reported average mass of CFZ loaded into the cell (100 fmols/cell) [7]. After the CLDI had fully solubilized, the respective concentration in the cytoplasm was estimated (Figure 5.3C). The corresponding time to complete destabilization of drug from the lysosome was then calculated (Figure 5.3D).

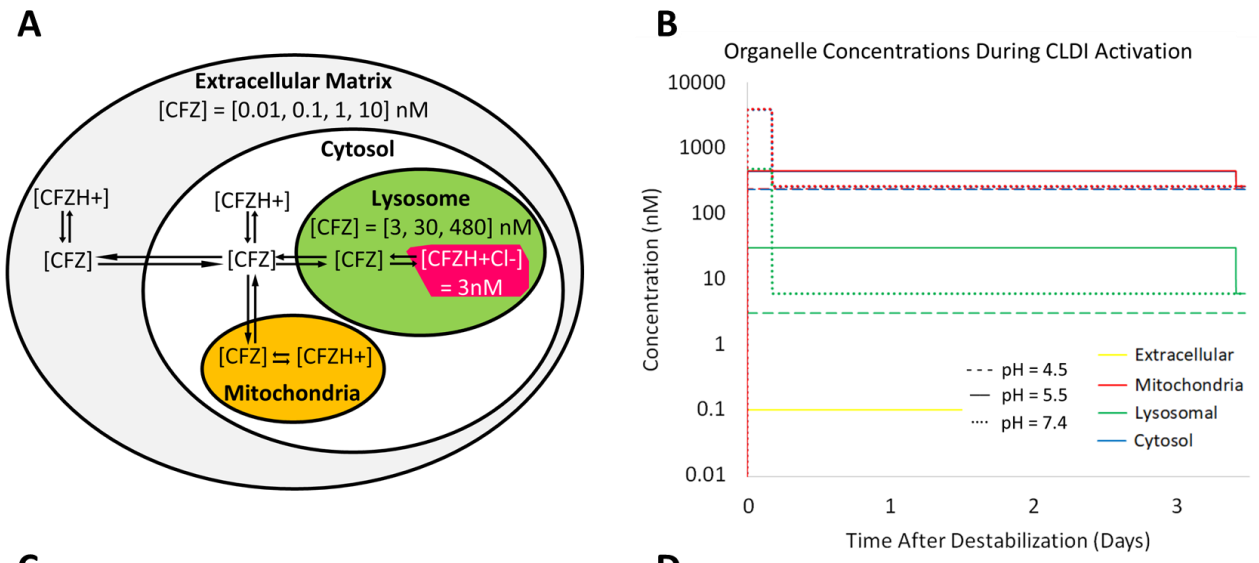

C

Peak Cytosolic Concentration (nM)

Extracellular Concentration	Lysosomal Concentration: 3 nM	30 nM	480 nM
0.01 nM	43.96	249.8	3,680
0.1 nM	233.8	439.6	3,870
1 nM	2,132	2,338	5,768
10 nM	21,120	21,320	24,750

D

Duration of CLDI Activation (Days)

Extracellular Concentration	Lysosomal Concentration: 3 nM	30 nM	480 nM
0.01 nM	34.07	2.79	0.17
0.1 nM	Inf	3.41	0.17
1 nM	Inf	Inf	0.19
10 nM	Inf	Inf	Inf

Figure 5.3: Computational drug elution model. A) Simulations were performed to compare the cellular pharmacokinetics of CFZ in the presence of four fixed extracellular concentrations (0.01, 0.1, 1, and 10 nM), and three fixed lysosomal concentrations of CFZ (3, 30, and 480 nM). B) The predicted drug concentrations in each of the four compartments are displayed with respect to time at a fixed extracellular concentration of 0.1 nM and variable lysosomal pH. C) The peak predicted concentrations within the cytosol are reported under varying lysosomal and extracellular concentrations. D) Time until total dissolution of CLDIs within the lysosomal compartment are reported under each modeled condition. "Inf" was used to illustrate a negative flux, and therefore no solubilization of drug from CLDIs.

With increasing freely soluble CFZ concentration as a function of increasing lysosomal pH, the resulting duration of drug efflux from the lysosome decreases. As expected, drug is retained in the lysosome for a longer duration of time if the intracellular environment is closer to homeostatic equilibrium. With high enough extracellular concentrations, and limited lysosomal destabilization, the direction of the flux favors accumulation in the lysosomal compartment, indicating that drug would continue to enter the lysosome and precipitate out. However, the more disrupted the lysosomal microenvironment becomes, the faster drug destabilizes in CLDI form,

leading to higher flux of drug from the lysosomal compartment out into the cytosol, in parallel to an accompanying increase in free drug concentrations. As expected, the cytoplasmic concentrations of CFZ increase with increasing drug efflux from the lysosome. Complete lysosomal membrane rupture results in large short-lived (hours) rise in cytosolic concentration. Minor lysosomal perturbation results in lower cytosolic concentration for a prolonged duration (days).

5.4.3 Molecular Impact of Insoluble-to-Soluble Phase Transitions

Using SARS-Cov-2 infection as a clinically relevant candidate therapeutic target for CFZ [59, 64-66], we evaluated the feasibility of this pathogen activated CLDI destabilization mechanism as a prophylactic treatment to prevent or curtail infection. Using the previously cited minimum inhibitory concentration (MIC) of CFZ against COVID-19 (0.32 μM), we evaluated whether the concentrations of CFZ that are predicted by the model exceed the minimum inhibitory concentration (MIC) of SARS-Cov-2 under varying conditions. To run these simulations, the CFZ concentrations in cytosol, lysosome, and mitochondria were predicted under various lysosomal pH and fixed extracellular concentrations, focusing on the effects of CLDI destabilization and the drug concentrations needed for the inhibition of viral replication and spreading (Figure 5.4).

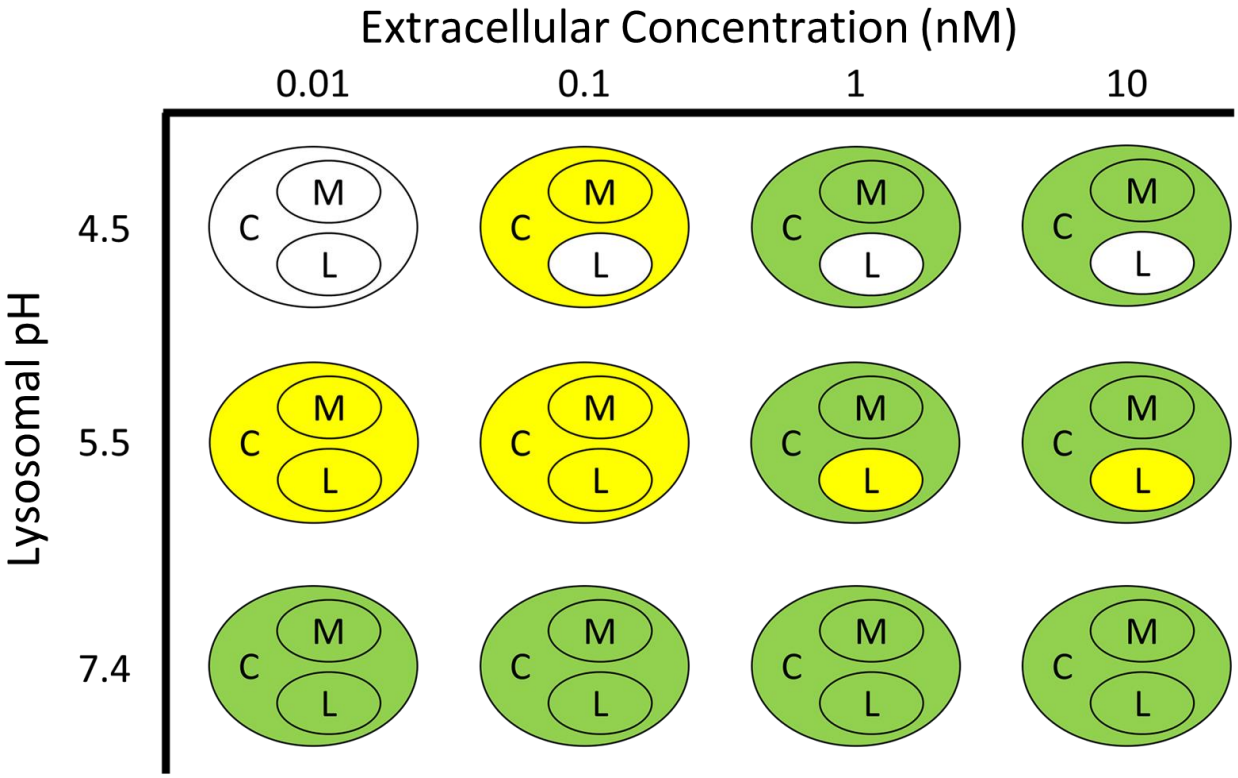

Figure 5.4: CFZ anti-infective potential in the presence of different extracellular concentrations (columns) and virus induced lysosomal membrane destabilization conditions affecting pH homeostasis (rows). Cytosolic (C), mitochondrial (M), and lysosomal (L) compartments were evaluated for COVID-19 anti-infective potential. Clear compartments represent predicted CFZ concentrations at least 1.5-fold below the MIC for COVID-19; yellow represents predicted CFZ concentrations within 1.5-fold of the MIC; and green represents predicted CFZ concentrations at least 1.5-fold above the MIC for COVID-19.

When an uninfected cell with an unperturbed lysosomal environment (lysosomal pH = 4.5) is in the presence of low extracellular concentrations of CFZ, there is a low likelihood of intracellular COVID-19 elimination. Following infection with virus, the extent of CLDI activation increases (by a virus-induced increase in lysosomal pH) or by an increase in the local extracellular concentration. Under these conditions, the likelihood of CFZ concentrations exceeding the COVID-19 MIC in various subcellular organelles continues to increase. Upon complete disruption of the lysosome, say, accompanying the death of the macrophage, cellular concentrations of CFZ exceed the MIC independent of the extracellular concentration. This

implies that even in the absence of circulating drug, or long after the last dose of drug has been administered, viral induced cell death of a pre-loaded macrophage has the potential to generate CFZ concentrations that suffice to eliminate a local infection.

This stimulus responsive property was then evaluated against many other infectious pathogens. According to the simulation results, CFZ could be efficacious by directly inhibiting the proliferations and transmission of a large variety of pathogens, by interfering with cellular host protein functions that are necessary for pathogenicity, or by directly interfering with macrophage viability by endowing these cells with a cyto-suicidal, self-defense mechanism (Table 5.3).

Table 5.3: Lysosomal pH dependent inhibition of molecular targets by CFZ Infectious targets and endogenous targets are inhibited by CFZ to varying degrees with lysosomal destabilization [15, 67-81]. At each lysosomal pH the corresponding molecular target is influenced by CFZ (+), uninfluenced (-), or potentially influenced (+/-) based on the model predicted cytosolic CFZ concentrations at 0.1 nM fixed extracellular concentration. Additionally, cellular interference at high fraction unbound (fu) or high local concentrations was evaluated by assuming a local extracellular concentration of 10 nM. [15, 64, 67-81]

Molecular Target	MIC/EC_{50} (μM)	Ki/Kd (μM)	Cellular Inhibition at Lysosomal pH			Inhibition at High f_u	ref
			pH = 4.5	pH = 5.5	pH = 7.4		
Infectious Targets							
Tuberculosis H(37)Rv	0.25 to 0.51		-	+/-	+	+	67
Tuberculosis MDR-TB	0.25 to 4.05		-	+/-	+	+	67
Non-Tuberculosis Mycobacterum (RGM)	2.28 (<0.066 to 8.44)		+/-	+/-	+/-	+	68,69
Non-Tuberculosis Mycobacterum (SGM)	1.16 (<0.066 to >16.88)		+/-	+/-	+/-	+	68, 69
SARS-CoV-2	0.31		-	+	+	+	64
MERS-CoV	1.48		-	-	+	+	64
Gram Positive Bacterium	1.05 to >67.52		-	-	+/-	+/-	70
Gram Negative Bacterium	> 67.52		-	-	-	-	70
Cryptosporidiosis	0.015		+	+	+	+	71
HepG2 CC_{50}	26.43		-	-	-	-	72
Giardia Lamblia	1.8		-	-	+	+	72
Endogenous Targets							
Kv 1.3 Potassium Channel Inhibition	0.3		-	+	+	+	73
Caspase-3 Activation	21.1#		-	-	-	+	74
PPAR-γ Activation	0.1		+	+	+	+	75
pRABV glycoprotein G	1.7	4.319	-	-	+	+	76
Cathepsin L Inhibition		71	-	-	-	-	77
CYP3A4/5 Inhibition		0.000786	+	+	+	+	78
CYP2C8 Inhibition		0.00372	+	+	+	+	78
CYP2D6 Inhibition		0.00246	+	+	+	+	78
hRKIP Activation		106*	-	-	+/-	+/-	79
Cell Death							
Macrophage (RAW 264.7)	10		-	-	-	+	15
Multiple Myeloma	9.8 (+/- 0.7)		-	-	-	+	80
Chronic Lymphocytic Leukemia	1.0^		-	-	+	+	81

**Activity shown at 3.2 μM*
#Apoptosis was observed at 21.1 μM concentration, however, the minimal concentration to induce apoptosis may be lower
^In combination with doxazosin, igmesine, or a B-RAF kinase inhibitor, the addition of CFZ initiated apoptosis

In the clinic, CFZ is now being tested as a treatment for several infectious diseases including multidrug resistant tuberculosis and nontuberculous mycobacterial infections. CLDI activation could also allow local concentrations of CFZ to supersaturate and increase beyond the

MIC of most tuberculosis and non-tuberculosis mycobacterium, SARS-CoV-2, MERS-CoV, giardia lamblia, and Rabies virus. CFZ also exhibits good *in vitro* activity against most Gram-positive bacteria species with minimum inhibitory concentrations (MICs) in range 0.5-2 mg/L [82], although Gram-negative bacteria are uniformly resistant to CFZ [64, 82, 83].

CFZ sequestered as CLDIs, in healthy lysosomal microenvironments, is unable to induce apoptosis in macrophage cells [15]. However, high concentrations of CFZ in the free base form, can activate caspase-3, leading to apoptosis [74]. As a result, with increasing CLDI activation, an increased likelihood of cell death is expected. Nevertheless, a CFZ induced (or pathogen induced) cytotoxic chain reaction is mostly expected in granulomas where macrophages are clustered together and loaded with CLDIs and infectious microorganisms, which could translate to improved likelihood of pathogen dependent anti-infective activity.

Indeed, site specific CFZ accumulation has shown to be most pronounced in granulomas [43]. As granulomas can form at sites of infection, a significant bystander effect is expected at these locations. Activation of the mechanopharmaceutical device in one macrophage can facilitate activation in the surrounding cells through local increases in extracellular concentrations. Based on our VCell simulations, granulomas could support a feed-forward, chain reaction mechanism whereby the released CFZ from one cell would likely destabilize the neighboring CLDI-loaded macrophages, interfering with the lysosomal ion homeostasis and thus giving rise to high local concentrations of free drug (Figure 5.5) [43]. In mice, ablating macrophages with liposomal clodronate inhibits CLDI formation and does not lead to any overt toxicity [43]. Nevertheless, when mice are loaded with CFZ prior to liposomal clodronate injection, CLDIs can be activated by liposomal clodronate, leading to a highly toxic reaction.

In a healthy pre-loaded cell (Figure 5.5A), both CFZ and $CFZH^+$ are initially in equilibrium at the normal lysosomal pH (pH of 4.5). Local activation of the lysosome results in increased solubilization of CLDIs, higher concentrations of free base, and faster flux across the lysosomal membrane (Figure 5.5B). This increase in soluble CFZ leads to the inhibition of targets mediating pathogen replication, assembly, and egress. As a result, an increase in pH brings about localized anti-infective activity. Upon further activation, through membrane penetration, or complete disruption of lysosomal acidification machinery, local freely soluble CFZ concentrations continue to increase (Figure 5.5C). Under complete destabilization, the lysosomal pH approximates 7.4, matching the neutral internal pH of the cytoplasm. As the lysosomal membrane breaks down, complete disruption of the conditions required for CLDI stability would lead to a bolus of soluble CFZ spreading to neighboring cells (Figure 5.5D).

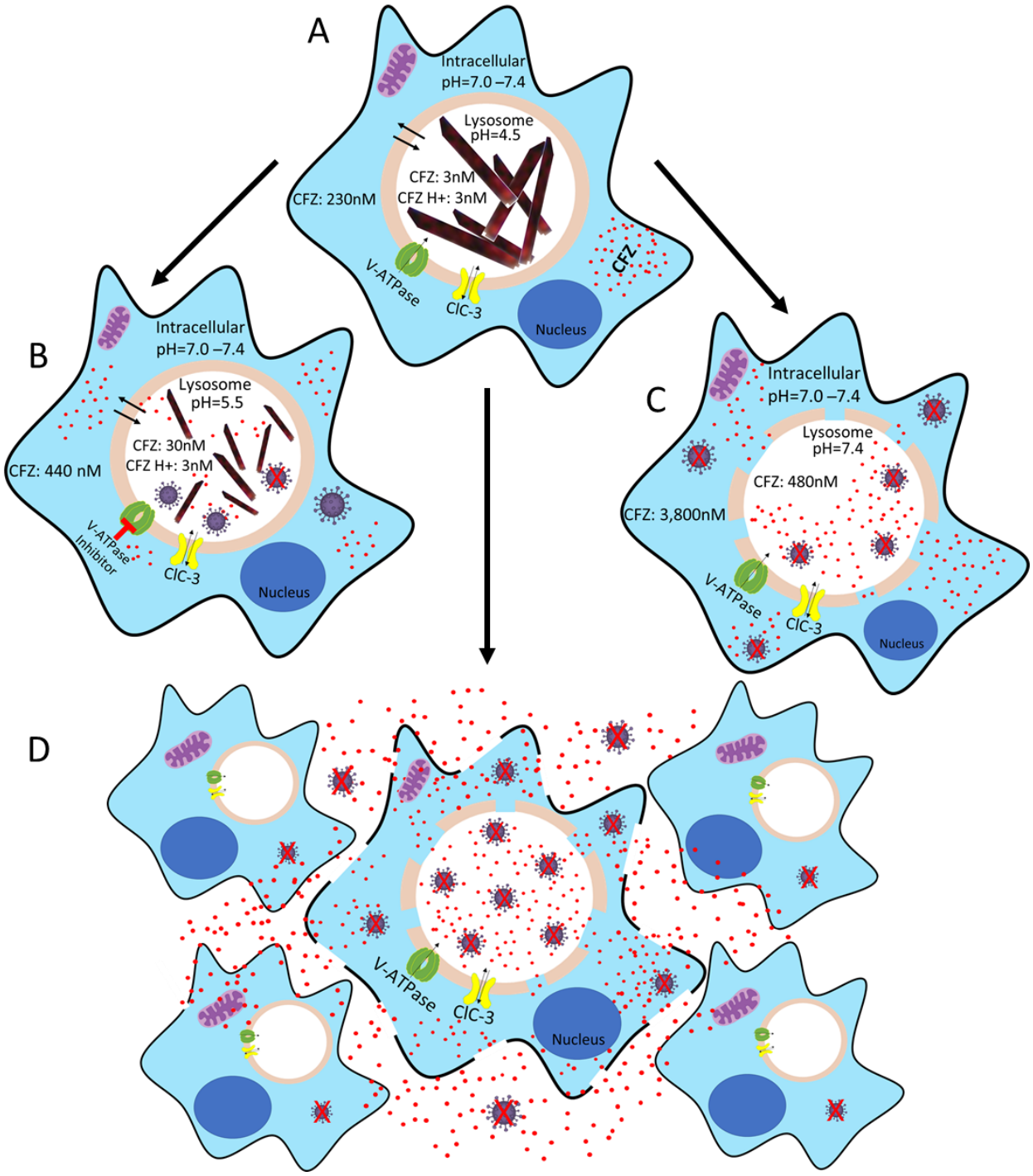

Figure 5.5: Disruption of lysosomal acidification machinery can lead to different levels of CLDI activation and anti-infective response. Model predicted CFZ concentrations in the lysosome and cytoplasm are reported alongside the hypothesized mechanisms of CLDI destabilization. A) Oral administration of CFZ achieves stable CLDI loading in a healthy cell. CFZ and CFZH+ are initially in equilibrium and lysosomal pH is 4.5. B) Local CLDI activation in lysosomes (following an increase in pH to 5.5) inhibits targets mediating pathogen replication, assembly, and egress within the cell. C) Increasing lysosomal pH to 7.4 in the presence of low to moderate CFZ loads leads to activation that suffices to inhibit cellular proteins involved in pathogen replication, assembly, and egress. D) In the presence of

a large CLDI load, complete activation induces cell death and then acts to inhibit viral and host mechanisms of neighboring cells.

5.4.4 Pre-Exposure Prophylaxis in at Risk Populations

With the stimulus responsive activation of CFZ, a new therapeutic strategy for pandemic prevention could be feasible and warrants exploration. Self-assembling drug depots with targeted and powerful anti-infective potential could allow for the development of broad-spectrum, pre-exposure prophylaxis regimens. The concept of pre-exposure prophylaxis for infectious pathogens has been adopted for HIV [84, 85] as well as considered for SARS-CoV-2 [86, 87]. While pre-exposure prophylaxis has been shown to be efficacious, patients are also exposed to relatively high levels of circulating drug, making long-term usage of prophylactic regimens potentially hazardous. As evident in the low toxicity of CFZ, the biocompatibility of CLDIs makes cytoplasmic construction of mechanopharmaceutical devices a clinically feasible prophylactic option. Accordingly, testing cytoplasmic construction as a prophylactic approach requires a completely different strategy from the short, post-infection treatment regimens that are being tested in clinical trials, as was recently the case with cryptosporidiosis [88]. If CFZ is to form a pathogen-activatable intracellular drug depot, pre-loading healthy individuals with the drug prior to infection is essential for the drug to accumulate in the macrophages and self-assemble into CLDIs. As an emerging field of study, careful experimental design and in-depth mechanistic analysis would be essential for understanding conditions governing the trigger mechanisms leading activatable drug release [89].

5.5 Properties of Self-Assembling Molecules

While CFZ is an inspiring drug, it cannot be expected to be a panacea to protect humanity against all pathogens. For this stimulus responsive self-assembling treatment approach to become, and remain viable, additional molecular entities should provide alternative starting points for mechanopharmaceutical device design and lead development efforts. Although the vast majority of small molecule drugs in clinical use are weak bases, CFZ is the only weakly basic drug which is known to accumulate and self-assemble as hydrochloride biocrystals in macrophages of mice and humans. Although lysosomotropic property of CFZ is common to weak base compounds, the extent of drug accumulation in lysosomes could vary significantly even for molecules with similar properties, such as pK_a, logP, and intrinsic free base solubility [90]. For many drugs, lysosomal accumulation is associated with toxic effects, such as perturbation of lysosomal ion homeostasis. These effects include increasing lysosomal pH, increasing the lysosomal size, and permeabilizing the lysosomal membrane [82, 90-93]. In the case of hydrophobic weak bases like amiodarone, carvedilol, and desipramine [94-96], the estimated degree of supersaturation of the salt form of the drugs in the lysosomal environment would be 1 to 12 orders of magnitudes lower than that of $CFZH^+Cl^-$, which would decrease the propensity of these other drugs to precipitate out and self-assemble.

Thus, amongst FDA-approved weakly basic drugs [94-96], CFZ is unique because of its extremely low solubility in the lysosomal microenvironment. Nevertheless, there may well be many other different *in vivo* self-assembling molecular entities that could serve as drug candidates and are awaiting discovery as molecular building blocks for cytoplasmic construction. In terms of alternative mechanisms that do not necessarily involve a lysosomal ion trapping and

precipitation pathway, the anomalous pharmacokinetics of anacetrapib exhibits the kind of behavior that would be expected from a soluble-to-insoluble phase transition phenomenon.

5.6 Conclusions

There are many cognate research areas that are relevant to cytoplasmic construction. For example, it may be feasible to identify functional supramolecular structures in high throughput screening experiments of biased libraries of small molecule chemical agents that are selected based on their putative ability to undergo soluble-to-insoluble phase transitions in the microenvironmental conditions of specific organelles. Alternatively, the *de novo* computational design of functional supramolecular structures that can self-assemble from certain classes of building blocks may yield promising drug candidates. Additionally, new computational modeling approaches within the realm of pharmacokinetics, cheminformatics, crystal engineering, and molecular dynamics simulations could all be relevant to advance cytoplasmic construction as a scientific and bioengineering field. Furthermore, biointerface science, including the design of specific proteins that bind to and interact with an intracellular mechanopharmaceutical device to transmit mechanical, optical, electrical, and other signals between the mechanopharmaceutical device and various cellular components is yet another relevant research area that has yet to be explored. Thus, cytoplasmic construction offers plenty of research opportunities in terms of exploring the self-assembly and interactions of intracellular mechanopharmaceutical devices with the natural components of cells.

The extraordinary transport properties of CFZ already allow this broad-spectrum anti-infective agent to accumulate as inert precipitates within macrophage lysosomes in a manner that warrants further clinical testing as the first, broad spectrum biodefense approach to pandemic

protection. Certainly, the stimulus responsive nature of CLDIs lends itself to the exploration of a new paradigm for anti-infective drug development. Self-assembling mechanopharmaceutical devices could be used to confer pre-exposure prophylaxis in the setting of high-risk transmission of pandemic level pathogens, such as hospitals or nursing homes. CLDIs and other mechanopharmaceutical devices are certainly worthy of further exploration as stimulus responsive intracellular drug depots.

5.7 References

1. Epelman S, Lavine KJ, Randolph GJ. Origin and functions of tissue macrophages. Immunity. 2014;41(1):21-35.
2. Zheng N, Tsai HN, Zhang X, Rosania GR. The subcellular distribution of small molecules: from pharmacokinetics to synthetic biology. Mol Pharm. 2011;8(5):1619-28.
3. Keswani RK, Yoon GS, Sud S, Stringer KA, Rosania GR. A far-red fluorescent probe for flow cytometry and image-based functional studies of xenobiotic sequestering macrophages. Cytometry A. 2015;87(9):855-67.
4. Rzeczycki P, Yoon GS, Keswani RK, Sud S, Stringer KA, Rosania GR. Detecting ordered small molecule drug aggregates in live macrophages: a multi-parameter microscope image data acquisition and analysis strategy. Biomed Opt Express. 2017;8(2):860-72.
5. Fu D, Zhou J, Zhu WS, Manley PW, Wang YK, Hood T, et al. Imaging the intracellular distribution of tyrosine kinase inhibitors in living cells with quantitative hyperspectral stimulated Raman scattering. Nat Chem. 2014;6(7):614-22.
6. Zheng N, Zhang X, Rosania GR. Effect of phospholipidosis on the cellular pharmacokinetics of chloroquine. J Pharmacol Exp Ther. 2011;336(3):661-71.
7. Rzeczycki P, Woldemichael T, Willmer A, Murashov MD, Baik J, Keswani R, et al. An Expandable Mechanopharmaceutical Device (1): Measuring the Cargo Capacity of Macrophages in a Living Organism. Pharm Res. 2018;36(1):12.
8. Min KA, Rajeswaran WG, Oldenbourg R, Harris G, Keswani RK, Chiang M, et al. Massive Bioaccumulation and Self-Assembly of Phenazine Compounds in Live Cells. Adv Sci (Weinh). 2015;2(8).
9. Brunaugh AD, Walz A, Warnken Z, Pearce C, Munoz Gutierrez J, Koleng JJ, et al. Respirable Clofazimine Particles Produced by Air Jet Milling Technique Are Efficacious in Treatment of BALB/c Mice with Chronic Mycobacterium tuberculosis Infection. Antimicrob Agents Chemother. 2022;66(9):e0018622.
10. Shedden K, Li Q, Liu F, Chang YT, Rosania GR. Machine vision-assisted analysis of structure-localization relationships in a combinatorial library of prospective bioimaging probes. Cytometry A. 2009;75(6):482-93.
11. Shedden K, Posada MM, Chang YT, Li Q, Rosania G. Prospecting for Live Cell BioImaging Probes With Cheminformatic Assisted Image Arrays (CAIA). Proc IEEE Int Symp Biomed Imaging. 2007:1108-11.
12. Shedden K, Rosania GR. Chemical address tags of fluorescent bioimaging probes. Cytometry A. 2010;77(5):429-38.
13. Horstman EM, Keswani RK, Frey BA, Rzeczycki PM, LaLone V, Bertke JA, et al. Elasticity in Macrophage-Synthesized Biocrystals. Angew Chem Int Ed Engl. 2017;56(7):1815-9.
14. Woldemichael T, Keswani RK, Rzeczycki PM, Murashov MD, LaLone V, Gregorka B, et al. Reverse Engineering the Intracellular Self-Assembly of a Functional Mechanopharmaceutical Device. Sci Rep. 2018;8(1):2934.
15. Yoon GS, Sud S, Keswani RK, Baik J, Standiford TJ, Stringer KA, et al. Phagocytosed Clofazimine Biocrystals Can Modulate Innate Immune Signaling by Inhibiting TNFalpha and Boosting IL-1RA Secretion. Mol Pharm. 2015;12(7):2517-27.

16. Swanson RV, Adamson J, Moodley C, Ngcobo B, Ammerman NC, Dorasamy A, et al. Pharmacokinetics and pharmacodynamics of clofazimine in a mouse model of tuberculosis. Antimicrob Agents Chemother. 2015;59(6):3042-51.
17. Livingstone C. Clofazimine. Tuberculosis.88(2):96–9.
18. Bannigan P. Investigation into the Solid and Solution Properties of Known and Novel Polymorphs of the Antimicrobial Molecule Clofazimine. Crystal Growth & Design.16(12):7240–50.
19. Baik J, Rosania GR. Macrophages sequester clofazimine in an intracellular liquid crystal-like supramolecular organization. PLoS One. 2012;7(10):e47494.
20. Willmer AR, Dunne S, Swanson R, Almeida D, Ammerman NC, Stringer KA, et al. An Adaptive Biosystems Engineering Approach towards Modeling the Soluble-to-Insoluble Phase Transition of Clofazimine. Pharmaceutics. 2021;14(1).
21. Dunne S, Willmer AR, Swanson R, Almeida D, Ammerman NC, Stringer KA, et al. Quantitative Analysis of the Phase Transition Mechanism Underpinning the Systemic Self-Assembly of a Mechanopharmaceutical Device. Pharmaceutics. 2021;14(1).
22. Xiong J, Zhu MX. Regulation of lysosomal ion homeostasis by channels and transporters. Sci China Life Sci. 2016;59(8):777-91.
23. Markovich D. Physiological roles and regulation of mammalian sulfate transporters. Physiol Rev. 2001;81(4):1499-533.
24. Chakraborty K, Leung K, Krishnan Y. High lumenal chloride in the lysosome is critical for lysosome function. Elife. 2017;6.
25. Cooper GM. Lysosomes.: Sinauer Associates, ; 2000.
26. Mindell JA. Lysosomal acidification mechanisms. Annu Rev Physiol. 2012;74:69-86.
27. Luzio JP, Pryor PR, Bright NA. Lysosomes: fusion and function. Nat Rev Mol Cell Biol. 2007;8(8):622-32.
28. Woldemichael T, Rosania GR. The physiological determinants of drug-induced lysosomal stress resistance. PLoS One. 2017;12(11):e0187627.
29. Kumar S, Jain A, Choi SW, da Silva GPD, Allers L, Mudd MH, et al. Mammalian Atg8 proteins and the autophagy factor IRGM control mTOR and TFEB at a regulatory node critical for responses to pathogens. Nat Cell Biol. 2020;22(8):973-85.
30. Giraud-Gatineau A, Coya JM, Maure A, Biton A, Thomson M, Bernard EM, et al. The antibiotic bedaquiline activates host macrophage innate immune resistance to bacterial infection. Elife. 2020;9.
31. Najibi M, Honwad HH, Moreau JA, Becker SM, Irazoqui JE. A Novel Nox/Phox-Cd38-Naadp-Tfeb Axis Important for Macrophage Activation during Bacterial Phagocytosis. Autophagy. 2022;18(1):124-41.
32. Li SS, Zhang M, Wang JH, Yang F, Kang B, Xu JJ, et al. Monitoring the Changes of pH in Lysosomes during Autophagy and Apoptosis by Plasmon Enhanced Raman Imaging. Anal Chem. 2019;91(13):8398-405.
33. Zhitomirsky B, Assaraf YG. Lysosomal sequestration of hydrophobic weak base chemotherapeutics triggers lysosomal biogenesis and lysosome-dependent cancer multidrug resistance. Oncotarget. 2015;6(2):1143-56.
34. Baik J, Stringer KA, Mane G, Rosania GR. Multiscale distribution and bioaccumulation analysis of clofazimine reveals a massive immune system-mediated xenobiotic sequestration response. Antimicrob Agents Chemother. 2013;57(3):1218-30.

35. Murashov MD, LaLone V, Rzeczycki PM, Keswani RK, Yoon GS, Sud S, et al. The Physicochemical Basis of Clofazimine-Induced Skin Pigmentation. J Invest Dermatol. 2018;138(3):697-703.
36. Stachowiak JC, Brodsky FM, Miller EA. A cost-benefit analysis of the physical mechanisms of membrane curvature. Nat Cell Biol. 2013;15(9):1019-27.
37. Vigant F, Santos NC, Lee B. Broad-spectrum antivirals against viral fusion. Nat Rev Microbiol. 2015;13(7):426-37.
38. Movita D, van de Garde MD, Biesta P, Kreefft K, Haagmans B, Zuniga E, et al. Inflammatory monocytes recruited to the liver within 24 hours after virus-induced inflammation resemble Kupffer cells but are functionally distinct. J Virol. 2015;89(9):4809-17.
39. Shi C, Pamer EG. Monocyte recruitment during infection and inflammation. Nat Rev Immunol. 2011;11(11):762-74.
40. Yoon GS, Keswani RK, Sud S, Rzeczycki PM, Murashov MD, Koehn TA, et al. Clofazimine Biocrystal Accumulation in Macrophages Upregulates Interleukin 1 Receptor Antagonist Production To Induce a Systemic Anti-Inflammatory State. Antimicrob Agents Chemother. 2016;60(6):3470-9.
41. Napolitano GB, A. . TFEB at a glance. Journal of Cell Science.
42. Trexel J, Yoon GS, Keswani RK, McHugh C, Yeomans L, Vitvitsky V, et al. Macrophage-Mediated Clofazimine Sequestration Is Accompanied by a Shift in Host Energy Metabolism. J Pharm Sci. 2017;106(4):1162-74.
43. Rzeczycki P, Yoon GS, Keswani RK, Sud S, Baik J, Murashov MD, et al. An Expandable Mechanopharmaceutical Device (2): Drug Induced Granulomas Maximize the Cargo Sequestering Capacity of Macrophages in the Liver. Pharm Res. 2018;36(1):3.
44. Schaad-Lanyi Z, Dieterle W, Dubois JP, Theobald W, Vischer W. Pharmacokinetics of clofazimine in healthy volunteers. Int J Lepr Other Mycobact Dis. 1987;55(1):9-15.
45. Abdelwahab MT, Wasserman S, Brust JCM, Gandhi NR, Meintjes G, Everitt D, et al. Clofazimine pharmacokinetics in patients with TB: dosing implications. J Antimicrob Chemother. 2020;75(11):3269-77.
46. Yawalkar SJ, Vischer W. Lamprene (clofazimine) in leprosy. Basic information. Lepr Rev. 1979;50(2):135-44.
47. Jadhav MV, Sathe AG, Deore SS, Patil PG, Joshi NG. Tissue concentration, systemic distribution and toxicity of clofazimine--an autopsy study. Indian J Pathol Microbiol. 2004;47(2):281-3.
48. Mansfield RE. Tissue concentrations of clofazimine (B663) in man. Am J Trop Med Hyg. 1974;23(6):1116-9.
49. McDougall AC, Horsfall WR, Hede JE, Chaplin AJ. Splenic infarction and tissue accumulation of crystals associated with the use of clofazimine (Lamprene; B663) in the treatment of pyoderma gangrenosum. Br J Dermatol. 1980;102(2):227-30.
50. Jopling WH. Complications of treatment with clofazimine (Lamprene: B663). Lepr Rev. 1976;47(1):1-3.
51. Sandler ED, Ng VL, Hadley WK. Clofazimine crystals in alveolar macrophages from a patient with the acquired immunodeficiency syndrome. Arch Pathol Lab Med. 1992;116(5):541-3.
52. Harbeck RJ, Worthen GS, Lebo TD, Peloquin CA. Clofazimine crystals in the cytoplasm of pulmonary macrophages. Ann Pharmacother. 1999;33(2):250.

53. Chicurel M, Garcia E, Goodsaid F. Modulation of macrophage lysosomal pH by Mycobacterium tuberculosis-derived proteins. Infect Immun. 1988;56(2):479-83.
54. Shaughnessy LM, Hoppe AD, Christensen KA, Swanson JA. Membrane perforations inhibit lysosome fusion by altering pH and calcium in Listeria monocytogenes vacuoles. Cell Microbiol. 2006;8(5):781-92.
55. Sibley LD, Weidner E, Krahenbuhl JL. Phagosome acidification blocked by intracellular Toxoplasma gondii. Nature. 1985;315(6018):416-9.
56. Malet JK, Cossart P, Ribet D. Alteration of epithelial cell lysosomal integrity induced by bacterial cholesterol-dependent cytolysins. Cell Microbiol. 2017;19(4).
57. Blomgran R, Zheng L, Stendahl O. Cathepsin-cleaved Bid promotes apoptosis in human neutrophils via oxidative stress-induced lysosomal membrane permeabilization. J Leukoc Biol. 2007;81(5):1213-23.
58. Laforge M, Limou S, Harper F, Casartelli N, Rodrigues V, Silvestre R, et al. DRAM triggers lysosomal membrane permeabilization and cell death in CD4(+) T cells infected with HIV. PLoS Pathog. 2013;9(5):e1003328.
59. Ghosh S, Dellibovi-Ragheb TA, Kerviel A, Pak E, Qiu Q, Fisher M, et al. beta-Coronaviruses Use Lysosomes for Egress Instead of the Biosynthetic Secretory Pathway. Cell. 2020;183(6):1520-35 e14.
60. Jiao Y, Sun J. Bacterial Manipulation of Autophagic Responses in Infection and Inflammation. Front Immunol. 2019;10:2821.
61. Okahashi N, Nakata M, Kuwata H, Kawabata S. Streptococcus oralis Induces Lysosomal Impairment of Macrophages via Bacterial Hydrogen Peroxide. Infect Immun. 2016;84(7):2042-50.
62. Zhao J, Beyrakhova K, Liu Y, Alvarez CP, Bueler SA, Xu L, et al. Molecular basis for the binding and modulation of V-ATPase by a bacterial effector protein. PLoS Pathog. 2017;13(6):e1006394.
63. Vylkova S, Lorenz MC. Modulation of phagosomal pH by Candida albicans promotes hyphal morphogenesis and requires Stp2p, a regulator of amino acid transport. PLoS Pathog. 2014;10(3):e1003995.
64. Yuan S, Yin X, Meng X, Chan JF, Ye ZW, Riva L, et al. Clofazimine broadly inhibits coronaviruses including SARS-CoV-2. Nature. 2021;593(7859):418-23.
65. Yuan S, Yin X, Meng X, Chan J, Ye ZW, Riva L, et al. Clofazimine is a broad-spectrum coronavirus inhibitor that antagonizes SARS-CoV-2 replication in primary human cell culture and hamsters. Res Sq. 2020.
66. Mirabelli C, Wotring JW, Zhang CJ, McCarty SM, Fursmidt R, Pretto CD, et al. Morphological cell profiling of SARS-CoV-2 infection identifies drug repurposing candidates for COVID-19. Proc Natl Acad Sci U S A. 2021;118(36).
67. Lu Y, Zheng MQ, Wang B, Zhao WJ, Li P, Chu NH, et al. [Activities of clofazimine against Mycobacterium tuberculosis in vitro and in vivo]. Zhonghua Jie He He Hu Xi Za Zhi. 2008;31(10):752-5.
68. Luo J, Yu X, Jiang G, Fu Y, Huo F, Ma Y, et al. In Vitro Activity of Clofazimine against Nontuberculous Mycobacteria Isolated in Beijing, China. Antimicrob Agents Chemother. 2018;62(7).
69. McGuffin SA, Pottinger PS, Harnisch JP. Clofazimine in Nontuberculous Mycobacterial Infections: A Growing Niche. Open Forum Infect Dis. 2017;4(3):ofx147.

70. Van Rensburg CE, Joone GK, O'Sullivan JF, Anderson R. Antimicrobial activities of clofazimine and B669 are mediated by lysophospholipids. Antimicrob Agents Chemother. 1992;36(12):2729-35.
71. Love MS, Beasley FC, Jumani RS, Wright TM, Chatterjee AK, Huston CD, et al. A high-throughput phenotypic screen identifies clofazimine as a potential treatment for cryptosporidiosis. PLoS Negl Trop Dis. 2017;11(2):e0005373.
72. Hennessey KM, Rogiers IC, Shih HW, Hulverson MA, Choi R, McCloskey MC, et al. Screening of the Pathogen Box for inhibitors with dual efficacy against Giardia lamblia and Cryptosporidium parvum. PLoS Negl Trop Dis. 2018;12(8):e0006673.
73. Ren YR, Pan F, Parvez S, Fleig A, Chong CR, Xu J, et al. Clofazimine inhibits human Kv1.3 potassium channel by perturbing calcium oscillation in T lymphocytes. PLoS One. 2008;3(12):e4009.
74. Fukutomi Y, Maeda Y, Makino M. Apoptosis-inducing activity of clofazimine in macrophages. Antimicrob Agents Chemother. 2011;55(9):4000-5.
75. Kumar H, Chattopadhyay S, Das N, Shree S, Patel D, Mohapatra J, et al. Leprosy drug clofazimine activates peroxisome proliferator-activated receptor-gamma and synergizes with imatinib to inhibit chronic myeloid leukemia cells. Haematologica. 2020;105(4):971-86.
76. Wu J, Cao S, Lei S, Liu Q, Li Y, Yu Y, et al. Clofazimine: A Promising Inhibitor of Rabies Virus. Front Pharmacol. 2021;12:598241.
77. Kamboj RC, Raghav N, Mittal A, Khurana S, Sadana R, Singh H. Effects of some antituberculous and anti-leprotic drugs on cathepsins B, H and L. Indian J Clin Biochem. 2003;18(2):39-47.
78. Sangana R, Gu H, Chun DY, Einolf HJ. Evaluation of Clinical Drug Interaction Potential of Clofazimine Using Static and Dynamic Modeling Approaches. Drug Metab Dispos. 2018;46(1):26-32.
79. Guo C, Chang T, Sun T, Wu Z, Dai Y, Yao H, et al. Anti-leprosy drug Clofazimine binds to human Raf1 kinase inhibitory protein and enhances ERK phosphorylation. Acta Biochim Biophys Sin (Shanghai). 2018;50(10):1062-7.
80. Durusu IZ, Husnugil HH, Atas H, Biber A, Gerekci S, Gulec EA, et al. Anti-cancer effect of clofazimine as a single agent and in combination with cisplatin on U266 multiple myeloma cell line. Leuk Res. 2017;55:33-40.
81. Szabo I, Trentin L, Trimarco V, Semenzato G, Leanza L. Biophysical characterization and expression analysis of Kv1.3 potassium channel in primary human leukemic B cells. Cell Physiol Biochem. 2015;37(3):965-78.
82. Arbiser JL, Moschella SL. Clofazimine: a review of its medical uses and mechanisms of action. J Am Acad Dermatol. 1995;32(2 Pt 1):241-7.
83. Cholo MC, Steel HC, Fourie PB, Germishuizen WA, Anderson R. Clofazimine: current status and future prospects. J Antimicrob Chemother. 2012;67(2):290-8.
84. Desai M, Field N, Grant R, McCormack S. Recent advances in pre-exposure prophylaxis for HIV. BMJ. 2017;359:j5011.
85. Spinner CD, Boesecke C, Zink A, Jessen H, Stellbrink HJ, Rockstroh JK, et al. HIV pre-exposure prophylaxis (PrEP): a review of current knowledge of oral systemic HIV PrEP in humans. Infection. 2016;44(2):151-8.

86. Rajasingham R, Bangdiwala AS, Nicol MR, Skipper CP, Pastick KA, Axelrod ML, et al. Hydroxychloroquine as Pre-exposure Prophylaxis for Coronavirus Disease 2019 (COVID-19) in Healthcare Workers: A Randomized Trial. Clin Infect Dis. 2021;72(11):e835-e43.
87. Smit M, Marinosci A, Agoritsas T, Calmy A. Prophylaxis for COVID-19: a systematic review. Clin Microbiol Infect. 2021;27(4):532-7.
88. Iroh Tam P, Arnold SLM, Barrett LK, Chen CR, Conrad TM, Douglas E, et al. Clofazimine for Treatment of Cryptosporidiosis in Human Immunodeficiency Virus Infected Adults: An Experimental Medicine, Randomized, Double-blind, Placebo-controlled Phase 2a Trial. Clin Infect Dis. 2021;73(2):183-91.
89. Hong X, Rzeczycki PM, Keswani RK, Murashov MD, Fan Z, Deng CX, et al. Acoustic tweezing cytometry for mechanical phenotyping of macrophages and mechanopharmaceutical cytotripsy. Sci Rep. 2019;9(1):5702.
90. Oliva B, O'Neill AJ, Miller K, Stubbings W, Chopra I. Anti-staphylococcal activity and mode of action of clofazimine. J Antimicrob Chemother. 2004;53(3):435-40.
91. Padayatchi N, Gopal M, Naidoo R, Werner L, Naidoo K, Master I, et al. Clofazimine in the treatment of extensively drug-resistant tuberculosis with HIV coinfection in South Africa: a retrospective cohort study. J Antimicrob Chemother. 2014;69(11):3103-7.
92. Koot D, Cromarty D. Anticancer efficacy and toxicokinetics of a novel paclitaxel-clofazimine nanoparticulate co-formulation. Drug Deliv Transl Res. 2015;5(3):257-67.
93. Sarracent J, Finlay CM. The action of Clofazimine on the level of lysosomal enzymes of cultured macrophages. Clin Exp Immunol. 1982;48(1):261-7.
94. Avdeef A. Equilibrium solubility measurement of ionizable drugs - Consensus recommendations for improving data quality. 2016;4.
95. Avdeef A. Solubility of sparingly-soluble ionizable drugs. Adv Drug Deliv Rev. 2007;59(7):568-90.
96. Bergstrom CA, Luthman K, Artursson P. Accuracy of calculated pH-dependent aqueous drug solubility. Eur J Pharm Sci. 2004;22(5):387-98.

Chapter 6 Impact of Asplenia on Pharmacokinetics

6.1 Abstract

Massive splenic bioaccumulation of clofazimine (CFZ) under physiologically relevant dosing schemes has been shown to induce immune system disturbances and splenomegaly. As an organ which extensively sequesters CFZ as insoluble drug precipitates, the spleen makes for an alluring system for further exploration. The following details two independent studies aimed at elucidating behavior of the spleen and its impact in drug sequestering phase transitions. Healthy mice were treated with one of six different dosing regimens to assess the impact of increasing drug load on pharmacokinetic behaviors of CFZ. A subgroup of these mice was given surgical splenectomies to assess the differential effects of CFZ on the immune system and pharmacokinetic behaviors of the drug. Under increasing drug loading, the spleen was observed to grow up to six times the size of the control and sequesters over 10% of the total drug in mice. Interestingly, when the spleen was removed prior to administering CFZ, the drug did not redistributed to other xenobiotic sequestering organs, and no adverse symptoms were noted. However, profound cytokine elevations were observed in the serum of asplenic CFZ treated mice, indicating a systemic compensation of both the immune response and pharmacokinetics after exposure to therapeutic drug treatment. These results point to another layer of consideration when dosing CFZ in patients with perturbed immune systems. Further studies should seek the

impact of immune modulation and risk for complications with long term drug dosing in asplenic patients.

6.2 Introduction

Clofazimine (CFZ) is a poorly soluble small molecule drug which precipitates in tissues such as the liver and spleen at therapeutic doses. [1] Following repeated dosing, CFZ is sequestered by tissue-resident macrophages and stored as crystalline deposits within lysosomes. [2-4] Proton pumps and chloride transporters in lysosomes stabilize the precipitation of CFZ as a hydrochloride salt, forming insoluble crystal-like drug inclusions (CLDIs). Soluble CFZ is highly reactive, has a broad spectrum of antimicrobial activity, [5-7], and crystallized CFZ precipitates have been shown to be well-tolerated with few toxicological effects. [8, 9]

CFZ has been shown to influence organ mass and total total body weight. It is well characterized as a catabolic agent, decreasing mouse weight gain despite no difference in food consumption. [10, 11] Additionally, with only eight weeks of CFZ treatment in mice, the size of the spleen has been shown to increase dramatically, likely as a result of increased activity and macrophage recruitment. [4, 12, 13] As a result, the tissue types that see the largest increase in sequestered drug after repeated dosing are the spleen and liver, organs with high numbers of resident macrophages. [12, 14] As the spleen is an important organ in storing CLDIs, further investigation into this process could underscore the mechanism behind sequestering unwanted particulates within our bodies. The dose at which this occurs, and extent of this transition is still largely unknown.

As CFZ undergoes a soluble-to-insoluble phase transition with continuous drug loading, the kinetics and distribution change in a non-linear context-dependent fashion. [15,16] As CFZ is sequestered into resident macrophages, immunological cascades result in large increases in total macrophage populations [13]. Cytokines are a group of inflammatory mediators that mount immune responses to external stimuli. [17] Upon damage or infection, cytokines initiate defense

and repair mechanisms to protect and restore tissue health. [18] The systemic levels of cytokine expression can indicate the prevalence and function of the immune cells that produce these cytokines, such as macrophages. [19,20] Changes in cytokine expression may therefore indicate adaptations of the immune system in response to injury. As an antibiotic, crystalline CFZ exerts anti-inflammatory and immunosuppressive effects when sequestered by macrophages such as increased expression of interleukin-1 receptor antagonist (IL-1RA), in contrast to the inflammatory effects of soluble CFZ by way of cytokines such as tumor necrosis factor alpha (TNF-alpha), caspase, and prostaglandin E2 (PGE2) production. [12, 21,22] The recruitment of macrophages through cytokine signaling leads to an immune driven mechanism of drug distribution and storage within macrophage containing organs.

This ultimately begs the question; what happens during the dosing of a spleen targeting drug to a patient without a spleen? Tens of thousands of splenectomies are conducted within the US annually, potentially exposing a large number of people to drugs that utilizes the spleen as part of its distribution [23]. As such, understanding CFZ disposition in asplenia is warranted. Investigation into the immune system dysfunction resulting from surgical intervention [24-26], splenectomy [27-29], and CFZ [9] may elucidate differences in CFZ distribution among splenectomized patients which are already more susceptible to infection, a therapeutic setting in which CFZ is most commonly used [30].

6.3 Methods

6.3.1 CFZ Dose Escalation and Asplenic Experiments

Two independent studies were conducted in four-week-old male mice (C57BL/6J, Jackson Laboratory, Bar Harbor, ME). Mice were dosed with either CFZ or vehicle feed for a

total of 8 weeks. In study 1, mice randomized into the CFZ treatment groups were given one of 5 different daily drug loads mixed into their feed (Figure 6.1A, B) with five mice in each group. A pilot study tested the weight of the spleen on mice treated for 65 weeks instead of 8, these mice were considered the 'Old' group and only used for the basis of spleen weight and total body weight comparisons.

A

CFZ Dose ID	% CFZ in Chow	CFZ (mg/d)	CFZ (mg/kg/d)	Total CFZ Load (mg)
Vehicle	0%	0	0	0
A	0.0510%	1.53	75.01	85.71
B	0.0276%	0.83	32.23	46.32
C	0.0144%	0.43	17.02	24.14
D	0.0073%	0.22	8.24	12.33
E	0.0030%	0.09	3.34	5.00
Old	0.0276%	0.83	32.23	376.38*

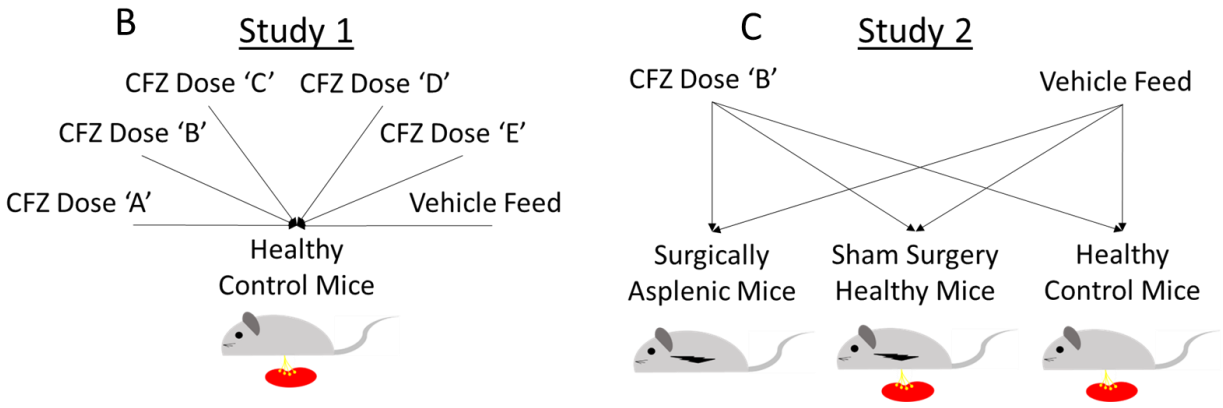

Figure 6.1: Experimental Setup. A) Mice were administered drug through their feed in one of five dosing regimens. CFZ Dose E contains a total daily dose of 3.34 mg/kg/day whereas CFZ Dose A contains 75.01 mg/kg/day. Dosing group 'B' is representative of the physiologically relevant dosing scheme used in humans. The dosing group 'Old' was used as a pilot study to determine splenic effects with long-duration CFZ administration. Groups 'A-E' and 'Vehicle' were treated for 8 weeks, and group 'Old' was treated for 65 weeks. 1. B) Study 1 consists of a dose escalation trial in healthy mice. Five mice were present in each group in study C) Study 2 consists of mice treated with either Dose 'B' or vehicle in healthy mice, healthy surgical sham mice, or surgical splenectomy mice. Eight mice were present in each group in study 2.

** Total drug load at the end of 65 weeks of treatment*

In Study 2, mice were randomized into one of six groups, drug-treated splenectomy, drug-treated sham, drug treated-control, vehicle-treated splenectomy, vehicle-treated sham, or vehicle-treated control (Figure 6.1C), with eight mice per group. Mice that received surgical operations were anesthetized with isoflurane, had the spleen pulled out from the upper left abdominal quadrant, at which point it was either removed (splenectomy group) or returned into the abdominal cavity (sham surgery group). Mice received 5 mg/kg of subcutaneous carprofen daily for 48 hours post-surgery, and a one-time dose of subcutaneous lidocaine 2 mg/kg prior to surgery. The abdominal cavity was closed with interrupted sutures, and the skin was closed with surgical glue. After ten days of postoperative recovery, mice were treated with either CFZ or drug-free vehicle for eight weeks. CFZ was orally administered through milled feed consisting of CFZ dissolved in sesame oil mixed with Powdered Lab Diet 5001, consistent with previously conducted experiments. [12] The drug diet was administered for 8 weeks, after which the mice were sacrificed for tissue collection. Animal care was provided by the University of Michigan's Unit for Laboratory Animal Medicine (ULAM), and the experimental protocol was approved by the Committee on Use and Care of Animals (Protocol PRO00011060).

6.3.2 Sample Preparation and Measurements of CFZ Concentrations

Whole blood, lung, liver, kidney, heart, and spleen were harvested from mice at the end of the 8-week dosing period. Whole blood was acquired from mice at the time of euthanasia by cardiac puncture, allowed to clot for 30 min, then serum was generated by centrifugation. The lung, liver, kidney, and spleen were harvested, rinsed and dried prior to freezing. Organs and serum were flash frozen in liquid nitrogen at the time of acquisition and both organs and serum were stored (-80ºC) until the time of assay. Prior to evaluating immune protein activity, serum

was thawed and 100µL was aliquoted for the measurement of cytokine concentrations. The remainder of the serum was refrozen and stored for concentration analysis. Serum and organ CFZ concentrations were analyzed by liquid chromatography-mass spectrometry (LC-MS), and skin concentrations were analyzed with absorbance spectroscopy. Further details on LC-MS methodology are described in the Appendix D.

6.3.3 Measurement of Cytokine Concentrations in Serum

40 unique cytokines were evaluated in mouse serum samples (Mouse cytokine array panel A, R&D ARY006 kits, Minneapolis, MN) [31]. Serum (100µL) from each mouse was diluted and placed on array membranes and incubated with detection antibodies for 24 hours per the manufacturer's instructions. After incubation, membranes were washed and treated with chemiluminescent reagents for imaging. Pixel density of each cytokine signal was evaluated with an iBright FL1500 imaging system (Invitrogen, Thermo Fisher Scientic, Waltham, MA). Duplicate analyte signals were averaged before subtracting the background signal after which they were normalized to the positive control on each individual membrane. The resulting value is referred to as the relative density and is used to compare relative cytokine concentrations between experimental groups.

6.3.4 Statistical Analysis

Differences in cytokine concentrations were evaluated by ANOVA with Cohen's D test followed by Tukey's post-hoc analysis to account for multiple comparisons. Significance was determined with $p<0.05$. Percent difference and effect size were used to determine the magnitude

of difference between cytokine concentrations of different experimental groups. CFZ concentrations were compared by an upaired Student's t-test to the therapeutically relevant dose 'B'. Organ weights at each dosing regimen were compared by an upaired Student's t-test to the vehicle-treated controls.

6.4 Results

6.4.1 Dose-Dependent Catabolism and Splenomegaly

As an initial benchmark, the total body and spleen weights of CFZ-treated mice were compared across all dosing regimens; the resulting body and organ weights were averaged and compared to those of the vehicle fed control mice.

A

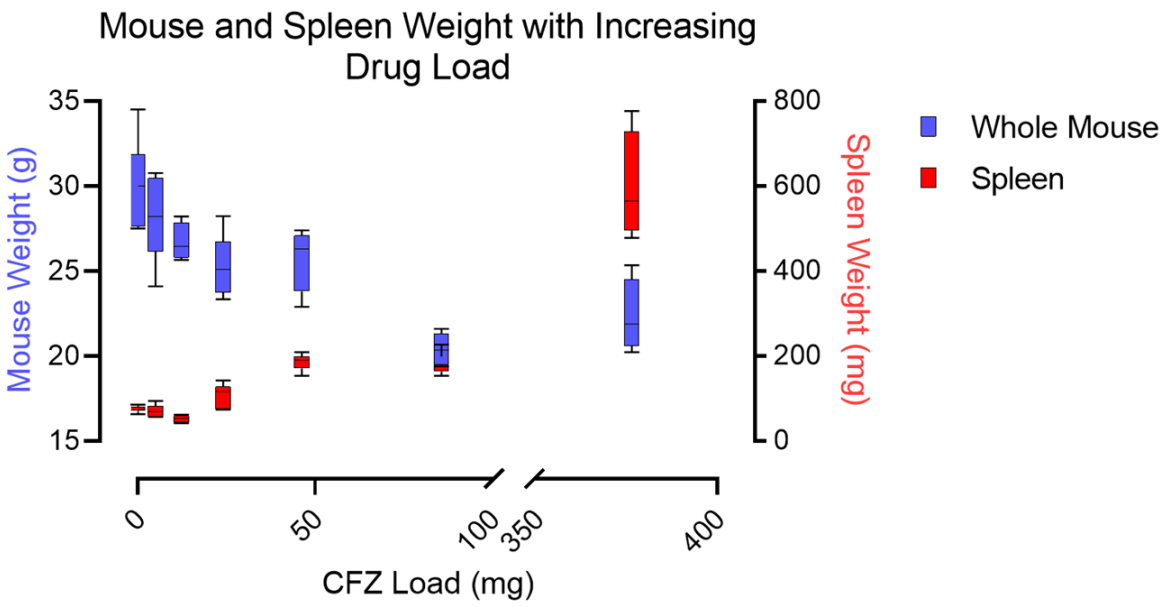

B

Group	Total CFZ Load (mg)	Mouse (g)	P-Value	Spleen (mg)	P-Value
A	85.71	20.41 ± 0.85	2.67E-04	184.58 ± 22.84	5.52E-05
B	46.32	25.67 ± 1.62	1.74E-02	186.1 ± 17.58	6.45E-06
C	24.14	25.32 ± 1.61	1.18E-02	108.12 ± 25.38	3.05E-02
D	12.33	26.72 ± 0.97	4.97E-02	52.22 ± 7.18	4.98E-04
E	5.00	28.08 ± 2.23	3.06E-01	71.05 ± 13.95	6.30E-01
Control	0	29.75 ± 2.63		74.53 ± 6.77	

Figure 6.2: CFZ induced changes in organ mass with increasing drug concentration A) Spleen weight (red) is plotted against total body weight (blue) across increasing drug load. B) Mean (± S.D.) total body weight (g) and spleen weight (mg) in 6 mice per dosing group. P-value was determined by an unpaired Student's t-test using the control group as the comparator.

Catabolic activity of CFZ administration was evident in all measured organ systems except for the spleen in which a profound increase in mass is observed (Figure 6.2). After 8 weeks of dosing, the spleen showed an initial decrease in size from group E to group D, indicating an initial loss in mass due to the catabolic effects of the drug without significant sequestering of CLDIs. Starting at a total load of 24mg, the spleen mass began to increase with drug load up until 42mg, then once again plateaus from 42 to 84 mg. When compared to the

'Old' group treated for 65 weeks, the spleen size increased dramatically once again. Collectively indicating that spleen size and total body weight are modulated by both the total load of drug and duration of administration.

6.4.2 Pharmacokinetic Analysis of CFZ with Increasing Drug Load and Asplenia

Tissue concentrations of drug were measured in serum, lung, liver, kidney, and spleen when applicable. Across increasing drug load, the organ concentrations were measured (Figure 6.3A), and the fraction of total drug administered which was sequestered in each organ was calculated using the mass of the organs (Figure 6.3B).

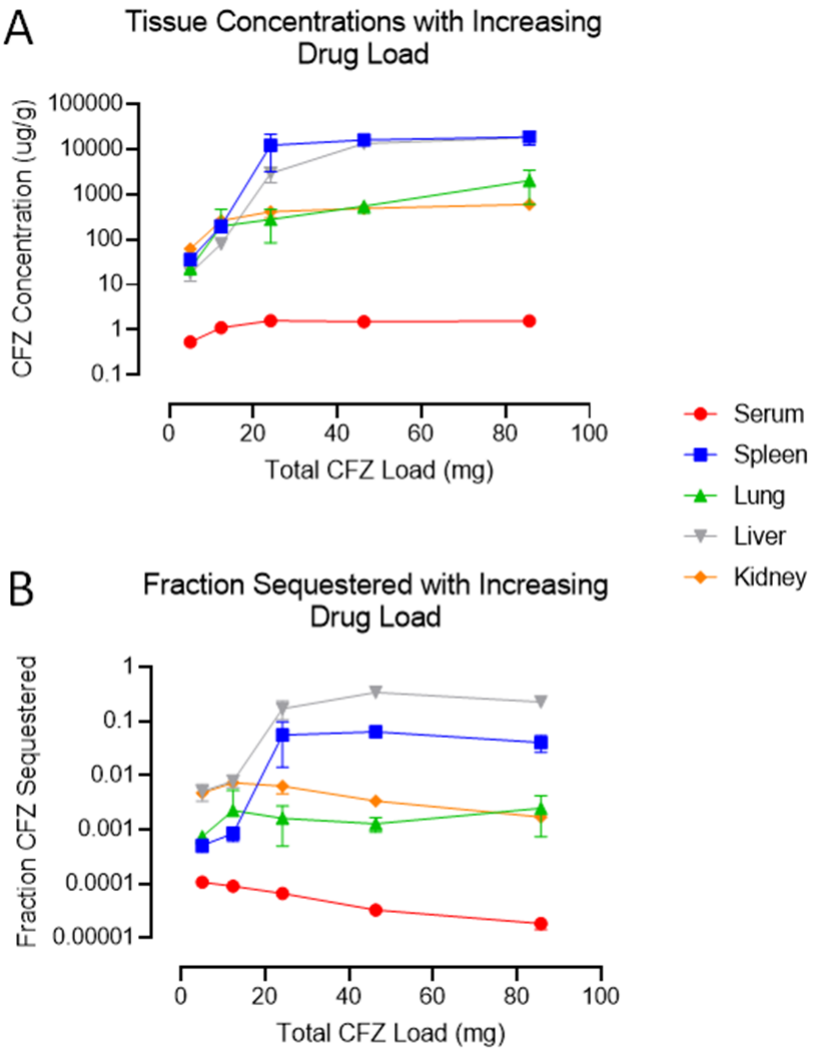

Figure 6.3: CFZ distribution with increasing drug load. A) Concentrations of CFZ in each organ with increasing drug load. B) Fraction of total administered drug sequestered in each organ with increasing drug load. Fraction sequestered was determined by dividing the mass measured in each organ by the total amount of drug administered over the 8-week dosing duration. Circulating serum was estimated to be 1000 µL in volume. N=6 per group

As total CFZ administered increased, measured drug concentration in every organ system also increased. Serum concentrations of CFZ plateaued at 1 µg/mL, consistent with literature values [14]. All solid organ systems continued to sequester increasing concentrations of drug until a total load of 42 mg. From 42 to 84 mg, a plateau was observed in every organ except for

the lungs, which continued to sequester drug. The lung was also the only organ system to continue sequestering increasing quantity of drug with increasing drug load.

The total organ dependent sequestered CFZ mass was then calculated and compared to the physiologically relevant dosing scheme 'B' (Figure 6.4).

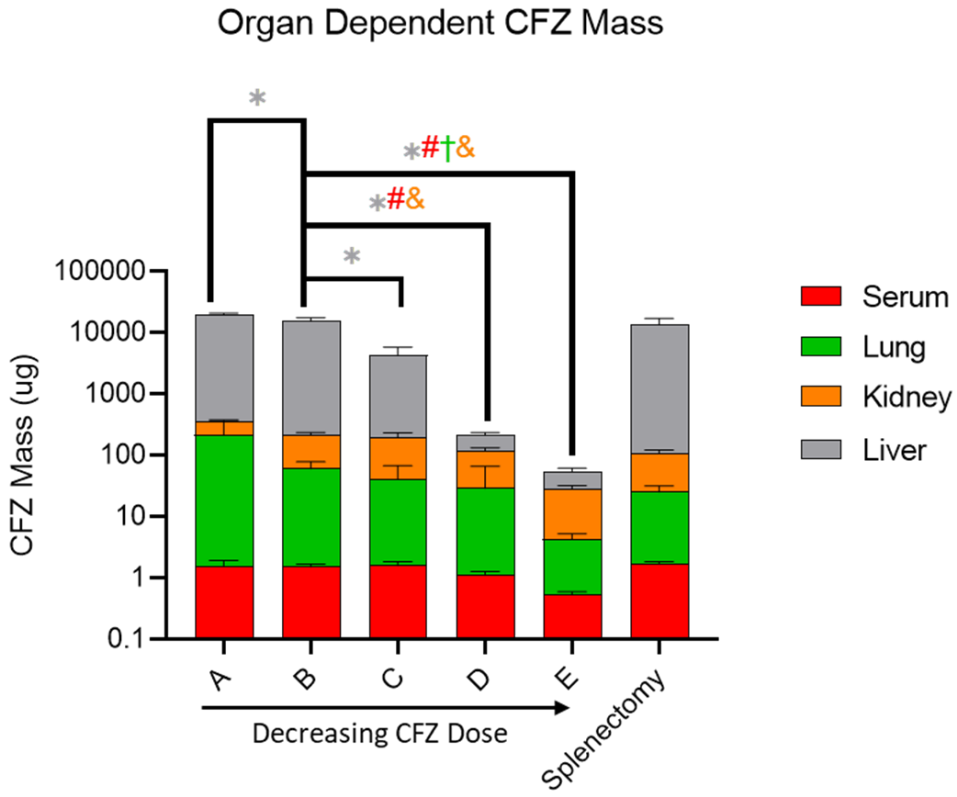

*Figure 6.4: Total CFZ Mass by Organ. Each of the five dosing schemes are represented alongside the splenectomized mice group. As the splenectomy group was compared to sham control, no quantitative comparisons were calculated. Significance was determined with $p<0.05$ by comparison to dosing group B with a different symbol based on the tissue type: #serum, †lung, &kidney, and *liver, N=6 in groups A-E, and N=8 in the splenectomy group.*

The mass of CFZ in the asplenic mice most closely resembled the organ mass in dosing group 'B'. In fact, when compared to the CFZ-treated sham surgery group, there were no significant differences in CFZ concentrations among the asplenic mice (Figure 6.5).

Additionally, absorption measurements in the ear indicated that neither asplenia nor surgical intervention impacted the concentration of CFZ in the skin (Figure D.1).

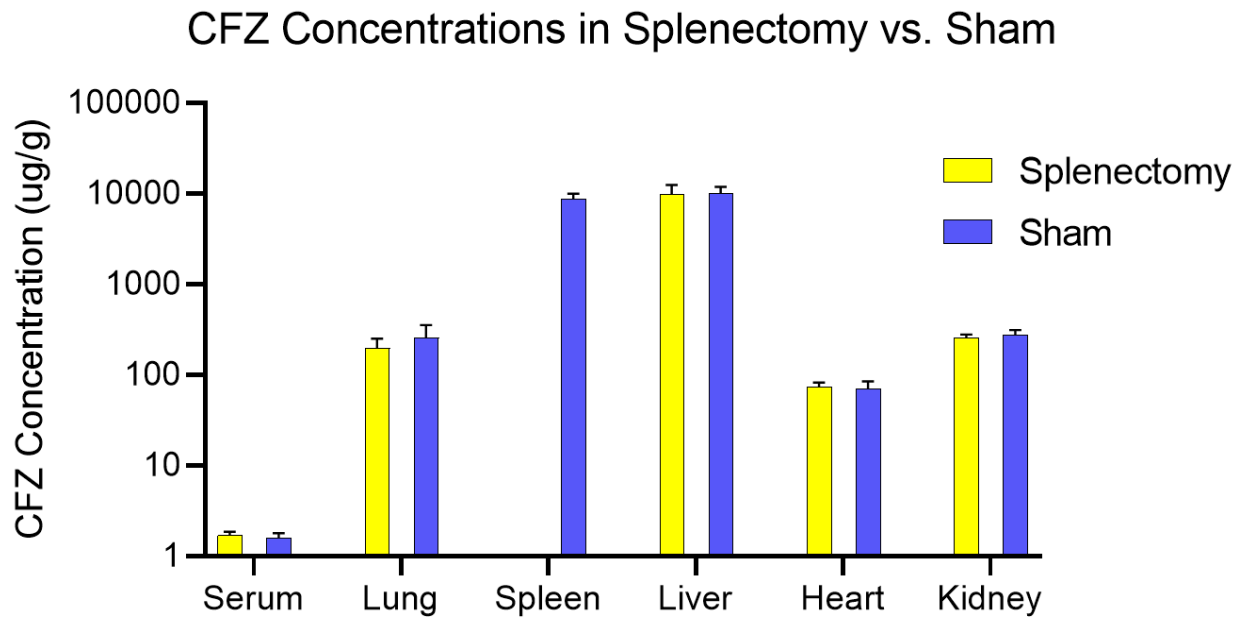

Figure 6.5: CFZ concentrations in organs from mice that underwent splenectomy (yellow) compared to mice that received sham surgery (blue). N=8 per group

It is important to note that a substantial quantity of drug was present in the spleen of the sham group, and despite no such available reservoir of drug in the splenectomy group, none of the other drug sequestering organs had different concentrations compared to the sham group. To assess for signs of redistribution of CFZ mass rather than concentration, relative amounts of sequestered drug were evaluated in the asplenic mice compared to the sham controls (Figure 6.6).

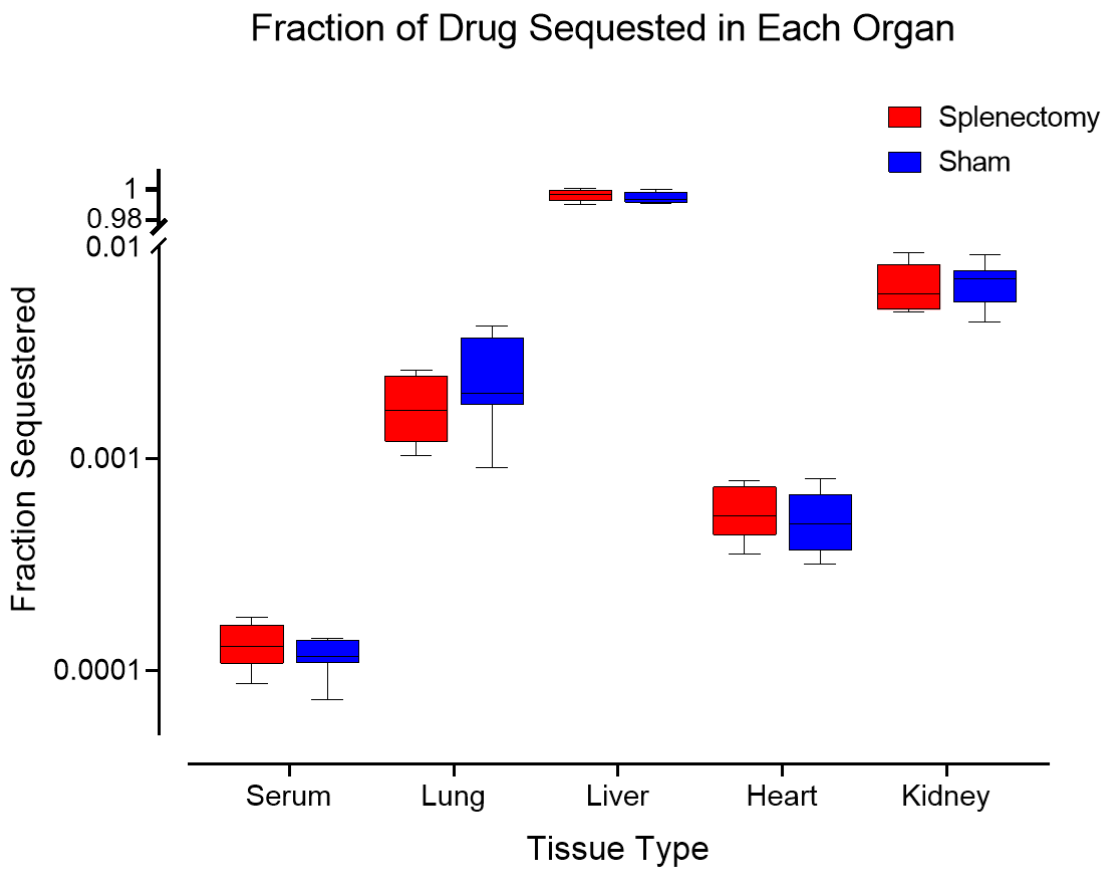

Figure 6.6: Drug sequestration in asplenic mice. The sham CFZ-treated mice (blue) compared to the asplenic CFZ-treated mice (red) show relative amounts of drug sequestered compared to the total amount of drug measured in these five tissue types. Values were calculated by dividing the mass in each tissue type by the sum of the mass sequestered in every organ (except the spleen in the sham group). 10th, 25th, 75th, and 90th percentiles are shown alongside the median values. N=8 per group.

Despite the absence of the spleen, there was no increase in CFZ mass in any of the measured drug sequestering organs in the splenectomy group. Furthermore, there were no differences in organ weights between these two groups indicating there was no difference in CFZ-induced catabolism between the asplenic group and sham surgery group. This implies that there is no significant change in gross metabolic activity in the sham group despite having an overall larger quantity of CFZ sequestered within the mouse in the observed organs. Of important note, in the sham surgery mice, 10.3% of the total CFZ mass in the mouse was

sequestered in the spleen, meaning that the asplenic mice sequestered roughly 10% less total drug amongst the observed organs over the eight week dosing period.

6.4.3 Immunomodulatory Effects of CFZ in Asplenic Mice

Previous work has shown that increasing sequestration of CLDIs results from proliferation of macrophage populations leading to an enlarged total volume to sequester drug [13]. Evaluation of a robust cytokine profile would lend insight to the mechanism of CFZ induced macrophage proliferation and the consequences of CFZ in asplenic mice. Differences in cytokines compared to controls were minimal in surgical intervention (Figure D.2A-B). However CFZ alone showed dramatic increases to tissue inhibitor matrix metalloproteinase 1 (TIMP-1) and IL1-RA (538% and 346% increases, respectively) alongside a modest increase in TNF-alpha (83%) and several other pro- and anti-inflammatory cytokines (Figure D.2C). To determine the relative effect of CFZ in asplenic mice, cytokine levels were compared in CFZ-treated asplenic and CFZ-treated sham surgery mice which were normalized to their respective controls (Figure 6.7).

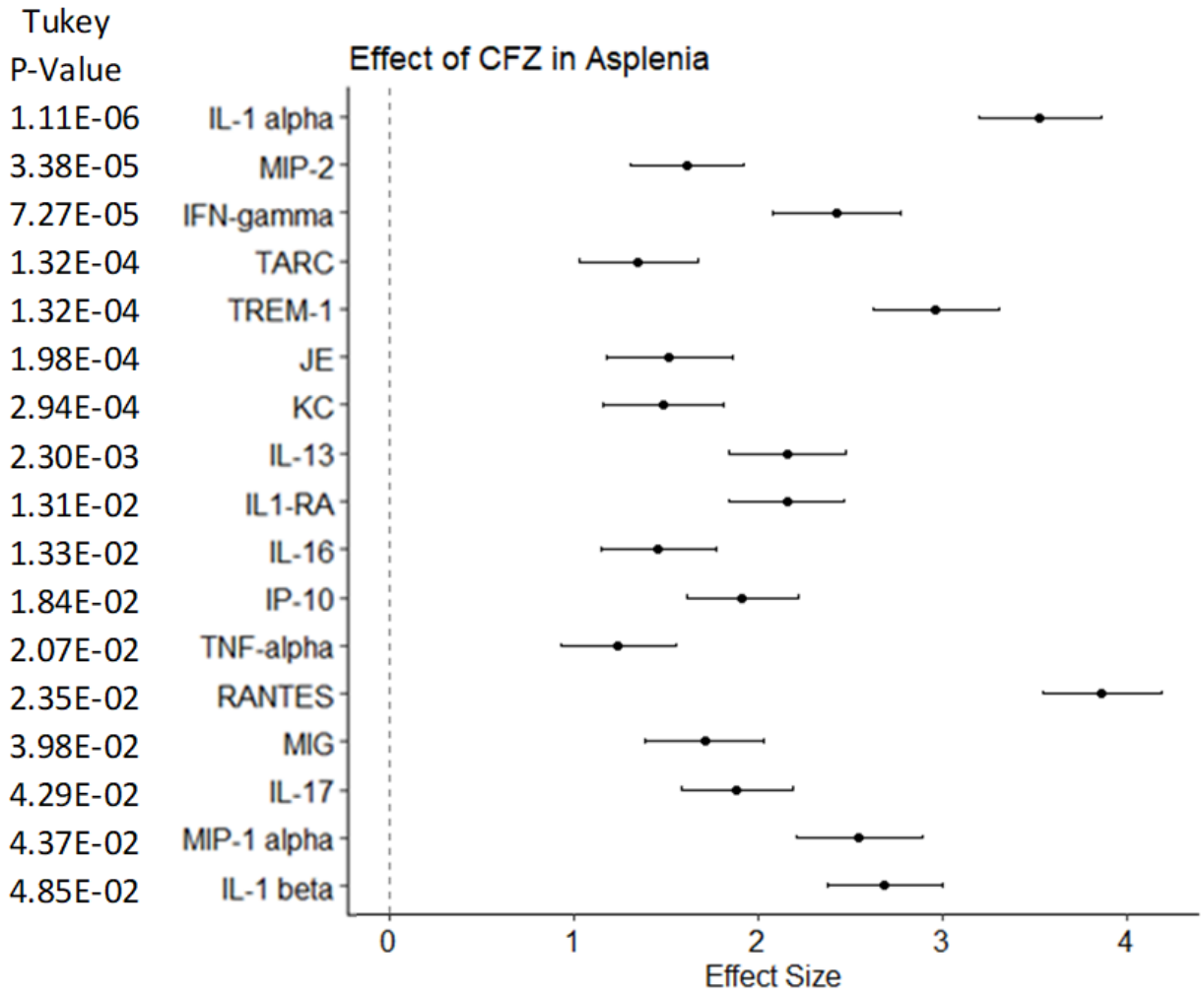

Figure 6.7: Relative density of cytokine measurements between the normalized CFZ-treated splenectomy group and normalized CFZ-treated sham group. Effect size was calculated using Cohen's D. Multiple comparisons were accounted for with Tukey's post-hoc analysis (shown p-values). Effect size > 0 indicates more activity in the splenectomy group, and effect size < 0 indicates more activity in the sham group. N=8 in each comparator group.

Of the evaluated cytokines, 17 of the 40 had a statistically significant difference in expression in the CFZ normalized splenectomy group compared to the CFZ normalized sham. All 17 of these cytokines were expressed at higher levels in the splenectomy group indicating a systemic increase in immune activity. Of particular interest, five of the seven upgregulated cytokines from the CFZ treatment group were magnified in the CFZ treated asplenic group (MIP-2, TREM-1, IL1-RA, IL-16, and TNF-alpha), indicating asplenia further increased the

immune effects seen with CFZ treatment. Additionally, IL-1 alpha, an immune protein important in macrophage recruitment and a marker of macrophage stress [33], had the most significant increase in the asplenic CFZ treated mice. This indicates an increased immune response that impacts macrophage populations implicated in CFZ sequestration and distribution.

6.5 Discussion

Across both a dose-escalation trial and surgical splenectomy trial in CFZ treated mice, profound physiological reactions were noted. Primarily the load-dependent splenomegaly, load-dependent catabolism, and systemic increases in CFZ-induced cytokine activity in control and asplenic mice. Collectively, this paints a complex picture of the systemic modulatory effects of the spleen.

Similar trends were observed in other CFZ pharmacokinetics studies, however absolute values differ for a handful of reasons. The dosing in this study was conducted through daily feed, whereas other studies use gastric lavage or injection in discrete daily intervals, potentially leading to differences in observed distribution patterns. And finally, the mice in the present study were given drug while still developing between 4-6 weeks of age. The maturity of the mice could impact both the developing immune system as well as organ development when compared to previous studies. As such, the organ dependent impacts may look different in adult mice or those with different developmental patterns.

One interesting takeaway from the dose escalation study is the profound increase in lung concentrations from group ‘B’ (the therapeutically relevant dosing scheme) to group ‘A’ (the largest daily dosing regimen). Potentially implicating the lung as the next depot site of CFZ after the spleen and liver have reached sequestered drug capacity. With CFZ used primarily to treat

mycobacterial infections such as leprosy and tuberculosis, lung-targeting formulations and dosing regimens are preferable. Future clinical studies should identify whether larger CFZ dosing regimens remain non-toxic to patients as the largest dose in this study showed a larger increase in lung concentration than any other observed tissue type. Additionally, when compared to studies of similar CFZ loads given over increasing time rather than comparing total drug load given at 8-weeks, similar exponential increases in splenic concentrations are observed [14-16]. This perhaps indicates that splenic drug sequestration is more load-dependent rather than time-dependent. Conversely, liver concentrations were much higher at 8-weeks than at 20-weeks when comparable drug loads were administered [14-16]. This could indicate that the temporal relationship of dosing plays a larger role in the drug sequestration within the liver when compared to the spleen.

All CFZ treated asplenic mice survived the drug treatment, had no additional discernable symptoms, and sequestered equal mass of CFZ in every measured organ compared to the sham treated group. Due to the lack of difference between CFZ sequestration in the absence of one of the largest CFZ depots, the difference in total sequestration must arise from decrease in cellular uptake or unexpected deposition. This leads to the possibility that the spleen does not aid in storing excess CFZ in the body, but rather its presence results in excess accumulation. The spleen acts as a receptacle for cellular cargo, but in its absence, no additional cargo could be stored. This could have implications on drug dosing and tissue retention for accumulating lysosomotropic medications such as chloroquine and amiodarone in asplenic patients [32]. Further research should identify whether this results from increased metabolism, decreased absorption, or increased elimination.

The increased immune protein expression in asplenic CFZ treated mice could have interesting implications. Primarily, the increased effect of CFZ on circulating cytokines could result from a decrease in immune stability granted by the spleen. Previous studies have shown immune dysregulation caused by asplenia and hyposplenia leading to overwhelming post-splenectomy infection, or other immune-mediated pathologies such as celiac disease [34]. With a disrupted immune equilibrium in the case of asplenia, the presence of certain drug treatment, such as CFZ, may have a larger proportional effect on immune signaling.

6.6 Conclusions

The well-studied splenic accumulation of CFZ is largely understood to be caused by an increase in resident macrophage populations. With increasing drug administered, the spleen increases in mass and total drug sequestration despite an observed catabolic effect throughout the other organ systems. This implicates a load dependent effect on CFZ catabolism as well as a load dependent effect in splenomegally. In the absence of a spleen, mice compensate by reducing total sequestration of CFZ and trigger a massive cascade of cytokine activity. The spleen was observed to sequester 10% of the total drug in the body, however this excess drug mass was not redistributed in asplenic mice indicating a compensatory pharmacokinetic phenomenon is present. The profound increase in cytokine activity amongst CFZ treated asplenic mice implicates the spleen as an immunomodulatory organ in drug treatment. This posits another layer of consideration in the prolonged drug treatment of immune targeting drugs in asplenic patients.

6.7 References

1. O'Connor R, O'Sullivan JF, O'Kennedy R. The pharmacology, metabolism, and chemistry of clofazimine. Drug Metab Rev. 1995;27(4):591-614.
2. Keswani RK, Baik J, Yeomans L, Hitzman C, Johnson AM, Pawate AS, et al. Chemical Analysis of Drug Biocrystals: A Role for Counterion Transport Pathways in Intracellular Drug Disposition. Mol Pharm. 2015;12(7):2528-36.
3. Baik J, Rosania GR. Molecular imaging of intracellular drug-membrane aggregate formation. Mol Pharm. 2011;8(5):1742-9.
4. Baik J, Rosania GR. Macrophages sequester clofazimine in an intracellular liquid crystal-like supramolecular organization. PLoS One. 2012;7(10):e47494.
5. Aplin RT, McDougall AC. Identification of crystals of the rimino-phenazine compound B663 (Lamprene: clofazimine) in mouse spleen macrophages by thin layer chromatography and mass spectrum analysis. Experientia. 1975;31(4):468-9.
6. Woldemichael T, Keswani RK, Rzeczycki PM, Murashov MD, LaLone V, Gregorka B, et al. Reverse Engineering the Intracellular Self-Assembly of a Functional Mechanopharmaceutical Device. Sci Rep. 2018;8(1):2934.
7. Willmer AR, Nie J, George De la Rosa MV, Wen W, Dunne S, Rosania GR. Molecular design of a pathogen activated, self-assembling mechanopharmaceutical device. J Control Release. 2022;347:620-31.
8. Costa Queiroz RH, de Souza AM, Sampaio SV, Melchior E, Jr. Biochemical and hematological side effects of clofazimine in leprosy patients. Pharmacol Res. 2002;46(2):191-4.
9. Yoon GS, Keswani RK, Sud S, Rzeczycki PM, Murashov MD, Koehn TA, et al. Clofazimine Biocrystal Accumulation in Macrophages Upregulates Interleukin 1 Receptor Antagonist Production To Induce a Systemic Anti-Inflammatory State. Antimicrob Agents Chemother. 2016;60(6):3470-9.
10. Trexel J, Yoon GS, Keswani RK, McHugh C, Yeomans L, Vitvitsky V, et al. Macrophage-Mediated Clofazimine Sequestration Is Accompanied by a Shift in Host Energy Metabolism. J Pharm Sci. 2017;106(4):1162-74.
11. Degang Y, Akama T, Hara T, Tanigawa K, Ishido Y, Gidoh M, et al. Clofazimine modulates the expression of lipid metabolism proteins in Mycobacterium leprae-infected macrophages. PLoS Negl Trop Dis. 2012;6(12):e1936.
12. Baik J, Stringer KA, Mane G, Rosania GR. Multiscale distribution and bioaccumulation analysis of clofazimine reveals a massive immune system-mediated xenobiotic sequestration response. Antimicrob Agents Chemother. 2013;57(3):1218-30.
13. Rzeczycki P, Woldemichael T, Willmer A, Murashov MD, Baik J, Keswani R, et al. An Expandable Mechanopharmaceutical Device (1): Measuring the Cargo Capacity of Macrophages in a Living Organism. Pharm Res. 2018;36(1):12.
14. Swanson RV, Adamson J, Moodley C, Ngcobo B, Ammerman NC, Dorasamy A, et al. Pharmacokinetics and pharmacodynamics of clofazimine in a mouse model of tuberculosis. Antimicrob Agents Chemother. 2015;59(6):3042-51.
15. Willmer AR, Dunne S, Swanson R, Almeida D, Ammerman NC, Stringer KA, et al. An Adaptive Biosystems Engineering Approach towards Modeling the Soluble-to-Insoluble Phase Transition of Clofazimine. Pharmaceutics. 2021;14(1).

16. Dunne S, Willmer AR, Swanson R, Almeida D, Ammerman NC, Stringer KA, et al. Quantitative Analysis of the Phase Transition Mechanism Underpinning the Systemic Self-Assembly of a Mechanopharmaceutical Device. Pharmaceutics. 2021;14(1).
17. Turner MD, Nedjai B, Hurst T, Pennington DJ. Cytokines and chemokines: At the crossroads of cell signalling and inflammatory disease. Biochim Biophys Acta. 2014;1843(11):2563-82.
18. Chen GY, Nunez G. Sterile inflammation: sensing and reacting to damage. Nat Rev Immunol. 2010;10(12):826-37.
19. Arango Duque G, Descoteaux A. Macrophage cytokines: involvement in immunity and infectious diseases. Front Immunol. 2014;5:491.
20. Conalty ML, Barry VC, Jina A. The antileprosy agent B.663 (Clofazimine) and the reticuloendothelial system. Int J Lepr Other Mycobact Dis. 1971;39(2):479-92.
21. Ren YR, Pan F, Parvez S, Fleig A, Chong CR, Xu J, et al. Clofazimine inhibits human Kv1.3 potassium channel by perturbing calcium oscillation in T lymphocytes. PLoS One. 2008;3(12):e4009.
22. Fukutomi Y, Maeda Y, Makino M. Apoptosis-inducing activity of clofazimine in macrophages. Antimicrob Agents Chemother. 2011;55(9):4000-5.
23. Kristinsson SY, Gridley G, Hoover RN, Check D, Landgren O. Long-term risks after splenectomy among 8,149 cancer-free American veterans: a cohort study with up to 27 years follow-up. Haematologica. 2014;99(2):392-8.
24. Lin E, Calvano SE, Lowry SF. Inflammatory cytokines and cell response in surgery. Surgery. 2000;127(2):117-26.
25. Baigrie RJ, Lamont PM, Kwiatkowski D, Dallman MJ, Morris PJ. Systemic cytokine response after major surgery. Br J Surg. 1992;79(8):757-60.
26. Dabrowska AM, Slotwinski R. The immune response to surgery and infection. Cent Eur J Immunol. 2014;39(4):532-7.
27. Drechsler S, Zipperle J, Rademann P, Jafarmadar M, Klotz A, Bahrami S, et al. Splenectomy modulates early immuno-inflammatory responses to trauma-hemorrhage and protects mice against secondary sepsis. Sci Rep. 2018;8(1):14890.
28. Deriy LV, Beno DW, Uhing MR, Jiyamapa-Serna VA, Kimura RE. Splenectomy ablates endotoxin-induced IFNgamma response in rats. Shock. 2002;17(4):312-5.
29. Moeniralam HS, Bemelman WA, Endert E, Koopmans R, Sauerwein HP, Romijn JA. The decrease in nonsplenic interleukin-6 (IL-6) production after splenectomy indicates the existence of a positive feedback loop of IL-6 production during endotoxemia in dogs. Infect Immun. 1997;65(6):2299-305.
30. Sinwar PD. Overwhelming post splenectomy infection syndrome - review study. Int J Surg. 2014;12(12):1314-6.
31. R&D Systems. Mouse Cytokine Array , Panel A [Available from: https://resources.rndsystems.com/pdfs/datasheets/ary006.pdf.
32. Parks A, Marceau F. Lysosomotropic cationic drugs induce cytostatic and cytotoxic effects: Role of liposolubility and autophagic flux and antagonism by cholesterol ablation. Toxicol Appl Pharmacol. 2016;305:55-65.
33. Malik A, Kanneganti TD. Function and regulation of IL-1alpha in inflammatory diseases and cancer. Immunol Rev. 2018;281(1):124-37.
34. Di Sabatino A, Carsetti R, Corazza GR. Post-splenectomy and hyposplenic states. Lancet. 2011;378(9785):86-97.

Chapter 7 Conclusions

Organs, cells, and proteins of the immune system may impact small molecule pharmacokinetics of clofazimine (CFZ) and many other weakly basic, highly lipophilic drugs. The research consolidated within this thesis points to this important consideration in the study of dosing, distribution, and the variability of half-life and steady state. While the immune system is often thought to interact primarily with biologics and pharmacologically relevant medications, the ubiquitous nature of xenobiotic sequestering macrophages allows for a more nuanced understanding of the pharmacokinetics of weakly basic, small molecule drugs.

To better study the pharmacokinetic impact of drug sequestering phase transitions, clofazimine was used as a prototype drug. The accumulation of CFZ within the lysosomes of macrophages as crystal-like drug inclusions (CLDIs) has been well characterized. This behavior changes the total sequestered load of the drug over time and subsequently the half-life and drug exposure to tissues throughout the body. The adaptive pharmacokinetics driven by ion-trapping, precipitation, and lysosomal targeting of CFZ were evaluated from whole body distribution patterns and single cell computational analysis supported by distribution data in mice. The impact of disrupting this immune equilibrium was subsequently assessed by reducing a large macrophage reservoir by removal of the spleen.

The results from this work show that computational pharmacokinetic techniques may improve predictive accuracy and improve dosing schemes important in reducing drug toxicity. The compensatory immune mechanisms in biological systems point to a complex and fascinating

aspect of drug delivery and distribution which furthers our understanding of the mysteries of immune driven pharmacokinetic phenomena.

7.1 Adaptive Modeling Better Characterizes Clofazimine Pharmacokinetics

Adaptive compartmental analysis was conducted with pharmacometrics software, utilizing mice spleen and serum concentrations to evaluate discrepancies in soluble and insoluble CFZ distribution. By evaluating the organism-wide pharmacokinetics of CFZ using whole organ tissue concentrations macro scale distribution patterns can be predicted.

Through the construction and evaluation of many compartmental pharmacometrics models utilizing tissue concentrations in mice, CFZ pharmacokinetics was better characterized by incorporating adaptive functions into computational models when compared to established, non-adaptive structural models. Allowing the volume of distribution and half-life to increase over the course of dosing more accurately predicted concentration profiles in the spleen and serum and provided insight into the rate and extent of drug distribution in healthy and tuberculosis infected mice.

With daily drug loading, fractional drug sequestration in the spleen compared to the serum points to separate insoluble and soluble steady states of CFZ. The difference in rate and extent of drug distribution between tissues and serum inherently calls into question whether therapeutic drug monitoring of serum samples accurately represents tissue concentrations. This necessitates more sophisticated predictive models to ensure drug concentrations are accurately being predicted at the site of action.

With continued drug loading, the presence of tuberculosis infection impacted the distribution profiles of CFZ. In the presence of infection, CFZ was not sequestered as profoundly

in the spleen indicating an underlying mechanism changing the distribution of the drug in tuberculosis infected individuals. This finding may implicate the importance of infection status on the dosing of lysosomal targeting compounds.

7.2 Single Cell Modeling Provides Foundation for Drug Depot Development

CFZ transport was computationally predicted throughout a macrophage using a physiologically informed transcellular kinetic model. Two independent approaches were taken to evaluate cellular drug distribution; accumulation of drug during dosing was predicted by maintaining relevant extracellular concentrations, and the rate and extent of drug elimination was predicted by modeling drug eluting from a CLDI under a variety of expected biological conditions.

Under therapeutic drug dosing regimens, physiochemical properties alone can account for the accumulating propensity of lipophilic, weakly basic chemical compounds. CFZ packs tightly into crystalline structures that allows for a high concentration of drug to exist within the lysosome. Independent of this crystalline formation, the transport and accumulation of clofazimine into the lysosome is a thermodynamically favorable phenomenon. This thermodynamically favorable effect enables the formation of self-assembling drug depots within macrophages, a therapeutic solution that could be explored for use in long term dosing or pre-exposure prophylaxis.

The presence of some intracellular pathogens may influence the equilibrium pH of the lysosome, deacidifying the lysosomal microenvironment. As a result, the cellular kinetics of drug transport may be affected by whether an individual is infected with viruses, bacteria, or fungi. With this in mind, rate and extent of drug elimination from a cellular depot may be impacted by

the presence and type of infection acquired, resulting in increases in drug concentration leaving the cell. This opens up the possibility to utilize cellular drug depots as pre-exposure prophylactic agents to have pathogen-activatable increases in local concentrations.

7.3 Immune System Disruption

The spleen is one of the largest sites of tissue resident macrophages, and subsequently an organ that accumulates large concentrations of macrophage targeting drugs. The impact of drug distribution and immune function was evaluated under multiple unique CFZ dosing regimens and in mice without spleens.

The catabolic effects of CFZ have been documented previously. However, under the dose escalation trial, load-dependent differences in total body and organ catabolic effects were observed, indicating a dose-dependent impact on organ mass. Paradoxically, however, with increasing dose, the organ mass of the spleen continued to increase perhaps due to the relationship between macrophage number and increasing sequestered CFZ mass.

Within increasing drug load, the fraction of drug sequestered in most organs increased up until a certain point, indicating load-dependent variability in pharmacokinetics likely stabilizes at a certain maximum dose, possibly due to biological restrictions in the rate of drug loading. This was not true in the lungs, which continued to sequester an increasing drug load, perhaps compensating for other tissues.

With the removal of a massive macrophage reservoir, the asplenic, CFZ-treated mice were expected to redistribute CFZ or exhibit increased toxicity, however no difference in mass was observed in any of the major macrophage containing organs. As the mice ingested the same quantity of drug, a compensatory mechanism in the distribution of CFZ was expected in mice

without a spleen. However, this and no difference in catabolic effects or organ weights were observed. There was though, a profound increase in the serum concentration of a number of cytokines indicating an interplay between immune protein expression and the drug treatment. The enhanced effects of CFZ on cytokine concentrations in asplenia points to an instability in immune function during drug treatment. The relative increase in immune impact warrants more careful consideration and closer monitoring of patients undergoing longitudinal drug treatment in instances of asplenia.

7.4 Future Directions

Much of this work is specific to the drug CFZ as its physicochemical properties make it easy to observe and study both *in-vitro* and *in-vivo.* However, the principles studied in this thesis can be applied to many other weakly basic accumulating molecules such as azithromycin, chloroquine, and amiodarone. Future applications of this modeling framework to other accumulating xenobiotic agents would enhance the external application of this work and increase viability of similar compounds in the drug development process.

With regards to CFZ, the drug itself is currently not used as monotherapy for any of its FDA indications. As such, the impact of drug interactions should be explored in the setting of its context-dependent pharmacokinetics. Lysosomotropic drugs or medications impacting the lysosomal pH may impact the propensity of CFZ to accumulate in macrophages.

Additionally, this work was primarily conducted in mouse models with limited clinical variability. Future research should use human patients to investigate covariate implications such as age, weight, disease status, and medical history in the development of soluble to insoluble

phase transitions. Allometric scaling from the predictive models presented here could provide insight into new human dosing regimens that could reduce the impact of adverse drug effects.

With respect to the pathogen-activatable drug depot, the current modeling is based upon many *in-vitro* tests and mice models. Further testing should be conducted to validate the hypothesis of CFZ as an activatable drug eluting depot and identify other small molecule drugs that may have similar behavior combined with therapeutic potential.

And finally, with the unexpected results in our asplenic experiments, further studies need to be conducted to determine the pharmacokinetics in asplenia. The elimination phase and absorption data of CFZ treatment in asplenia may help take strides toward elucidating the discrepancies in drug distribution. The exploration of immune cell recruitment and metabolic differences in asplenia may help generalize treatment to asplenic patients taking macrophage targeting drugs.

Appendices

Appendix A: Supplemental Materials for Chapter 2

Supplemental Table A.1: Soluble Phase Models

Model	Model Description	Differential Equations
1a	1 - Compartment Serum Only	DADT(1) = - K*A(1))
1b	1 - Compartment Peripheral Only	DADT(1) = - K*A(1))
2a	2 - Compartment Unidirectional (C1 Elimination)	DADT(1) = - (K1*A(1) + K12*A(1)) DADT(2) = K12*A(1)
2b	2 - Compartment Unidirectional (C2 Elimination)	DADT(1) = - K1*A(1) DADT(2) = K12*A(1) - K12*A(2)
3a	2 - Compartment Bidirectional (C1 Elimination)	DADT(1) = (K21*A(2)) - (K12*A(1) + K*A(1)) DADT(2) = K12*A(1) – (K21*A(2))
3b	2 - Compartment Bidirectional (C2 Elimination)	DADT(1) = (K21*A(2)) - (K12*A(1)) DADT(2) = K12*A(1) – (K21*A(2) + K*A(2))
4	2 - Compartment Bidirectional (C1 & C2 Elimination)	DADT(1) = (K21*A(2)) - (K12*A(1) + K*A(1)) DADT(2) = K12*A(1) – (K21*A(2) + K*A(2))
5a	2 - Compartment Split Administration (50:50)	DADT(1) = (K21*A(2)) - (K12*A(1) + K*A(1)) DADT(2) = K12*A(1) – (K21*A(2))
5b	2 - Compartment Split Administration (75:25)	DADT(1) = (K21*A(2)) - (K12*A(1) + K*A(1)) DADT(2) = K12*A(1) – (K21*A(2))
5c	2 - Compartment Split Administration (25:75)	DADT(1) = (K21*A(2)) - (K12*A(1) + K*A(1)) DADT(2) = K12*A(1) – (K21*A(2))
6	3 - Compartment (C1 Elimination)	DADT(1) = (K21*A(2)) - (K12*A(1) + K*A(1)) DADT(2) = (K12*A(1) + K32*A(3)) – (K21*A(2) + K23*A(2)) DADT(3) = (K23*A(2)) – (K32*A(3))

A.1 Compartmental Modeling of Soluble CFZ Pharmacokinetics Prior to the Formation of Precipitates Traditional Compartmental Modeling in the Soluble Phase

Compartmental Modeling of Soluble CFZ Pharmacokinetics Prior to the Formation of Precipitates Traditional Compartmental Modeling in the Soluble Phase

Prior to modeling the phase transition, soluble state CFZ concentration data (the first 4 weeks of dosing) was used to determine the pharmacokinetics of CFZ before significant CLDIs are seen in vivo. A soluble model was defined as a compartmental model without an expansion function, intended to model the kinetics of clofazimine prior to significant accumulation of CLDI

precipitates. 11 compartmental models were tested to determine the best fit for the soluble state. The corresponding names and model number are listed in supplemental table A.1. All models were constructed in NONMEM using a multiplicative error model in ADVAN9 with the associated differential equations for each compartment listed in table A.1. Each soluble phase model was evaluated on the basis of objective function and visual predictive accuracy (supplemental table A.2). Model 1a and 1b did not contain the entire dataset and were not considered for the full phase transition model. The remaining nine models were similar in fit and OVF values. Model 3a (2-compartment bidirectional model with elimination through compartment 1) was selected for the full phase transition model due to the lowest OVF value and physiologically relevant compartmental structure.

Supplemental Table A.2: Soluble Phase Model Results

Model	OFV	K (day^{-1})	K12 (day^{-1})	K21 (day^{-1})	V1 (L)	V2 (L)	K2 (day^{-1})	K23 (day^{-1})	K32 (day^{-1})
1a	-67.46	0.211	--	--	2.67	--	--	--	--
1b	93.49	0.00129	--	--	--	0.504	--	--	--
2a	53.32	0.189	1.24	--	0.233	0.373	--	--	--
2b	53.52	0.00129	1.23	--	0.305	0.421	--	--	--
3a*	48.42	0.0948	1.23	0.0145	1.26	0.31	--	--	--
3b	49.92	0.00129	1.06	0.01	0.498	0.411	--	--	--
4	49.87	0.00129	1.03	0.0102	0.521	0.409	0.00129	--	--
5a	50.44	0.123	0.061	0.00109	2.02	0.266	--	--	--
5b	49.65	0.00129	0.813	0.0193	1.26	0.416	--	--	--
5c	49.95	0.00129	0.35	0.00401	0.729	0.44	--	--	--
6	54.44	0.664	4.4	0.00142	0.0613	1.09	--	0.667	11.3

Further soluble phase modeling was conducted on model 3a (Table A.2) to supply the full phase transition model with relevant fixed estimates to reduce complexity and improve confidence in the selected model. Soluble models were tested with model 3a (Figure 2.1A) and a parameterized model (Figure 2.1B).

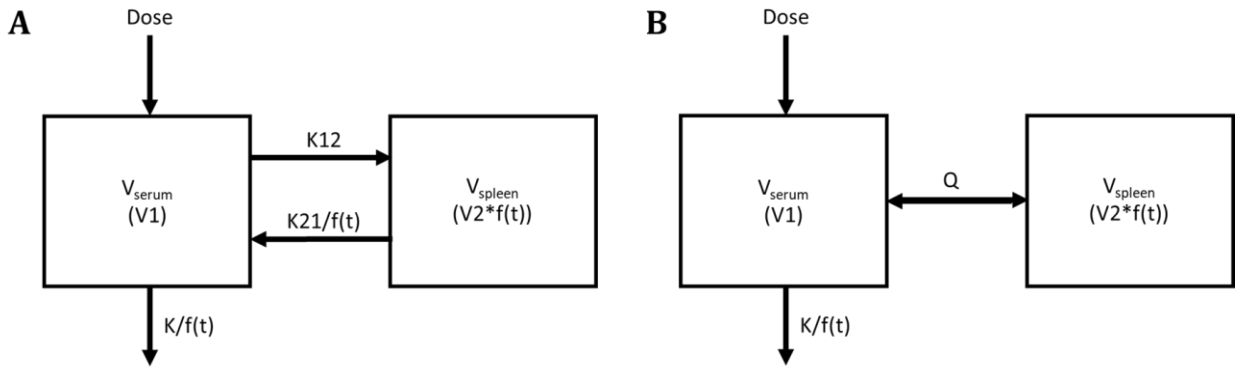

Supplemental Figure A.1: Structural models considered for soluble and phase transition model. A) Unparameterized bidirectional model B) Bidirectional model with parameterized intercompartmental rate constants. For the soluble models, f(t)=1, for the expansion models, f(t) is set to the exponential Hill function.

Four soluble models were constructed using previously published CFZ concentration data in healthy BALB/c mice in the first four weeks of treatment [13]. Soluble model A used the unparameterized structural model (Figure A.1A) with the first 4 weeks of data from the 20 week dosing study [13]. Soluble model B used the unparameterized model with the first 4 weeks of data and single dose concentrations in healthy mice [13]. Soluble model C used the parameterized structural model (Figure A.1B) and the first 4 weeks of data. And finally soluble model D used the parameterized structural model alongside the first 4 weeks of data and single dose concentrations. The resultant parameter estimates from each of the soluble models were used as initial conditions for each of the full phase transition models. The number of fixed parameters were varied to determine the best subset of full models to run a bootstrapping analysis. Soluble model B was determined to be superior to soluble models A, C, and D from resultant AIC, and visual predictive accuracy. Bootstrapping analysis was then conducted on nine full phase transition models from the fixed estimates of soluble model B using the exponential Hill function as the expansion function. From the resulting bootstrap analysis of the

nine full phase transition models, the unparameterized model with fixed V1 and K12 performed the best based on 95% confidence intervals, coefficients of variation, and histogram plot distribution. This model was then used for comparative analysis with different expansion function equations (Table A.1).

A.2 Incremental Compartment Modeling

By incrementally increasing the number of compartments, a peripheral compartment (V3) was added to the base model. The chosen 3-compartment model structure alongside the resulting objective function value, correlation of residuals, and PK parameters are shown in supplemental figure A.1. The 3-compartment model was derived from an established pharmacokinetic model of CFZ. [12] The OFV, R2, and distribution of residuals (supplemental figure A.2) are correlated with an improvement upon the base model when supplied the entire data set, and inferior predictive capacity compared to the adaptive Vd models.

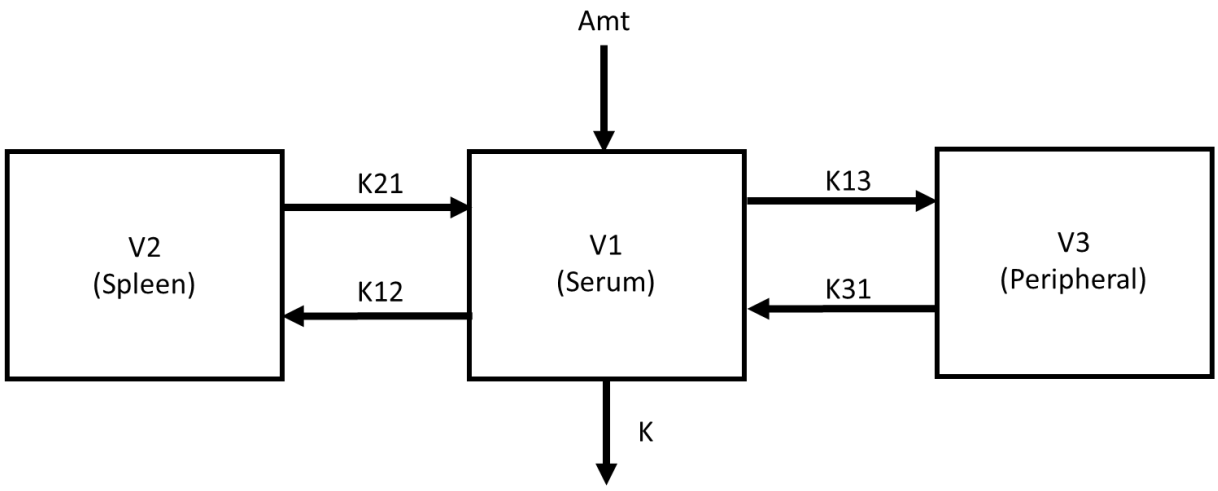

$$DADT(1) = (K21*A(2) + K31*A(3)) - (K12*A(1) + K13*A(1) + K*A(1))$$
$$DADT(2) = (K12*A(1)) - (K21*A(2))$$
$$DADT(3) = K13*A(1) - (K31*A(3))$$

AIC	R^2	K (day^{-1})	^K12 (day^{-1})	K21 (day^{-1})	K31 (day^{-1})	K13 (day^{-1})	^V1 (L)	V2 (L)	V3 (L)
300.8	0.92	0.007 (165.6%)	0.183	0.0225 (0%)	57.8 (164.6%)	603 (157.8%)	2.43	0.00622 (9.9%)	0.56 (0%)

Supplemental Figure A.2: Structural models considered for soluble and phase transition model. A) Unparameterized bidirectional model B) Bidirectional model with parameterized intercompartmental rate constants. For the soluble models, f(t)=1, for the expansion models, f(t) is set to the exponential Hill function. ^Fixed parameter estimates from soluble phase model

Figure A.3. The differential equations for the model and the predicted PK parameters are listed below the diagrammatic view of the 3-compartment model. The parameter estimates are provided alongside the respective coefficients of variation. The OFV of 275.4 and R2 of 0.92combination of AIC, CV% and R2 indicates superiority to the base model, and inferiority to all four adaptive Vd models.

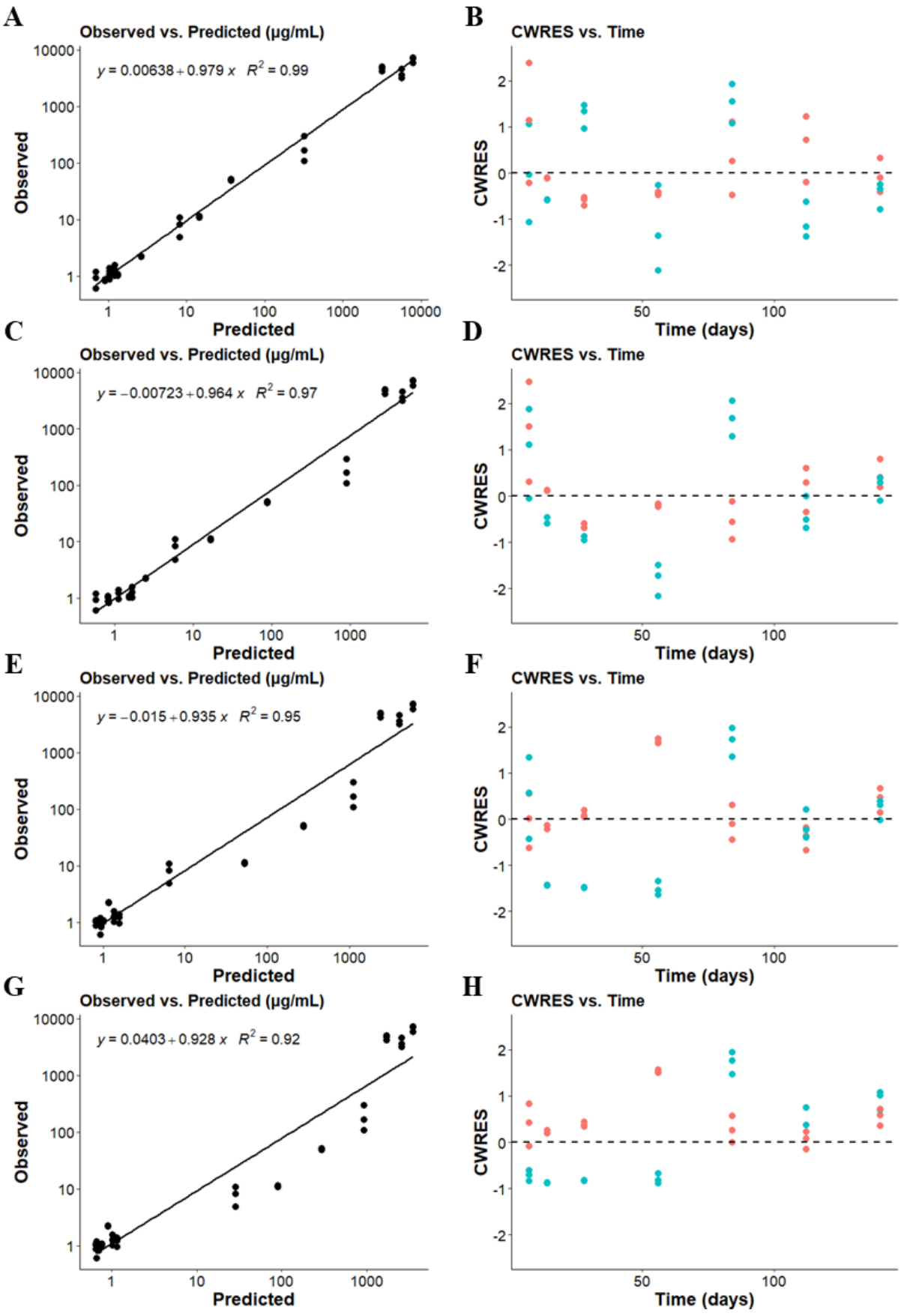
A
Observed vs. Predicted (µg/mL)
y = 0.00638 + 0.979 x R² = 0.99
Observed
Predicted
B
CWRES vs. Time
CWRES
Time (days)
C
Observed vs. Predicted (µg/mL)
y = −0.00723 + 0.964 x R² = 0.97
Observed
Predicted
D
CWRES vs. Time
CWRES
Time (days)
E
Observed vs. Predicted (µg/mL)
y = −0.015 + 0.935 x R² = 0.95
Observed
Predicted
F
CWRES vs. Time
CWRES
Time (days)
G
Observed vs. Predicted (µg/mL)
y = 0.0403 + 0.928 x R² = 0.92
Observed
Predicted
H
CWRES vs. Time
CWRES
Time (days)

Supplemental Figure A.3: Supplemental diagnostic plots. A and B are residual plots of the rational square root function. C and D are residual plots of the log growth function. E and F are plots for the linear function. And plots G and H are residual plots of the 3-compartment model. A, C, E, and G are plots of the observations vs. predictions and B, D, F, and H are plots of the conditional weighted residuals.

A.3 Supplemental Equations

Supplemental Equation A.1: Akaike Information Criterion

AIC=2*K+OFV

The Akaike information criterion was calculated by multiplying 2 times the number of parameters (K) plus the resultant objective function value (OFV) reported in NONMEM [15].

Supplemental Equation A.2: Combined Dose Fraction

$$DF_{comb}(t) = \frac{Mass_{spleen} * Conc_{pred}(t)/\delta}{Dose_{total}(\mathrm{t})}$$

Cumulative dose fraction (DFcomb(t)) was calculated to estimate quantity of dose expected to be sequestered as drug is continuously loaded into mice at each timepoint in weeks. Where Masspleen is the mass of the spleen, Concpred(t) is the predicted concentration at timepoint t, and Dosetotal(t) is the total administered dose up until timepoint t. The average mass of the spleen in the experiment is 0.179g and the density (δ) of the spleen was assumed to be 1.0 g/mL.

Supplemental Equation A.3: Individual Dose Fraction

$$DF_{ind}(t) = \frac{Mass_{spleen} * Conc_{pred}(t)/\delta - Mass_{Drug}(t^*)}{Dose_{total}(t - t^*)}$$

Individual dose fraction (DFind(t)) was calculated to estimate the quantity of a single dose that is sequestered as the total sequestered mass is increased. The predicted dose fraction since the previous timepoint is divided by the total dose since the previous time point. Where t is the time in weeks, and t* is the time in weeks at which the previous measurement was recorded.

Supplemental Equation A.4: Total Volume of Distribution

$$Vd = V1 + V2 + \cdots + Vn$$

Vd is the total volume of distribution calculated by the sum of the volume in all compartments. Most models used in this study were 2 compartment models.

Supplemental Equation A.5: Model Half-Life

$$T_{\frac{1}{2}} = 0.693/K_e$$

Half-life was determined based on 1st order elimination.

A.4 References

See chapter 2 for reference details.

Appendix B: Supplemental Materials for Chapter 3

B.1 Statistical Analysis of Population Pharmacokinetics

To establish the relative importance of parameters B1, B2 and B3 on the systemic pharmacokinetics of clofazimine (CFZ), we used the Root Mean Squared Logarithmic Error (RMSLE) as a measure of error (Figure B.1A).

Supplemental Equation B.1: Root Mean Squared Logarithmic Error

$$RMSLE = \sqrt{\sum(\log(y_{predicted}) - \log(y_{actual}))^2}$$

RMSLE more accurately resembles error in order of magnitude by using the difference in natural logarithms between the adjusted parameter model and the optimized model at each timepoint instead of the exact difference used in the more standard Root Mean Squared Error (RMSE) analysis.

B.2 THETA Outputs From NONMEM

The optimized model constants defined in the $THETA record were recorded as well as the OFV in the table below.

Supplemental Table B.1: Constant Values in the $THETA Record

OFV	K_e	^K_{12}	K_{21}	^V_1	V_2	B_1	B_2	B_3
188.79	0.107 (54.1%)	0.183	2.16 (53.4%)	2.43	0.00533 (2.00%)	*1150 (32.3%)	80.2 (3.20%)	*8.84 (36.5%)

^*Fixed parameter estimates from the soluble phase model*
**Parameters with ETA values*

B.3 Diagnostic Plots of Parameter Sensitivity Analysis

To further monitor the effect of parameter changes on prediction accuracy, the observed CFZ concentration in each compartment was plotted on the y-axis with a corresponding model-predicted concentration for each data point plotted on the x-axis. A fully optimized model would then have the same observed and predicted concentration for each model, corresponding to the linear regression equation y=x, which has a slope of 1. Models optimized with different parameters can thus be compared by calculating a linear regression line for these plots and comparing slope, with values nearer to 1 corresponding to more accurate models. The optimized RSR model (blue in the plots B, C, and D of Figure B.1) uses a regression line with slope 0.84 and the altered parameter models show lines with a higher slope or lower slope to indicate underestimation or overestimation, respectively. These plots make it even more obvious that variations in B2 cause far more significant extent than the other two parameters.

A

Parameter	RMSLE for 10-fold Increase	RMSLE for 10-fold Decrease	OFV for 10-fold Increase	OFV for 10-fold Decrease
B_1	0.239	0.321	316.419	209.998
B_2	0.749	0.297	335.703	326.066
B_3	0.237	0.314	317.759	211.809

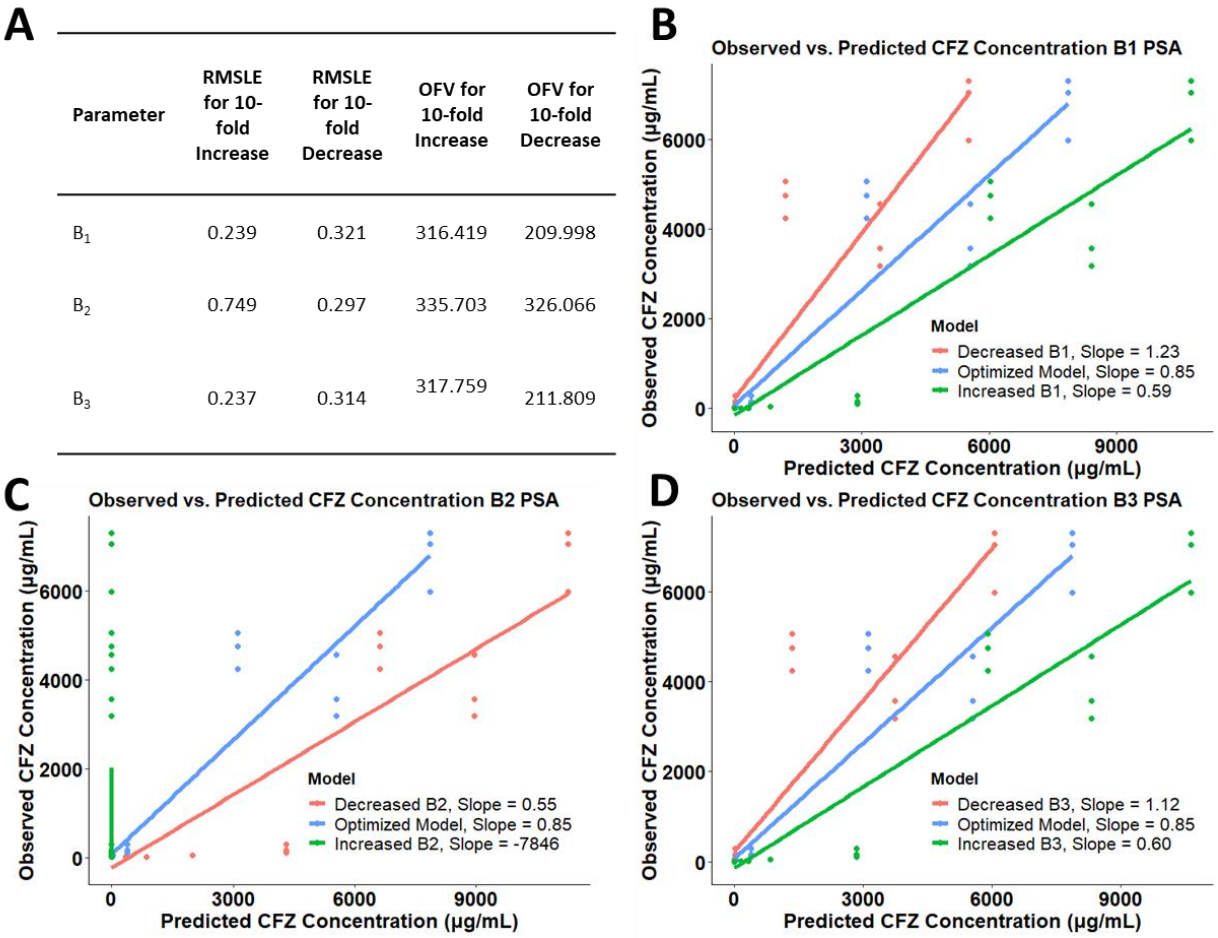

Supplemental Figure B.1: PSA Diagnostic Plots. Table A shows the Root Mean Squared Logarithmic Error (RMSLE) for each PSA. B, C, and D show observed CFZ concentration plotted against model predicted CFZ concentration with regression lines, where more accurate regression lines produce slopes closer to 1. Plot B shows the PSA results for B1, Plot C for B2, and Plot D for B3. Plots were generated for a 10-fold decrease in parameter value (red), the base model (blue), and a 10-fold increase in parameter value (green).

As B1 set a limit for the maximal cargo capacity of the spleen macrophages, a natural question that followed was whether the total volume of the spleen ever approached an upper limit during the 20-week time course of the treatment regimen. Plotting total volume of distribution Vtotal over time, we observed that in the optimized model, the curve begins to flatten around 100 days (Figure B.2C, green line). Thus, the B1 parameter is of physiological relevance, and is not simply acting as a scaling factor. Accordingly, splenomegaly and the

increase in xenobiotic sequestering macrophage population are candidate biological mechanisms associated with this parameter under the experimental conditions used in this study. Interestingly, the estimated half-life calculated for different values of B1 (Figure B.2D) all show an upper limit at around approximately 100 days of treatment. While this half-life is an estimate from calculations, it follows that the increased cargo capacity in the spleen will parallel the nonlinear increase in half-life. Indeed, in mice treated with CFZ for many weeks, CLDIs can remain in the mice for several months after treatment has been discontinued [7].

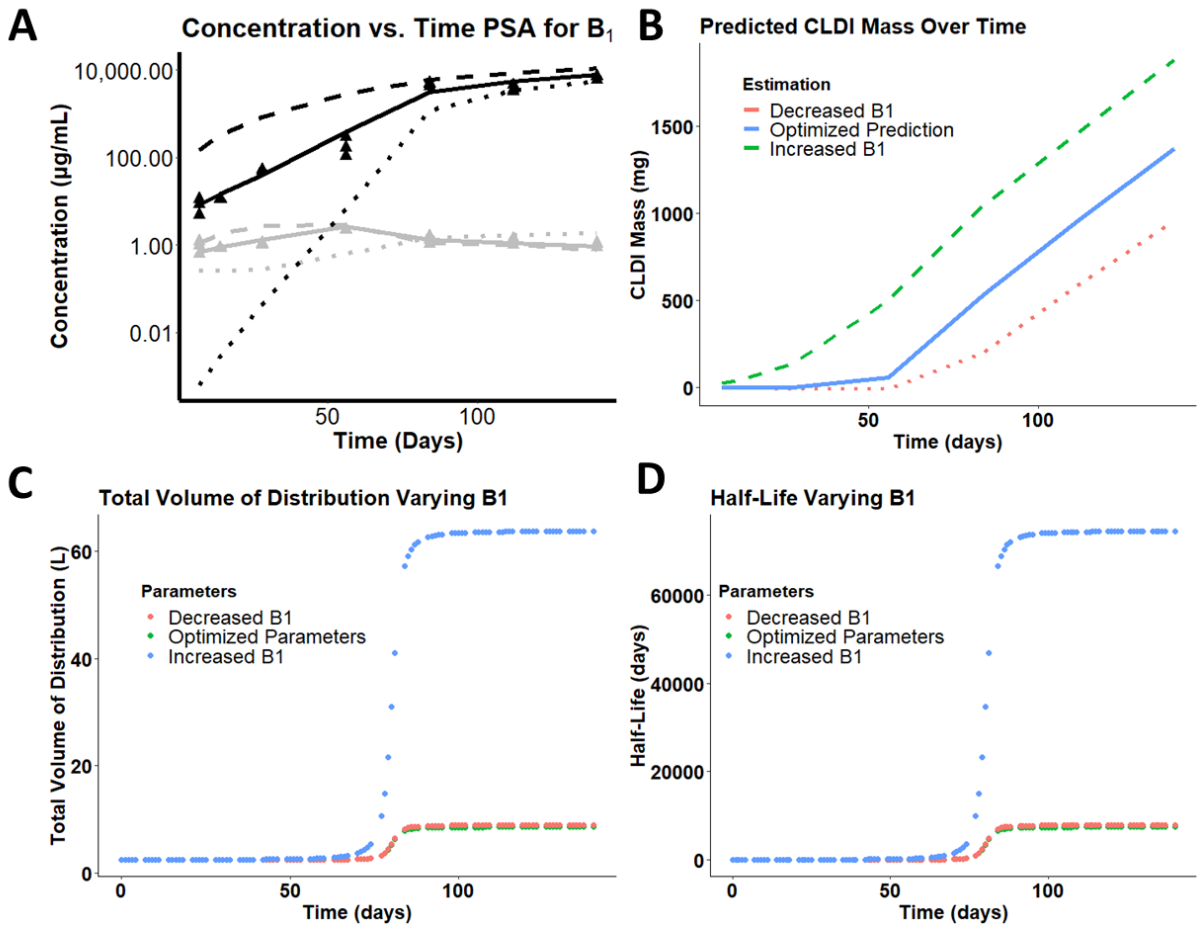

Supplemental Figure B.2: Pharmacokinetic Analysis of B1 A) Plot showing the effect of varying B1 on the concentration over time profile of CFZ in the serum (orange) and spleen (blue) based on a 10-fold increase or decrease of B1 relative to the optimally fitted parameter value. B) Plot showing the effect of varying B1 on the

predicted CLDI mass in the spleen over time. C) Plot showing the effect of varying B1 on the total volume of distribution. D) Plot showing the effect of varying B1 on the estimated half-life.

Changing parameter B2 in the RSR function led to a shift in the inflection point of the output of f(t), in which larger values represent a delay in the expansion of the volume of distribution in relation to the amount of time the mice have been treated, as well as the amount of drug administered to the mice. This parameter is also related to how much CFZ must be given to the organism before the spleen and the associated xenobiotic sequestering macrophages that are found therein will begin to accumulate significant amounts of precipitated CFZ as CLDIs. This parameter will also reflect the treatment time at which the maximal spleen cargo loading capacity will be reached. An important pharmacokinetic question regarding B2 is whether the inflection found in f(t) causes real impact on the model. Thus, by changing B2 by an order of magnitude, we can study a range of behaviors in models using modulated inflection in the f(t) function Figure B.3). For example, Figure B.3C shows the altered Vtotal over time plot with ±10-fold changes in B2, wherein an increased B2 decreased the amount of time that volume of distribution was near its upper limit and a decreased B2 increased the amount of time volume of distribution was near its upper limit. We see that in either of these cases, the inflection curvature has been replaced by more linear behavior. When parameter B2 shifted the curve significantly to later time points, there was very little predicted CFZ mass accumulation in the spleen (Figure B.3A) with very little associated CLDI formation (Figure B.3B). While a 10-fold increase in B2 all but eliminated CLDI formation, a 10-fold decrease in B2 created a linear relationship between CLDI mass and time which overpredicted CLDI formation during early timepoints (Figure B.3B). The changes induced by increasing or decreasing B2 on the Total volume of distribution (Figure B.3C) and the half-life (Figure B.3D) closely paralleled each other, as expected. Accordingly, a

faster expansion of the volume of distribution was associated with a faster increase in half-life, and a slower or undetectable expansion in the volume of distribution was associated with no effect on the half-life.

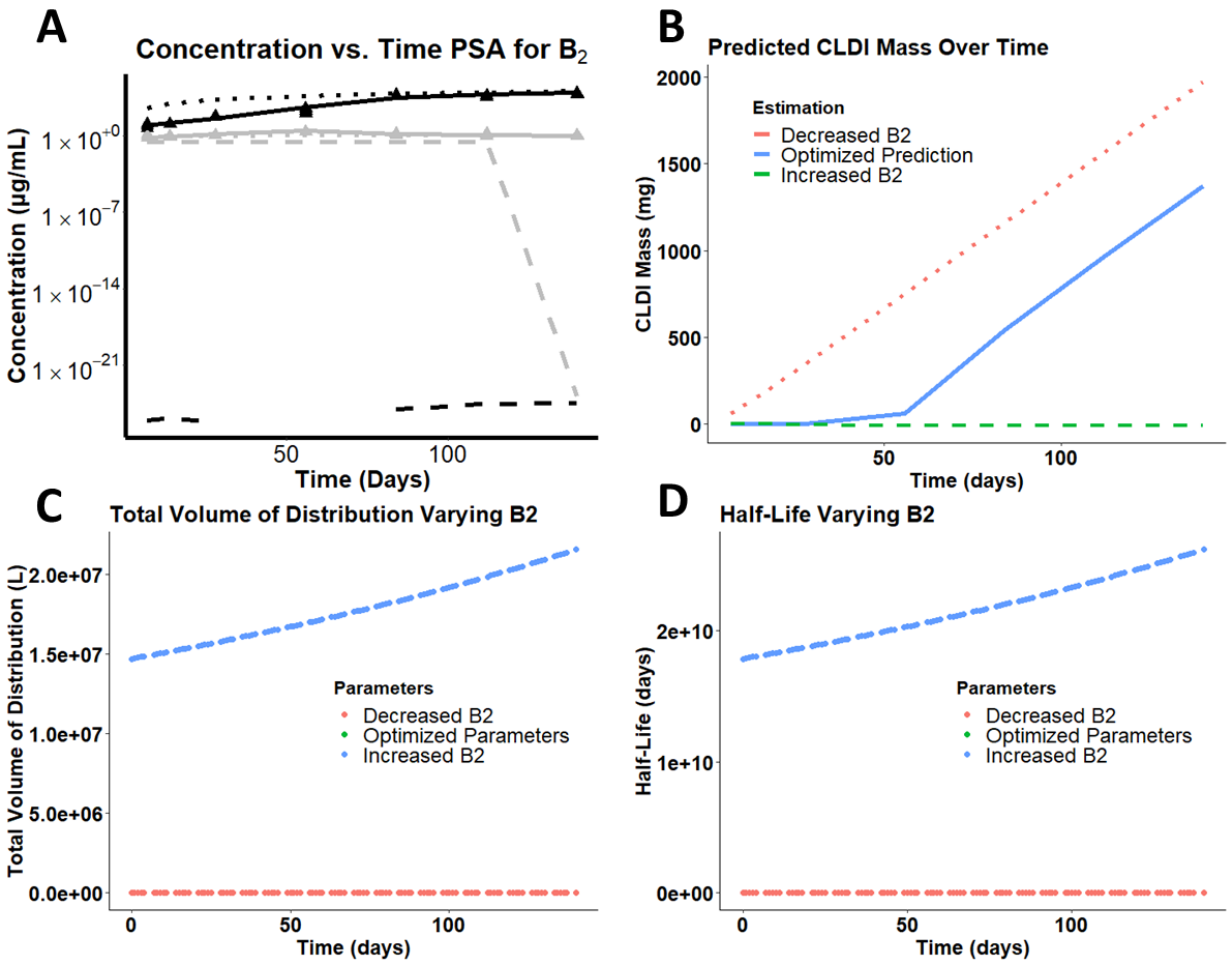

Supplemental Figure B.3: Pharmacokinetic Analysis of B2 A) Plot showing the effect of varying B2 on the concentration over time profile off CFZ in the serum (orange) and spleen (blue)based on 10-fold increase (dotted) and decrease (dashed) in the B2 parameter values (relative to the optimally fitted curve). B) Plot showing the effect of varying B2 on the predicted CLDI mass in the spleen over time. C) Plot showing the effect of varying B2 on the total volume of distribution. D) Plot showing the effect of varying B2 on the estimated half-life.

Parameter B3 in the RSR equation governing function f(t) provided an additional degree of freedom to fully capture the way the phase, affecting the slope and overall curvature of the expansion function. Reflecting the rate of precipitation of CFZ in the spleen as CLDIs, B3 manifests itself in the slope of f(t) at the time of inflection point of the curve generated by f(t). As such, B3 changes the 'maximal phase transition rate,' with an increased B3 decreasing this rate, and thus flattening the shape of the curve governed by function f(t).

To study the effect of B3 on the systemic pharmacokinetics of CFZ, simulations were performed by increasing or decreasing this parameter 10-fold (Figure B.4). Looking at the effects of B3 on CFZ concentrations in the blood and spleen, most of the impact associated with varying this parameter was on the spleen concentrations of the drug during the first 100 days of treatment (Figure B.4A). Relative to the optimized B3 value, increasing B3 mostly affected the amount of CLDI accumulation during the first fifty days of treatment (Figure B.4B). The effect of varying B3 on the increase in the Total volume of distribution over time (Figure B.4C) was relatively less sensitive than the effects of B1 (Figure B.4C) and B2 (Figure B.4C). Similarly, the effect on half-life paralleled the effects on Vtotal (Figure B.4D) and these effects were small compared to those exerted by parameters B1 (Figure B.4D) and B2 (Figure B.4D).

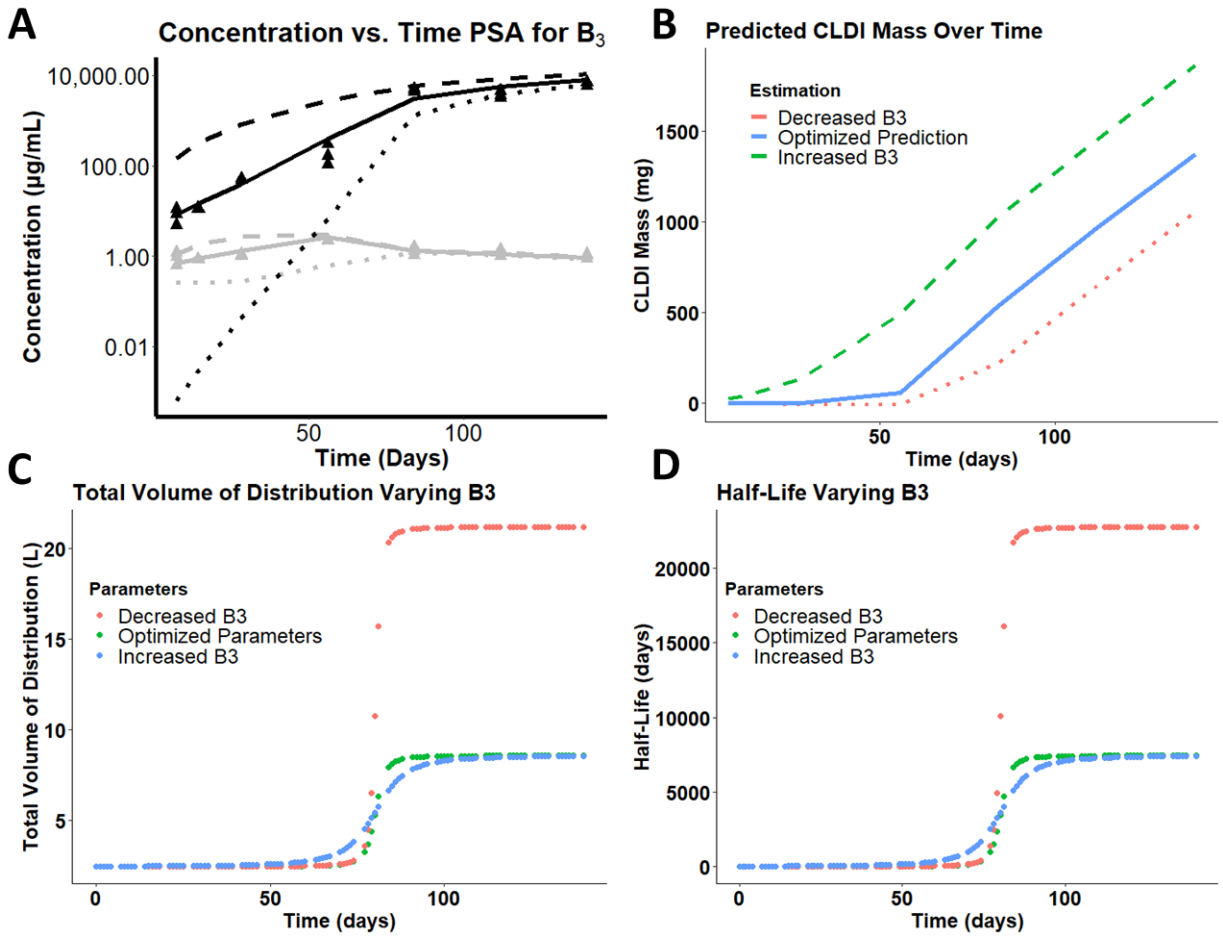

Supplemental Figure B.4: Pharmacokinetic Analysis of B3 A) Plot showing the changes in concentration over time profile following a 10-fold increase (red)decrease (green) in B3, using pharmacokinetic data for serum (orange) and spleen (blue). B) Plot showing the effect of varying B3 on the predicted CLDI mass in the spleen over time, C) Plot showing the effect of varying B3 on the total volume of distribution. D)Plot showing the effect of varying B3 on the estimated half-life.

Appendix C: Supplemental Materials for Chapter 4

Supplemental Table C.1: Cellular drug accumulation parameters for the Virtual Cell model (awillmer: Macrophage Cargo Capacity)

Symbol	Description	Value	Units
init $C_{T,E}$	Initial total extracellular drug concentration	10	μM
init $C_{T,C}$	Initial total cytoplasmic drug concentration	0	μM
init $C_{T,M}$	Initial total mitochondrial drug concentration	0	μM
init $C_{T,L}$	Initial total lysosomal drug concentration	0	μM
init $C_{T,CM}$	Initial total cell membrane drug concentration	0	μM
init $C_{T,MM}$	Initial total mitochondrial membrane drug concentration	0	μM
init $C_{T,LM}$	Initial total lysosomal membrane drug concentration	0	μM
$[Cl^-]_L$	Lysosomal chloride concentration	110	mM
pH_E	Extracellular pH	7.4	
pH_C	Cytoplasmic pH	7.2	
pH_M	Mitochondrial pH	8	
pH_L	Lysosomal pH	4.5	
L_E	Extracellular lipid fraction	0	
L_C	Cytoplasmic lipid fraction	0.05	
L_M	Mitochondrial lipid fraction	0.05	
L_L	Lysosomal lipid fraction	0.05	
W_E	Extracellular water fraction	1	
W_C	Cytoplasmic water fraction	0.95	
W_M	Mitochondrial water fraction	0.95	
W_L	Lysosomal water fraction	0.95	
γ_n*	Activity coefficient of unionized drug	1	
γ_d*	Activity coefficient of ionized drug	0.74	
Ψ_{CM}	Cell membrane potential	-70	mV
Ψ_{MM}	Mitochondrial membrane potential	-160	mV
Ψ_{LM}	Lysosomal membrane potential	10	mV
V_E	Extracellular volume	$1x10^{-4}$	L
D_C	Cytoplasmic diameter	12.4	μm
D_M	Mitochondrial diameter	5.76	μm
D_L	Lysosomal diameter	5.76	μm

** activity coefficients of unionized and ionized molecules were obtained from the literature(1). The physicochemical properties were obtained from experimental data fitting (2) for CFZ free base and CFZ-HCl salt. The diameters of the cellular compartments were used to calculate volume and surface area, assuming spherical geometry.*

C.1 Theoretical calculations of the concentration of neutral and protonated (charged) species of a weakly basic drug molecule in different subcellular compartments

The total drug concentration output obtained after running the Virtual Cell model is comprised of the concentration of the neutral and ionized forms of the drug:

Supplemental Equation C.1: Total Drug Concentration

$$C_T = [B] + [BH^+]$$

Where CT is the total drug concentration, [B] is the concentration of the neutral drug, and [BH+] is the concentration of the ionized drug.

Thus, using equation (C.1) and the Henderson-Hasselbalch equation (equation C.2), we calculated the concentrations of the neutral and ionized forms of the weak base drug from the total drug concentration in the extracellular, cytoplasm, mitochondria, and lysosome:

Supplemental Equation C.2: Henderson-Hasselbalch

$$pH - pK_a = \log\frac{[B]}{[BH^+]}$$

Determining the degree of supersaturation of the neutral and protonated drug species in the different subcellular compartments

Drug concentration above thermodynamic drug solubility leads to supersaturation(3). Thus, using experimentally determined thermodynamic solubility value of the free base and

protonated species of drug in aqueous media and octanol, we estimated the degree of supersaturation –DS(n)- of the free base as follows(3):

Supplemental Equation C.3: Degree of Supersaturation of the Free Base

$$\mathrm{DS(n)} = \frac{[\mathrm{B}]}{[\mathrm{B}]_s}$$

Where [B] is the steady state, free base drug concentration in aqueous compartment, and [B]s is the experimentally measured thermodynamic solubility of the free base drug in water. Similarly, we estimated the degree of supersaturation (DS+) of the charged protonated species in aqueous media as follows:

Supplemental Equation C.4: Degree of Supersaturation of the Protonated Species

$$\mathrm{DS(+)} = \frac{[\mathrm{BH^+}] \times [\mathrm{Cl^-}]}{K_{\mathrm{sp}}}$$

Where Ksp is the solubility product of the salt form of the drug, [BH+] is the dissolved concentration of the ionized drug, and [Cl-] is the chloride concertation that interacts with the ionized drug through ion-ion interaction, producing the salt solubility product of the drug. Using pHmax and the intrinsic free base solubility of CFZ obtained from the literature(4), the Ksp was calculated assuming the counterion forms a 1:1 complex with the drug, using the following relationship:

Supplemental Equation C.5: Ksp of CFZ in the Lysosome

$$K_{sp} = \left(\frac{[B]_s}{10^{pH_{max} - pK_a}}\right)^2$$

C.2 Biochemical Analysis of Drug Concentrations in Plasma

Mobile phase A was 5 mM ammonium acetate, adjusted to pH 9.9 with ammonium hydroxide, and mobile phase B was acetonitrile. The flow rate was 0.35 ml/min, with a linear gradient from 50 to 100% phase B over 1.5 min, followed by holding at 100% for 1.5 min, a return to 50% phase B, and then re-equilibration for 2.5 min. The mass spectrometer source conditions were set as follows: 325°C, gas flow at 10 liters/min, nebulizer at 40 lb/in2, capillary at 4,000 V, and positive ion mode. The MS acquisition parameters were as follows: MRM mode, transition 1 set at 473.1 to 1:431.1, a dwell time of 400 ms, fragmentor set at 180, a collision energy of 40; transition 2 set at 473.1 to 429.1, a dwell time of 100 ms, fragmentor set at 180, and a collision energy of 40.

C.3 References

1. Zhang X, Shedden K, Rosania GR. A cell-based molecular transport simulator for pharmacokinetic prediction and cheminformatic exploration. Mol Pharm. 2006;3(6):704-716.
2. Woldemichael T, Keswani RK, Rzeczycki PM, Murashov MD, LaLone V, Gregorka B, Swanson JA, Stringer KA, Rosania GR. Reverse Engineering the Intracellular Self-Assembly of a Functional Mechanopharmaceutical Device. Scientific reports. 2018;8(1):2934.
3. Hens B, Brouwers J, Corsetti M, Augustijns P. Supersaturation and Precipitation of Posaconazole Upon Entry in the Upper Small Intestine in Humans. J Pharm Sci. 2016;105(9):2677-2684.
4. Bergstrom CA, Luthman K, Artursson P. Accuracy of calculated pH-dependent aqueous drug solubility. Eur J Pharm Sci. 2004;22(5):387-398.

Appendix D: Supplemental Materials for Chapter 6

D.1 Surgical Operation

Mice who received surgical operations were anesthetized with isoflurane 5%. A 5mg/kg carprofen injection, followed by a 2mg/kg lidocaine injection was then administered under 2.5% isoflurane maintenance. Scissors were used to open a surgical site at a pre-shaved and sterilized section of the mouse's body. Then, the spleen was pulled out from the upper left abdominal quadrant, where the spleen was either removed (splenectomy group) or returned into the abdominal cavity (sham surgery group). To close the wound, the muscle layer was sutured, and the skin was glued together. Ten days of postoperative monitoring were conducted, during which a 5mg/kg carprofen injection was administered 48 hours after the operation.

D.2 Mass Spectrometry

Tissue samples were weighed and homogenized with either 10 times (spleen and lung) or 15 times (liver) volume of 80% N-Dimethylformamide (DMF)-PBS solution, and vertex-mixed. No dilution of lung samples was conducted, but liver and spleen samples were diluted 20 times with 1X PBS and vortex mixed. A calibration curve was prepared with concentration range from 1 – 50 µg/ml of Clofazimine in respective blank tissues. Analytical curves were constructed by plotting the peak area ratio of Clofazimine to the internal standard versus the concentration. The concentration range was evaluated from 1 – 50 µg/ml for quantification. A blank sample (matrix sample processed without internal standard) was used to exclude contamination or interference. The curves were built with linear regression with weighing (1/X or 1/X^2).

D.3 Skin Absorbance of Clofazimine (CFZ)

The high lipophilicity of clofazimine leads to profound partitioning into the skin, causing pigmentation. [1] To assess CFZ distribution to the skin, relative changes in CFZ induced pigmentation was evaluated in mouse ears. Previous studies have demonstrated that CFZ concentration in the skin can be assessed through absorption wavelengths which correspond to different phases of CFZ deposition. [2] The free base form of CFZ was shown to maximally absorb visible light at 450 nm, while the hydrochloride salt of CFZ has a shifted visible absorbance peak at 495 nm. [3] The extent of clofazimine accumulation in the skin was evaluated in mice undergoing surgical asplenia. Four available single-band bandpass optical filters were placed onto an iPhone 13 camera lens for image acquisition. These optical filters screened light at 450 nm, 485 nm, 528 nm, and 620 nm. The flash, high dynamic range (HDR), and night mode options on the camera were disabled. Camera editing filters were not applied. Images of the severed ear sourced from each mouse were captured immediately after euthanasia. Quantification of skin pigmentation was performed using ImageJ image processing software.

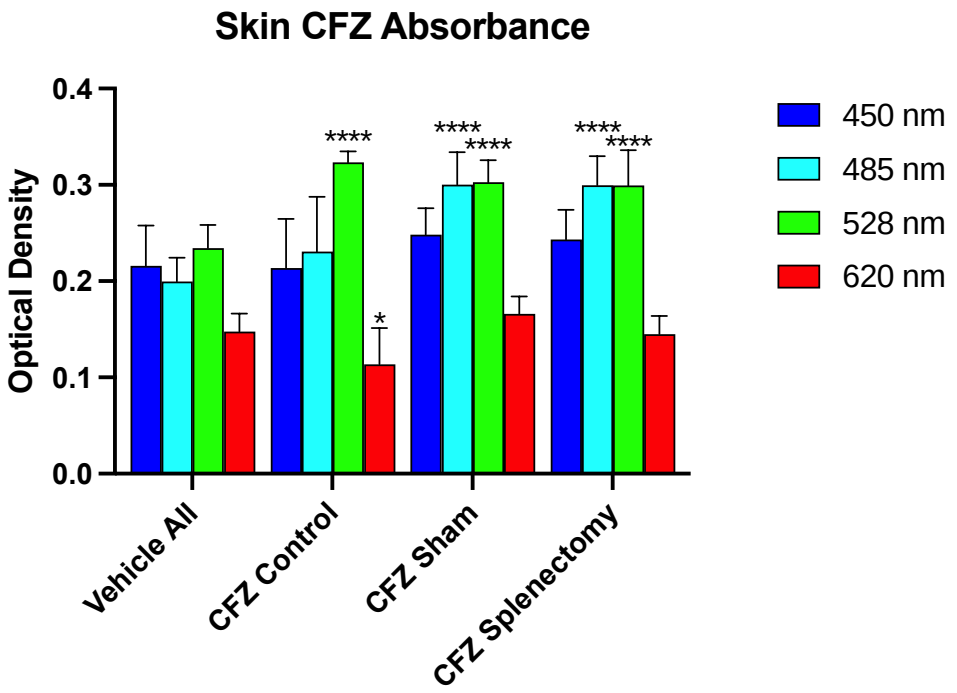

Supplemental Figure D.1: Quantitative analysis of CFZ concentration in the skin after 8 weeks of CFZ treatment. Vehicle All corresponds to the combined average of all vehicle treated groups (vehicle control, vehicle sham, and vehicle splenectomy) Mean ± SD for each group are shown with four different band-pass filters. For a given wavelength, significant differences compared to the vehicle mice are marked. (blue = 450 nm filter; cyan = 485 nm filter; green = 528 nm filter; red = 620 nm filter).
($p < 0.05$, **p< ,*** p< ,**** $p < 0.0001$, ANOVA single factor, Tukey's HSD).*

Significance was determined by performing ANOVA single factor with Tukey's HSD test in GraphPad Prism. The comparisons were made between the clofazimine treated splenectomy mice, clofazimine treated sham mice, clofazimine treated unoperated mice, and all vehicle treated mice regardless of operation at each wavelength. Significant differences in optical density were observed between vehicle-treated mice and clofazimine-treated mice regardless of surgical procedure at 528 nm, indicating the presence of CLDIs. However, no significant absorbance differences were observed between splenectomy, sham, nor unoperated mice at 528 nm. Clofazimine-treated mice did have significant differences in absorbance at 485 nm depending on whether they received surgery, but the surgical operation performed – sham or splenectomy – did not produce significant differences in absorbance. Vehicle treated mice had

significantly lower absorbances at 485 nm than either CFZ-treated sham or splenectomy mice, but not unoperated CFZ-treated mice. At 620 nm, significant differences in absorbance were observed between vehicle mice and CFZ-treated unoperated mice, and CFZ-treated unoperated mice and CFZ-treated sham mice. Significant differences in optical density were not observed between splenectomy and sham surgery mice at any wavelength. No significant differences between any groups were observed at 450 nm.

Clofazimine treatment produced differences in skin absorbance, in agreement with previous studies describing its pigmentation qualities. Across all wavelengths, the loss of spleen does not produce significant changes in CFZ-induced skin pigmentation when compared to general surgical trauma.

D.4 Additional Cytokine Analysis

Significant differences in cytokines compared to controls are provided for splenectomy (fig D.2A) sham (fig D.2B), and CFZ (fig D.2C) compared to vehicle fed control.

A

Vehicle Splenectomy compared to Vehicle Control

Label	% Change	P-Value	Function
No differences			

B

Vehicle Laparotomy compared to Vehicle Control

Label	% Change	P-Value	Function
TIMP-1	-24%	2.16E-02	Pro-inflammatory, regulates matrix metalloprotienases regulating wound healing
C5	-23%	3.49E-02	Pro-inflammatory, key component in pathogen membrane disruption

C

CFZ Control compared to Vehicle Control

Label	% Change	P-Value	Function
TIMP-1	538%	7.53E-06	Regulates matrix metalloprotienases regulating wound healing, ECM composition
IL1-RA	346%	4.81E-04	Anti-Inflammatory, inhibits macrophage activation
I-TAC	215%	2.01E-02	chemotactic for T-cells
IL-16	170%	3.77E-03	Chemoattractant, pro-inflammatory
TREM-1	148%	8.25E-03	Activates macrophages and potentiates their inflammatory cytokine production
MIP-2	114%	3.63E-02	Macrophage-produced neutrophil chemoattractant
TNF-alpha	83%	3.34E-02	Amplifies macrophage cytokine production, pro-inflammatory

Supplemental Figure D.2: Cytokines analysis compared to control.

D.5 Supplemental Equations

Supplemental Equation D.1: Spleen-Independent Fraction of Drug Sequestered

$$FS(Organ) = \frac{CFZ\ Mass\ in\ Organ}{Total\ CFZ\ Mass\ - CFZ\ Spleen\ Mass}$$

D.6 References

1. Tang, Shenjie et al. “Clofazimine for the treatment of multidrug-resistant tuberculosis: prospective, multicenter, randomized controlled study in China.” *Clinical infectious diseases : an official publication of the Infectious Diseases Society of America* vol. 60,9 (2015): 1361-7.
2. Murashov, Mikhail D et al. “The Physicochemical Basis of Clofazimine-Induced Skin Pigmentation.” *The Journal of investigative dermatology* vol. 138,3 (2018): 697-703. doi:10.1016/j.jid.2017.09.031

3. Min KA, Rajeswaran WG, Oldenbourg R, Harris G, Keswani RK, Chiang M, et al. Massive Bioaccumulation and Self-Assembly of Phenazine Compounds in Live Cells. Adv Sci (Weinh). 2015; 2(8)